Investigation on the Use of Wall Reflections to Simulate Wave Energy Converter Array Effects

by

Brian John Winship
MSc(Hydrodynamics and Ocean Engineering)
B.Eng(Hon)(Mechanical)

Submitted in fulfilment of the requirements for the degree of Doctor of Philosophy

National Centre for Maritime Engineering and Hydrodynamics
Australian Maritime College
University of Tasmania

July, 2019

The full text with supporting videos is available at: https://cloudstor.aarnet.edu.au/plus/s/iWWrFApMNNZ3DEs

Declarations

Originality

This thesis contains no material which has been accepted for a degree or diploma by the University or any other institution, except by way of background information and duly acknowledged in the thesis, and to the best of my knowledge and belief no material previously published or written by another person except where due acknowledgement is made in the text of the thesis, nor does the thesis contain any material that infringes copyright.

Signed: _____
Brian John Winship

Date: 15 July 2019

Co-Authorship

The following individuals have contributed to the publications presented for this thesis:

- Brian John Winship, AMC, University of Tasmania (**Candidate**)
- Dr Alan Fleming, AMC, University of Tasmania (**Author 1**)
- Assoc. Prof. Gregor Macfarlane, AMC, University of Tasmania (**Author 2**)
- Assoc. Prof. Irene Penesis, AMC, University of Tasmania (**Author 3**)
- Dr Mark Hemer, CSIRO (**Author 4**)

Publications and proportion of work:

1. **Preliminary investigation on the use of tank wall reflections to model WEC array effects**

   This publication is a journal article which presents the initial study presented in this thesis, the contents are split between Chapters 2 and 3; with the full text presented in Appendix F.1. The work consists of experimental and numerical studies of a cylinder in a channel and the measurement accuracy of stereo-videogrammetry. The candidate was lead author and contributed 70 % to design, planning and execution of the experiments as well as writing. Authors 1 and 3 contributed 10 % to design of experiments as well as critical revision of the paper. Author 2 contributed 5 % to experimental design while Author 4 contributed 5 % to critical revisions.

2. **Application of photogrammetry for spatial free surface elevation and velocity measurement in wave flumes**

   This publication is a journal article which describes the development of the stereo-videogrammetry approach and presents a case study, this case study is distinct from the PhD research. This article is presented in Appendix F.2. The candidate contributed 10 % to experimental design and manuscript preparation. Author 1 was the lead author and contributed to 80 % to experimental design and manuscript preparation. Author 2 contributed 10 % to experimental design and critical revisions.

We the undersigned agree with the above stated proportion of "work undertaken" for each of the above published (or submitted) peer-reviewed manuscipts contributing to this thesis.

Signed:

Assoc. Prof. Irene Penesis *Primary Supervisor* National Centre for Maritime Engineering and Hydrodynamics Australian Maritime College University of Tasmania	Dr Vikram Garaniya *Acting Director* National Centre for Maritime Engineering and Hydrodynamics Australian Maritime College University of Tasmania
Date: 15 July 2019	Date: 15 July 2019

Abstract

Wave Energy Converter (WEC) technologies are under development internationally. WECs are of value to society as alternatives to geological hydrocarbons, with depleting reserves and concerns of the implications of anthropogenic climate change. The development of WECs will at some point require devices to be placed in groups or arrays; such arrangements induce hydrodynamic effects which have the potential to materially affect energy capture. These hydrodynamic array effects need to be understood to maximise return on investment. However, simulation of large arrays, both experimentally and numerically, can be prohibitively expensive. This work explores the use of reflections to simulate WEC array effects as an approach to reducing the cost of array investigations; this is done numerically with linear potential flow and experimentally in the Australian Maritime College's towing tank. The experimental investigation includes the use of novel experimental techniques including stereo-videogrammetry and the implementation of a real-time control system for modelling a WEC Power Take Off (PTO).

The results show it is possible to explore WEC array interactions with the use of wall reflections. This approach can reduce the overall cost of experimental array investigations, thereby allowing further studies to be completed and ultimately reducing the cost of commercial WEC arrays. Through this exploration it has been shown that phase is just as important as amplitude for understanding WEC array interactions. As amplitude describes the potential interaction effect, but without an understanding of phase it is not possible to know if the interactions are constructive, destructive or neutral.

Adjunct to this, the stereo-videogrammetry approach employed is shown to be able to measure an area of approximately 12 m^2 with a 3 mm horizontal discretisation and sub-millimetre accuracy on the vertical measurement. This novel measurement approach has the potential to be useful to investigations ranging from validation of theoretical wave models through to assessment of wave-structure interactions in commercial development. While the approach, at present, is expensive to implement, it has capabilities which conventional wave probes cannot match. For example the large spatial area considered and velocity measurements.

In the numerical study, the linearized investigations of diffraction and heave radiation showed very good correlation with experimental results, with respect to both loads and free surface deformation. For the relaxed condition where a PTO system was employed it is shown that the linearized assumption allowed for accurate prediction of power capture, however did not allow for accurate prediction of the resulting wave climate. This suggests that for different array arrangements that more complicated modelling may be required.

Through the numerical modelling it was evident that wave shoaling must be taking place. This implicitly means that the results are incomplete, as shoaling requires that there must be additional harmonics for loads and free surface deformations. Such harmonic components are not able to be considered by linear potential flow.

There is further work which can be completed based on the material in this thesis. While the linear PTO system employed was functional, extending the study to more advanced control strategies would be beneficial to enable higher energy capture. In addition, comparing the experimental results presented here with more advanced numerical models, such as Computational Fluid Dynamics, that are able to better capture the nonlinear dynamics of the WEC should be considered. Lastly, the novel use of stereo-videogrammetry to look at the free surface effects could be applied to other WEC devices (and hydrodynamic problems) where complex fluid-structure interactions are important to understand their design including a range of analytical models.

Acknowledgements

There is the obvious acknowledgement to my supervisors Irene Penesis, Mark Hemer, Alan Fleming and Gregor Macfarlane for the advice, encouregment and patience in assisting me in completing this thesis. To the others from around AMC, like Nick Johsnon, Jean-Roch Nader, Tom Mitchell Ferguson, Jarrah Orphin, Ahmed Elhanafi and Aidan Bharath to name a few, that have listened to my at times outlandish ideas. The longsuffering technical support from the towing tank team Liam Honeychurch, Tim Lilienthal, Kirk Meyer and Adam Rolls as well as the various interns and undergraduate students whom I've worked with.

The funding by CSIRO Oceans and Atmosphere Climate Research Centre and the Australian Renewable Energy Agency (ARENA) Emerging Renewables Program (ERP A00521 – The Australian Wave Energy Atlas Project), as well as access to resources through the ARENA Emerging Renewable Program (ERP A00575 - Towards an Australian Capability in Arrays of Ocean Wave-Power Machines). The conversations with various project stakeholders has been very informative, especially the team at Carnegie Clean Energy, Ashkan Rafiee, Daniel Taylor and Alireza Valizadeh.

Finally to my family, the support you've offered has been priceless.

Table of Contents

List of Figures

List of Tables

Nomenclature

Abbreviations

Abbreviation	Description
2D/3D	Two/Three Dimensional
ARENA	Australian Renewable Energy Agency
AWavEA	Australian Wave Energy Atlas
BA	Buoyant Actuator
CFD	Computational Fluid Dynamics
CSIRO	Commonwealth Scientific and Industrial Research Organisation
DIC	Digital Image Correlation
DoF	Degree of Freedom
FFT	Fast Fourier Transform
IR	Infra-red
ITTC	International Towing Tank Conference
PID	Proportional, Integral and Derivative
PIV	Particle Image Velocimetry
PTO	Power Take Off
PWEP	Perth Wave Energy Project
RAO	Response Amplitude Operator
RCW	Relative Capture Width
RMSE	Root Mean Square Error
UV	Ultraviolet
WEC	Wave Energy Converter
WP	Wave Probe

Constants

Symbol	Description	Value	Units
ρ	Density of Water	1000	kg/m^3
g	Acceleration due to Gravity	9.81	m/s^2

Dimensionless Numbers

Symbol	Description	Definition
ν_{WA}	Array Non-Dimensional Linear Wavenumber	$\frac{\lambda}{L_A}$
ν_{WD}	Device Non-Dimensional Linear Wavenumber	$\frac{\lambda}{L_D}$
F_{ND-D}	Non-Dimensional Normalised Diffraction Force	$\frac{F_{ex}}{aA_w g\rho}$
F_{ND-R}	Non-Dimensional Normalised Radiation Force	$\frac{F_R}{aA_w g\rho}$
M_{ND-D}	Non-Dimensional Normalised Diffraction Moment	$\frac{M_{ex}}{aL_D A_w g\rho}$

Arithmetic Symbols

Symbol	Description	Definition	Units
ϵ_A	Absolute Error	-	–
ϵ_R	Relative Error	-	–
η	Surface Elevation	-	m
η_D	Diffraction Surface Elevation Component	-	m
η_I	Incident Surface Elevation Component	-	m
η_R	Radiation Surface Elevation Component	-	m
η_S	Scattered Surface Elevation Component	-	m
λ	Wavelength	-	m
ω	Angular Frequency	$\frac{2\pi}{T}$	rad/s
θ	Wave Direction	-	deg
ζ	Mooring Extension	-	m
ζ_0	Mooring Extension Zero Point	-	m
A	Hydrodynamic Added Mass Coefficient	-	kg

a	Wave Amplitude	-	m
A_w	Wetted Surface Area	-	m^2
B	Radiation Damping Coefficient	-	$N.s/m$
B_{PTO}	PTO Damping Coefficient	-	$N.s/m$
d	Water Depth	-	m
F	Force	-	N
k	Wave Number	$\frac{2\pi}{\lambda}$	rad/m
K_{PTO}	PTO Spring Stiffness Coefficient	-	N/m
L_A	Array Critical Dimension	-	m
L_D	Device Diameter	-	m
L_H	Device Height	-	m
M	Moment	-	$N.m$
M_{PTO}	PTO Added Mass Coefficient	-	$N.s^2/m$
P	Power	-	$-$
T	Wave Period	-	s
t	Elapsed Time	-	s
X	X Position	-	m
Y	Y Position	-	m
$\boldsymbol{x}$	Position Vector	-	m

Chapter 1

Introduction

1.1 Introduction

Any object which is located within a fluid domain will interact with that fluid; these interactions are reciprocal and so result in dynamic coupling. There are a range of such coupling mechanisms including viscous stress, dynamic pressure, turbulence or compressibility as examples. These mechanisms can be leveraged so as to extract energy from natural phenomena such as wind, river flows, tides or ocean waves; the mechanisms which extract this energy are broadly termed renewable energy devices. The development of these technologies is of value to society as alternatives to energy from geological hydrocarbons, especially as reserves deplete and as a response to the implications of anthropogenic climate change. This research focuses on Wave Energy Converters (WECs), that capture the energy in surface ocean waves.

It is implicit for any WEC that an interaction with the natural (incident) wave climate will occur; it is typical for these interactions to be segregated into what are termed diffraction and radiation (Budar and Falnes 1975; Falnes and Kurniawan 2015). In maritime hydrodynamics, the diffraction problem describes the results induced when subjecting a stationary structure to incident waves. The radiation problem stems from the energy transferred to the water due to the motions of a structure. Diffraction and radiation problems need to occur for energy conversion to take place. Falnes and Kurniawan (2015) provides a recent synthesis of the underlying theorems important to WEC hydrodynamics.

There are many types of WEC operating principles in a range of stages of development around the world; common examples include point absorbers, oscillating water columns or wave surge converters (Babarit, Hals, et al. 2012). Irrespective of device operating principle it is intrinsic that any deployment of WECs will cause a variation in the natural wave field. A single WEC, with a capacity on the order of 100kW-1MW will have only limited effect on the surrounding wave field. However, if wave energy is to be a notable contributor to the world's energy needs, then WECs must be deployed in arrays of devices, or in 'WEC farms'. The deployment of an array of devices increases the importance of the wave field variation, with the introduction of intra-array effects and exacerbation of extra-array effects (collectively referred to as array effects) (Babarit 2013; Folley, Babarit, et al. 2012; Stratigaki

2014). Intra-array interactions are those which relate how the variation of the wave climate caused by one device will affect the performance of any other device. These interactions will affect the power conversion of WECs, with the potential to either increase or decrease power capture (Babarit 2013). Extra-array effects are the variations of the natural wave field surrounding the array of WECs in the far field. Ocean waves are an important physical process in the near-shore and coastal zones, responsible for maintaining coastal sediment budgets (shoreline position through erosional/accretion processes) and the level of energy is a key characteristic of an ecosystem (Warner et al. 2010). Furthermore, in some locations waves provide opportunities for surfing, which can provide an important economic stimulus for a region (Lazarow et al. 2007). Thus, an important consideration before widespread deployment of WEC arrays is to understand the effects of deployment on the surrounding natural climate via extra-array effects.

WEC development has now progressed to the point where small arrays of WECs are being deployed in-situ. For example, Carnegie Clean Energy Ltd (formerly Carnegie Wave Energy Ltd) deployed an array of three of their proprietary CETO 5 units, each rated at 240 kW, during the year 2015 as part of the Perth Wave Energy Project (Fievez and Sawyer 2015). Concurrent to this deployment Contardo et al. (2018) conducted an investigation to measure the wave attenuation; this work observed a 20% reduction in wind-sea height 40 m down-wave of a single WEC, and a 12% reduction at 80 m. This activity, and those similar, provides a valuable opportunity to learn how the natural wave field responds. However, measuring variation of a natural wave field in-situ is exposed to many factors which makes it more difficult to quantify the effect of a WEC array, particularly when the array is small. An idealised setting, such as in a wave basin or a wave channel provides opportunity to measure the array effects around a scaled device. An alternative to physical testing is numerical modelling, however numerical array modelling is not yet fully validated (Babarit 2013; Folley, Alves, et al. 2016; Folley, Babarit, et al. 2012).

WEC intra-array effects can manifest with a variety of outcomes. Through this thesis they are discretised into three categories with reference to amplitude measurements; they are neutral, positive and negative. Neutral effects refer to conditions where there is no change in amplitude, however change in phase is possible. Positive refers to an increase in amplitude of the relevant measure through constructive interference. While negative is the reciprocal with a decrease in amplitude through destructive interference.

This research has been funded through *The Australian Wave Energy Atlas Project* (CSIRO Oceans and Atmosphere Climate Research Centre and the Australian Renewable Energy Agency (ARENA) ERP A00521) and has been completed in collaboration with *Towards an Australian capability in arrays of ocean wave-power machines* (ARENA ERP A00575). The overarching intent of the thesis is to *develop methods useful for the investigation of WEC*

array effects and *provide context to full scale in-situ measurements*, presented by Contardo et al. (2018).

1.2 Current Status of WEC Array Studies

There have been several extensive reviews published in recent times pertaining to WECs. Greaves and Iglesias (2018) presents a very broad description of the state of development of WECs; including technical, social and economic aspects. Babarit (2018) presents a review focusing on technical aspects, including the historic development of WECs. Folley, Alves, et al. (2016) explores the numerical modelling for the prediction of WEC behaviour and effects. Falnes and Kurniawan (2015) presents the formulation of fundamental equations for assessment of WEC mean power capture. Ringwood, Bacelli, et al. (2014) presents an extensive review on the challenges pertaining to extracting energy with the Power Take Off (PTO). Given these extensive recent reviews by notable researchers in the field, there is no extensive review presented in this thesis.

Modelling of system dynamics frequently involves the linearisation of phenomena to allow for simpler computations (Folley, Alves, et al. 2016). For WEC hydrodynamic studies there are a variety of aspects which can be independently linearised; these include wave dynamics, hydrodynamic (fluid structure) interactions and system dynamics. In the instance of wave dynamics this is characterised by assuming water waves can be represented by sine waves. In hydrodynamic interactions, assumptions of linearity relate to water being inviscid and irrotational, while the system effects can be separated into diffraction and radiation. These assumptions also greatly effect the type of PTO which can be considered and the degrees of freedom of the whole WEC system. Such assumptions of linearity are implemented both numerically (Babarit 2018; Falnes and Kurniawan 2015; Folley, Alves, et al. 2016) and experimentally (McNatt 2016; Nader et al. 2017). As with any assumptions there are however limitations, with many studies finding limitations as applied to WECs (Babarit 2018; Clément and Babarit 2012; Folley, Alves, et al. 2016; Folley, Babarit, et al. 2012; Garcia-Rosa et al. 2015; Greaves and Iglesias 2018; Hals et al. 2011; Orszaghova, Wolgamot, Eatock Taylor, et al. 2017; Orszaghova, Wolgamot, Draper, et al. 2018; Penalba Retes et al. 2015; Rafiee and Fievez 2015; Ringwood, Bacelli, et al. 2014; Ringwood, Ferri, et al. 2017; Wolgamot and Fitzgerald 2015).

With the transition from full scale single device deployments to WECs arrays (Chatzigiannakou et al. 2017; Fievez and Sawyer 2015), there will be a need to design these future arrays. Factors which need to be considered include the cost, environmental effect and hydrodynamic characteristics of different configurations (Greaves and Iglesias 2018). While there have been many numerical models which have been developed for the prediction of hydrodynamic ar-

ray interactions, few have been validated with physical measurements (Folley, Alves, et al. 2016). One of the numerical modelling tools which has been developed to facilitate the commercialisation of WECs is *NEMOH* (Babarit and Delhommeau 2019). *NEMOH* is an open source linear potential flow boundary element method model, which was released in 2015. Experimental investigations for the purpose of validating these numerical models typically see the use of the largest experimental facility available and multiple model scale devices (Haller et al. 2011; Mercadé Ruiz et al. 2017; Nader et al. 2017; O'Boyle et al. 2017; Porter 2012; Stratigaki 2014). Such scale experiments are technically complicated and consequently expensive, due to the many physical models and measurements required. Furthermore, many experimental studies on WEC arrays indicate uncertainty in results due to reflections from the facility walls impacting measurements. As all facilities are different, these reflections vary depending on the experimental facility, as such there is on ongoing need to perform cross-validation between facilities to enable better understanding of facility bias. Limited studies have been conducted between two facilities (Wan et al. 2016) and there is a larger study being conducted (Gaurier et al. 2018; MaRINET2 2019) on addressing these concerns; however at writing the author has no knowledge of a comprehensive published study considering facility bias on WECs or wave structure interactions more broadly. There is a potential that in many instances these reflection effects will dominate array interactions.

Understanding the variation in the wave field for development of full scale WEC arrays has several implications. There is the effect of the hydrodynamic coupling between multiple WECs and the impacts on the broader environment (Babarit 2013; Folley, Babarit, et al. 2012; Hemer et al. 2017; McInnes et al. 2018; Stratigaki 2014). This need is expressed in experimental studies by endeavours to measure the free surface of large domains (Haller et al. 2011; McNatt et al. 2015; McNatt 2016; O'Boyle et al. 2017; Stratigaki 2014). Such studies typically employ arrays of resistive wave probes. An alternative is the use of Digital Image Correlation (DIC) for the purpose of spatial free surface measurement (Black 2014; Fleming, Winship, et al. 2018). Such DIC measurement approaches are still under development with validation and optimisation required for broad acceptance. The primary challenge for DIC in experimental hydrodynamic testing is detecting the water surface in images. This is challenging as the water is typically clean and therefore transparent.

1.3 Research Objectives

This thesis presents the assessment of tools, both experimental and numerical, for the exploration of hydrodynamic WEC intra-array effects. This is explored by using wall reflections to simulate multiple devices and stereo-videogrammetry to measure the free surface effects. By using a single device and wall reflections to simulate array effects, the experimental com-

plexity is greatly reduced, with fewer models required and the possibility of using smaller experimental facilities. In addition, the use of stereo-videogrammetry to measure a large spatial area in a single experimental run is achievable, effectively increasing the value of findings.

This overarching research objective is broken down into the following points:

- *Exploration on the use tank wall reflections to simulate WEC array interactions.*
- *Study on the value of stereo-videogrammetry for WEC array interaction experimental studies.*
- *Consideration of NEMOH, and its linearized assumption, for WEC array interaction studies.*

To answer these questions idealised studies are initially completed. The stereo-videogrammetry measurement approach is assessed for its validity in experimental hydrodynamics. This considers both possible effects of the approach on the results and the accuracy of the measurements. An initial study is used to explore diffraction effects about a cylinder in a channel both experimentally and numerically.

Following the initial study an exploration on the linear components of an actual WEC is conducted. Here the diffraction and heave radiation effects are explored separately with regards to a submerged WEC in a channel. The WEC used in this study is based upon the Carnegie Clean Energy CETO 5 design.

The research concludes by relaxing the linearization and explores the same submerged WEC in a channel. The distinction being a PTO system is employed to simulate all the dynamics important for WEC hydrodynamic array interactions.

1.4 Novel Component

The contributions of the research are the exploration of tools that improve the cost versus value proposition of hydrodynamic WEC interactions studies. The novel aspects of this study are:

- Stereo-videogrammetry
  - Evaluation of stereo-videogrammetry as a tool for wave field measurement in experimental hydrodynamics.
  - Post-processing of DIC results for error identification and correction.

- Wall reflections to simulate WEC array effects
  - Experimental study where wall reflections are considered equivalent to a WEC array.
  - Numerical study in *NEMOH* with a wall to simulate a WEC array.

The measurement of surface deformations with stereo-videogrammetry is a developed tool which is commonly employed in material science studies. The challenges in experimental hydrodynamics for wave measurement primarily relate to detecting the free surface. The approach herein seeds the water with buoyant particles to create a texture. However, to trust the resulting measurement it is necessary to consider the validity of the results compared with conventional wave measurement approaches. With the novelty in the use of stereo-videogrammetry for experimental hydrodynamics the processing has not been optimised for the application. The post-processing of the DIC results presented in this thesis employs hydrodynamic principles for the identification of erroneous measurements.

Many experimental hydrodynamics investigations experience reflections from tank walls which affect results. It is common practice to minimise these reflections so that it is possible to infer open water results. By instead considering these reflections to be a beneficial component of the experiment, there is a potential to leverage more experimental facilities to considering WEC array effects than are currently being employed.

1.5 Outline of Thesis

This thesis is presented as a series of chapters. The structure and content of the chapters is as below.

Chapter 1: In the introductory chapter the problem being researched is presented. The research question and methodology are formulated along with an exploration of prior work pertinent to both. It also includes an outline of the structure of the following chapters.

Chapter 2: An exploration of the viability of a stereo-videogrammetry approach to the hydrodynamic investigations relating to wave structure interactions. It commences by introducing the problems and value of measurement of water waves in experimental facilities. It then presents an approach for stereo-videogrammetry that is employed in this thesis. Studies in this chapter include an exploration of the effects the measurement equipment have on wave dynamics and the accuracy of the measurement. The measurement accuracy study involves a cylinder fixed in a channel to create a non-uniform wave climate. Both studies indicate that the approach is suitable for experimental hydrodynamic investigations, however there are limitations surrounding highly non-linear wave conditions. The stereo-videogrammetry

method described and tested in Chapter 2 is used in all experimental studies presented in subsequent chapters.

Chapter 3: An initial study on the concept of using wall reflections to simulate WEC array effects, the theory of *method of images* is introduced along with *NEMOH*, the numerical tool used through subsequent work. The experimental work includes the same cylinder centrally located in a channel and compares this with a range of numerical simulations. The numerical work considers a range of array arrangements to explore the viability of the approach. The comparisons suggest that the variation between array configurations are negligible, however it is apparent that the largest array simulation is closest to the experimental results.

Chapter 4: This chapter commences by introducing the realistic WEC, the Carnegie Clean Energy CETO 5, which will be used through the subsequent chapters of the thesis; it explores the wave conditions at full scale and completes dimensional analysis to determine the model scale. It then focuses on the diffraction effects by completing numerical and experimental studies using the tools tested above. The numerical work includes an exploration of the effects of the submersion depth on the excitation force characteristics.

Chapter 5: Here the realistic WEC geometry study is extended to consider heave radiation. An analogous submersion depth study is completed numerically with an experimental study for one depth.

Chapter 6: Having completed the study into the linear components pertinent to the energy capture of the realistic WEC, this chapter explores the actual performance of the WEC at model scale. The study implements a linear PTO both numerically and experimentally. The numerical study remains fully linear while the experimental allows aspects of linearity relating to the degrees of freedom of the system to be relaxed. The chapter again includes a numerical study on the effect of submergence depth. A discussion is made on the uncertainty of experiments on WEC array interactions.

Chapter 7: The final chapter provides a summary of the work conducted through the thesis. It presents the key findings of the research and discusses the implications for the development of WEC arrays. It then presents possible future work which extend on the research.

Chapter 2

Assessment of Stereo-Videogrammetry

2.1 Introduction

In experimentation considering interactions between water gravity waves and structures, measurement of the free surface is fundamental. In controlled facilities, such as wave flumes and towing tanks, it is common for single point measurement equipment to be employed. These technologies can largely be described as either non-contact (ultrasonic or optical) or contact (surface following floats, resistive gauges or capacitive gauges); all are capable of sub-millimetre precision with appropriate calibrations and have good temporal resolution (Payne 2008; Payne et al. 2009; Robertson et al. 2018).

For testing where spatial information is required, such as WEC testing (both single device and array), single point measurement technologies can be co-located to inform on the broader wave field. Efforts by Haller et al. (2011), Stratigaki (2014) and McNatt et al. (2015) have seen static arrays of 22, 41 and 59 wave gauges respectively deployed to measure the wave field variation around WEC(s). In a variation O'Boyle et al. (2017) used an approach where 32 wave gauges were iteratively moved around the experimental domain in a series of repeated experiments to quantify the 2D wave field; resulting in 1120 discrete measurement locations over an area measuring 4.65 by 5.1 m. These sequentially larger measurement arrays indicate a clear trend for greater levels of spatial information of the wave field in experiments considering wave structure interactions. This methodology is restricted by the possible proximity of individual gauges before interference occurs, with the minimum spacing being on the order of tens of millimetres. Additionally, the cost of measurement arrays increases proportionally with the number of gauges; as an example, the experiments by McNatt et al. (2015) were only able to measure 22 of the 59 wave gauges per run, requiring multiple repeats to capture a full data set.

Alternative non-contact systems have seen development for the spatial measurement of wave fields, frequently utilising optics in conjunction with digital image correlation (DIC) algorithms. These DIC algorithms are typically based upon combinations of particle image velocimetry (PIV) and stereo-photogrammetry; reviews on the different algorithms are given in Campbell (2014), Fleming, Winship, et al. (2018), and Gallego Bonet (2011). One of

the key challenges in optical surface measurements of water waves is how to discern the free surface, exacerbated in experimental facilities where the water is normally clean enough as to be transparent and the floor visible. In Turney et al. (2009) this challenge is resolved by seeding particles of $\sim 50\mu m$ in the experimental area, over an area of 0.07 by 0.07 m and required approximately three billion particles. While Black (2014) deployed small glass particles and achieved a measurement area of 2.5 by 4 m, this work also compared the stereo-videogrammetry measurements with collocated wave gauges. This error analysis found a variation between measurements to be between 1.8 % and 45.2 %, where the larger variation was associated with poor seeding of the free surface.

The approach employed through this body of work for spatial measurement of water waves is to use neutrally buoyant and fluorescent particles of wax to create a textured image in conjunction with the commercially available software (LaVision 2016) for the image processing. A description of the development is given by Fleming, Winship, et al. (2018), available in Appendix F.2.

This chapter focuses on the assessment of the precise stereo-videogrammetry method applied through this thesis to the measurement of water gravity waves. This comprises the effect of the seeding material on the wave dynamics and the measurement accuracy. In order to create a more complex wave field, a structure in the form of a rigidly mounted cylinder is employed to create a scattered wave climate. Conclusions are drawn around the benefits and limitations of the method and areas where the system can be further improved.

The work described in this chapter is partially drawn from Winship et al. (2018), which is available in Appendix F.1.

2.2 Method

The work discussed in this chapter is drawn from two experimental set-ups; both carried out in the Towing Tank at the Australian Maritime College (University of Tasmania). The facility is 100 m long, 3.55 m wide and the water depth used is 1.5 m; the wave making capabilities are via a single bottom hinged paddle.

The free-surface measurements were accomplished using a stereo-imaging set-up consisting of two cameras with the processing completed with the commercial software DaVis 8.2 (LaVision 2016), with the Surface Flow add-in. The software uses DIC to identify corresponding points in stereoscopic camera image pairs to map the objectives' surface. Through a calibration process, the position of the two cameras relative to the experimental area is determined as well as some characteristics of the lens distortion. Then, with an iterative least square matching (LSM) algorithm equivalent pixels in the two cameras are identified, from which it

is possible to deduce the 3D surface, and the relative pixel locations. Sub-pixel interpolation is achieved with cubic B-spline interpolation. The LSM algorithm is then applied to a subsequent 3D image to deduce the velocity of the particles with an affine transform. The processing uses a region grow pyramid from a user defined seeding point (LaVision 2016).

The DaVis software relies on DIC. For this process to work a texture is required across the image; that is to say recognisable differences are required between different pixels across of the image. The approach employed here to accomplish this is to seed the water with hundreds of thousands of fluorescent particles, approximately 5 x 5 x 1 mm in size. These particles were made of a blend of paraffin wax, carnauba wax and ultraviolet fluorescent pigment in a ratio by mass of 90 : 7.5 : 2.5 respectively. In order to minimise the dispersion of the particles away from the experimental area a pair of fences were deployed immediately up and down wave of the experimental area. These fences were constructed of 60 mm wide strips of 3 mm thick closed cell foam, small lead weights were affixed evenly along the length of the fence to create a righting moment to ensure they sat upright. The fences were connected at the wall with cylindrical floats restricted to a heave motion, these floats had a mass of approximately 400 g, a diameter of 100 mm and height 100 mm. The fence and connection can be seen in Figure 2.1. Fluorescence was accomplished by bathing the particles with a diffused ultraviolet (UV) light, cameras are fitted with lowpass filters to exclude the UV light such that they only capture the orange florescence; this requires that non-UV light sources were minimised.

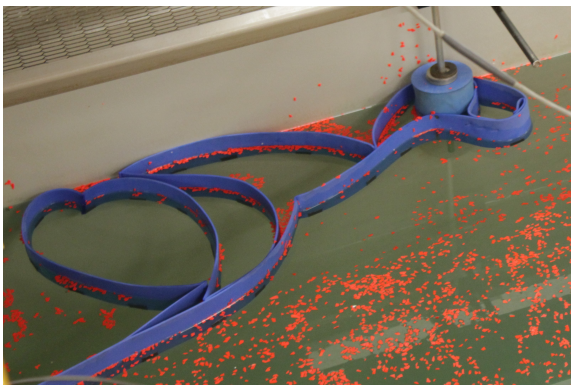

Figure 2.1: Image of one of the particle fences in-situ; top-right of shot shows buoy which connects the fence to the wall. The photo is not with experimental lighting condition.

2.2.1 Effect on Wave Dynamics

In order to assess the effect that the stereo-videogrammetry equipment has on wave dynamics, a series of tests were carried out with an array of four wave gauges, the equipment of interest are the fences and particles. The measurements were conducted with three states of equipment deployment,

1. No stereo-videogrammetry equipment.
2. Particle fences in place with no particles.
3. Particles and fences in place.

The wave conditions employed for this wave dynamics study were with a wave amplitude of 25 mm and frequencies of 0.6, 0.8 and 1.0 Hz. Details of the layout of the wave probes (WP) is given in Table 2.1.

Table 2.1: Resistive Wave Probe Positions. Origin is the wave paddle on the longitudinal centreline of the facility, with positive x being the direction of wave propagation.

Label	**x-Coordinate (m)**	**y-Coordinate (m)**
Incident	5.825	-1.425
WP 1	14.06	1.375
WP 2	15.1	1.375
WP 3	16.13	1.375

Measurements were compared between the three different states, the absolute error (ϵ_A) is found by,

$$\epsilon_A(t) = M_R(t) - M_T(t) \tag{2.1}$$

where the no equipment arrangement was assumed the reference measurement (M_R) and the alternate arrangements considered the test measurement (M_T). From this the relative error (ϵ_R) is found,

$$\epsilon_R(t) = \frac{|\epsilon_A(t)|}{a} \tag{2.2}$$

where a is the incident wave amplitude. The root mean square error (RMSE) of each error is then found

$$RMSE_i = \sqrt{\epsilon_i^2} \tag{2.3}$$

where i relates to either the absolute or relative error, depending on what is of interest. This process compares the instantaneous free surface elevation and not the wave statistics of amplitude or frequency.

2.2.2 Measurement Accuracy

To assess measurement accuracy, it was decided that a wave field more complicated than a 2D regular wave was necessary. As such a cylinder was fixed mid channel in the wave flume

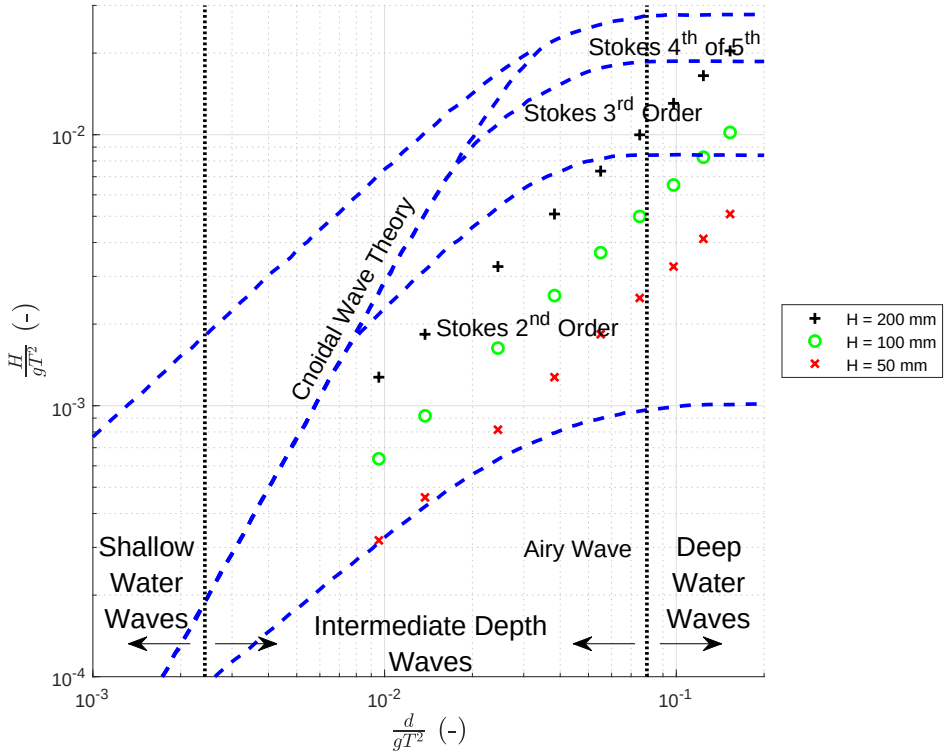

Figure 2.2: Characteristic of experimental wave conditions (Le Méhauteé 1976). H is wave height, T is wave period, d is water depth and g is gravitational acceleration.

in order to create a symmetrical scattered wave field. The cylinder had a diameter of 315 mm and a height of 1800 mm, it was positioned 100 mm above the tank floor and 20 m from the wave paddle. Fixing was such that pitch and roll excitation moments about the bottom fixing point were measured. The characteristics of the waves employed are presented in Figure 2.2, the specific conditions are:

- Amplitude: 25, 50 and 100 mm.
- Frequencies: 0.25, 0.3, 0.4, 0.5, 0.6, 0.7, 0.8, 0.9 and 1.0 Hz.

The cylinder was placed on the centreline of the wave flume (using the assumption of symmetry) hence allowing for half the tank width to be reserved for the stereo-videogrammetry while on the opposite side an array of 11 wave gauges were positioned. This was necessary as direct line of sight is required for the cameras. The cameras used were two Baser ACE 12-bit, 4 megapixel USB3 cameras, each fitted with a Kowa 6mm LM6HC, 1.5 X Edmund optics lens extender and c mount orange long pass filter (Midopt LP550-25.4). They were mounted in conjunction with five UV light sources as shown in Figure 2.5. The ultraviolet lights (stage washlights) were reflected off the ceiling to create a diffused light field over the water surface. Images were captured in synchronised image pairs, from the two cameras, at 25 Hz. The experimental set-up is shown in Figures 2.3 and 2.4 with a photograph and a

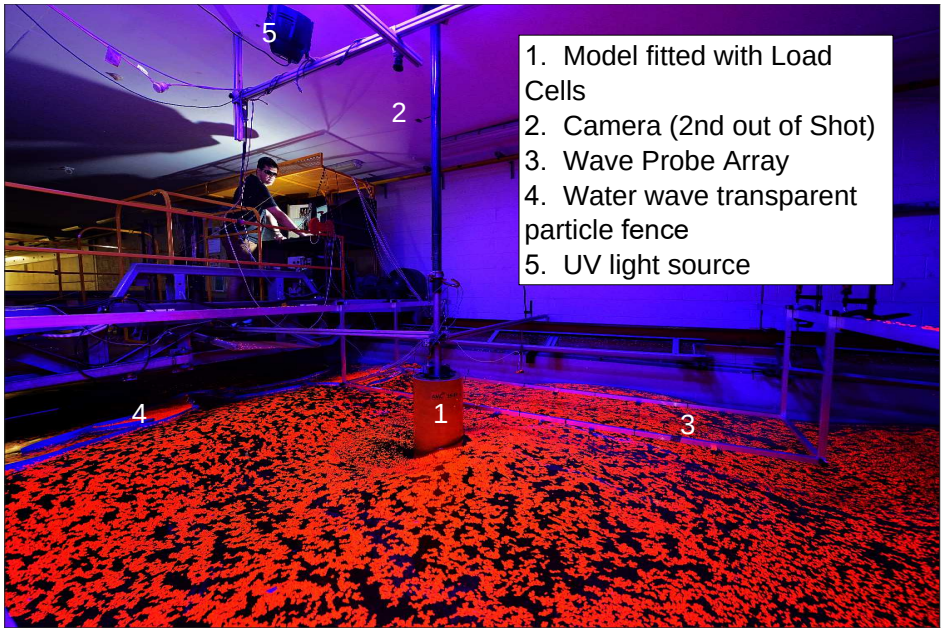

Figure 2.3: Photograph of experimental setup.

schematic respectively. From Figure 2.3 it can be seen that the particle seeding extends beyond the measurement area; this is a result of two mechanisms. The particles will naturally drift and disperse through weak dispersive forces if left for extended periods (hours-days) and will also be dispersed by the hydrodynamic forces during experimental tests. Furthermore, it was decided not to put an additional fence down to centreline of the tank to control particle dispersion on this axis. Consequently the full tank width was seeded with particles.

The calibration process for the photometric measurement requires a series of images be taken with different views of a calibration plate (LaVision 2016). The calibration plate used was 2.4 m x 2.4 m, white in colour with an array of black dots (50 mm spacing, 10 mm diameter). The calibration plate was mounted on a polystyrene sheet such that it could be floated in the experimental area, the plate sitting 49 mm above the water free surface. The images for the calibration were taken by keeping the relative position of the cameras fixed while moving the cameras relative to the calibration plate. Examples of one image set is given in Figure 2.6, two sets were used for the calibration. With the calibration complete, it was important that the camera properties are not altered; this includes aperture, focus and relative position. The resulting calibration coefficients are given in Appendix A in Table A.1.

As discussed above, the stereo-videogrammetry approach requires that the water be seeded with particles. The left image in Figure 2.7 gives a sample of the particle density used in these experiments, in this installation the particles were approximately 5x5 pixels on the image. The DaVis output employed is this surface, a sample with still water is given in the top right plot of Figure 2.7. The processing was completed within the DaVis Surface Flow

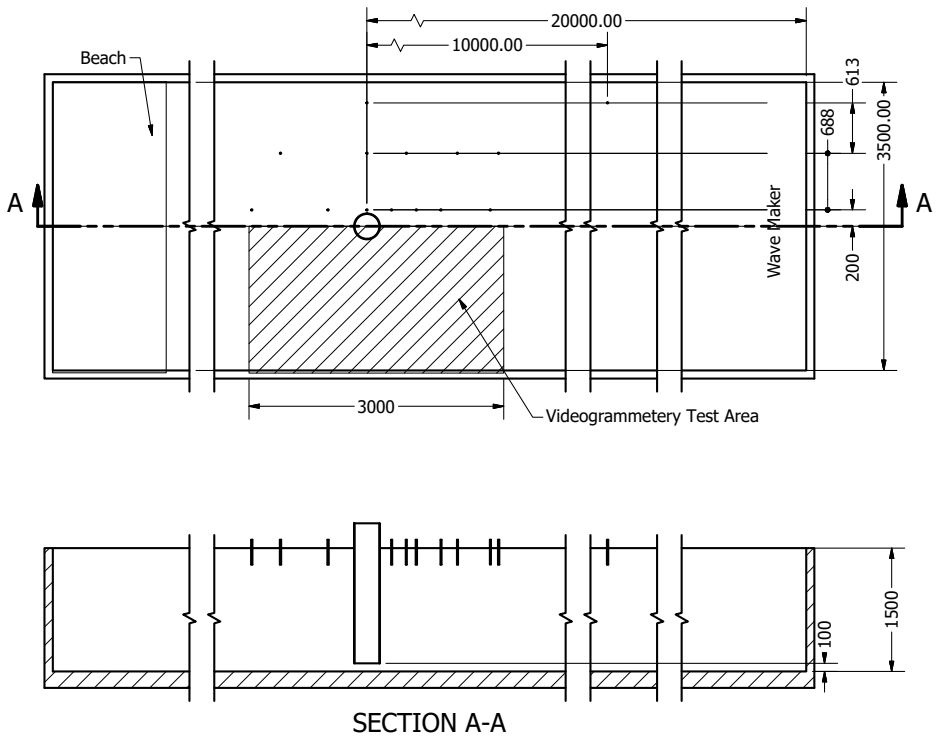

Figure 2.4: Schematic of experimental setup.

Figure 2.5: UV wash lights on a frame directed towards the ceiling to diffuse light for even distribution on the water surface.

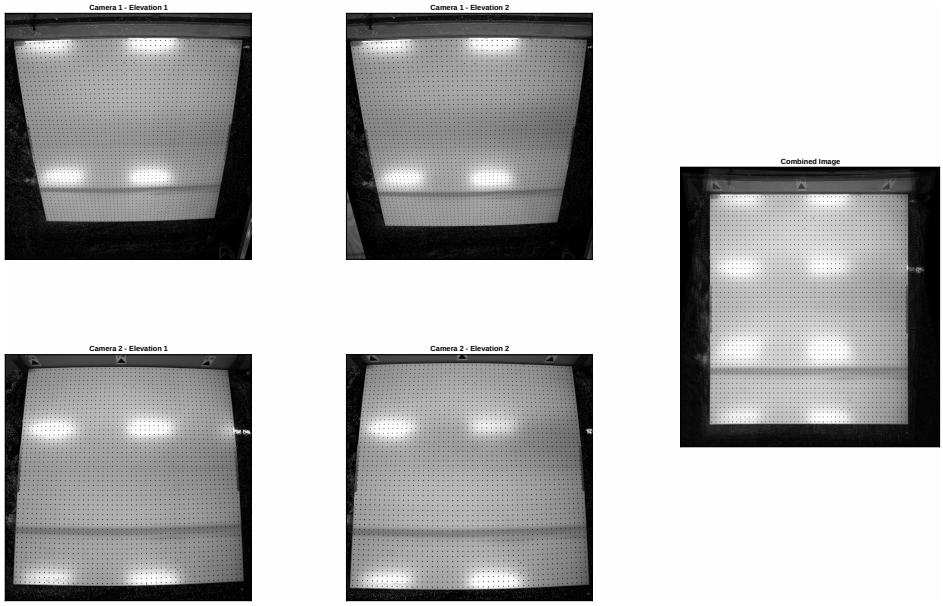

Figure 2.6: Calibration raw images and final corrected image.

environment, the processing settings used were subset size = 33, step size = 9, calculation mode = fast, and maximum expected pixel displacement = 50 pixels. It can be seen that along the continuous surface there is a variation of 10 mm, and localised discontinuities where jumps in the surface which exceed 25 mm vertically within 15 mm on the horizontal plane. These discontinuities are clearly fictitious and are a legacy of a poor match in the DIC, where the errors are not corrected. This poor match is partially a result of insufficient particles in the measurement area, as such subsequent testing presented in this thesis greatly increased the seeding density resulting in less issues relating to this.

To address the localised discontinuities it is recalled that free surface elevation for regular linear waves is defined by (2.4), where η is the surface elevation, a is the wave amplitude, k is the wave number, θ is the wave direction, ω is the angular frequency and t is time.

$$\eta(x, y, t) = acos(k(xcos\theta + ysin\theta) - \omega t) \tag{2.4}$$

From which it can be shown that the maximum of the absolute of the gradient can be expressed by,

$$max(|\nabla\eta(x, y)|) = ka \tag{2.5}$$

Taking this relationship for maximum wave gradient; it can be inferred that any location greatly exceeding this gradient is fictitious. Allowing for some variation from this single linear wave component, the regions with a gradient ($|\nabla\eta(x, y)| \geq 2ka$) are considered erroneous.

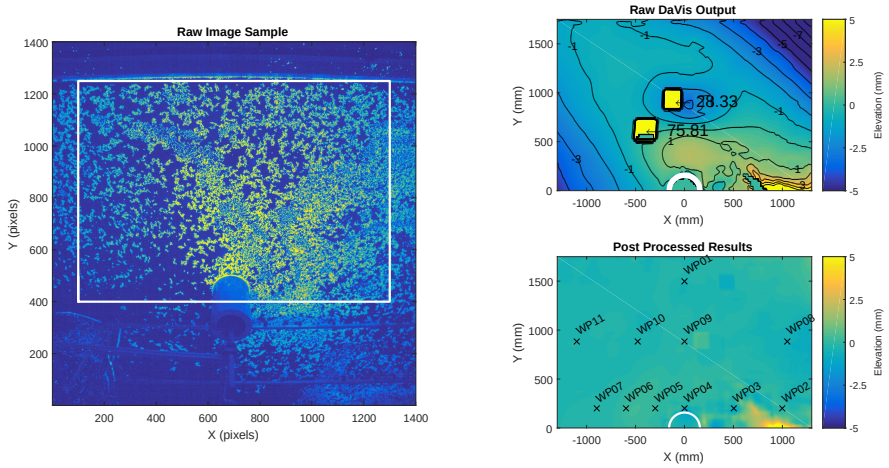

Figure 2.7: Still water condition. (Left) Raw image used for processing, one of a pair with area investigated highlighted (Top Right) Elevation Plot output from DaVis (Bottom Right) Post processed surface & Wave probe positions.

In addition, regions bound by high steepness areas and within 4 pixels are discarded. The holes left by the error rejection are then filled from the outer most pixels; the filling process computes the discrete Laplacian over the region and solves the Dirichlet boundary value problem. While this filtering criteria may erroneously remove correctly measured areas, for example close to the structure, this research is more focused on the large spatial area.

To resolve the variation in elevation, a zero surface was subtracted from all raw surfaces results. This zero surface was the result of an average across 50 frames of the still water condition. Where the discontinuities were ignored through averaging, interpolation occurs across the average zero surface. A sample of the resulting corrected zero surface is given in the bottom right of Figure 2.7; this plot also indicates the analogous positions of the wave gauges.

The DIC processing was completed on a PC with 64 GB RAM and with two Intel Xeon E5-2630v2 CPU, which results in 24 logical processors @ 2.6 GHz processing speed. This setup resulted in processing times of roughly 10 seconds per frame. The post DaVis processing (error removal) was completed on a machine with 16 GB RAM with an Intel Core i7-4770 CPU with 8 logical processors @ 3.4 GHz processing speed. Post processing takes approximately 2 s per frame. Raw data volume was 3.5 MB per frame and processed totals 10 MB per frame.

From the processed data the time series analogous to the wave gauge location, given in the bottom right of Figure 2.7, are determined. The absolute and relative errors were then determined using (2.1) and (2.2) respectively, where the wave gauge measurements constituted the reference and the surface flow measured. The RMSE for both the absolute and relative errors were then determined with (2.3).

2.3 Results

2.3.1 Wave Dynamics

The variation in the wave dynamics induced by the stereo-videogrammetry is explored initially in the time domain in Figure 2.8. The nominal wave condition is 0.8 Hz frequency and 25 mm amplitude. For these tests there is no model in the experimental area. The top plot is for the incident wave gauge, which is located between the wavemaker and the start of the experimental area, and the bottom plot is for a location in the centre of the experimental area. Both plots have four time series displayed for comparison. These include a clear water condition; two runs with the particle fences in place; and a run where the particles were in the experimental area. This qualitative comparison indicates that there is exceptional agreement between shape and frequency, with a very slight variation in peak values (< 0.5 mm). As the wave probes were not moved between runs, this variation can be attributed to either equipment effects or lack of repeatability in the wavemaker.

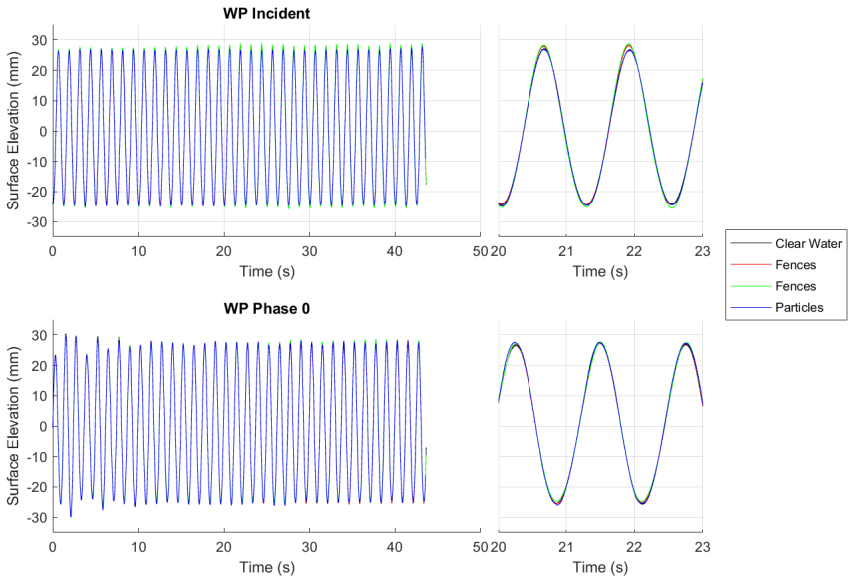

Figure 2.8: Time comparison between wave gauge measurements to assess effect of stereo-videogrammetry equipment on wave dynamics for 0.8 Hz 25 mm. (Left) extended time series (Right) restricted time series.

A quantitative study on the discrepancies between experimental set-up conditions is presented in Figure 2.9, this plot shows relative RMSE for the three frequency conditions explored in this study. The data is differentiated by the incident wave gauge, which should be consistent, and the experimental set-up for the other wave gauges. This plot indicates that irrespective of wave gauge location or experimental equipment, the variation between set-ups is in the range of 1-5 %. This testing was restricted to limited conditions, with an expectation that

the effects of the particles become less important at lower wave frequencies.

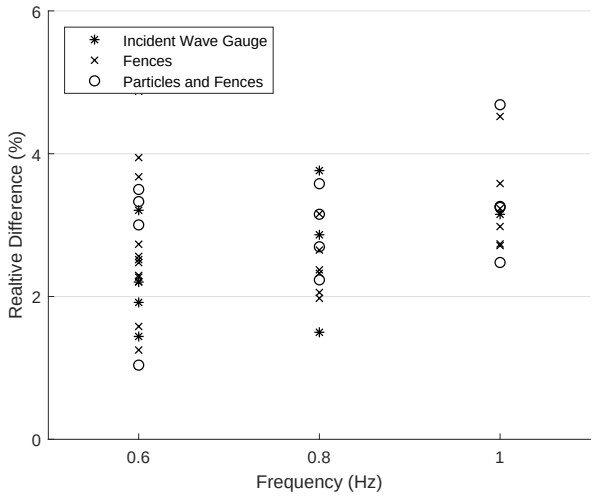

Figure 2.9: Relative error study of wave gauge measurements to assess effect of stereo-videogrammetry equipment on wave dynamics.

2.3.2 Measurement Accuracy

The comparison between the wave gauges and the stereo videogrammetry is of importance due to the relative novelty of the stereo videogrammetry approach. All experimental results presented are for a setup with the cylinder present. A time domain comparison for a wave with frequency 0.9 Hz and amplitude 25 mm at WP 10 is given in Figure 2.10, the top plot is an overlay of the two approaches and the bottom presents the relative and absolute errors. For this condition it is clear that there is very good agreement, with only slight discrepancies around the crests and troughs.

A similar comparison is made in Figure 2.11 except the condition has a frequency of 1.0 Hz and amplitude 50 mm and location WP 06. These plots show that for the period of t=0-10 s a similar accuracy is evident to the previous condition. Following this, very large instantaneous error occurs around 12.5 s; these errors are due to entire time steps failing to compute correctly. The accuracy returns until 15 s at which point errors increase until the processing completely fails at 22 s. These increasing errors and eventual failure to compute have been attributed to the particles being dispersed by non-linear wave drift effects, from Figure 2.2 this condition is from Stokes 3^{rd} order.

Extending the investigation from the two runs given above to all test conditions, the RMSE is compared with wave steepness in Figure 2.12. Wave steepness is used as RMSE varies with both the wave frequency and amplitude. The conditions ranged in frequency from 0.25 Hz to 1.0 Hz and amplitude from 25 mm to 100 mm. The left plot shows a comparison between the RMSE of each run and the wave steepness while the right shows the processing failure rate

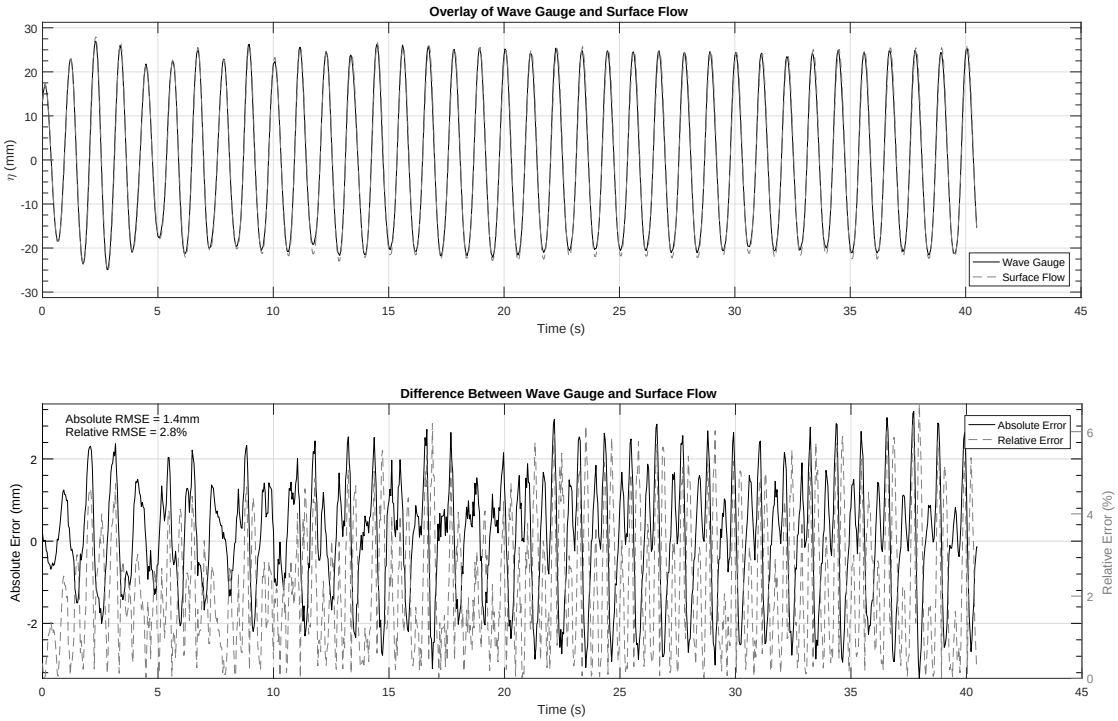

Figure 2.10: Comparison between wave gauge and DaVis measurements for a wave with frequency of 0.9 Hz and amplitude of 25 mm (Top) Overlay (Bottom) Absolute Error on Left Axis and Relative error on Right Axis.

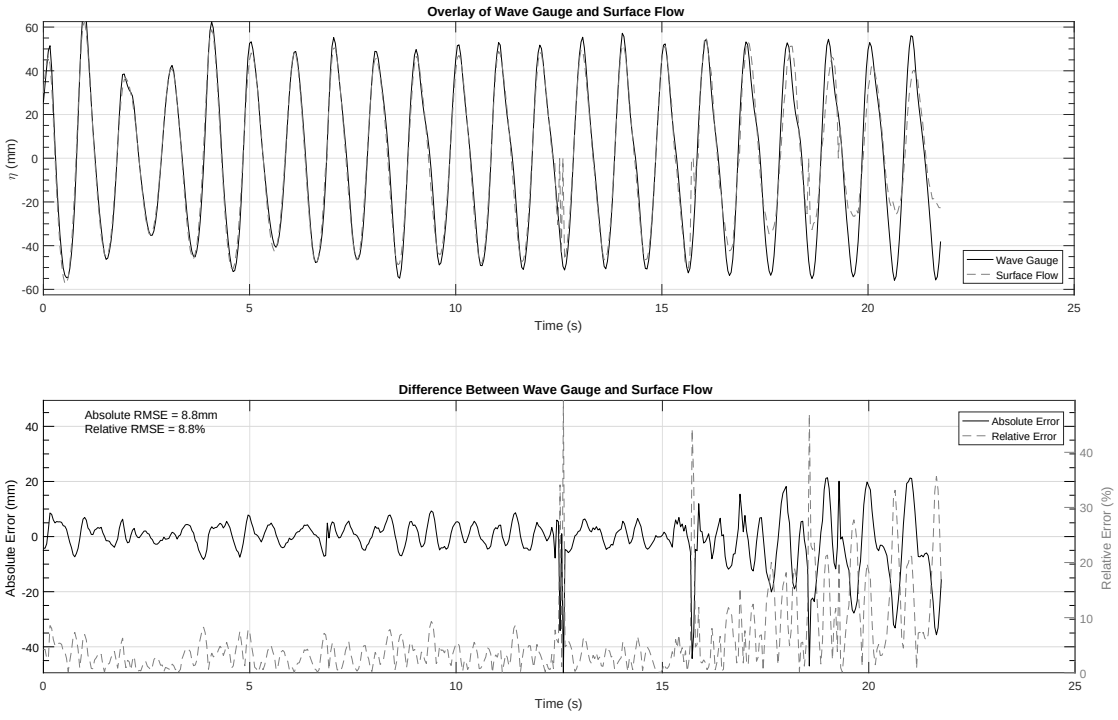

Figure 2.11: Comparison between wave gauge and DaVis measurements for a wave with frequency of 1.0 Hz and amplitude of 50 mm (Top) Overlay (Bottom) Absolute Error on Left Axis and Relative error on Right Axis.

and the total number of frames captured compared to wave steepness. The wave steepness is that which was measured through phase averaging experimental results. From these plots it is clear that for low steepness waves, stereo-videogrammetry has low error relative to wave gauges and there is a very low risk of processing failure. A caveat to this is WP 04 which routinely exhibits the largest RMSE; this wave gauge is the measurement point closest to the cylinder. This is thought to be a result of higher nonlinearities in this region causing higher drift resulting in fewer particles for the digital image correlation. Errors increase however as wave steepness increases. Furthermore, the processing failure rate increases beyond 40% as steepness increases above 0.2. As highlighted above with Figure 2.11 this is not due to the inability of DaVis to operate in these conditions, rather it is a result of the seeded particles being swept away from the experimental area. An alternate presentation of Figure 2.12 (left) is presented in Appendix A in terms of wave frequency and amplitude.

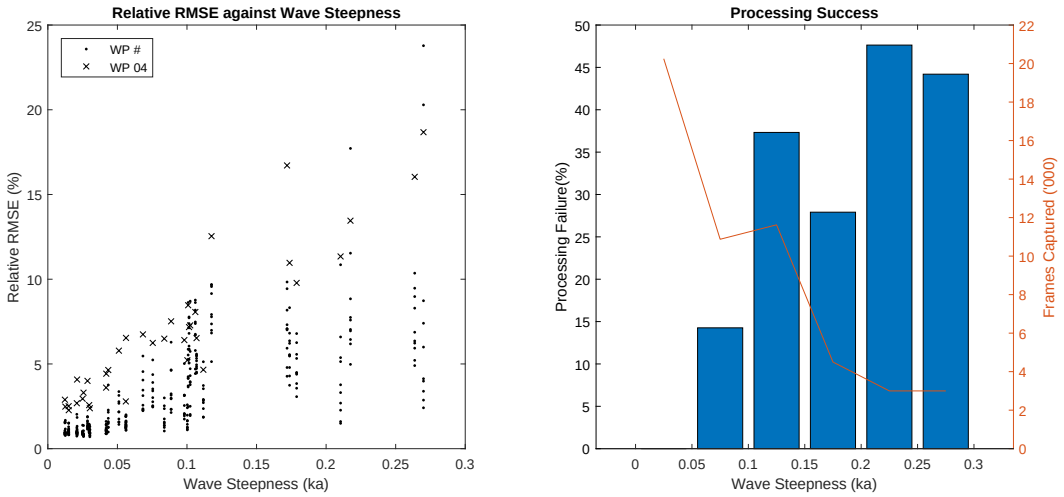

Figure 2.12: (Left) $RMSE_A$ between stereo-videogrammetry and resistive wave probes. With WP # indicating all wave probes except WP 04. (Right) Failure rate of processing data and total frames captured.

2.3.3 Surface Data Sample

A sample data set for the cylinder case study will now be considered, with an incident wave of frequency 0.9 Hz and amplitude 50 mm, this is presented in Video 2.1, Figure 2.13 and Figure 2.14. The phase averaged measured wave steepness is 0.17, which suggests an error of 5-10% compared to wave gauges from the investigation above.

Figure 2.13 presents a sequence of five frames spaced evenly from just prior to when the developed incident wave front first arrives, through to when the first wave reflected from the diffraction field returns. The data presented consist of the free surface on the left, the gradient magnitude in the centre and gradient direction on the right. The gradient magnitude is expressed as a proportion of wave steepness and direction is aligned with the centreline. In

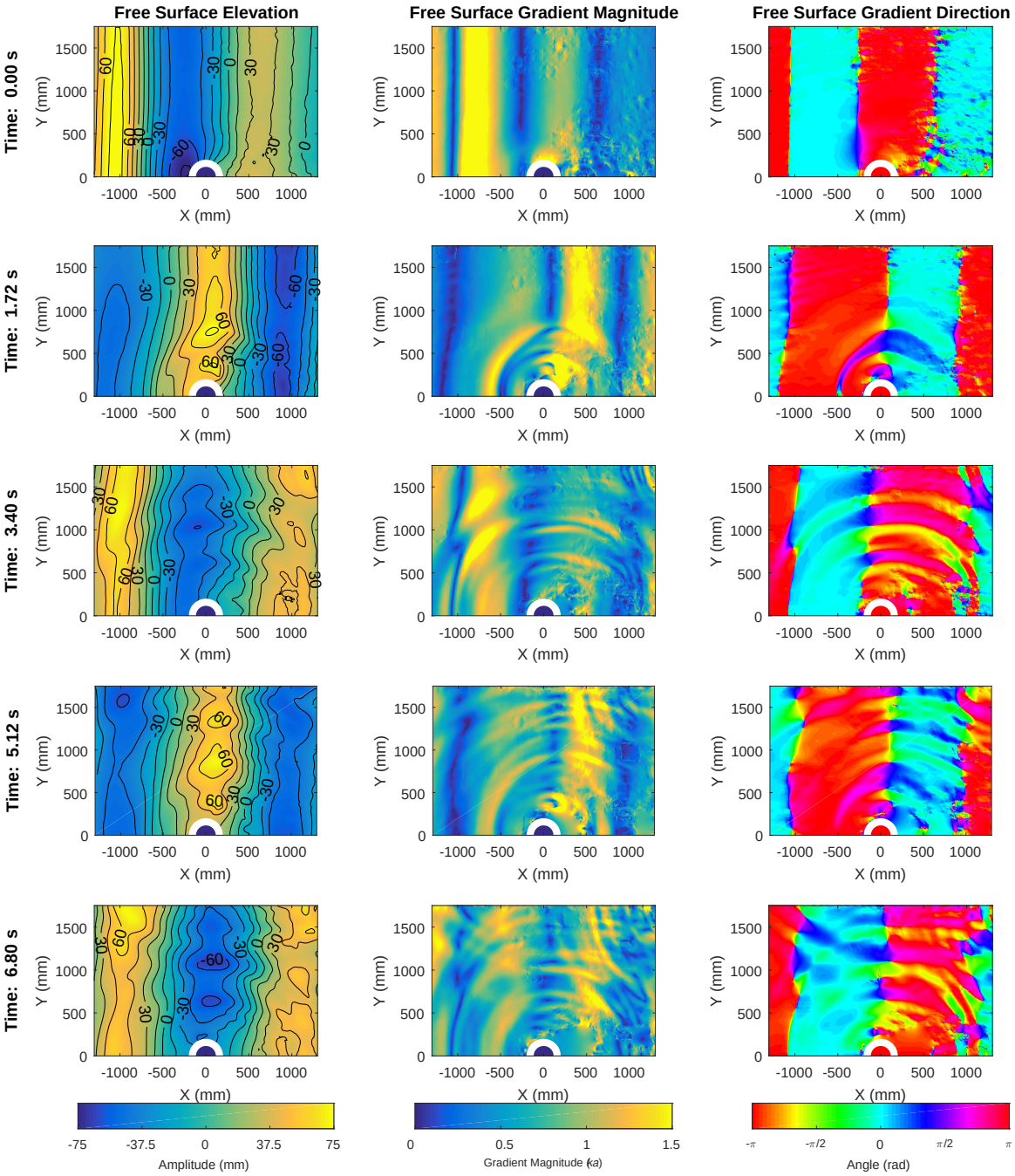

Figure 2.13: Incident wave with 0.9 Hz frequency 50 mm wave amplitude, first node of interaction. Time steps are 0, 1.72, 3.4, 5.12 and 6.8 seconds. First column is free surface elevation, second column is magnitude of the free surface gradient and third column is direction of free surface gradient. The incident wave is propagating in the positive x direction.

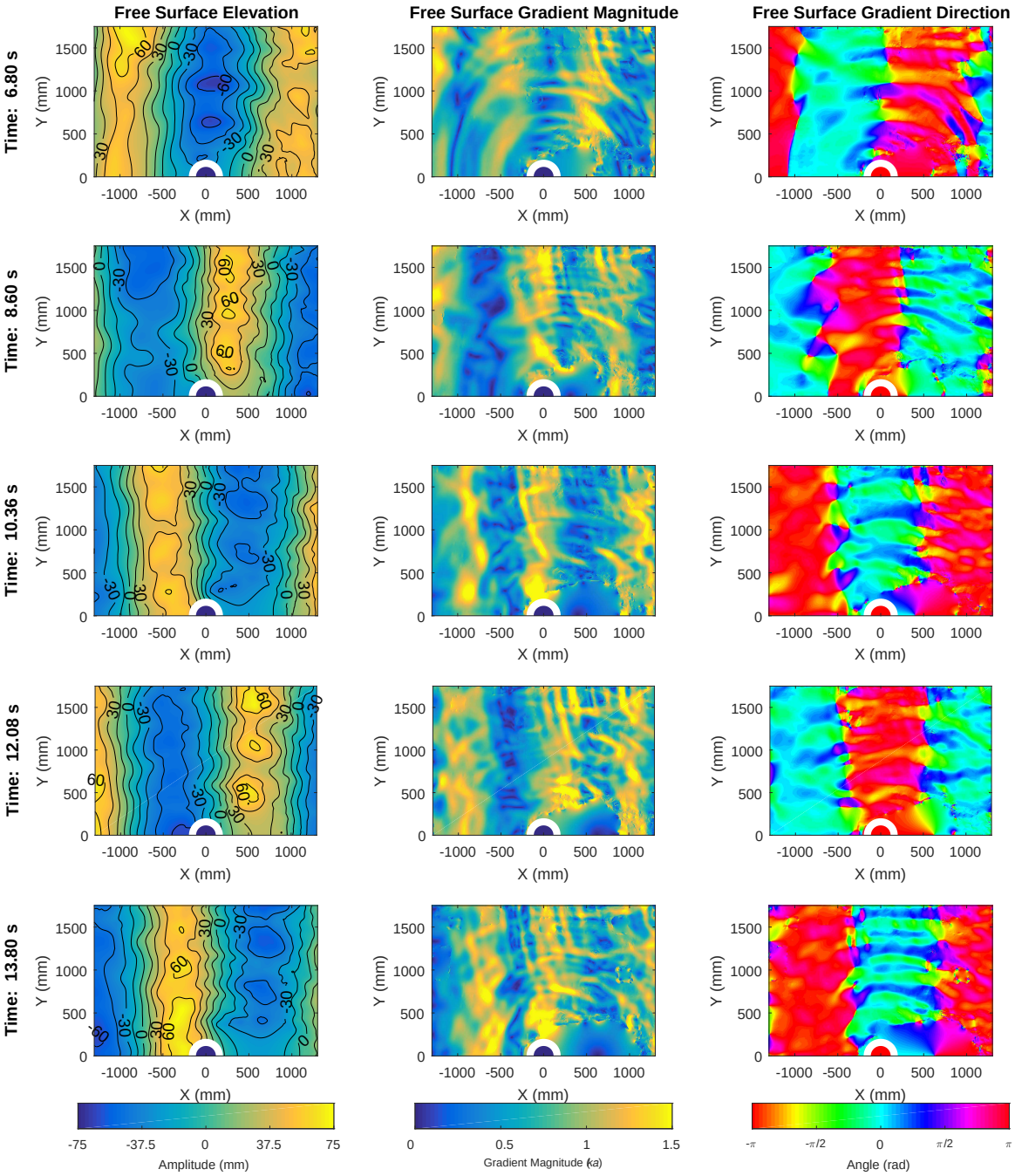

Figure 2.14: Incident wave with 0.9 Hz frequency 50 mm wave amplitude, second node of interaction. Time steps are 6.8, 8.60, 10.36, 12.08 and 13.8 seconds. First column is free surface elevation, second column is magnitude of the free surface gradient and third column is direction of free surface gradient. The incident wave is propagating in the positive x direction.

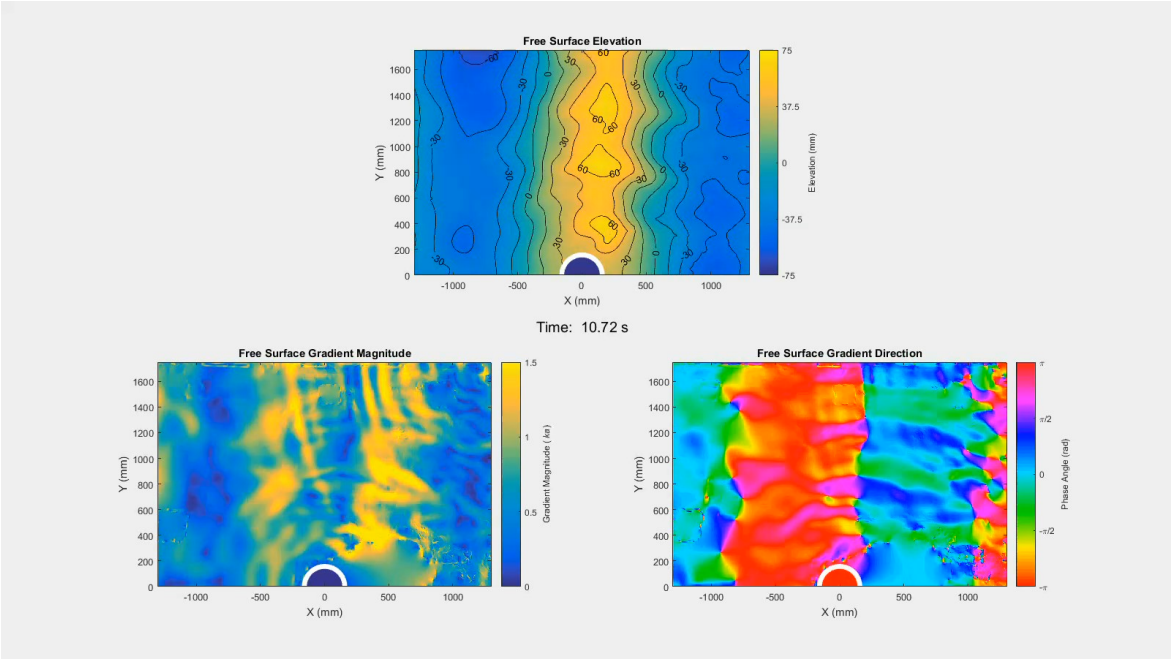

Video 2.1: Incident wave with 0.9 Hz frequency and 50 mm amplitude. The top plot shows the free surface elevation, bottom left the free surface gradient magnitude and the bottom right the free surface gradient direction. The video is available at: `https://cloudstor.aarnet.edu.au/plus/s/EdDtQDXRn4GCak0`.

the first frame it can be seen that the initial wave has not yet struck, however a very small part of the diffracted field is evident slightly up-wave of the cylinder formed by the ramp up waves. In the second frame as the incident wave has passed, a clear scattered wave is evident, especially in the gradient plots. As time passes the scattered wave field is seen to develop with a reflection of the scattered wave apparent in the fifth frame on the gradient plot. It is interesting to note through the data that the scattered waves are much more evident in the gradient plots relative to the free surface plot and that some of the scattered waves have a shorter wavelength than the incident waves. One concern in these plots is the radiated wave evident in the gradient plots in the top right corner (1300 mm, 1500 mm) from the third frame onward. This wave has been attributed to a small buoy used to connect the conceptually transparent particle fence to the tank wall. The floats (four used throughout the setup) had mass of approximately 400g and diameter 100mm. Furthermore, it can be observed that the region directly in the lee of the cylinder has increased errors as the run progresses, this is the result of non-linear drift forces causing the particles to disperse.

Figure 2.14 shows the progression of the wave following from Figure 2.13. The development of the scattered wave field is more evident. The time period shown corresponds to the second order of interaction. The hole in the lee of the cylinder is yet more evident as is the radiated wave from the fence in the top left corner of the frame. As the run progresses errors increase,

evidenced by the larger hole and increased number of reconstruction errors (squares). This failure to process the surface can be attributed to high particle drift, as a result of high steepness, causing DaVis to fail to find correlation between the two raw images. This failure is not a fault of the DIC, but an experimental challenge of keeping a texture on the image for the DIC to employ. As suggested by Figure 2.12 such challenges are less severe for conditions with lower wave steepness.

2.4 Discussion

The potential use of stereo-videogrammetry as an approach to quantify the spatial wave field for wave structure interaction experiments has been demonstrated.

In this study there is no relative mean flow between the structure and the fluid, this means that further validation testing is required for testing problems where viscous forces become important; such as wave-wake or sea-keeping studies. The results, presented in Section 2.3.1, from this initial study show that the variation induced in the wave field is negligible. The variation is lower than the repeatability of the wavemaker and as such it is not possible, with the dataset collected, to ascertain if there are any further effects attributable to the particles.

The measurement accuracy of the stereo-videogrammetry approach was explored in Section 2.3.2. The process employed through this work requires two assumptions to be true. Firstly, that there is perfect symmetry about the centreline of the tank and secondly that wave gauges return the true surface elevation. The variation from these precepts, specifically spatial variation of the wave front, could easily account for the errors experienced with low wave steepness's (< 0.06). Furthermore, these errors are within the repeatability of the wave making capabilities observed in the wave dynamics study. The exception to this is the measurement closest to the cylinder, WP 04, which has a consistently greater error relative to the other measurement locations. There is also a trend for greater errors as the incident wave steepness increases. The dynamics of steeper waves and the water-structure interfaces both induce greater non-linearities in the wave; this consequently creates increased flow. This suggests the cause for the greater RMSE's is particle dispersion due to larger currents. However even at the maximum steepness considered the lowest RMSE is similar in magnitude to the low steepness conditions; this implies that there is potential in the methodology to work in these high flow conditions.

The case study presented highlights the exciting potential for identification of wave field components which might be otherwise unidentifiable, and also the necessity to develop processes for analysing the surface data to maximise the return on the investigation. This is demonstrated by the radiated wave field from the fence connection float; these radiated waves are indistinguishable in the surface plot but are clear in the gradient plots. These gradient plots

are well adapted to highlight waves which have higher localised steepness, typically shorter wavelengths.

While the work gives an indication of the potential for stereo-videogrammetry there are clearly a range of drawbacks to its use. There is experimental risk in the ability to continuously check data validity, due to the extended post processing time it is not possible to confirm all the data collected can be resolved into a surface. The likelihood of this can be quite high in certain instances, as is indicated by the right hand plot in Figure 2.12. The noise induced by the particle fence is of minimal concern in ongoing work as it is thought practical to reduce the weight of the connection floats and move them further from the experimental area.

2.5 Conclusion

In this chapter a study has been conducted into the use of stereo-videogrammetry for the measurement of the wave field in a towing tank. Initially the work explored whether the equipment required by the measurement technique has a substantial effect on the waves and then continued to assess the validity of the measurement approach compared to established wave gauge technology. In the first phase of work, three wave conditions were explored, indicating that no variation was induced by the particles or fences. Subsequently the accuracy of the measurement approaches was considered with 18 wave conditions, with a frequency range of 0.25-1.0 Hz and amplitudes of 25 and 50 mm. This work clearly indicated that for studies with low steepness and a suitable distance from any structure the measurement approach works well, with no discernible difference found between approaches. This implies that the approach begins to break down in areas of higher flow, however there is evidence that the issue is high flow causing particle dispersion leaving a sparse surface and not a fundamental incapability of the software. Ultimately the stereo-videogrammetry approach described through this chapter is fit for purpose for the research goals of this thesis.

Chapter 3

Study on the Use of Wall Reflections with an Idealised WEC

3.1 Introduction

In the previous chapter a stereo-videogrammetry approach was explored for its applicability to the study of wave structure interactions; experimentally using a cylinder fixed rigidly in the centre of a wave flume. It shows that for studies with low mean flow conditions, there is almost no distinction with the measurement approaches considered. In cases with higher mean flow the measurement validity reduces, such as areas in proximity to fluid structure interfaces and wave cases with high steepness. This chapter will explore the concept of using the reflections from the channel walls to model array effects, both experimentally and numerically, using the method of images. The investigation employs the same case as the above chapter with a cylinder fixed rigidly in the centre of the wave channel.

Experimental hydrodynamic investigations on WECs typically consist of scale model tests in a wave basin where tank reflections are avoided or minimised. Techniques include using smaller scale models and larger facilities to maximise the equivalent full scale area and absorptive facility features, such as beaches or reactive wave paddles. Extending beyond single device testing it quickly becomes necessary to compromise between larger facilities and smaller scale devices. Similar analogies can be made with numerical modelling of array interactions, with numerical array modelling requiring much larger domains than single devices. This results in increased computational expense which restricts the abilities to complete studies.

There are a number of numerical modelling techniques which are available to investigate WEC dynamics and the effects of an array of devices. Very good reviews of the current state of these are available from Folley, Alves, et al. (2016) and Folley, Babarit, et al. (2012). At present there is no single best approach for the numerical modelling of WEC array effects, with a trade-off required between computational expense and accurate representation of physical phenomena. Techniques such as spectral wave, boussinesq and mild slope models are approaches which suit modelling wave propagation, but none are capable of modelling the hydrodynamics of WECs. An improvement of this are non-hydrostatic wave flow models

(Rijnsdorp et al. 2017). To include device hydrodynamics, approaches based on potential flow or computational fluid dynamics need be applied. A common approach is to use linear potential flow theory with boundary element method to solve; commercial examples are WAMIT and Ansys Aqwa while Babarit and Delhommeau (2015) released an open-source solver *NEMOH*. Owing to the recent release of this code very little work has been completed on validation. An alternative to boundary element method is to use a finite element approach to solve the potential flow equations; this method is suited to oscillating water column WEC's (Nader 2013).

A common approach to modelling wave structure interactions is to apply potential flow theory (Folley, Babarit, et al. 2012). General potential flow theory assumes the fluid is inviscid and incompressible and the flow is irrotational. These assumptions lead to a set of non-linear equations. It is possible to linearize these equations, and reduce computational expense, by assuming small amplitudes of waves and body motion, as well as structures and the sea floor being impermeable. With the problem linearized it is possible to solve the calculations in the frequency domain. This three-dimensional problem is transformed into a two-dimensional problem with the application of Green's second identity and an appropriate Green's function. The two-dimensional domain is defined by discretising the structures wetted surface into a series of panels. This study shall use the open source code *NEMOH*.

The method of images is a theory which states that a mirror image can be applied about a symmetry plane to simulate a larger domain, it can be expressed for fluid problems by the boundary condition,

$$\frac{\partial \phi}{\partial n} = 0 \tag{3.1}$$

Where ϕ is total velocity potential and n is the unit vector normal to the mirror plane. The theory has applications in many problems which are represented by fields, such as electromagnetism and fluid dynamics and their associate linear wave theories (Butler and Thomas 1993; Dalrymple et al. 1989; Thomas 1991). Applying the theory with two symmetry planes to create a channel it is possible to simulate a repeating array which is proportional to the period of investigation, or an infinitely wide array for a frequency-based study. Early work by Spring and Monkmeyer (1975) was completed with a vertical cylinder centrally located in the channel in the frequency domain, this simulates a row of the same structure of infinite width with a separation of the tank width. Figure 3.1 depicts a representation of the phenomena for the first reflection set. The intent with the work was to infer open water hydrodynamic characteristics from experimental work in towing tanks with side-wall effects. Extensions have been made by Thomas (1991) for prediction of effects with the cylinder located anywhere on the transverse section of the facility.

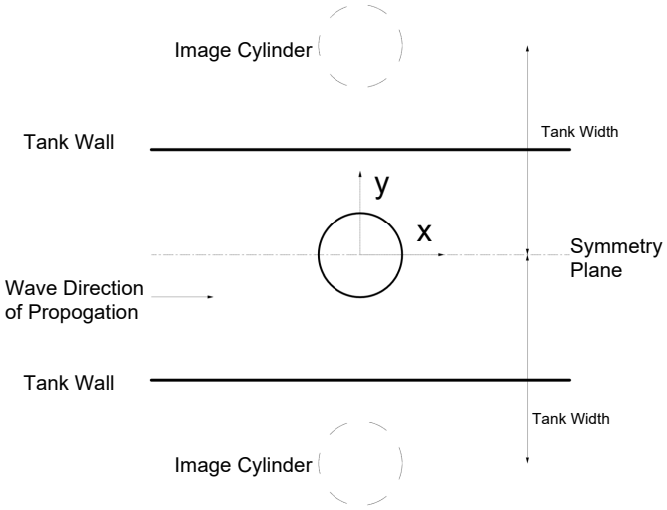

Figure 3.1: Method of images concept.

The same theory has been applied to a viscous hydrodynamic problem by Zurcher (2015), where a catamaran demi hull was run alongside a towing tank wall, where the positioning was such that the wall is analogous to the vessel centreline.

As with any assumptions, there are implications inherent to the approached employed in this thesis with the use of potential flow and wall reflections. The assumption of inviscid fluid is made on the basis of small amplitude of motion of the device and the free surface elevation. This stems from small motions on a cyclic phenomona implies low velocities; if velocity (or velocity gradient) is small this suggests that any forces associated to viscousity become negligible. Additionally under this assumption the boundary layer induced by the wall is considered non-important as there is a zero-mean flow along the wall.

The work described in this chapter is partially drawn from Winship et al. (2018), which is available in Appendix F.1.

3.2 Method

The experimental set-up for the testing conducted in this chapter was detailed above in Chapter 2. All experimental data presented in this chapter has been treated with a band-pass filter, the filter is centred on the incident wave frequency with a width of 0.5 Hz. The excitation moment has had additional post-processing in the form of phase-averaging for a frequency-based consideration.

The numerical modelling study has been completed in *NEMOH*. *NEMOH* is an open source linear potential flow solver which applies boundary element method. A detailed description of the formulation of the problem and the modelling procedure is given by Babarit and

Table 3.1: Cylinder numerical modelling characteristics.

	Panels	**Excitation Moment**		**Free Surface**	
		Frequency Range (Hz)	Discretisation's	Frequency Range (Hz)	Discretisation's
Single Cylinder	816	0.1-1.5	100	0.3-1.0	8
Three Cylinders	2472	0.1-1.5	150	0.3-1.0	8
Five Cylinders	4128	0.1-1.5	150	0.3-1.0	8
Cylinder and Wall	1512	0.1-1.5	200	0.3-1.0	8

Delhommeau (2015). The modelling completed in this work was accomplished with MATLAB wrappers based upon those downloadable with the code (Babarit and Delhommeau 2019). Modifications relate to modelling arrays and activating the surface post-processing.

Four scenarios were considered with *NEMOH*. These are illustrated in Figure 3.2 and include a) a single cylinder, b) three cylinders, c) five cylinders and d) cylinder and wall. All modelling in this study was completed with the assumption of symmetry about $y = 0$. For the infinite array a reflective wall is positioned as per the physical tank wall. The water depth considered is 1.5 m and wave frequencies in the range of 0.2 to 1.2 Hz. Mesh convergence was completed with the characteristics selected given in Table 3.1.

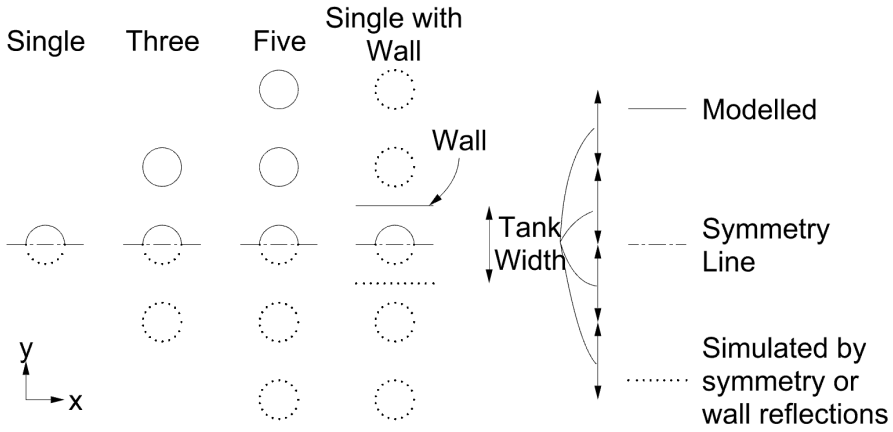

Figure 3.2: Numerical domains simulated a) Single b) Three c) Five d) Single with Wall

The outputs from *NEMOH* that have been used are the pitch excitation moment and the free surface. The free surface used for comparison with the stereo-videogrammetry is discretised into 4000 points (200 by 200) over an area 3.5 m by 3.5 m.

The time domain free surface diffraction expression for *NEMOH* is given by (3.2) for a single frequency component, a is the incident wave amplitude, k is the wave number, x and y are

position on the surface, ω is angular frequency, t is time, $|\eta_S|$ is normalised scattered wave amplitude and $\angle\eta_S$ is phase angle of the scattered wave field. Where diffracted refers to the resulting wave field of placing a structure into a wave climate and scattered wave field the change to the incident wave.

$$\eta_D(x,y,t) = a \cdot \mathrm{Re}(e^{i(k(xcos\theta+ysin\theta)-\omega t)} + |\eta_S|(x,y,\theta)e^{i(\angle\eta_S(x,y,\theta)-\omega t)}) \tag{3.2}$$

The pitch excitation moment $M_{ex}(\omega)$ is normalised to find the normalised pitch excitation moment $M_{ND-D}(\omega)$,

$$M_{ND-D}(\omega) = \frac{M_{ex}(\omega)}{a\rho A_w g L_D} \tag{3.3}$$

Where a is the incident wave amplitude, ρ density of water, A_w is the wetted surface area, g is acceleration due to gravity and L_D is the cylinder diameter.

3.3 Results and Discussion

3.3.1 Free Surface Modelling from *NEMOH*

The results presented are focused on waves with a frequency of 0.9 Hz and an amplitude of 50 mm, the frequency is the same as the case study explored in the previous chapter. The results presented are for a single, three, five and cylinder and wall conditions in Figures 3.3-3.6. All figures show the same region, from the centreline of the tank to the wall. The same format is applied across all four figures, with the top two plots giving the frequency domain results, consisting of the amplitude on the left and the phase angle on the right. Below on the bottom are an instance in the time domain, with the elevation on the left, surface gradient magnitude in the centre and surface gradient direction on the right.

The frequency domain surface components generated by *NEMOH* show a convergence towards the infinite array as the number of cylinders vary from a single cylinder through to an infinite row. A key indication is the variation in the amplitude, with the localised zero region developing, from (-1.5, 1.0) extending in the wave direction around to the lee of the structure. Similarly, the time domain modelling is barely distinguishable after more than one cylinder is present, with only slight changes to the peaks and troughs occurring. It is important to note that the gradient plots seem to show that the incident wave is slightly oblique, but this is not the case and in fact a coincidence for this time step.

An extended time series of all four scenarios are presented in Video 3.1, where two wave periods are shown.

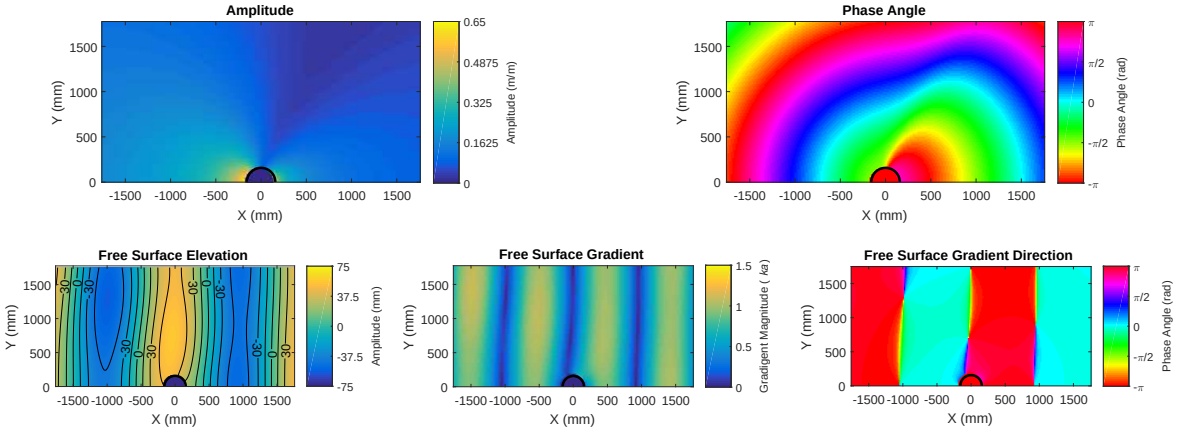

Figure 3.3: *NEMOH* free surface modelling of a cylinder without any other structures for an incident wave frequency of 0.9 Hz. (Top) Frequency domain description of free surface with amplitude (left) and phase angle (right). (Bottom) Time domain instance of the free surface with a 50 mm amplitude wave, free surface elevation on the left, magnitude of the free surface gradient in the centre and direction of free surface gradient on the right.

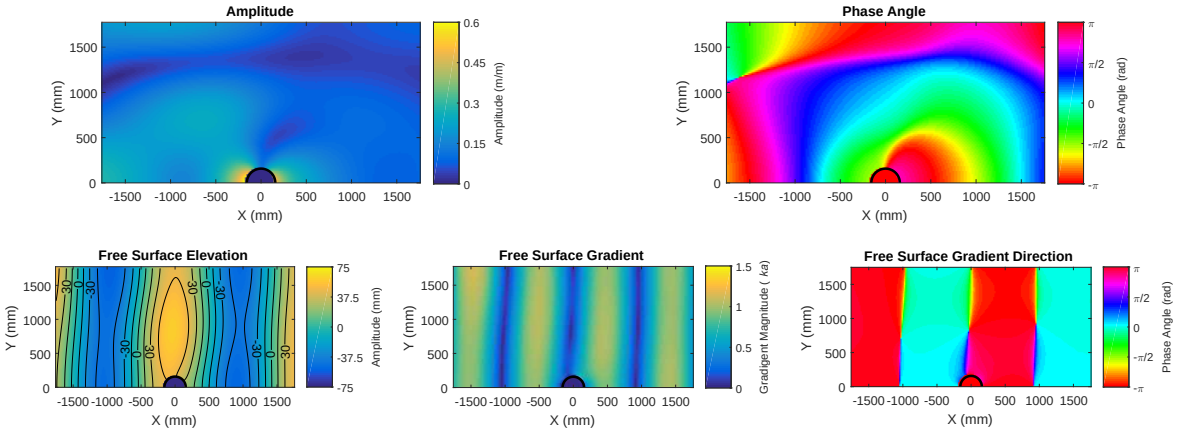

Figure 3.4: *NEMOH* free surface modelling about a central cylinder with two cylinders (out of frame) positioned in a row for an incident wave frequency of 0.9 Hz. (Top) Frequency domain description of free surface with amplitude (left) and phase angle (right). (Bottom) Time domain instance of the free surface with a 50 mm amplitude wave, free surface elevation on the left, magnitude of the free surface gradient in the centre and direction of free surface gradient on the right.

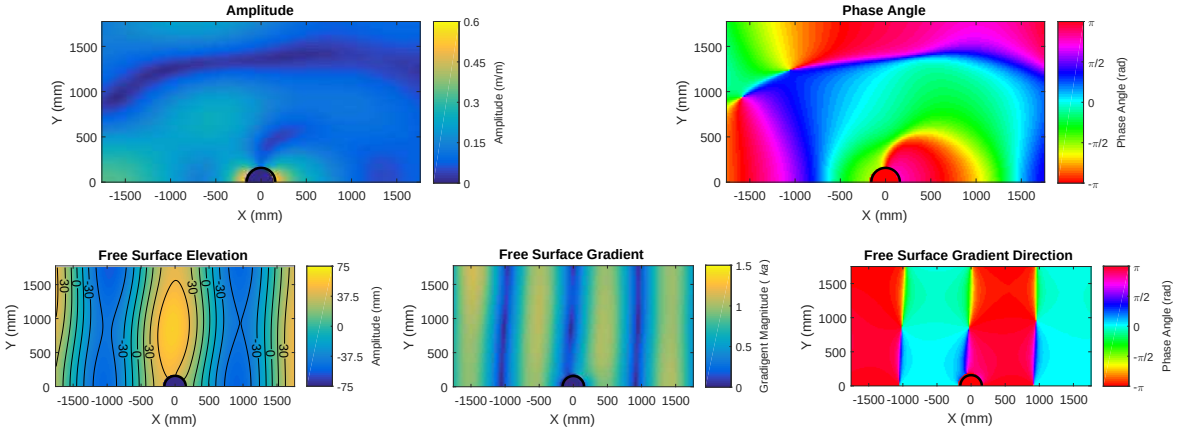

Figure 3.5: *NEMOH* free surface modelling about a central cylinder with four cylinders (out of frame) positioned in a row for an incident wave frequency of 0.9 Hz. (Top) Frequency domain description of free surface with amplitude (left) and phase angle (right). (Bottom) Time domain instance of the free surface with a 50 mm amplitude wave, free surface elevation on the left, magnitude of the free surface gradient in the centre and direction of free surface gradient on the right.

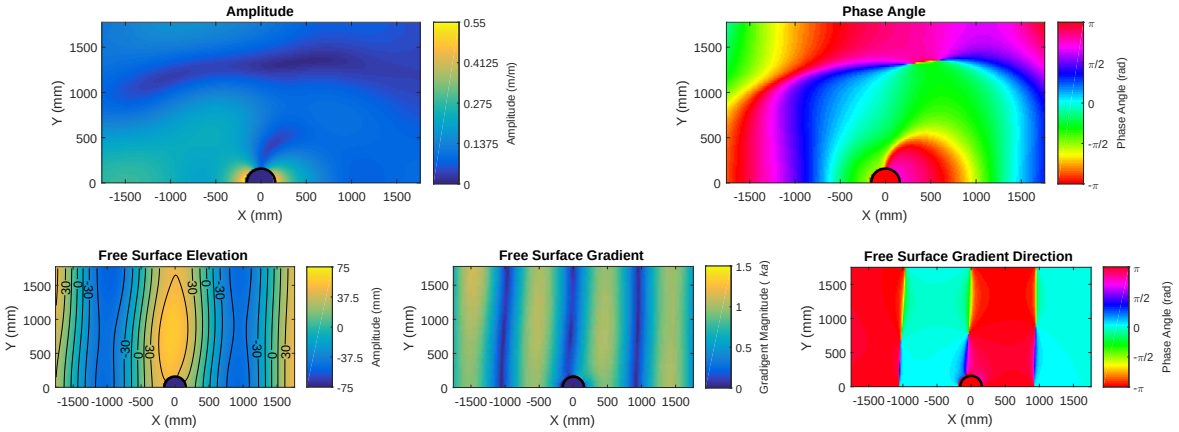

Figure 3.6: *NEMOH* free surface modelling about a central cylinder with a wall simulating method of images for an incident wave frequency of 0.9 Hz. (Top) Frequency domain description of free surface with amplitude (left) and phase angle (right). (Bottom) Time domain instance of the free surface with a 50 mm amplitude wave, free surface elevation on the left, magnitude of the free surface gradient in the centre and direction of free surface gradient on the right.

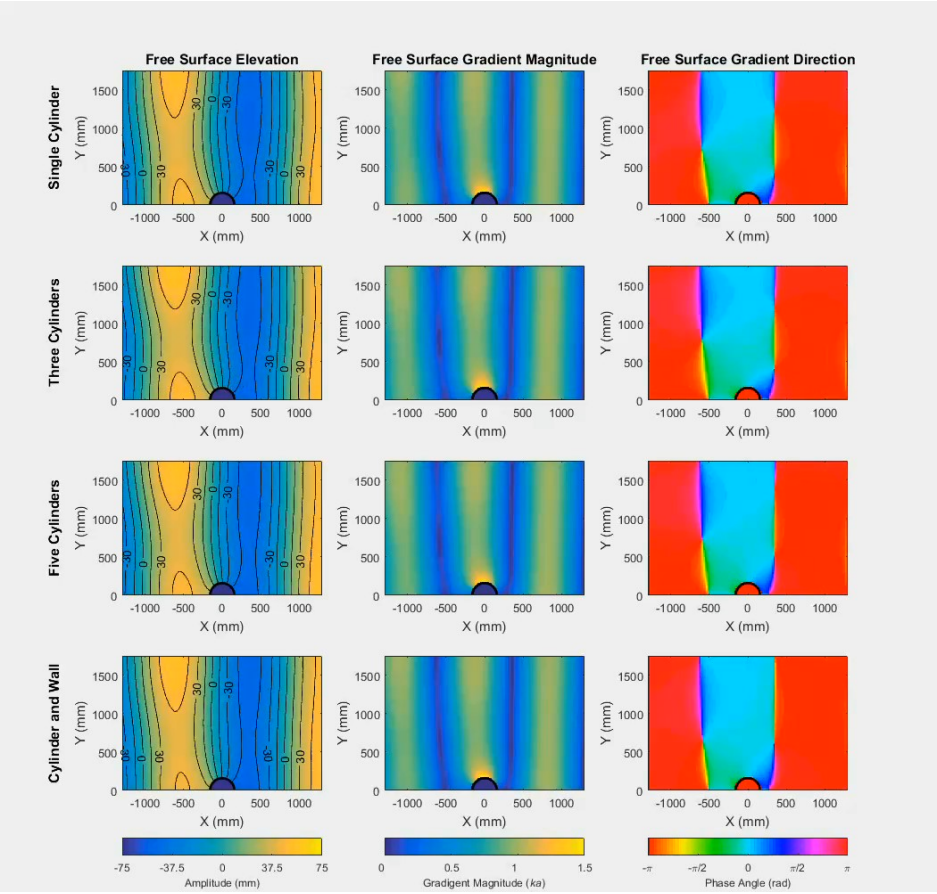

Video 3.1: *NEMOH* free surface modelling. First column is free surface elevation, second column is magnitude of the free surface gradient and third column is direction of free surface gradient. Single Cylinder (first row) Three Cylinders (second row) Five Cylinders (third row) Cylinder and wall (forth row). The video is available at: `https://cloudstor.aarnet.edu.au/plus/s/Wi0NeoSRUm6KKpa`.

The *NEMOH* modelling has shown that the free surface results are almost indistinguishable for both time and frequency domain for all simulations besides the single cylinder. Although, there was a variation in the processing times of the different simulations. With an order two relationship between the number of panels and the processing time (Babarit and Delhommeau 2015; Folley, Babarit, et al. 2012) the simulation with the walls was distinctly faster to process than the three and five cylinder symmetries explored. In addition, as the width of the array is extended the required number of panels per cylinder increases; this is a result of the relative errors associated with discretisation of a cylinder surface into a series of quadrilaterals. When these relative errors are propagated a short distance, as for the case of a single cylinder, the resulting absolute error may be acceptable. Propagating the same relative error, a greater distance, as is required for array simulation, the resulting absolute error is greater. This means that considerable processing savings can be made with utilisation of symmetry planes.

3.3.2 Surface Comparison between Numerical and Experimental

Comparison between stereo-videogrammetry and *NEMOH* is now completed for incident wave conditions of 0.9 and 0.4 Hz both with amplitude of 25 mm. Figures 3.7 and 3.8 present time steps with Videos 3.2 and 3.3. These qualitative comparison shows that the data sets are almost identical. A band-pass filter is applied to the stereo-videogrammetry, a Butterworth filter was used with a band of 0.1 to 1.2 Hz.

If *NEMOH* predictions are compared with the unfiltered stereo-videogrammetry surface for this wave frequency, as with Figures 2.13 and 2.14, it is clear that not all hydrodynamic interactions are accounted for. However, these discrepancies are largely attributable to the assumptions of linearity used in the numerical formulation.

Further study is required to fully assess the validity of the use of reflections to simulate array effects. The ideal would be a quantitative assessment of the reflections including energy loss and phase shift.

The comparison made here is largely qualitative between the numerical prediction and the experimental measurement. While it would be very useful from a scientific perspective to implement a quantitative comparison this is considered out of scope for this thesis. Such a quantitative comparison would need to account for uncertainties in location on the horizontal plane, surface elevation, phase differences and the variation between experimental and numerical frequencies. The difference in frequencies is evidenced by the different propagation speed of the waves in Video 3.2.

3.3.3 Excitation Moment

The experimentally measured excitation moments are compared with the four *NEMOH* simulations in Figure 3.9. The numerical simulations were completed in the frequency domain so are for an infinite time period and are normalised by wave amplitude. The experimental measurements are the result of phase-averaging over the experimental period. This period is defined as the interval from when the wave arrives at the structure to when the reflection from the beach arrives. As such the experimental period is subjective on the group velocity of the wave condition. The experimental waves presented include runs with amplitude 25 and 50 mm, the excitation moments are normalised by the incident wave amplitude. The mechanical connection for measurement of loads is described in Chapter 2.2.2.

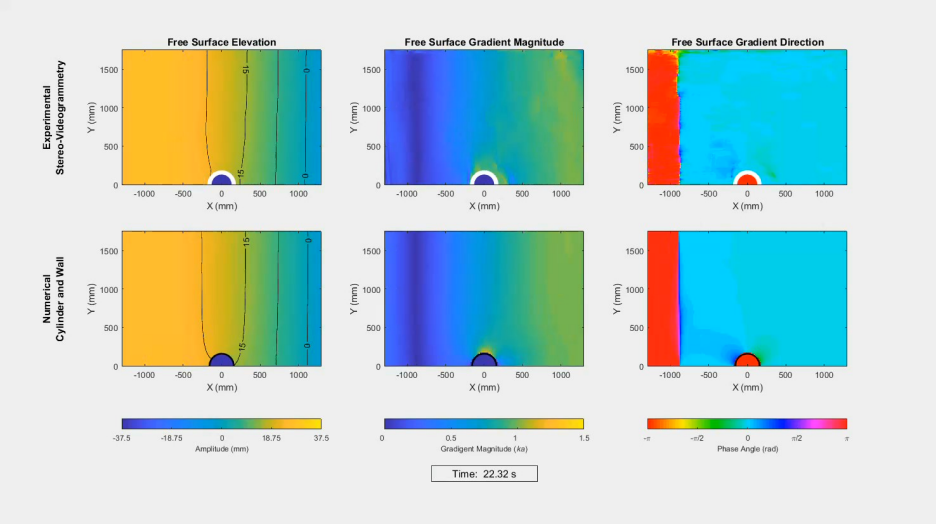

Video 3.2: A comparison between stereo-videogrammetry measurement and *NEMOH* modelling for an incident wave with 0.4 Hz frequency and 25 mm amplitude (steepness 0.0195) with t(0) when the first wave arrived at the cylinder. (Top Row) Stereo-Videogrammetry (Bottom Row) *NEMOH* modelling for cylinder and wall case. (Left Column) Free Surface Elevation (Middle Column) Free Surface Gradient Magnitude (Right Column) Free Surface Gradient Direction. The video is available at: `https://cloudstor.aarnet.edu.au/plus/s/RBzqfhMq2XGAcfX`.

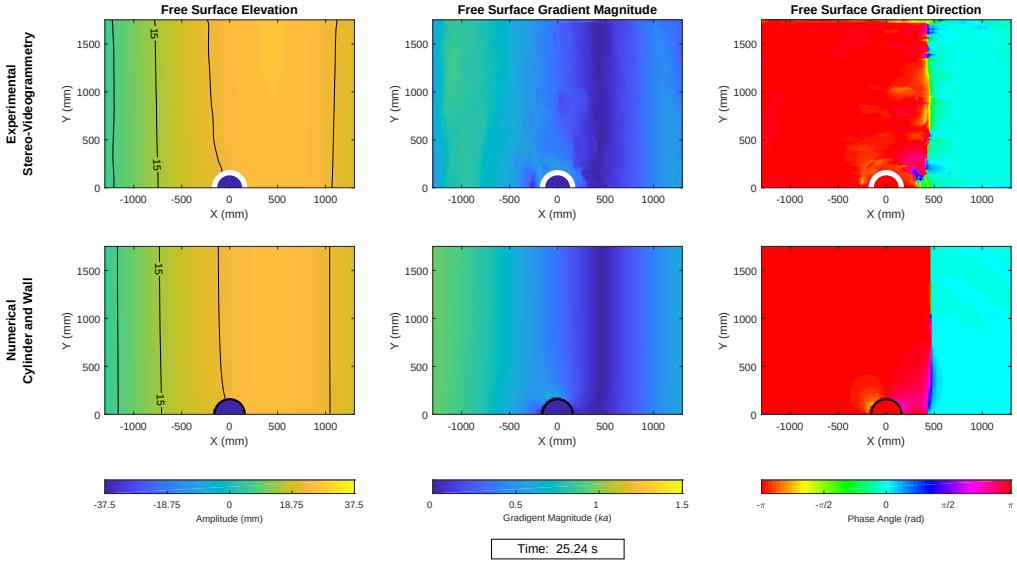

Figure 3.7: A comparison between stereo-videogrammetry measurement and *NEMOH* modelling for an incident wave with 0.4 Hz frequency and 25 mm amplitude (steepness 0.0195) at an instant 25.24 s after the first wave arrived at the cylinder. (Top Row) Stereo-Videogrammetry (Bottom Row) *NEMOH* modelling for cylinder and wall case. (Left Column) Free Surface Elevation (Middle Column) Free Surface Gradient Magnitude (Right Column) Free Surface Gradient Direction.

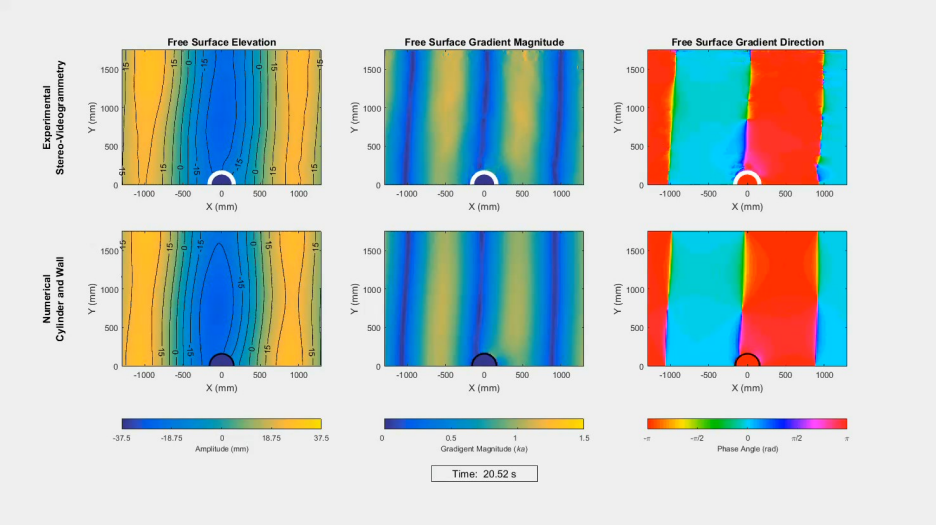

Video 3.3: A comparison between stereo-videogrammetry measurement and *NEMOH* modelling for an incident wave with 0.9 Hz frequency and 25 mm amplitude (steepness 0.0815) with t(0) when the first wave arrived at the cylinder. (Top Row) Stereo-Videogrammetry (Bottom Row) *NEMOH* modelling for cylinder and wall case. (Left Column) Free Surface Elevation (Middle Column) Free Surface Gradient Magnitude (Right Column) Free Surface Gradient Direction. The video is available at: `https://cloudstor.aarnet.edu.au/plus/s/V7oRZiYitf4I99f`.

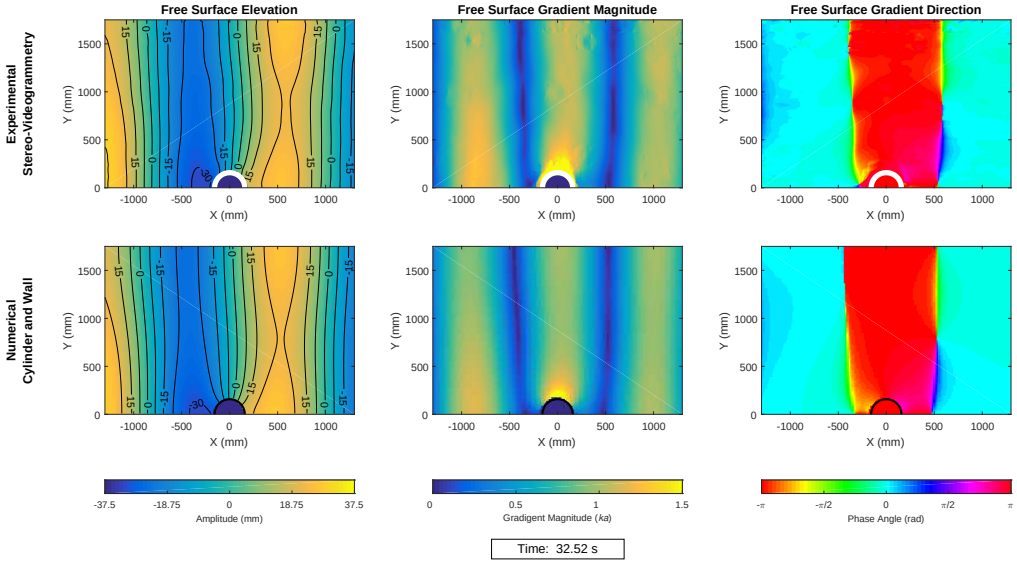

Figure 3.8: A comparison between stereo-videogrammetry measurement and *NEMOH* modelling for an incident wave with 0.9 Hz frequency and 25 mm amplitude (steepness 0.0815) at an instant 32.52 s after the first wave arrived at the cylinder. (Top Row) Stereo-Videogrammetry (Bottom Row) *NEMOH* modelling for cylinder and wall case. (Left Column) Free Surface Elevation (Middle Column) Free Surface Gradient Magnitude (Right Column) Free Surface Gradient Direction.

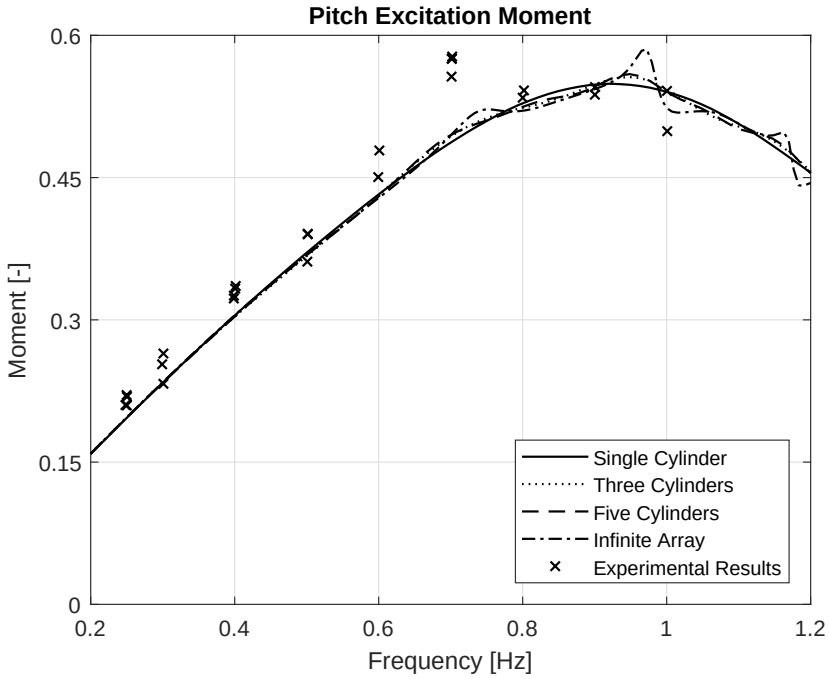

Figure 3.9: Pitch excitation moment, the four numerical simulations are compared with experimental measurements.

The four *NEMOH* simulations indicate the importance of multiple bodies for WEC intra array effects. Further to this it is important to recall the relationship between computation time and number of panels. Comparing the numerical predictions with the experimental measurements it is difficult to discern a distinction, such that it is possible to comment on the applicability of method of images. While the general trend and magnitudes align, there is more in common between the numerical predictions than the experimental measurements.

This is largely attributable to the symmetries of the study; the only variation is induced by the small change in pressure about the vertical-longitudinal centreline of the cylinder. The only measured excitation moment which deviates from the general trend is the 0.7 Hz case, this is thought to be a secondary effect as a result of this frequency being the closest to the transverse tank resonance. This effect is as a result of the wavelength being close to the same as the tank width. The transverse tank resonance had no noticeable effect in the free surface measurements.

3.4 Conclusion

In this study an investigation was made into the use of reflections from walls to simulate arrays of WECs, with the use of a simplified WEC in the form of a cylinder. The work applied novel experimental techniques in a wave flume, applying stereo-videogrammetry to

measure the free surface and compare the results to numerical simulations with *NEMOH*. The experiments consisted of regular wave frequencies ranging from 0.25 Hz to 1 Hz with wave amplitudes of 25 mm and 50 mm. In the *NEMOH* investigation different domains were considered, including a single cylinder, through to small arrays with three and five cylinders before considering the infinite case using walls to model infinitely-wide arrays. For the primary condition in this study, a regular wave with a frequency of 0.9 Hz and amplitudes of 25 and 50 mm, analysis of the moments and free-surface effects were provided.

The numerical work showed that the use of a wall to simulate array effects is a valuable tool to reduce computational expense. The comparison of the free surface generated by *NEMOH* and the measured free surface were almost indistinguishable. The consideration of the excitation moment showed similar trends between the numerical studies and the experimental measurements, however the symmetries involved in the study did not highlight these effects well. While the results are supportive, it is not feasible to make definitive statements around the applicability of the use of reflections to the study of WEC arrays, from this chapter alone.

Chapter 4

Diffraction by a Submerged WEC in a Channel

4.1 Introduction

In the previous chapter the concept of utilising wall reflections to model WEC array effects was explored both numerically and experimentally. The study was restricted to the diffraction about a cylinder rigidly mounted in the centre of a wave channel. This idealised study indicated a very good correlation for the free surface results, however due to the symmetries involved, the array effects observed were negligible and there was no tangible benefit. This chapter constitutes an evolution of this previous work by considering a more realistic WEC in a diffraction study. The WEC considered is the CETO 5, which was developed by Carnegie Clean Energy (Fievez and Sawyer 2015; Rafiee and Fievez 2015). A full scale deployment of this technology was completed as a part of the Perth Wave Energy project (PWEP). The Australian Wave Energy Atlas project performed measurements around this full scale deployment (Contardo et al. 2018). This thesis forms a component of the Wave Atlas project which lead to the selection of the specific WEC.

The CETO 5 is a submerged, bottom referenced, pressure differential point absorber; the full system consists of a submerged buoy (from here referred to as the buoyant actuator (BA)) which is connected to the sea floor with a tether incorporating a hydraulic pump. The BA is excited into motion by incident waves which allows the pump to capture energy. The CETO 5 system encompasses many technical components, however for this research only the hydrodynamic characteristics of the BA are of interest. Figure 4.1 presents three CETO 5 BA units during (left) and after (right) the PWEP. The wave conditions from this full scale deployment are expressed in Figure 4.2, this includes a bivariate probability distribution of seastate by the energy period (T_E) and the significant wave height (H_{M0}) as well as the independent probability distribution of the two variables. While the full scale geometric properties are given in Appendix B.1. All these full scale characteristics were employed in determining the model scale testing conditions and parameters.

While the full scale PWEP deployment was clearly not an infinitely wide row of CETO

Figure 4.1: (left) Array of three CETO 5 units during PWEP in 2015. (right) Three CETO 5 units post 2015 deployment (Carnegie Clean Energy 2015).

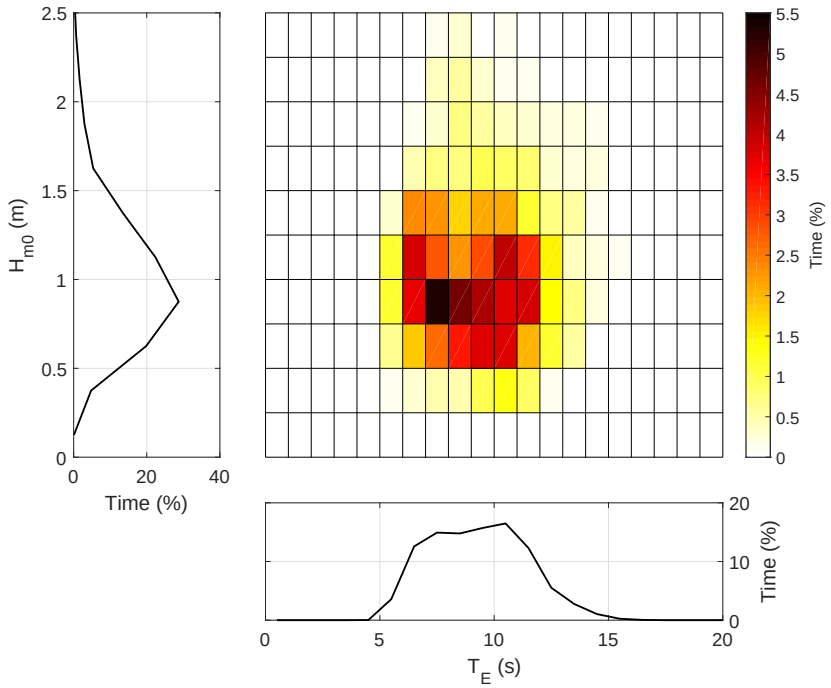

Figure 4.2: Scatter plot of the wave conditions at the PWEP test site. Including the probability distribution of the energy period (T_E) and the significant wave height (H_{M0}) as well as the bivariate probability distribution. Measurements from the AWavEA project (Contardo et al. 2018).

5 units it signals an intention to deploy WECs in arrays. However, as discussed above in Chapters 1 and 3 the complexity of WEC array interactions quickly causes studies to become very expensive both numerically and experimentally.

The diffraction problem is of interest for WEC dynamics as it dictates the excitation force which induces motion and allows for energy capture (Babarit 2013; Falnes and Kurniawan 2015; Folley and Forehand 2016; Folley, Alves, et al. 2016; Folley, Babarit, et al. 2012; Rafiee and Fievez 2015).

WEC intra-array effects can manifest with a variety of outcomes. Through this thesis they are discretised into three categories with reference to amplitude measurements; they are neutral, positive and negative. Neutral effects refer to conditions where there is no change in amplitude, however change in phase is possible. Positive refers to an increase in amplitude of the relevant measure through constructive interference. While negative is the reciprocal with a decrease in amplitude through destructive interference.

This chapter explores tools to reduce the cost of investigating WEC array interactions; this is done with the use of walls to simulate array effects both experimentally and numerically. The numerical study includes variation in the submersion depth of the BA to explore some of the many possibilities for array optimisation. The experimental study employs stereo-videogrammetry to assess the near field wave conditions.

4.2 Method

4.2.1 Experimental

The experimental work described in this chapter was also conducted in the Towing Tank at the AMC. The model used is 1:16 scale of a CETO 5. The scale was selected through a dimensional study on the full scale information and the experimental facilities; a summary of the critical information is provided in Table 4.1.

Table 4.1: Dimensional study to determine experimental scale.

	Full Scale	Model Scale (Ideal)	Model Scale (Actual)
Array Spacing	50.9 m	3.2 m	3.55 m
Wave Period	4-15 s	1 - 3.75 s	0.8 - 3.2 s
Water Depth	24-25 m	1.5-1.56 m	1.5 m

The model can be seen in Figure 4.3, with a drawing depicting the BA on the left and a photo taken during setup on the right. The key characteristics of the experimental setup are given in Table 4.2. An internal structure for the BA was designed to mount the load cell as close

to the centre of gravity as possible. The 6-DoF load cell employed was an ATI-mini 58 in the IP-68 axial cable variant, a calibration was performed such that loads and moments measured are all about the centre of gravity of the model. A frame was fitted to the top surface of the BA, with reflective balls attached to facilitate a Qualisys motion capture system (Qualisys AB 2017).

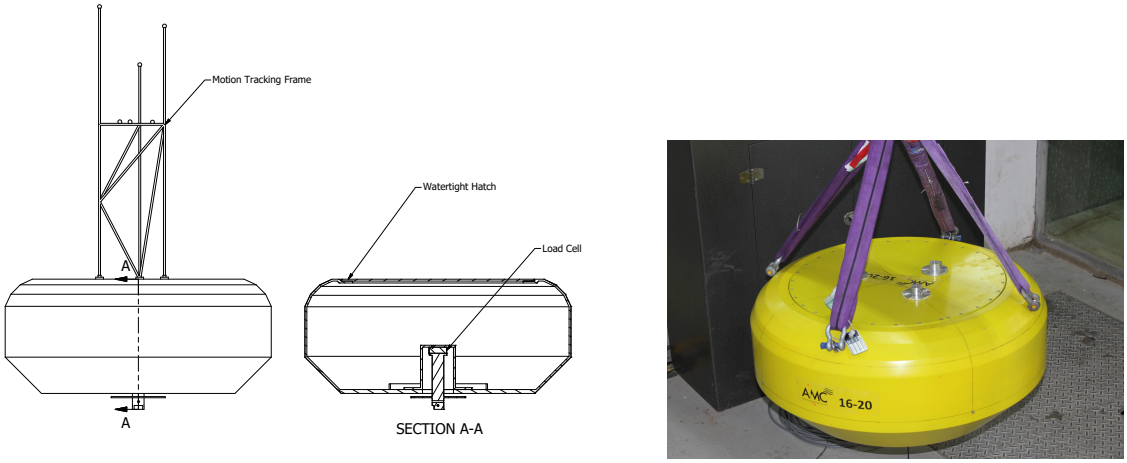

Figure 4.3: (left) Drawing of Buoyant Actuator with cut-out (right) Photo of Buoyant Actuator during setup.

The model was mounted on a frame, which was bolted to the floor such that the BA was on the longitudinal centre-line of the tank. The frame included a rail mechanism which limited motion to heave. The vertical motion was driven by a linear electric motor, Linmot PS01-48x240F-SSC-FC stator, PL0127x800/720 slider and an E1200-GP-UC controller (LinMot 2016b). Motion in other DoF was restricted by two rails on either side of the linear motor, each rail was fitted with two bearing carriages. Figure 4.4 illustrates the supporting structure and its location.

Table 4.2: Key characteristics of model and experimental arrangement.

Scale	16	-
Diameter of BA (L_D)	687.5	mm
Height of BA (L_H)	295.3	mm
Tank Width(L_A)	3550	mm
Water Depth(d)	1500	mm
Wetted Surface Area (A_w)	1.167	m^2
Mass of BA	83.8	kg
Mass of Displaced Fluid	97.7	kg
Vcg (above bottom of BA)	123.5	mm
Rxx (Cg)	127	mm
Ryy (Cg)	127	mm
Rzz (Cg)	183	mm

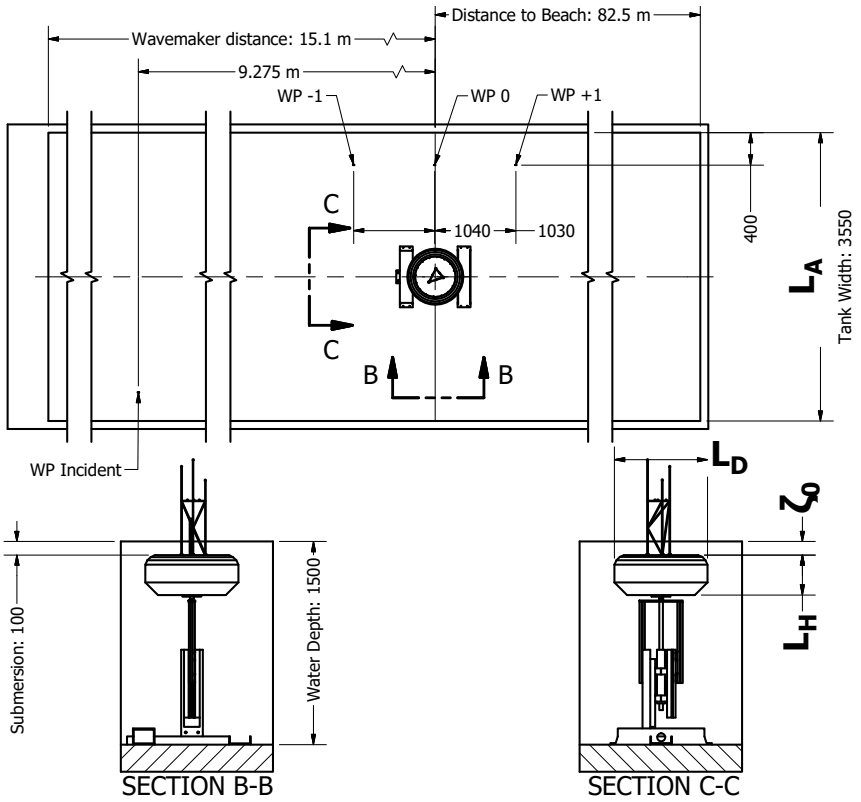

Figure 4.4: Tank Layout, dimensions are in mm unless otherwise indicated.

For the measurement of the free surface, stereo-videogrammetry was employed along with an array of six resistive wave probes. The locations of the resistive wave probes is given in Table 4.3. The stereo-videogrammetry deployment consisted of two camera pairs arrayed on a beam. The beam was attached to the ceiling of the facility with two vertical stepper motor driven linear stages. The linear stages were installed to provide vertical translation for the stereo-videogrammetry calibration and validation. The stereo-videogrammetry cameras used were four Basler ACE 12-bit, 4-megapixel USB3 cameras, each fitted with a Kowa 6mm LM6HC, 1.5 X Edmund optics lens extender and c mount orange long-pass filter (Midopt LP550-25.4). The cameras were positioned to create two overlapping surface regions. All four stereo-videogrammetry cameras were configured to capture with a shared hardware trigger; the trigger frequency was 25 Hz. The UV lights employed were LED wash lights, these were fitted along the side of the tank and reflected off the ceiling to create a diffuse light over the experimental area. The motion tracking system required four additional cameras positioned around the experimental area, the vision-based system operates within the IR light band and so is unaffected by UV light employed by the stereo-videogrammetry system. The reciprocal was not true, and so care was taken to ensure reflections from the IR light emitted by the motion capture system was not visible in the field of view of the stereo-videogrammetry cameras; noting that had a band-pass filter been used instead of a long-pass, this would not

Table 4.3: Arrangement of resistive wave probes. The co-ordinates are relative the BA with positive X in the direction of incident wave propagation.

Label	X-Coordinate (m)	Y-Coordinate (m)
WP_{IN}	-9.3	-1.425
WP_{-1}	-1.0	1.375
WP_{0}	0	1.375
WP_{+1}	1.0	1.375
WP_{+10}	10	1.275
WP_{+20}	20	1.275

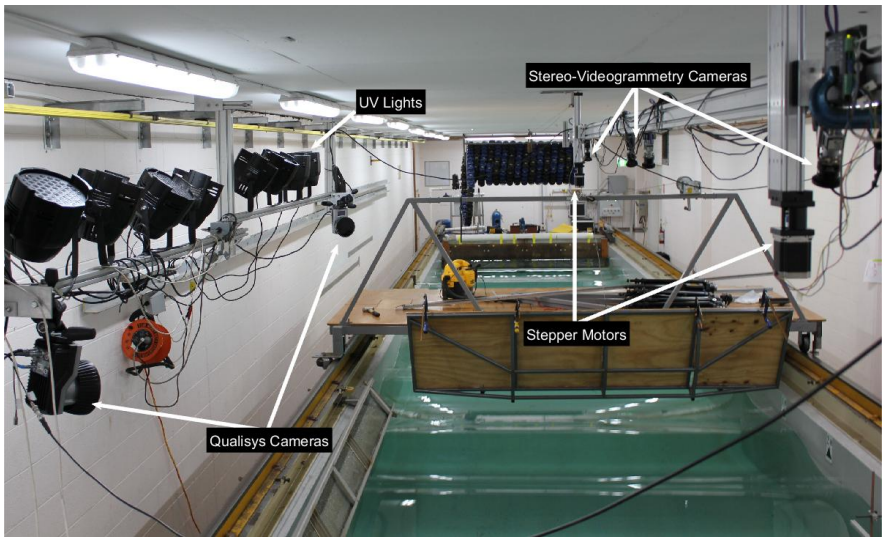

Figure 4.5: Camera and light layout for vision based data collection, two additional Qualisys cameras were positioned to the right of frame.

have been an issue. The camera and light set-up can be seen in Figure 4.5. The facility employed in the experiments has no natural lighting, consequently there is a high level of control of the lighting conditions. Diffused and consistent light intensity was found to improve image processing and also enables use of a lower image sensor bit depth without saturation. A further discussion on the lighting system is available in Appendix F.2.

4.2.2 Stereo-Videogrammetry Processing

The calibration of the stereo-videogrammetry images was undertaken by the same procedure as outlined in Chapter 2.2.2. Calibrations were required for each of the two camera sets, five elevations were employed, where the linear stepper motors were used for vertical translation. The resulting coefficients from the calibration process are given in Appendix B.3 in Table B.1. The subsequent processing in DaVis was completed with a subset size of 21, step size of 9, calculation mode set to fast and a maximum expected displacement of 100 px. The same correction to the zero surface was applied by subtracting the static water level from all

frames, where the static water level was determined by averaging 50 frames. This process is thought to be required due to distortion of the floating calibration plate, the resolution was employed as getting a 2.4×2.4 m plate lying completely flat and level floating on water was deemed impractical. The approximation is thought valid as the maximum expected motion of the free surface, 100 mm, is small compared to the displacement of the cameras to the free surface, 2000 mm. As with Chapter 2 localised discontinuities were identified by regions of excessive gradient, it was found however that as a result of a more complex wave field the assumption of $|\nabla\eta(x,y)| \geq 2ka$ was too stringent and correctly measured surface sections were being removed, as such the condition was relaxed to $|\nabla\eta(x,y)| \geq 3ka$.

The above processing was completed on the two distinct measurement regions, all data was referenced to the same spatial reference frame with theoretically no warping. The two measurement areas were combined by the following process;

1. Find lateral cross section (constant X) with lowest variance in surface elevation.
2. Join data sets along the cross section.
3. Dilate the join by 6 pixels.
4. Interpolate the dilated region.

A pixel-wise temporal reconstruction was employed to fill instances where the frame failed to compute; this was done using a cubic spline. As with any stitching of data sets there is a risk of a poor match, the quality of the resulting surface is discussed in the Discussion section of this Chapter. The experimental area achieved with this approach measures approximately 4.5 m by 3 m, with a discretisation of 3 mm on across the horizontal domain.

4.2.3 Data Analysis

The primary component of analysis of the experimental results is in the frequency domain with a Fast-Fourier Transform (FFT); a description on the underlying principles are given by Chakrabarti (1987). The primary explicit assumptions of the approach is that a signal is repeating and can be described as a sum of trigonometric functions. For a signal of finite length this drives the possible precise periods able to be detected to rational fractions of the measurement period, with a limit of the Nyquist Frequency.

All time series data has been trimmed such that t_0 is the zero up-crossing preceding the first wave crest greater than 60% of the nominal wave amplitude at WP 0. The experimental period is determined by the phase velocity of the wave and the distance the wave travels to the beach and back. Phase velocity is employed as this describes the speed at which the wave

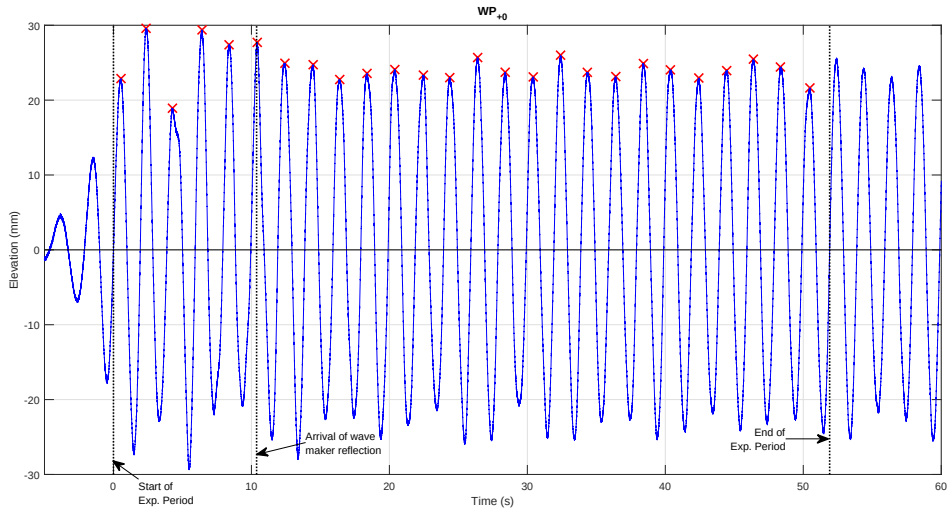

Figure 4.6: Time series of WP_{+0}, for a condition of 0.5 Hz and 25 mm. Dotted lines indicate key points in experimental time. Red crosses are all peaks exceeding 60 % of wave amplitude within the experimental period.

front propagates. This implicitly means that reflections from the wavemaker are evident in the data, these reflections are considered to have only minor impact on the results. The reason for this is that the reflections from the wave maker will induce a change to the amplitude and phase of the already existing incident wave, this change will be small compared to the characteristics of the expected wave. Conversely the reflection the beach end will introduce a new wave component with energy travelling in the opposite direction to the desired incident wave. The point when reflections from the wavemaker arrive at the measurement point are indicated on any time series data that is presented. A sample of the experimental period is shown in Figure 4.6.

Frequency domain analysis is completed with a Fast-Fourier Transform (FFT). This assumes a steady state for this spectral approach, there are many similar approaches described through literature, but the specific approach used here can be described by process flow chart in 4.7. Where phase averaging refers to a process where the precise wave period is determined with average time between zero up crossings. Cubic interpolation has the potential of augmenting the noise floor of a signal; in this study only the peak frequencies are of interest; consequently any change to the non-harmonic frequencies are considered irrelevant.

A sample of the resulting FFT amplitude spectrum are presented in Figure 4.8, the sample is for pitch excitation moment of a run with a 0.8 Hz and 25 mm incident wave. The results from the resampling method employed in this work is presented in comparison with an alternative of zero-padding a time series to the next power two data points. The extended frequency range plot (left) includes a graphical indication of the harmonic components. In the restricted frequency range view (right) it can be seen that almost all the energy in the

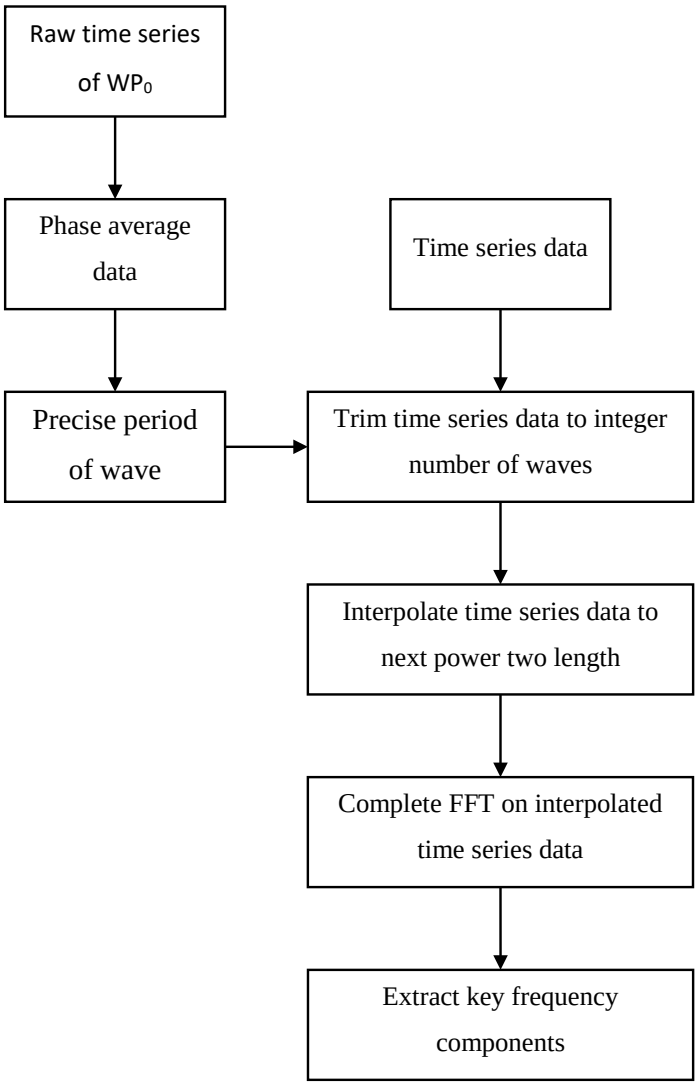

Figure 4.7: Process flow chart for completing spectral analysis.

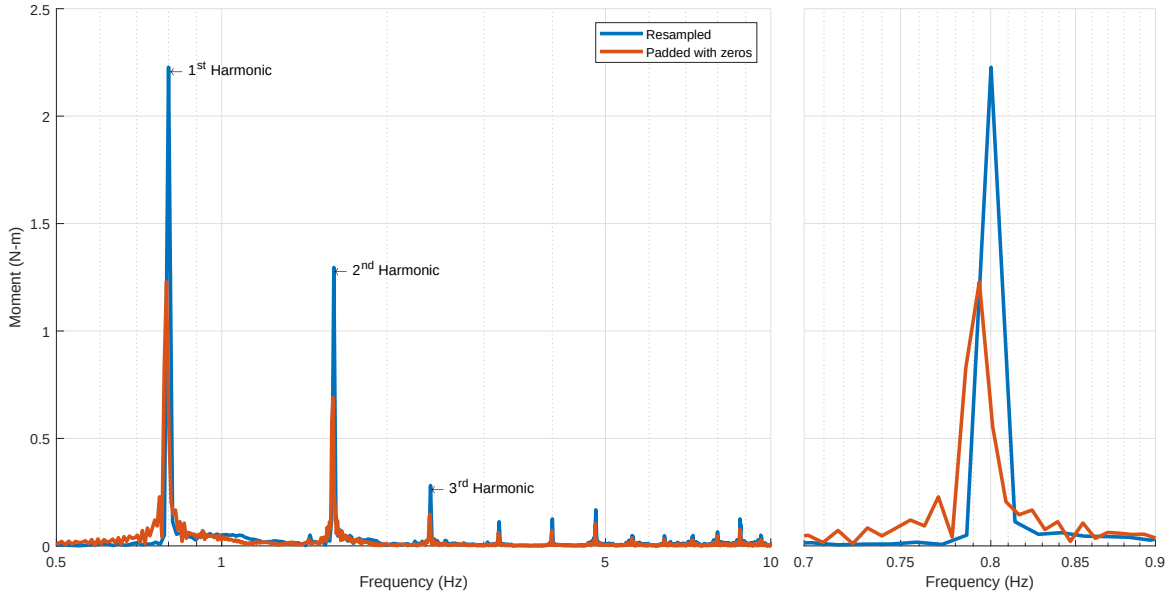

Figure 4.8: Sample of FFT results obtained, this example is for a 0.8 Hz 25 mm incident wave considering the pitch excitation moment (N-m). (left) Extended frequency range and (right) restricted frequency range.

signal is concentrated in a single frequecny component of the resampled amplitude spectrum, whereas the spectrum for the zero padded time series sees the energy spread between more frequency bins. This results in the amplitude of the resampled spectrum being seemingly higher than the zero padded. With all the energy being placed into a single frequency bin it is possible to use both the amplitude and phase of the results. Noting this procedure uses no filtering on the final results, as such there is no attenuation of the amplitude nor any phase shift.

As appropriate results have been normalised and non-dimensionalised. Incident wave frequency has been non-dimensionalised with two approaches,

$$\nu_{WD} = \frac{L_D}{\lambda} \tag{4.1a}$$

$$\nu_{WA} = \frac{L_A}{\lambda} \tag{4.1b}$$

Where ν_{WD} is the device non-dimensional linear wave number, ν_{WA} is the array non-dimensional linear wave number, λ is wavelength, L_D is the critical length of the BA (diameter) and L_A is the critical dimension of the array (tank width). The relationship between these non-dimensional linear wave numbers and the experimental incident wave frequency employed is given in Table 4.4.

Table 4.4: Relationships between experimental incident wave frequencies compared with device and array non-dimensional linear wave numbers.

Frequency (Hz)	Array Non-Dimensional Linear Wavenumber (ν_{WA})	Device Non-Dimensional Linear Wavenumber (ν_{WD})
0.3	0.31	0.059
0.4	0.44	0.085
0.5	0.61	0.12
0.6	0.84	0.16
0.7	1.1	0.22
0.8	1.5	0.28
0.9	1.8	0.36
1	2.3	0.44
1.1	2.8	0.53
1.2	3.3	0.63

The forces and moments are normalised with,

$$F_{ND-D}(\omega) = \frac{F_{ex}(\omega)}{a\rho A_w g} \tag{4.2a}$$

$$M_{ND-D}(\omega) = \frac{M_{ex}(\omega)}{a\rho A_w g L_D} \tag{4.2b}$$

Where a is the incident wave amplitude, ρ density of water, A_w is the wetted surface area and g is acceleration due to gravity. The incident wave amplitudes, a, used here are from separate measurement runs of the pure incident wave with no BA in place. The data reduction equations for the associated uncertainty of these measurements is given in Appendix E.2.

All results presented include both amplitude and phase, where the phase definition is expressed by,

$$X(t) = \mathrm{Re}\left(Ae^{-i(\omega t-\phi)}\right) \tag{4.3}$$

where X is an arbitrary measurement which is a function of time, ω is angular wave frequency, t is time, i is the imaginary unit and ϕ is the phase.

The processing for the stereo-videogrammetry was completed on a PC with 64 GB RAM and with two Intel Xeon E5-2630v2 CPU, which results in 24 logical processors @ 2.6 GHz processing speed. The processing time for two sets of raw images through to the final frequency domain free surface results was approximately 10 min per sec of experimental time. This processing was completed in three steps,

1. DIC to turn raw images into surface measurements (Parallelised accross all cores).
2. Combining distinct measurement areas into a single surface as well as error identification and correction.
3. FFT of over free surface with respect to time (Parallelised accross 10 cores).

4.2.4 Numerical Modelling

As a complement to the experimental study described above numerical modelling with the linear potential flow, boundary element method solver *NEMOH* was completed, details of the software are given in Chapter 3.2. The processing methods are largely the same, including both loads and free-surface elevation components. The numerical study formed the basis for the calibration of the load cell in the experimental study. Initially a submersion depth study is presented for a single and wall conditions. Then for the experimental submersion depth case an additional three device case is added. The mesh characteristics and cases considered are presented in Table 4.5 with the meshes shown in Figure 4.9.

Table 4.5: Numerical modelling key characteristics.

	Panels		**Frequency**	
	BA	**Wall**	**Range (Hz)**	**Quantity**
Single	816	-		100
Three	2482	-	0.3-1.2	600
Wall	816	1881		600

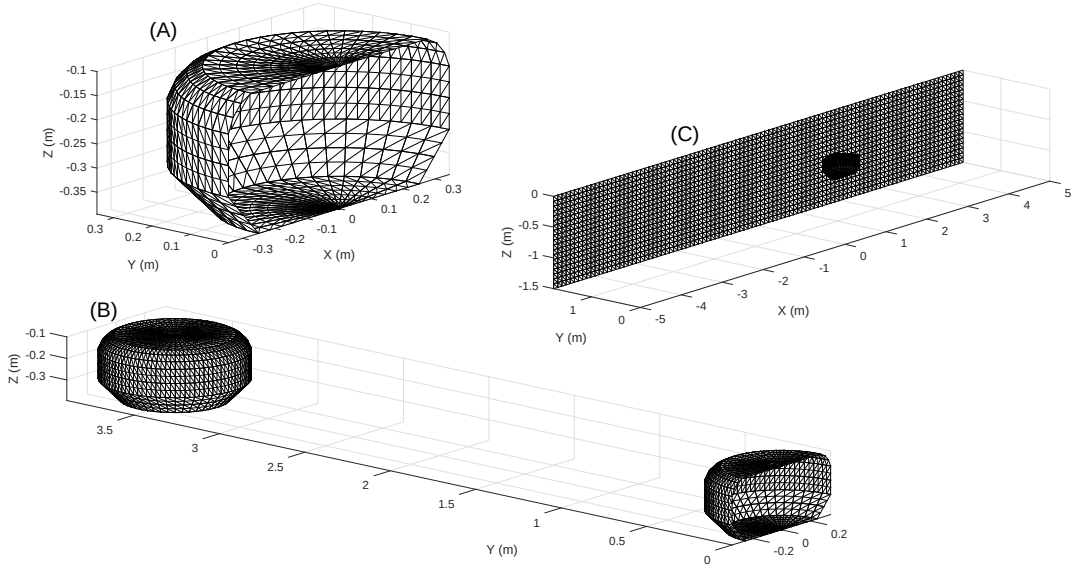

Figure 4.9: Meshes used in *NEMOH* modelling. Single, Three and Wall simulation meshes are presented as (A), (B) and (C) respectively.

The depth dependence study non-dimensionalises submersion depth by

$$S_{DR} = \frac{\zeta_0}{L_H} \tag{4.4}$$

where ζ_0 is submersion depth and L_H is height of the BA (here 295.3 mm). These dimensions are indicated in Figure 4.4.

4.3 Results

It is inherent to the technology that the BA can be positioned at multiple submersion depths; Figures 4.10 and 4.11 present the heave excitation force for such a study. Figure 4.10 presents the information in polar plot format with no reference to incident wave condition and Figure 4.11 presents the results as amplitude (left) and phase (right) with respect to incident wave condition. Submersion depth is expressed in the legend as a ratio of submersion depth and height of the BA, with (4.4). The force is non-dimensionalised by (4.2) and the incident wave condition is expressed by the non-dimensional linear wave numbers defined by (4.1). The numerical arrangements considered are the single and wall configurations. Equivalent surge and pitch results are included in Appendix B.2.

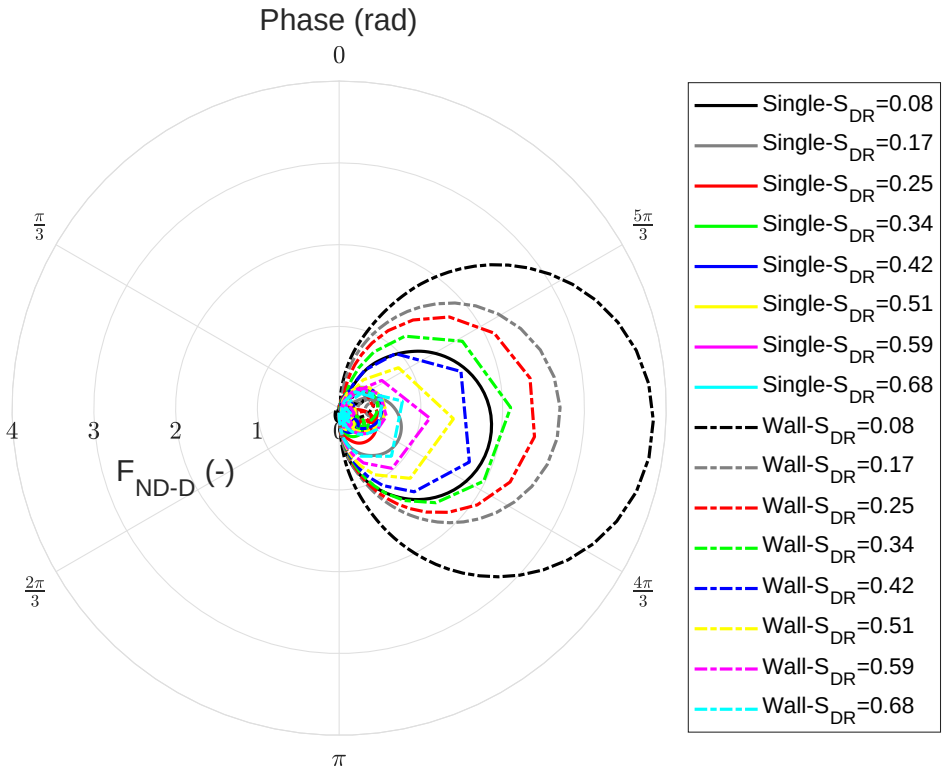

Figure 4.10: Effect of submersion depth on heave excitation force for single and wall conditions presented in polar format.

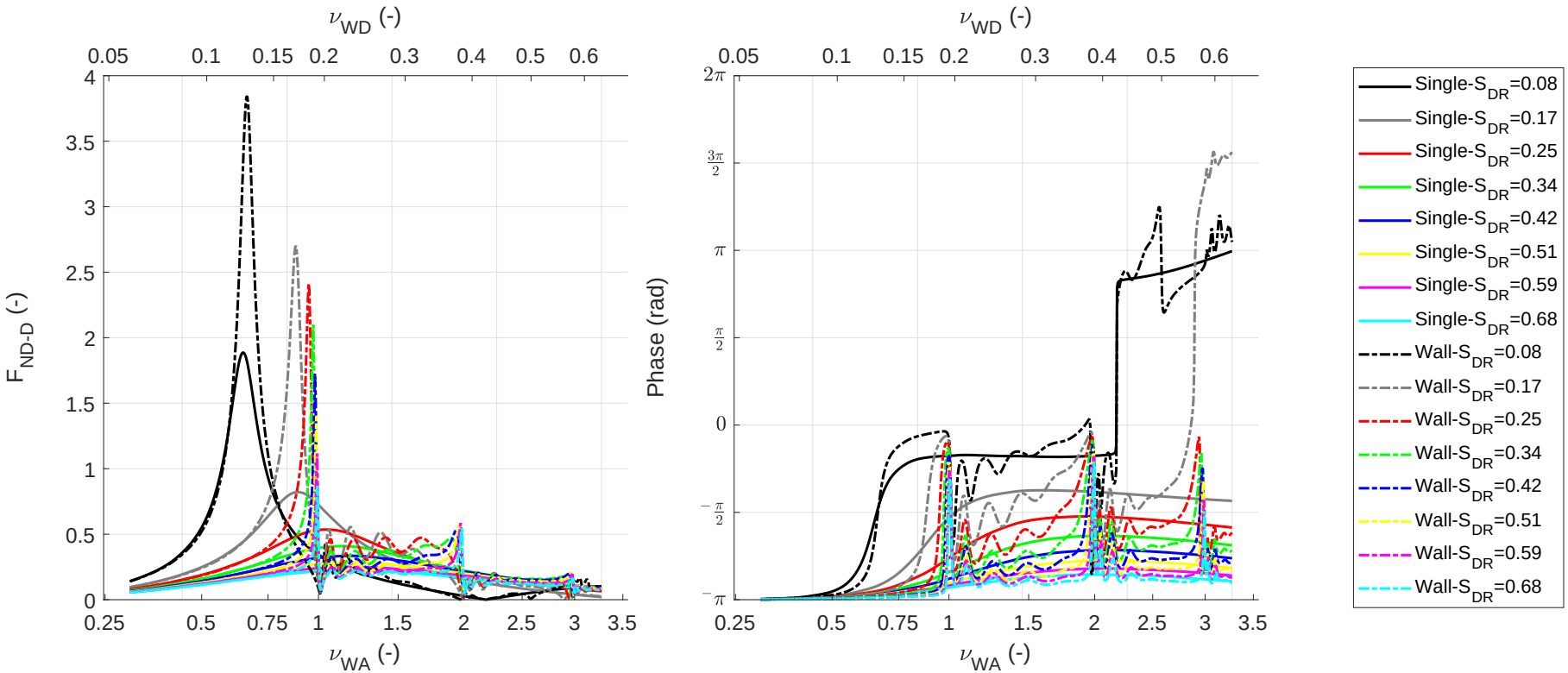

Figure 4.11: Effect of submersion depth on heave excitation force for single and wall conditions, (left) amplitude (right) Phase angle.

As is to be expected there is clear evidence that the excitation force varies considerably with submersion depth, in the single and wall configurations concurrently. Furthermore, while there is a relationship between the configuration it varies with submersion depth. These traits are evident in the variation in the wave number of the peak amplitudes, ranging from $\nu_{WA} \approx 0.7$ for $S_{DR} = 0.08$ through to $\nu_{WA} \approx 1$ for $S_{DR} = 0.68$ for the wall study as an example.

The nodes in Figure 4.11 ($\nu_{WA} \approx \{1, 2, 3\}$) have similar characteristics to the irregular frequencies which are a recognised issue with *NEMOH* (Babarit and Delhommeau 2015), in this instance though they are thought to be real due to the expected resonance from the wall reflections.

With this study, where 600 frequency discretions were employed, it can seen in Figure 4.10 that more frequencies are required to get a true trend in excitation force. Observing the step-like nature of the excitation force for $S_{DR} > 0.25$ at Phase$\approx \frac{4\pi}{3}$. These steps suggest that the excitation force is highly subjective on the precise frequency under these conditions. The highly stepped regions coincide with incident wave conditions of $\nu_{WA} \approx \{1, 2, 3\}$.

Focusing on the condition where the BA has a submersion depth of 0.1 m ($S_{DR} \approx 0.34$), Figure 4.12 presents the excitation loads from experimental measurements in comparison with the corresponding numerical study presented with amplitude on the left and phase on the right. Figure 4.13 presents the same numerical results in a polar format without reference to incident wave condition. For both figures, A is surge, B is heave and C is pitch. Wave condition and loads have been non-dimensionalised as above. Phase angle is prescribed as shown by (4.3). The expanded uncertainty is presented for the experimental measurements to a 95% confidence level (ITTC 2017b). The determination of the measurement uncertainty is described in Appendix E.2 and random uncertainty was assessed by the maximum variance observed of conditions where three or more runs were completed.

It is important to note the runs that were completed with a 50 mm amplitude and $\nu_{WA} = \{2, 2.75, 3.25\}$ had saturation induced on the load cell; as such these data points are not included in the force study. This saturation is suspected to be related to pitch excitation moments being higher than expected as a result of large harmonic components, but this cannot be causally proved given the load balance style. For the type of load cell employed, if any channel becomes saturated all load measurements are invalidated (ATI Industrial Automation 2018).

For the condition $\nu_{WA} = 1$ no testing was completed for an amplitude of 50 mm, this was due to concerns around damage to equipment with the resonance occurring. An additional amplitude was completed with 12.5 mm amplitude for this wave condition only.

Figure 4.14 presents the harmonic orders, one and two, of the diffraction excitation loads

and moments. The data is treated in the same way as Figure 4.12, with the exception that no numerical simulations are included. The second order harmonic is the peak in spectral frequency defined by $2f_1$, this is also illustred in Figure 4.8.

The first harmonic excitation load results indicate a good correlation between the experimental and numerical results, in terms of both amplitude and phase, for all (but one) conditions considered. The only exception was the larger amplitude wave at $\nu_{WA} \approx 0.8$ on pitch excitation where the phase angle is almost π rad out of phase, this is the condition shown in Figure 4.19. The wave breaking which is evident suggests large higher order load components, this is evident in the second order component for pitch amplitude exceeding the first order. The stereo-videogrammetry has not been presented for this condition as it was not possible to fully compute, as can be seen in the images there was a large area in the lee of the BA without particles, making the DIC challenging.

The second order components of the forces were generally small as compared to the first order, as shown in Figure 4.14. The pitch excitation moment however did not follow this trend, within the range studied it was always important, to an extent that the second order exceeds the first order for $\nu_{WA} < 1.5$.

Videos 4.1 and 4.2 present a sample of the time series from the stereo-videogrammetry results, this includes the free surface and velocity vectors. The conditions shown are for $\nu_{WA} \approx 1.1$ and $\nu_{WA} \approx 1.8$ both with an incident amplitude of 25 mm. Playback speed is at 1/4 true, with experimental time displayed in the bottom of frame.

It can be seen that with the relaxation of the error level $|\nabla\eta(x, y)|$ there is an increased frequency of the localised discontinuities than in previous chapters, this is especially evident close to the BA (located at $(X, Y) = (0, 0)$). Where localised discontinuities refers to locations where DIC has either incorrectly or failed to determine the free surface elevation. Then the correction method has failed to identify and correct the erroneous result. Considering the velocity vectors, it can be seen along $y = 0$ that the velocity is almost exclusively along X; this suggests that the energy in the wave reflected from the walls is near balanced. This suggests that the BA was located very close to the centre-line of the channel. The free surface indicates a very large disturbance in the lee of the BA, with many harmonic components evident (seen by the comparatively short wavelengths).

While there is extensive potential for both the free surface measurements and velocity vectors, the balance of the results will focus on only the frequency domain of the free surface elevation.

A selection of free surface frequency domain first harmonic results are shown in Figures 4.15, 4.16 and 4.17 for wave conditions $\nu_{WA} \approx 0.61$, $\nu_{WA} \approx 1.1$ and $\nu_{WA} \approx 1.8$ respectively. In all figures the amplitude and phase surfaces are shown in the left and right columns respectively. The four rows, from top to bottom, represent the numerical simulations for single, three and

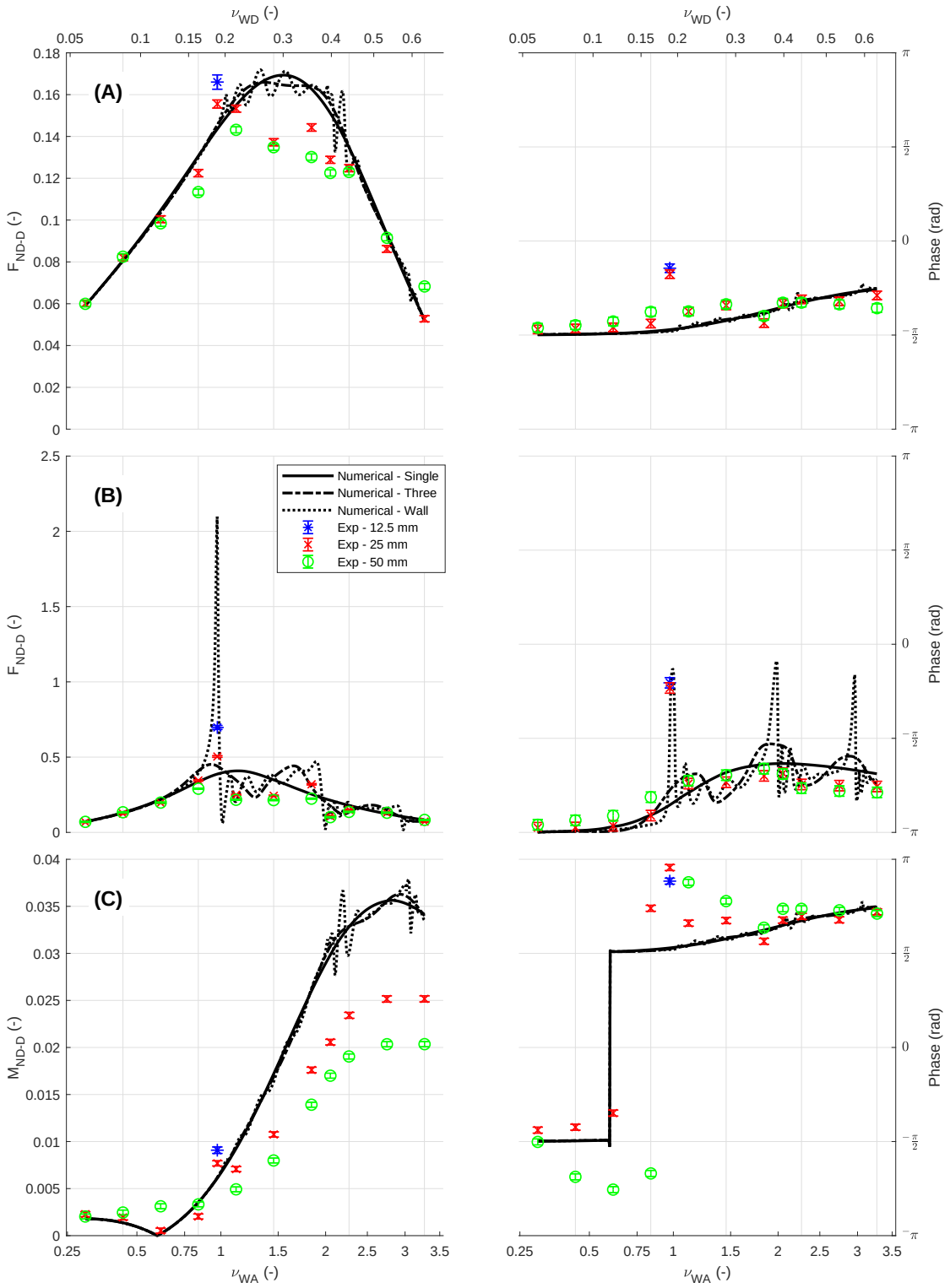

Figure 4.12: First order harmonic diffraction excitation (A) surge, (B) heave and (C) pitch loads for 0.1 m submersion depth ($S_{DR} \approx 0.34$) from experimental and numerical testing. Experimental data is discretised by incident wave amplitude and the numerical modelling includes single, three and wall conditions. The loads are presented as amplitude (left column) and phase angle (right column), with the loads non-dimensionalised and phase relative to incident wave. Incident wave is expressed by the device and array non-dimensional linear wave numbers on the top and bottom x-axes respectively.

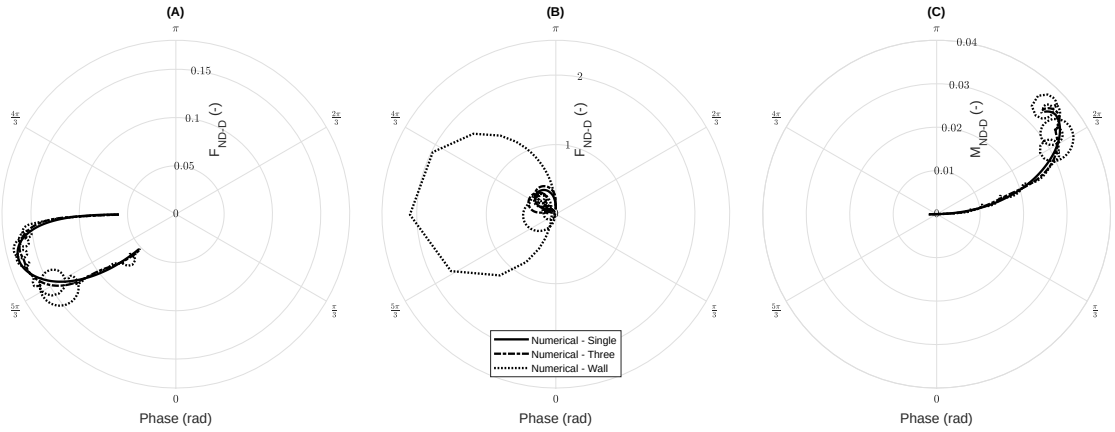

Figure 4.13: First order harmonic diffraction excitation (A) surge, (B) heave and (C) pitch loads for 0.1 m submersion depth ($S_{DR} \approx 0.34$) from numerical study; including single, three and wall conditions. Loads are non-dimensional with results presented in polar format.

wall and then the experimental measurement.

The free surface study generally indicates that the experimental results lie somewhere on the sequence of the array widths considered by the numerical study. It can be seen that within the comparison the phase angle is frequently as valuable as amplitude in assessing the relationship between configurations.

In Figure 4.15, where there are neutral array effects, there is no clear variation in the free surface (besides absolute phase which is addressed below) such that the numerical simulations have no meaningful difference to the free surface in the immediate vicinity of the BA. As the wave number increases for Figures 4.16 and 4.17 it can be seen that the change to of the free surface elevation amplitude at the BA, coordinates (0,0), increases between the simulations. In Figure 4.16 there is a reduction in amplitude from ≈ 2.5 to ≈ 1.5 between the single and wall conditions, this reduction is termed negative array effects and is also evident in the heave excitation force for this wave condition in Figure 4.12. While for Figure 4.17 the reciprocal is true with an increase from ≈ 2 to ≈ 3 between the single and wall conditions, this is termed postive array effects. For all three conditions, while the experimental measurements identical to the numerical predictions, it seems probable that the experimental measurements constitute a row of width somewhere between the wall case and the three device arrangement.

Figure 4.18 presents an additional set of free surface frequency components from the Fourier transform for the condition $\nu_{WA} \approx 1.1$ which relates to Figure 4.16. The harmonics one, two, three and six are presented as well as an additional frequency component, the amplitude is kept dimensional at model scale. Harmonic one and two relate to Figure 4.14 for the measured excitation loads. The additional non-harmonic frequency component is presented as it is representative of many frequency bins from the FFT process giving results which are seemingly not random noise.

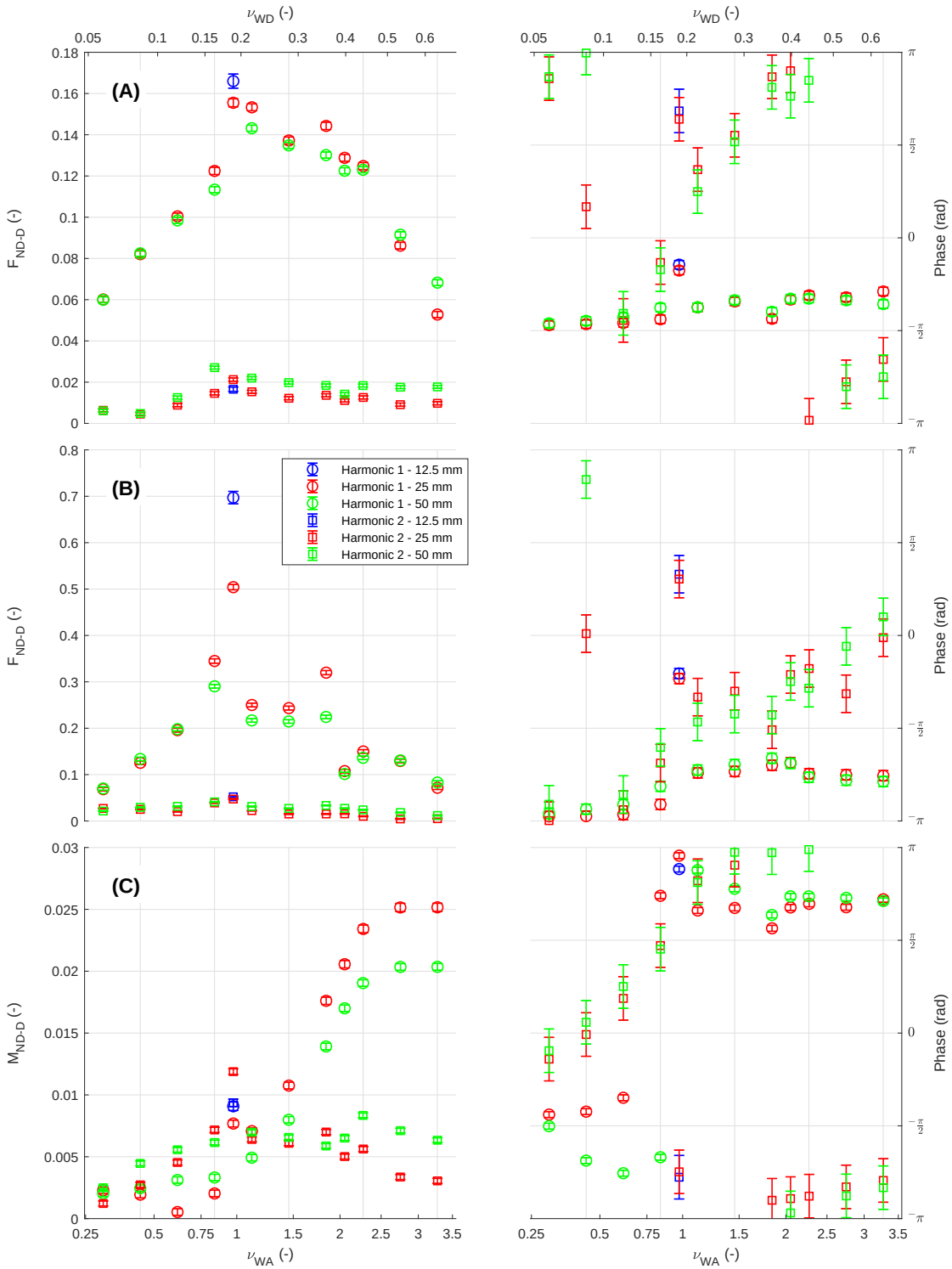

Figure 4.14: First and second order diffraction excitation (A) surge, (B) heave and (C) pitch loads for 0.1 m submersion depth ($S_{DR} \approx 0.34$) from experimental testing. The data presentation is the same as Figure 4.12.

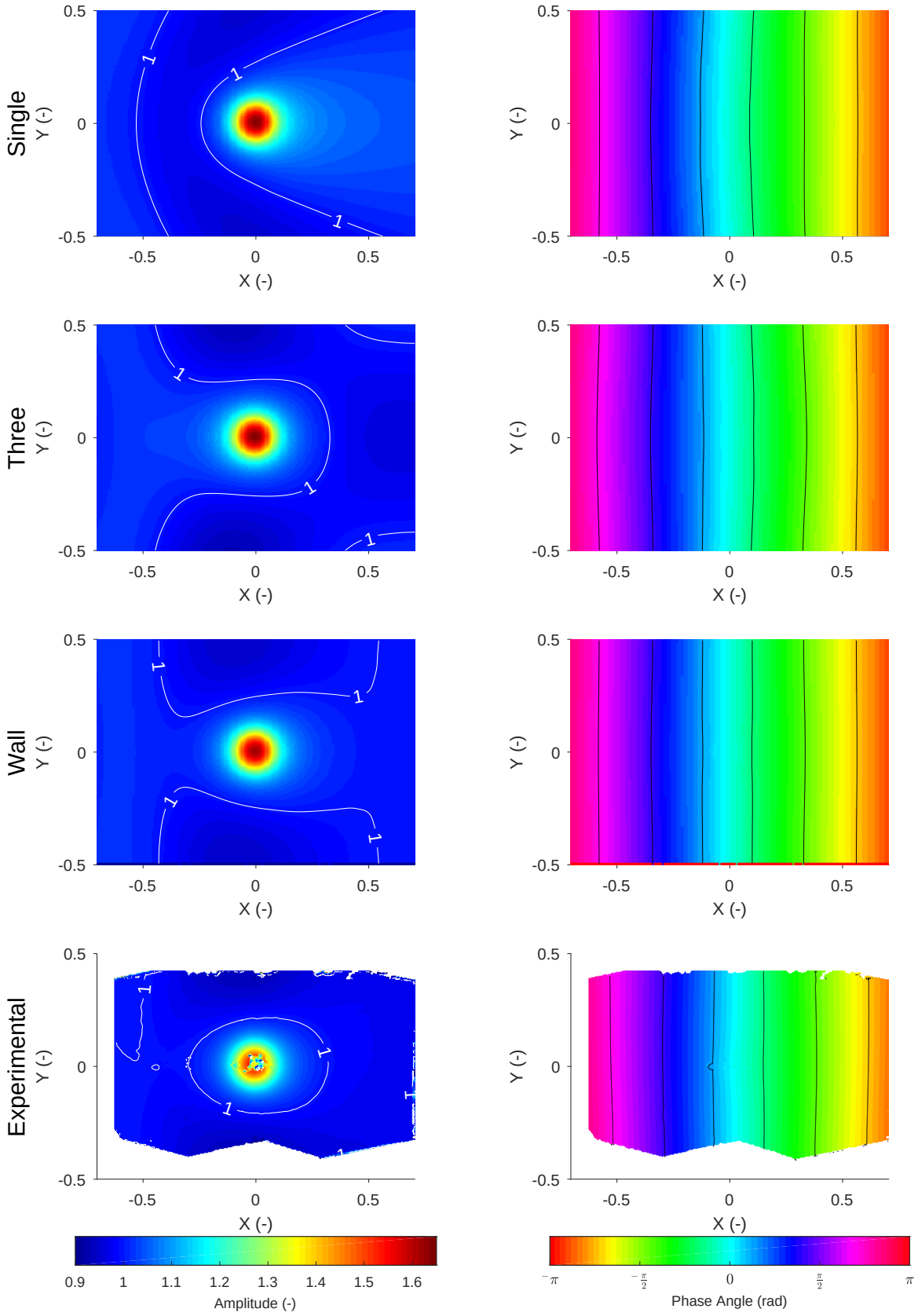

Figure 4.15: Frequency domain free surface for condition $\nu_{WA} \approx 0.61$ ($S_{DR} \approx 0.34$), this represents neutral array effects. Left column is amplitude, right column is phase. Top three rows are numerical predictions for the single, three and wall conditions; the bottom row is experimental measurement.

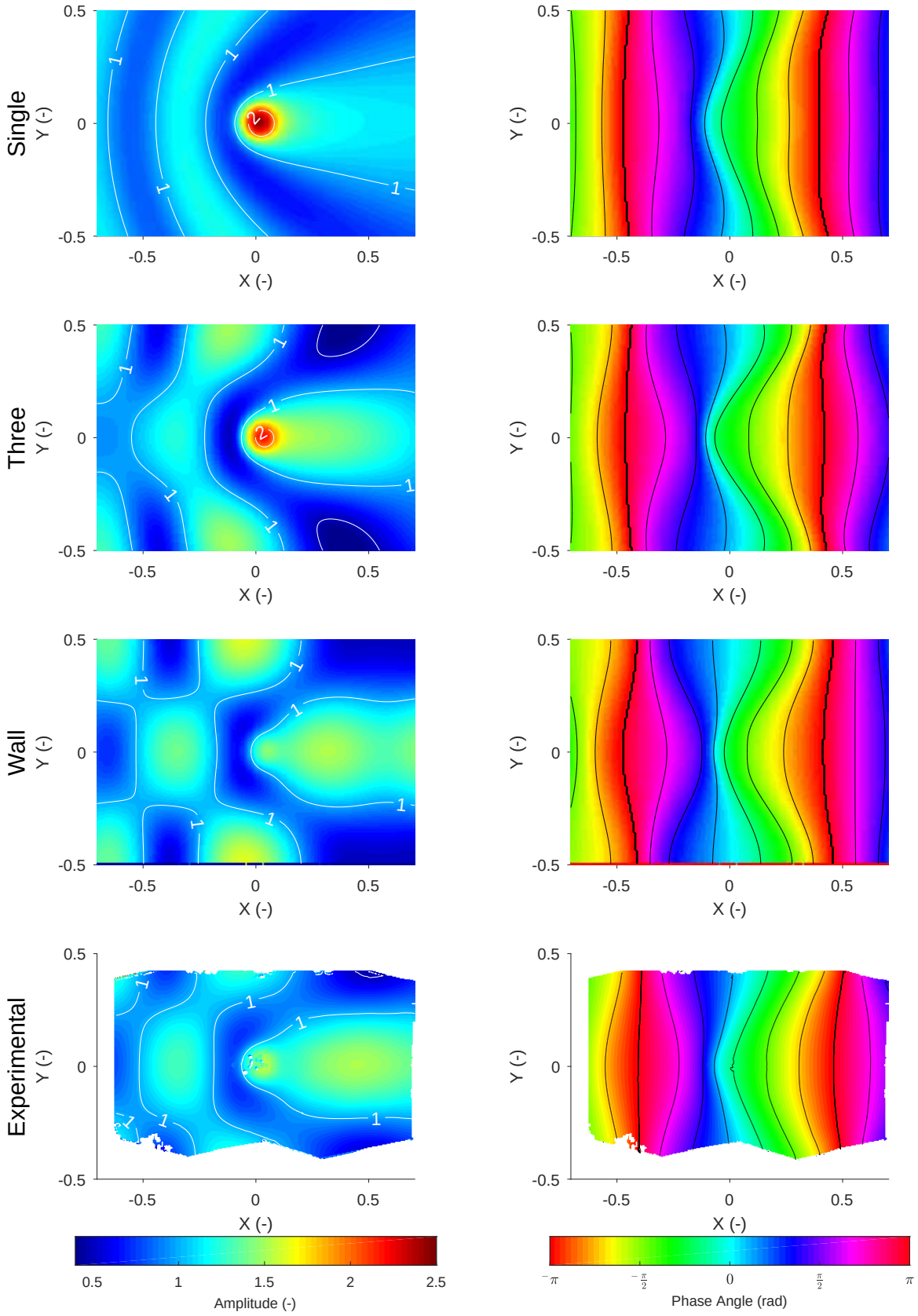

Figure 4.16: Frequency domain free surface for condition $\nu_{WA} \approx 1.1$ ($S_{DR} \approx 0.34$), this represents negative array effects. Left column is amplitude, right column is phase. Top three rows are numerical predictions for the single, three and wall conditions; the bottom row is experimental measurement.

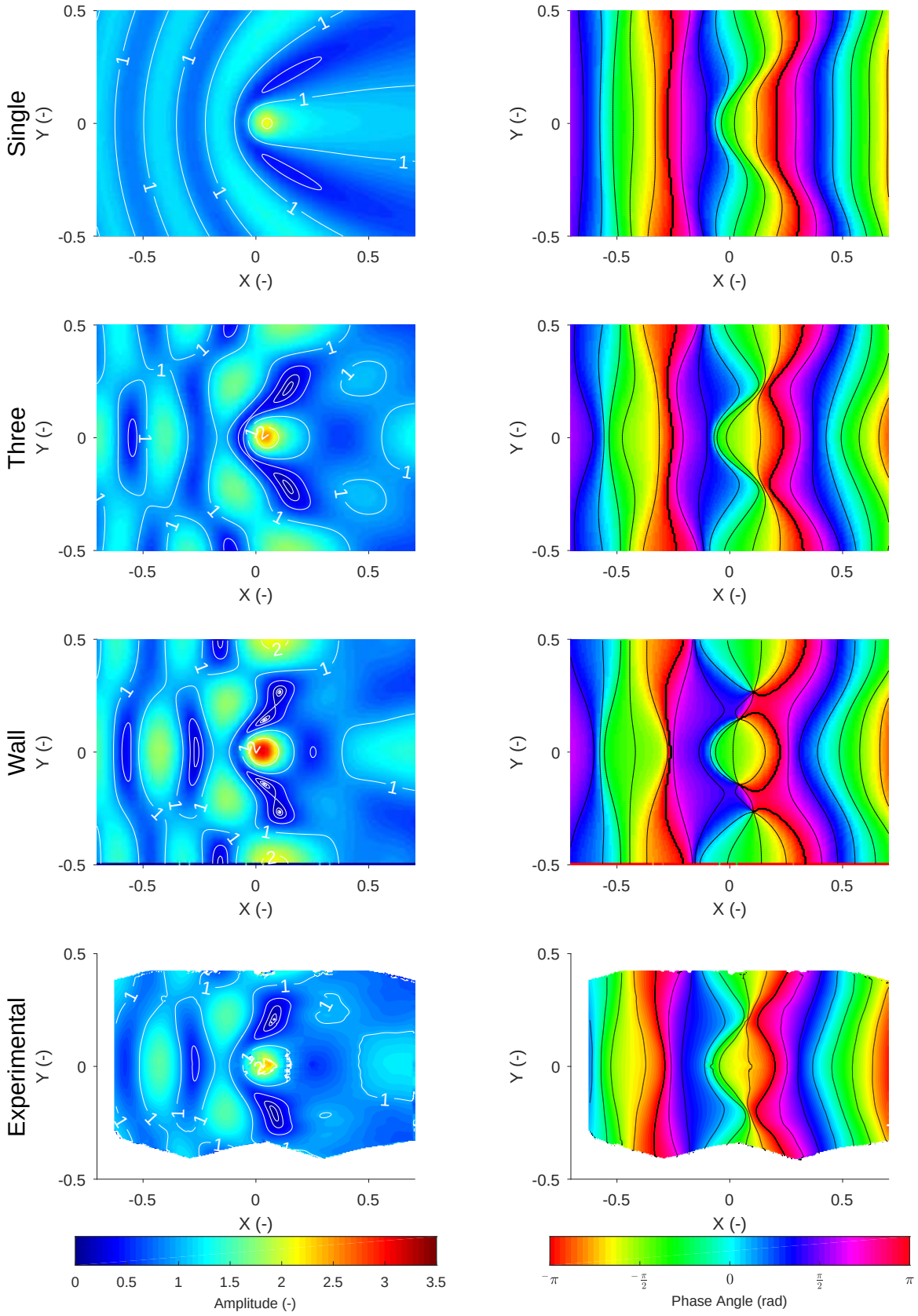

Figure 4.17: Frequency domain free surface for condition $\nu_{WA} \approx 1.8$ ($S_{DR} \approx 0.34$), this represents positive array effects. Left column is amplitude, right column is phase. Top three rows are numerical predictions for the single, three and wall conditions; the bottom row is experimental measurement.

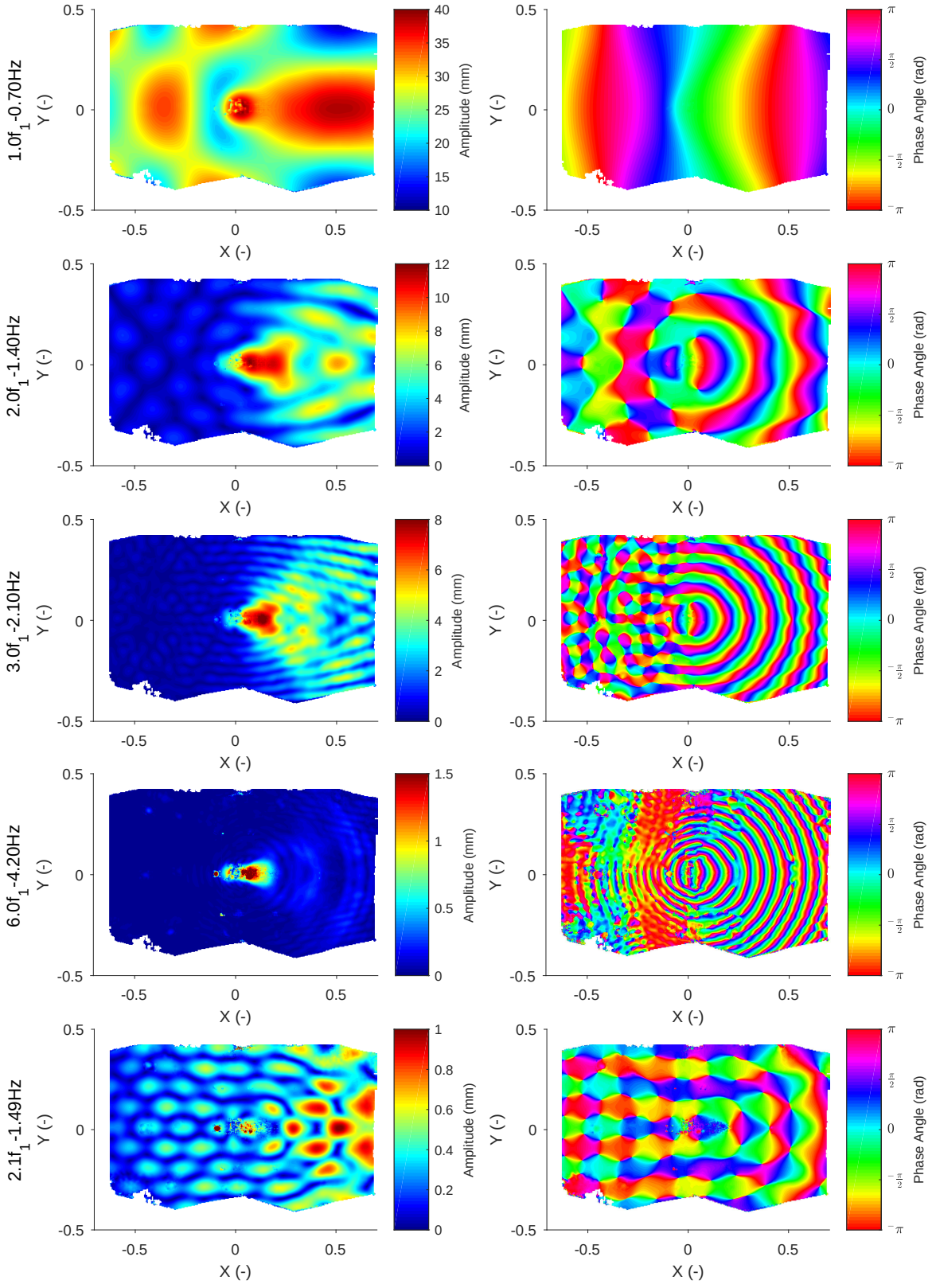

Figure 4.18: Different Frequency Components from experimental condition $\nu_{WA} \approx 1.1$. Top to bottom first, second, third and sixth harmonics and a non-harmonic.

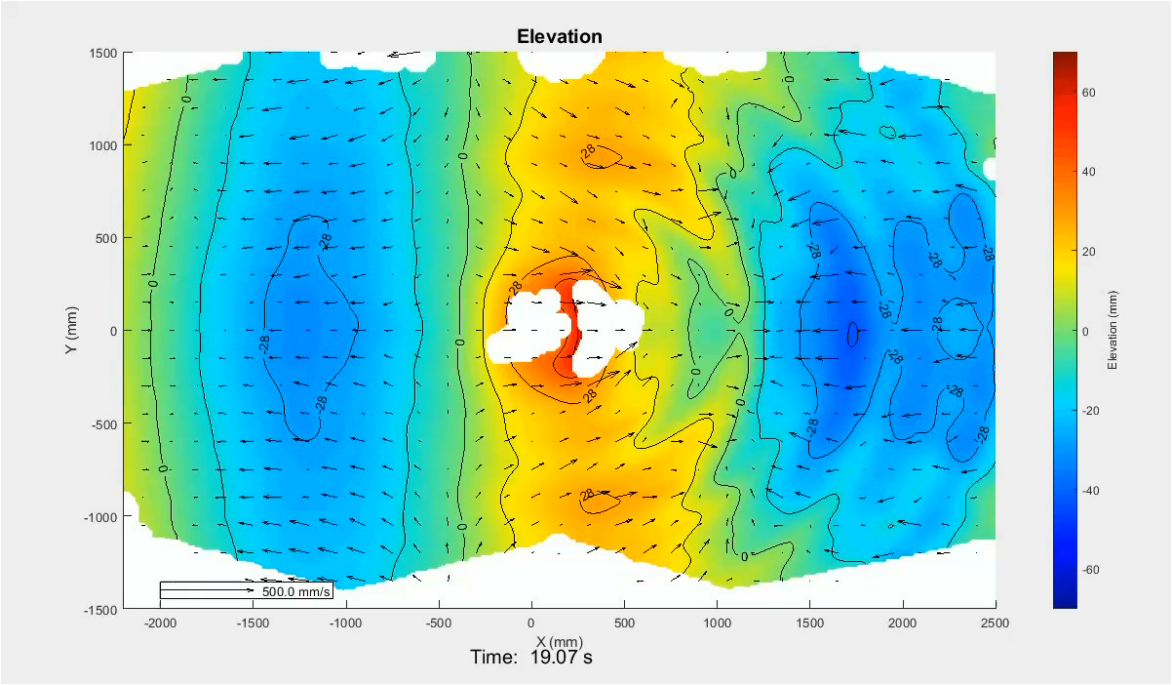

Video 4.1: Time domain free surface of condition with $\nu_{WA} \approx 1.1$. The video is available at: `https://cloudstor.aarnet.edu.au/plus/s/qL890GMwD6R7Krh`.

The free surface harmonic frequency components highlight the measurement capability of the stereo-videogrammetry approach. In the instance of the sixth harmonic it can be seen that there are large sections where no wave is recorded, evidence by the zero amplitude and the seemingly random phase. It is important to recall that the sixth harmonic has been recorded with a maximum amplitude of 1.5 mm within a wave condition exceeding 80 mm of free surface variation.

It can be seen in the stereo-videogrammetry results that there is no evidence of the join between the measurement areas, as was evident in the time domain. Additionally, the localised discontinuities are almost non-existent in the low harmonics and the noise around the top of the BA less evident. Conversely in the higher harmonics and non-harmonics the discontinuities become much more obvious, as with noise above the BA. This is due to the discontinuities occurring with an irregular frequency and the energy associated with them consequentially being dispersed to non-harmonic frequencies. As with the cylinder study the region in the immediate vicinity of the BA has challenges in capturing the free surface, the two principle reasons are the obstruction caused by the motion capture support frame and the non-linear wave interactions causing strong dispersion in this region, leaving no particles.

Supplementary frequency domain free surface results are available in Appendix B.3, these include the first harmonics of $\nu_{WA} \approx \{0.97, 2.05\}$.

During the experiments extreme breaking waves were observed, Figure 4.19 presents one such

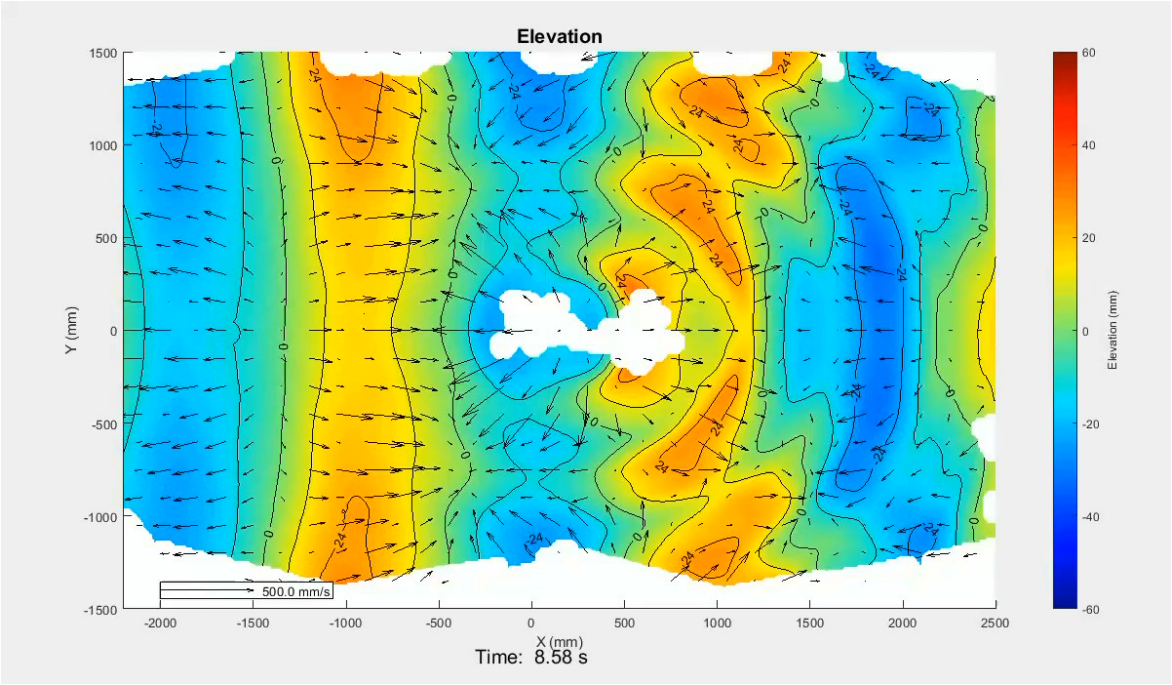

Video 4.2: Time domain free surface of condition with $\nu_{WA} \approx 1.8$. The video is available at: `https://cloudstor.aarnet.edu.au/plus/s/mRnhQ1D1GgUtnUO`.

case where $\nu_{WA} \approx 0.84$ and $a = 0.05$ m; (left) still water condition, (Centre) wave trough directly over the BA and (right) crest over the BA with the breaking. Additionally, Video 4.3 presents the condition $\nu_{WA} \approx 0.97$ and $a = 0.0125$. In both these examples it can be seen that the water fully displaces to the top of the BA. This implies strong non-first order responses, which are represented above in the harmonic free surface study.

It may be argued that the frame used for mounting the motion tracking balls induces errors in the experimental study. Figure 4.19 presents a set of three stills for a condition with $\nu_{WA} \approx 0.84$ with wave amplitude 0.05 m. In this sequence it is evident that the localised amplitude of wave motion exceeds the 0.1 m submersion depth. For this condition it is therefore evident that the frame has minimal impact on the primary dynamics.

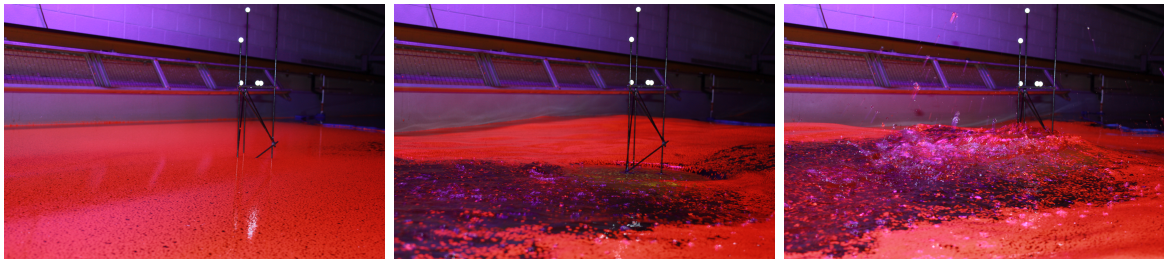

Figure 4.19: Photographs of three time steps from a condition with $\nu_{WA} \approx 0.84$ with wave amplitude $50mm$. (Left) Still water (Centre) Trough over device (Right) Crest over device.

Video 4.3: Wave breaking with $\nu_{WA} \approx 0.97$ and 12.5 mm amplitude. The video is available at: `https://cloudstor.aarnet.edu.au/plus/s/fmiBh1KeHbXctZu`.

While motions were captured, they are not presented given their trivial nature for diffraction testing. Similarly results are not presented for sway, roll and yaw loads given their trivial nature for the study considered here.

4.4 Discussion

The investigation on how submersion depth affects the excitation force indicated a potential for great variation for both the single device and the array, with a trend towards convergence as submersion depth increases. Of particular note is the variation in the wave number where the array nodes and anti-nodes occur. This implies that the transverse wave group velocity has a different mean, which is dependant on the submersion depth; from which it can be deduced that wave shoaling is occuring through interaction with the BA. With shoaling occurring this implicitly means that there must be higher order harmonics in the diffracted wave field and consequently harmonic loads must be induced on the structure. This means that any results produced by *NEMOH* are incomplete for this type of device; this is corroborated by the harmonic free-surface and loads observed experimentally. Even with the expectation that the numerical results are incomplete it is important to note the first harmonic predictions are quite good when compared with the experimental measurements, this can be seen in Figure 4.12.

The three *NEMOH* conditions presented in Figure 4.12 present the single, three and wall configurations show the effects of the symmetries involved in this study. The surge and pitch excitation loads both exhibit modest variations as a result of array effects, while the heave indicates array effects where the amplitude of the force becomes quadruple the single device prediction. This phenomenon is attributable to the waves reflected from the wall almost entirely cancelling themselves with respect to surge and pitch; with only the slight variation fore and aft of the centre-line inducing array effects. Conversely for heave, the reflected waves will add in all respects creating much greater interaction effects.

In many of the *NEMOH* cases there are frequencies where the phase angle switches by π in jumps, for instance the pitch moment in Figure 4.12 at $\nu_{WA} \approx 0.6$. This characteristic coincides with inflections on the amplitude plot, this indicates that these jumps in phase correspond to frequencies where there is no excitation moment (or force). The explanation for this in the example of pitch is the equivalent force vector acts through the moment centroid leading to a zero moment, then adjusting frequency slightly results in either a slight positive or negative radius; and consequently, a positive or negative moment. This can be corroborated by considering Figure 4.13, where there is a point where the excitation transits through the center of the polar plot

It can be seen that all the experimental frequency domain free surface results have some amount of phase shift relative to the numerical predictions, this is especially evident in Figure 4.15. However, the relative phase across the free surface correlates quite well to the pattern in the numerical prediction. This difference in the absolute is attributed to the challenge of measuring the true absolute phase for a signal with a 25 Hz sample rate with a phase velocity of ≈ 2.9 m/s; this means the zero up crossing transits ≈ 115 mm per frame for this experimental condition. This difficulty in precisely determining the absolute phase with this method leads to an inability to ascertain the pure scattered wave, as understanding the absolute phase is required to subtract the incident wave. However, the pure scattered wave is non-real and primarily of interest for the purpose of validating numerical models. It is comparatively trivial to add the incident wave to the numerical predictions to facilitate a comparison, as has been done in this work. Additionally, this presentation format gives the ability to clearly identify regions of constructive ($a > 1$) from destructive ($a < 1$) interference; this is the critical consideration for understanding intra array effects. It should also be noted that removing the experimental incident component would introduce uncertainty into the final results, the converse of adding the incident component to the numerical results does not introduce any meaningful uncertainty.

The experimental results indicate an effective row with somewhere between three and infinite devices, which is clearly a large level of uncertainty. Herein lies the principle issue in this approach, it is not possible to make a causal statement as to the width of the effective

row. However, it is possible to deduce the number of interactions for each imaginary pair of devices, through to the widest pair which will have one order of interaction. This widest pair is located no more than the distance the wave would propagate in the experimental period. While it is conceivable to complete analogous numerical work with wider rows of devices, a decision was made not to extend the study as the precise solution would never be reached. As such this indicative study was considered appropriate.

The first harmonic of the free surface is clearly of interest as it is associated with the main excitation force components. However, it is possible to consider other frequency components that are given from the Fourier Transform. Although the amplitudes of the wave components are very small compared to the first order, they do add credence to the precept that there must be some level of higher order components to the wave interactions. In the instance the studies conducted herein are extended to consider more realistic irregular wave conditions the effects of these harmonic interactions will need to be accounted for when analysing results. The effect of these frequency components on broader array interaction dynamics also requires further thought.

Considering the non-harmonic component of the Fourier Transform presented it can be seen that the ability to detect wave components with the methodology employed is less than 0.1 mm. This implies that the stereo-videogrammetry method is very good at detecting the relative position of the surface between two time steps. Even if the absolute position measurement is not always perfect.

This work has been completed under the explicit assumption that there is a steady-state in effect for the duration of the experimental run. Where steady-state refers to an assumption that the amplitudes of waves and forces are constant.The intentional use of the reflections however means that there must be transient effects in the measurements. Some of these effects are evident in Video 4.1. Appendix B.4 presents a study using wavelet analysis which allows for consideration of these transient effects. However, with the load data it was determined that valid results were very short and highly susceptible to reflections from the wave-maker paddle, which was 15 m from the experimental area. Furthermore, it was deemed infeasible to use this analysis approach with the free surface data due to the high computation cost which would be associated.

The stereo-videogrammetry post processing (from raw photos) to final FFT results over the measurement domain given in this chapter (and subsequent chapters) was approximately 10 min per sec of experimental time. This was due to both the DIC computations and performing FFT analysis over approximately 1.5 million discrete data points. This expensive post-processing is high compared to conventional testing with resistive wave probes and results in an ability to complete real-time data analysis for quality control purposes. However analogous

wave probe testing, would not be feasible to the same spatial resolution and completing such testing over an analogous region has it's own challenges and limitations (McNatt et al. 2015; O'Boyle et al. 2017). As such, there is no real alternative at present to the approach. It is expected though that there are many optimisations which could be done to reduce the post-processing time. These optimisations include completing the DIC, error correction and region joining in a single process.

The value in capturing such a large measurement domain with the spatial resolution accomplished herein is a possible reduction in quantity of experimental runs required. Considering the loads predicted numerically it is evident that there is a large variation in load amplitude with respect to wave frequency, especially in heave. To fully explore the frequency space experimentally would require many runs, numerically 600 frequencies were studied, this quantity of experimental runs is not feasible. With the free surface measurements, the additional spatial information provides a greater level of confidence in the correlation between the experimental and numerical. Thereby reducing the number of experimental conditions required to develop confidence in the numerical model.

4.5 Conclusion

In this chapter the diffraction array effects associated with a submerged pressure differential WEC has been explored by employing reflections from walls, through the principle of method of images. The study included a numerical component with *NEMOH* and an experimental study which was completed in a wave flume with stereo-videogrammetry to measure the free surface. The study explored regular wave conditions ranging from 0.3 Hz to 1.2 Hz at model scale.

The numerical study included a brief exploration as to the effect of the submersion depth of the device on the array interactions; where it was shown that the effect could be substantial but decreased as submersion depth increased. This implies the numerical results are incomplete and missing higher order components due to shoaling. This is substantiated in both the loads and free surface experimental components of the study.

The implementation of stereo-videogrammetry has resulted in a very large experimental area of approximately 4.5 by 3 m, with a horizontal spatial discretisation of 3 mm. It has been shown that although the localised discontinuties observed in Chapter 2 persist the use of Fourier Transforms have the ability to restrict their effect.

The experimental investigation showed quite good agreement with the numerical prediction for one specific submersion depth ($S_{DR} \approx 0.34$); with both the loads and free surface measurements. It was shown to be challenging to distinguish the experimental load measurement

to the different numerical configurations. The free surface comparison, which although expensive to implement, gave much greater confidence that the reflections from the walls were inducing array effects.

The submersion depth study indicates that hydrodynamic array optimisation could well be more complicated than relative position of different optimum devices, for this type of device.

Chapter 5

Heave Radiation by a Submerged WEC in a Channel

5.1 Introduction

In the previous chapter the diffraction of a submerged pressure differential WEC was considered. It was shown that the use of wall reflections is a useful strategy to develop an understanding of WEC diffraction array effects both experimentally and numerically. In this chapter the concept is extended to consider the heave radiation effects of the same geometry.

The oscillation of a body in water requires an excitation force which is customarily decomposed (arbitrarily) into components in phase with velocity and acceleration of the body, these being radiation damping and added mass respectively. The damping coefficient is associated with the energy flux in the waves radiating away from the body and is non-negative. The added mass coefficient is primarily associated with the kinetic energy in the water induced by the oscillation of the body. This is generally an acceptable model when the free surface effects are negligible. However when the free-surface effects are important the associated potential energy can cause the added mass coefficient to become negative (Falnes and Kurniawan 2015; McIver and Evans 1984; Ogilvie 1963). The free-surface effects are important (large) in situations such as submerged structures which are proximal to the free surface or for oscillating water columns (the type of WEC).

For a heaving motion such as that considered in this chapter, the expected radiation pattern is described as a monopolar. A monopolar radiated waves is characterised as axisymmetric wave field propagating from a device. This ignores other modes of motion, such as surge, sway, pitch and roll which generate dipolar radiated waves. Dipolar radiated waves are axisymmetric in terms of amplitude of propagating wave, however phase is opposite across a plane of symmetry which is normal the mode of oscillation (Falnes and Kurniawan 2015; Fleming and Manasseh 2017; Nader et al. 2017).

This chapter follows much the same format as that presented in Chapter 4 with the distinction of focusing on radiation instead of diffraction. The work includes a numerical investigation on the effect of submersion depth on the radiation impedance. Then a comparison between

numerical and experimental is completed for a specific submersion depth. The experimental work includes measurement of the free surface with stereo-videogrammetry.

5.2 Method

The work described in this chapter employed the same experimental set-up as that described in Chapter 4. The distinction between the two chapters is that in Chapter 4 the facilities wavemaker was employed to study the diffraction effects while in this chapter the linear motor attached to the model is actuated to investigate wave radiation, the study focused on monopolar heave radiation.

For the experiments the linear motor was driven with a PID based position controller. This controller is a standard feature included with the linear motor employed. Information relating to expected contributors to the required force are included to improve accuracy of the controller. Given the motions studied are sinusoidal the controller was employed in PD condition. Details of the position control system and the implementation used are given in Appendix C.1. The motion of the BA required to generate the radiated wave is defined by (5.1).

$$\zeta(t) = \zeta_0 - a(\cos(\omega t) - 1) \tag{5.1}$$

Where ζ is the body position, ζ_0 is the submersion depth, a is the amplitude of motion, ω is the angular frequency of motion and t is time. For the experimental radiation study the submersion depth (ζ_0) employed is 0.115 m this is different to the 0.1 m employed above in Chapter 4. This change was driven by issues with higher than acceptable vibration when operating around the lower submersion depth, which was caused by greater extension of the structure.

Numerical modelling of the radiation case was completed using *NEMOH* to determine the hydrodynamic radiation damping and added mass coefficients relevant to the heaving BA. The mesh and run characteristics are the same as those employed in Chapter 4, they are repeated for convenience in Table 5.1.

Table 5.1: Numerical modelling key characteristics.

	Panels		**Frequency**	
	BA	**Wall**	**Range (Hz)**	**Quantity**
Single	816	-		100
Three	2482	-	0.3-1.2	600
Wall	816	1881		600

The experimental results, as employed in this chapter, are in the form of complex coefficients from a Fourier Transform, with the phase relative to ζ. The loads measured in the study are associated to the forced oscillation of a body in water. The resulting force measurement comprises loading from the inertia of the body and the hydrodynamic coefficients of added mass and radiation damping. The numerical results *NEMOH* provide are the added mass and radiation damping coefficients. Therefore, in order to compare the experimental results to the numerical either the hydrodynamic coefficients need to be extracted from the experimental measurements or the numerical results need to be treated so as to be analogous to the experimental. In the body of the thesis it was decided to use the experimental measurement as the basis. This implicitly relates to net loading associated with the movement of the BA with the exception of any power take-off system. To determine the expected heave radiation excitation force $F_{ex-R,i,j,k}$ from the numerical predictions (5.2) is employed. For this study only heave radiation is considered, for such a study only the heave excitation force is interesting for the central device.

$$F_{ex-R,k,l,m}(\omega) = -a\omega^2 I_{k,l} + \sum_n a\left(-\omega^2 A_{k,l,m,n} + i\omega\left(B_{k,l,m,n}\right)\right) \tag{5.2a}$$

$$\eta_{R,m}(x,y,\omega) = \sum_n a\left(\eta_{R,m,n}\right) \tag{5.2b}$$

Where A is the added mass, I is the body inertia and B is the damping coefficient. The subscripts k and l represent the force DoF and device respectively while the subscripts m and n are for the motion DoF and device. The sum on n is a trivial exercise on all but the three-device configuration for this study; as for the other configurations there is only a single device. It is required however, as the use of wall reflections explicitly assumes all devices are oscillating in phase.

To normalise and non-dimensionalise the force results (5.3) is applied,

$$F_{ND-R} = \frac{F_{exR}}{aA_w g\rho\omega i} \tag{5.3}$$

where A_w is the wetted surface area, g is gravity and ρ is density of water. Note this changes the phase to be relative to velocity instead of position.

To normalise and non-dimensionalise the free surface results (5.4) is applied,

$$\eta_{ND-R}(x,y,\omega) = \frac{\eta_R(x,y,\omega)}{a} \tag{5.4a}$$

$$X_A = \frac{x}{L_A}$$
$$Y_A = \frac{y}{L_A} \tag{5.4b}$$

where X_A and Y_A are the non-dimensional positions.

5.3 Results

Figure 5.1 considers the effect of submersion depth on F_{ND-R}; the left and right plots give the amplitude and phase angle respectively. The force is non-dimensionalised by (5.3) and the incident wave condition is expressed by the non-dimensional linear wave numbers defined by (4.1). The position of the BA in the water column is expressed by submersion depth ratio. Figure 5.2 presents the same results in a polar format. For reference on the phase plot $\frac{\pi}{2}$ corresponds to effective mass (inertial and hydrodynamic) and 0 corresponds to damping; interpreting this implies,

- $0 \leq \phi \leq \frac{\pi}{2}$ Positive effective mass and damping.
- $\frac{\pi}{2} \leq \phi \leq \pi$ Positive effective mass and negative damping.
- $-\frac{\pi}{2} \leq \phi \leq 0$ Negative effective mass and positive damping.
- $-\frac{\pi}{2} \leq \phi \leq \pi$ Negative effective mass and damping.

where ϕ is phase angle.

The submergence depth study exhibits many of the characteristics observed in Chapter 4. Including the variation in both single device and array characteristics; with convergence as the submergence depth increases. Interesting is can be observed that there is a greater propensity for negative effective mass in the array condition than for a single device.

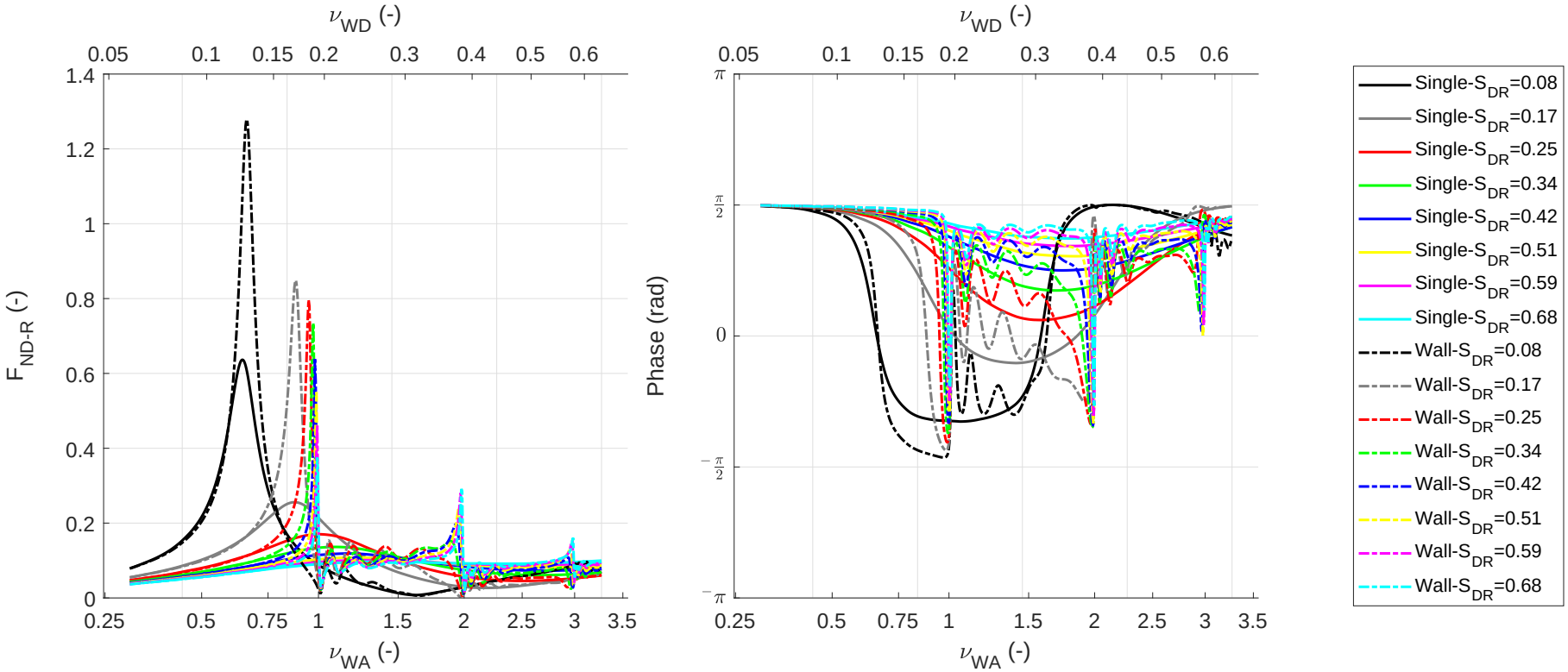

Figure 5.1: Effect of Submersion Depth on Array Interactions study with *NEMOH*, non-dimensional heave radiation force. Device oscillation frequency is expressed by the device and array non-dimensional linear wave numbers on the top and bottom x-axes respectively.

Figure 5.3 present the condition where the submersion depth is 115 mm, ($S_{DR} \approx 0.39$), and provides a comparison between the experimental results and numerical modelling results. The numerical study includes the three geometric arrangements, the single, three and wall conditions. It can be seen that the amplitude and phase of the experimental measurements tend to indicate a good correlation with the numerical predictions for the array effects. It can also be seen that for this submersion depth the array interactions are negligible below $\nu_{WA} = 0.75$. The uncertainty analysis associated with these results are presented in Appendix E.3. Figure 5.3 is repeated in Figure 5.4 in a polar format, with the experimental results omitted.

The results of Figures 5.1 and 5.3 are alternatively presented in Appendix C.2 in terms of added mass and radiation damping coefficients. These again indicate the trend towards negative added mass and has a good correlation between the numerical and experimental results.

While load measurements were made which correspond to other harmonics, they are not presented as motions were also detected operating at these frequencies. As such it was not possible to differentiate the force component associated with the desired oscillation from the responses to the unwanted oscillation. These unwanted oscillations were caused by imperfect control. The other DoF of motions and loads are not presented given their trivial nature for this testing condition.

The free surface frequency domain first harmonic results are given by Figures 5.5, 5.6 and 5.7 for conditions $\nu_{WA} \approx 0.61$, $\nu_{WA} \approx 1.1$ and $\nu_{WA} \approx 1.8$ respectively. All present the amplitude and phase in the left and right columns respectively for four distinct studies. From top to bottom they are the single, three and wall arrangements computed numerically and the experimental results.

Videos 5.1 and 5.2 present the experimental radiation condition with $\nu_{WA} \approx 1.1$; they show the stereo-videogrammetry results and the experimental observation respectively. The stereo-videogrammetry includes the free surface elevation and velocity vectors, the playback at at quarter speed with the true time step indicated at bottom of frame. Through the video there are many instances where the join between the two camera pairs are evident, the join is characterised by a line with constant X location. There are numerous instances across the surface where the measurements were unsuccessful, areas where the surface is white; comparing with the frequency domain plot shown at the bottom of Figure 5.6 it can be seen that there was minimal impact. These errors have been concentrated into the frequency components which are not of interest to this investigation. It can be seen that as the run progresses that a reflection from the wavemaker is evident, this commences at approximately 15 s. By the end of the oscillations, at 28.5 s, it is apparent the reflected wave has become

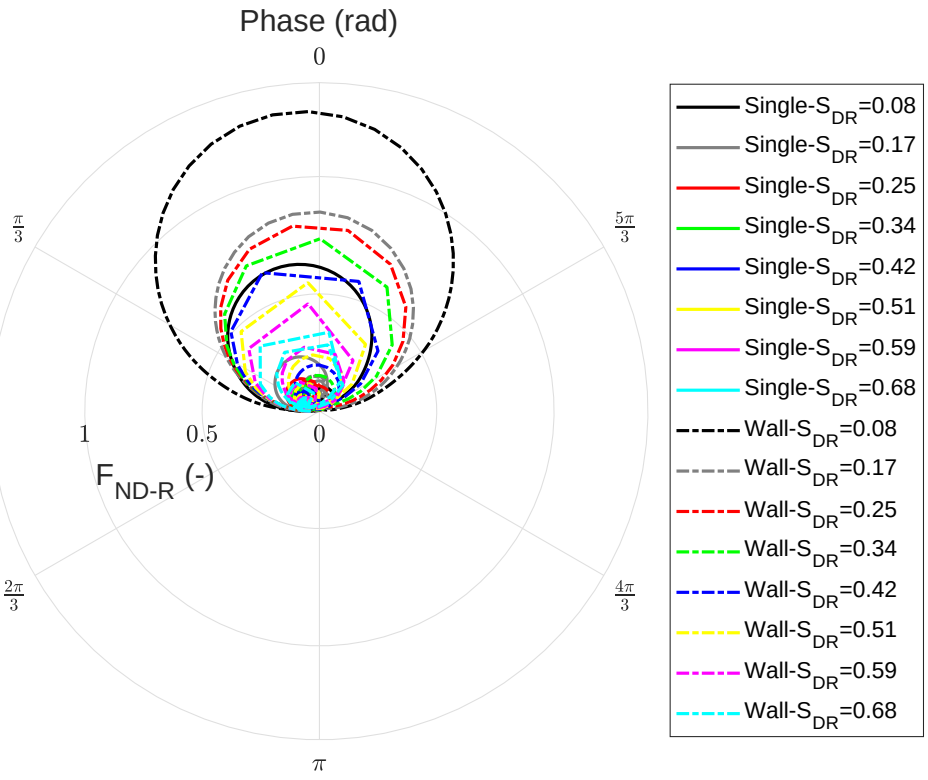

Figure 5.2: Effect of Submersion Depth on Array Interactions study with *NEMOH*, non-dimensional heave radiation force.

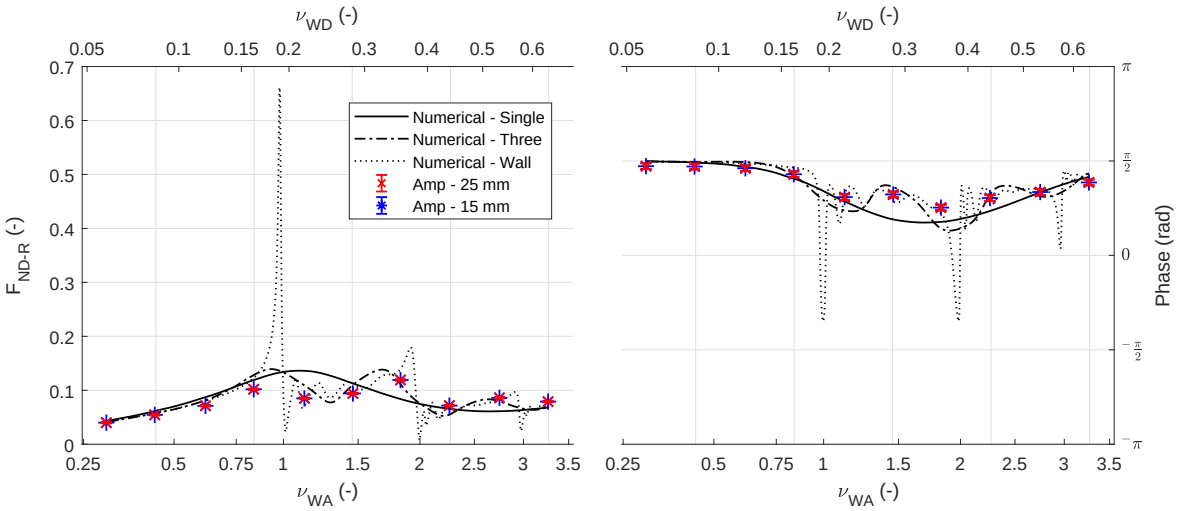

Figure 5.3: First order harmonic radiation excitation force for heave. $S_{DR} = 0.39$ from experimental and numerical studies. Experimental data is differentiated by motion wave amplitude and the *NEMOH* modelling includes a single, three and wall conditions. The loads are non-dimensional and have been normalised and the velocity of motion. Device oscillation frequency is expressed by the device and array non-dimensional linear wave numbers on the top and bottom x-axes respectively.

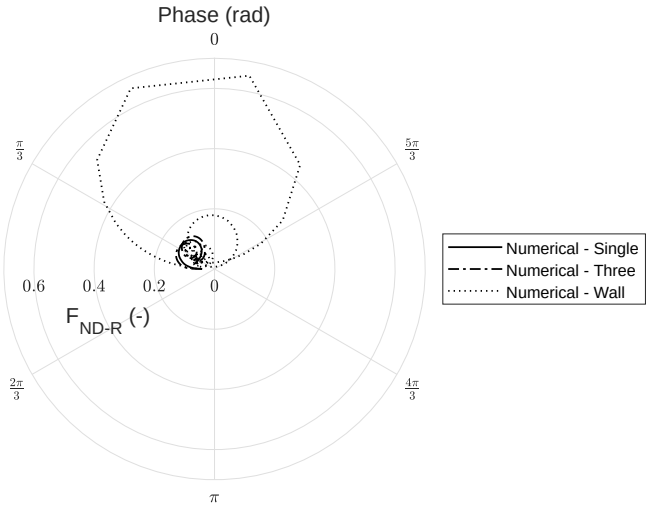

Figure 5.4: First order harmonic radiation excitation force for Heave. $S_{DR} = 0.39$ for *NEMOH* modelling of a single, three and wallconditions. The loads are non-dimensional and have been normalised and the velocity of motion.

important to the measurement. These reflected waves necessitate trimming the time series data to when the reflected wave arrives in the frame, this is done with the phase velocity of the wave. Phase velocity is employed as it describes the velocity that the wave front propagates. This issue is more intrusive at lower frequencies due to the higher wave velocities, both group and phase.

It was observed during the experiments that vibrations in the motion capture frame were occurring, from which there was concern of corruption of results. However, the free surface measurement results showed no indication of these vibrations detrimentally effecting the measurements of interest.

Videos 5.3 and 5.4 present the experimental radiation condition with $\nu_{WA} \approx 1.8$; they show the stereo-videogrammetry results and the experimental observation respectively. The stereo-videogrammetry presentation is the same as described above for Video 5.1. Many of the observations of this condition are the same as the previous. Additionally, it is evident here that the wave condition develops to have significantly higher displacements than the amplitude of motion of the BA, also the area over the BA has a greater tendency to an inability to compute the elevation as the run progresses. The reason for this can be seen in the observation video with significant wave breaking occurring. Once again vibrations relating to the control system and structure can be seen.

An explicit assumption of steady state has been made in determining the above results, Appendix C.3 briefly presents an alternative analysis with the use of wavelet analysis to explore the transient effects of the investigation. This has not been included in the main text as confidence in the methodology is not sufficient.

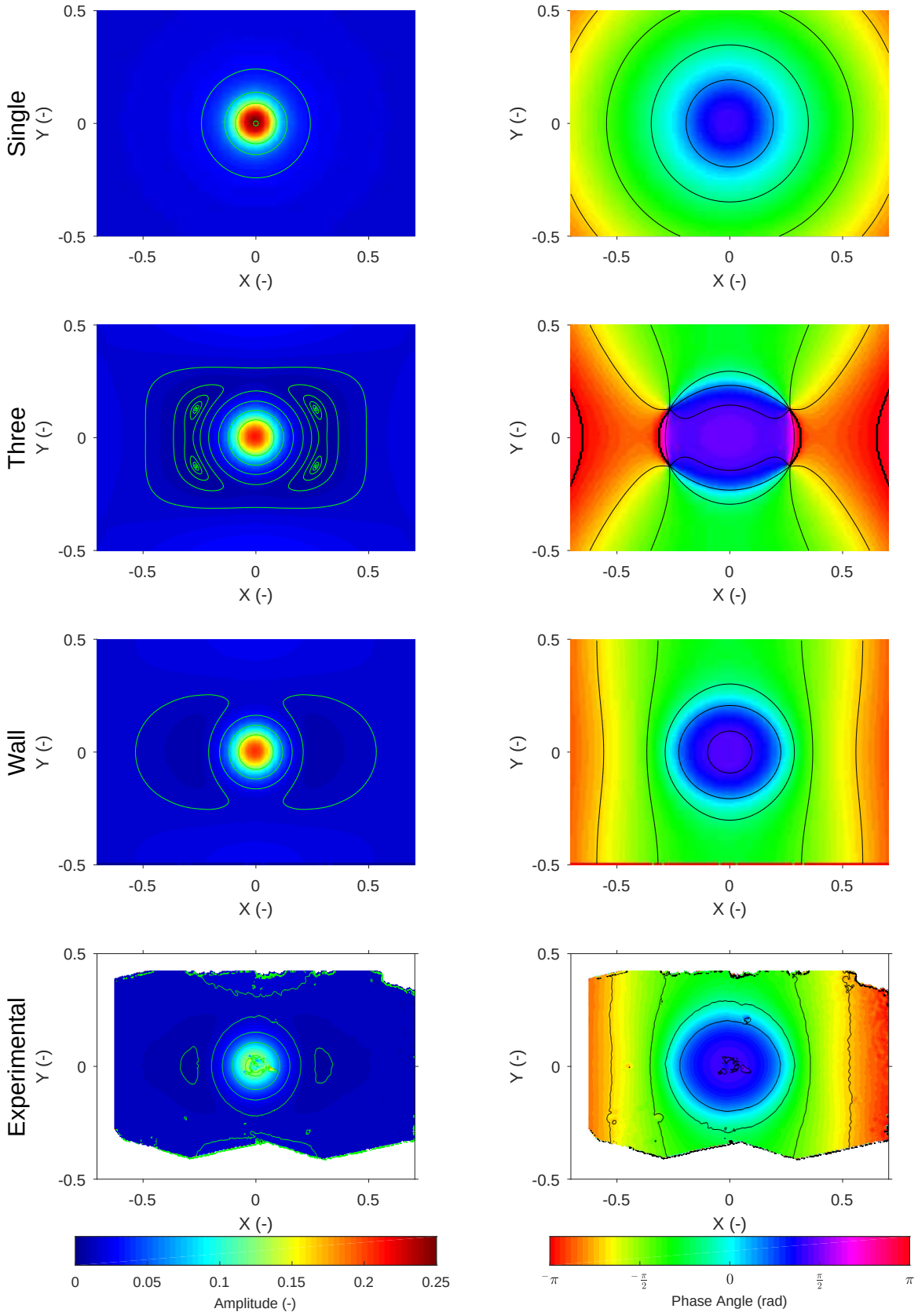

Figure 5.5: Frequency domain free surface for condition $\nu_{WA} \approx 0.61$, this represents neutral array effects. Left column is amplitude, right column is phase. Top three rows are numerical predictions for the single, three and wall arrangements; the bottom row is experimental results.

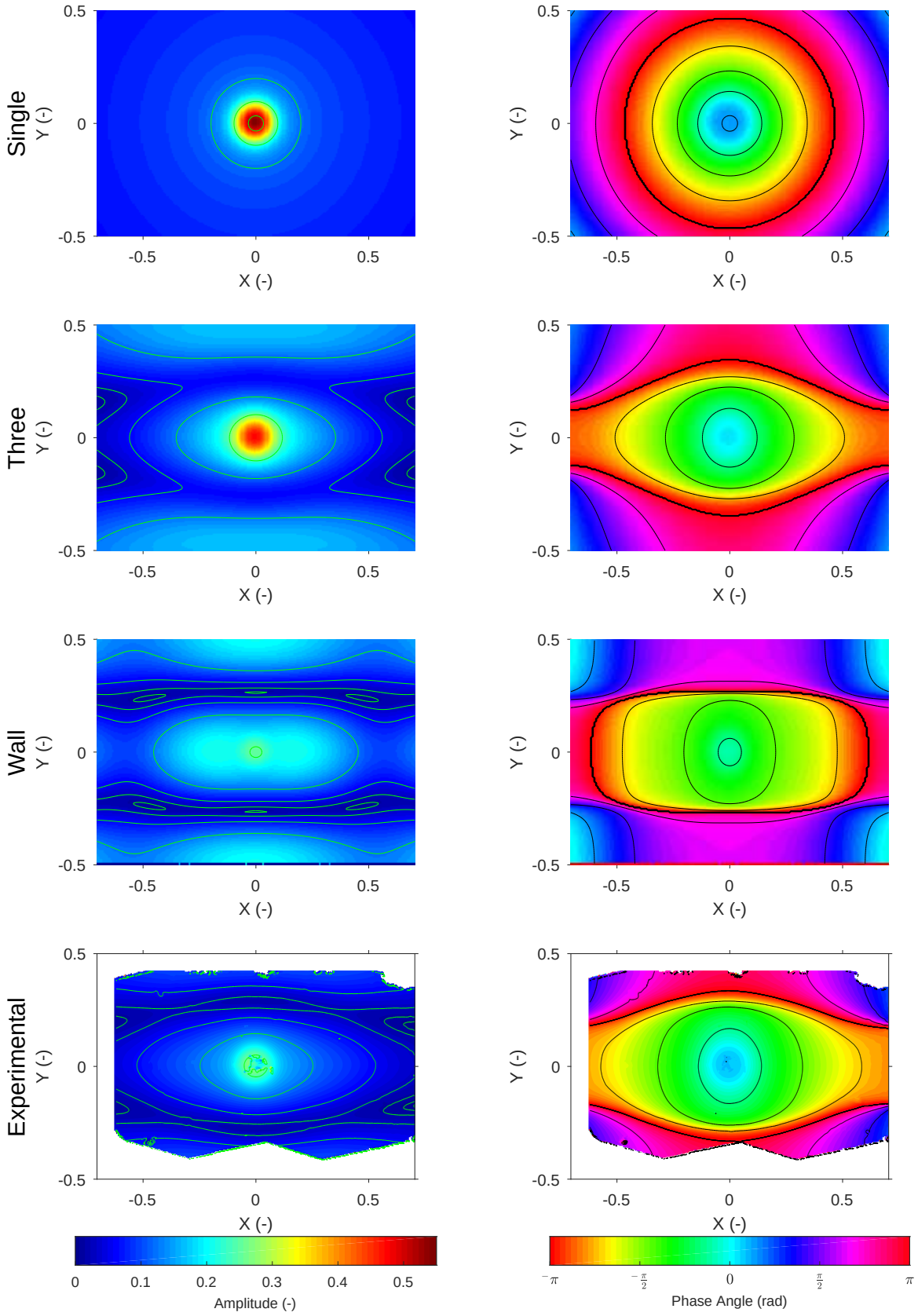

Figure 5.6: Frequency domain free surface for condition $\nu_{WA} \approx 1.1$, this represents negative array effects. Left column is amplitude, right column is phase. Top three rows are numerical predictions for the single, three and wall arrangements; the bottom row is experimental results.

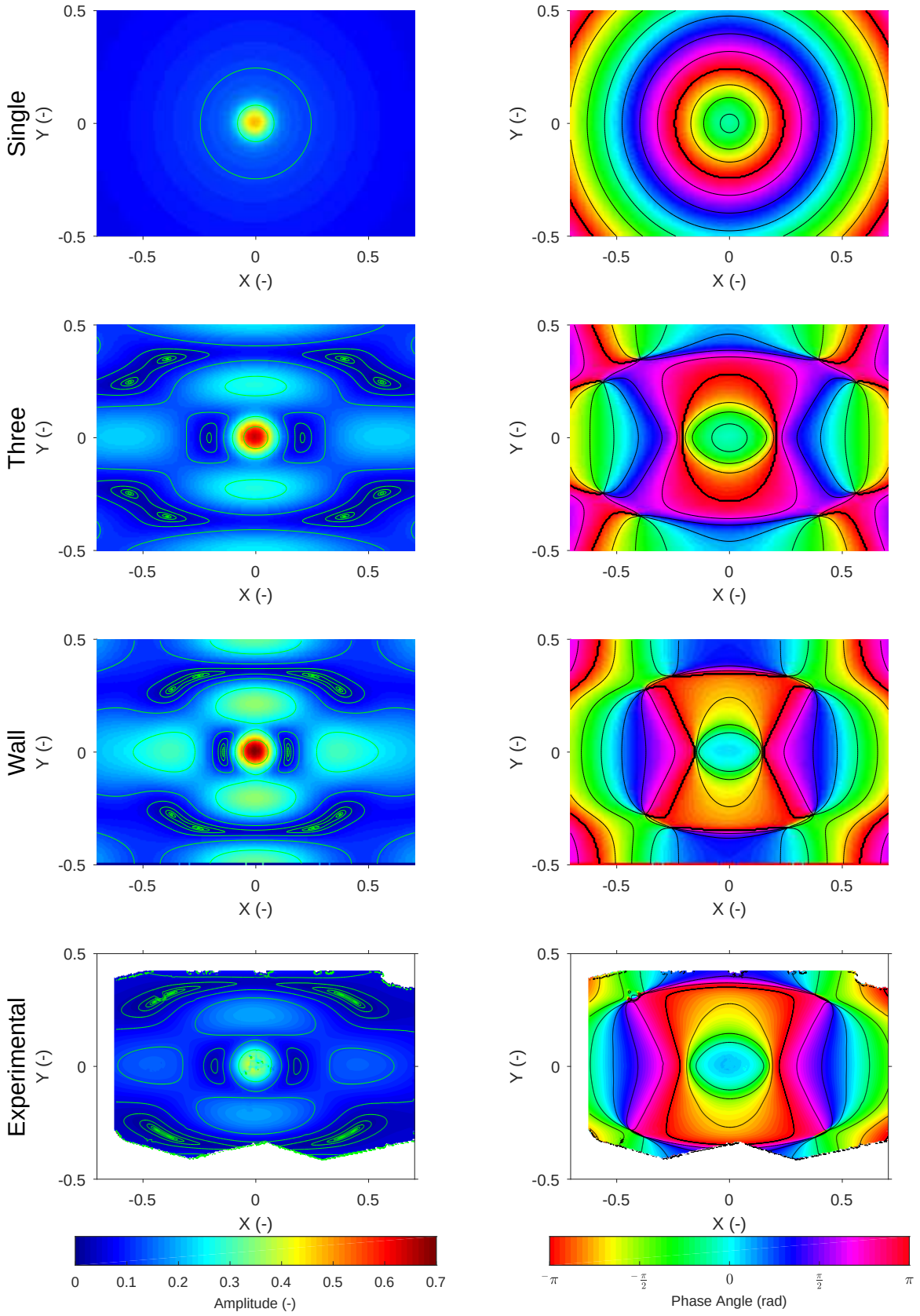

Figure 5.7: Frequency domain free surface for condition $\nu_{WA} \approx 1.8$, this represents positive array effects. Left column is amplitude, right column is phase. Top three rows are numerical predictions for the single, three and wall arrangements; the bottom row is experimental results.

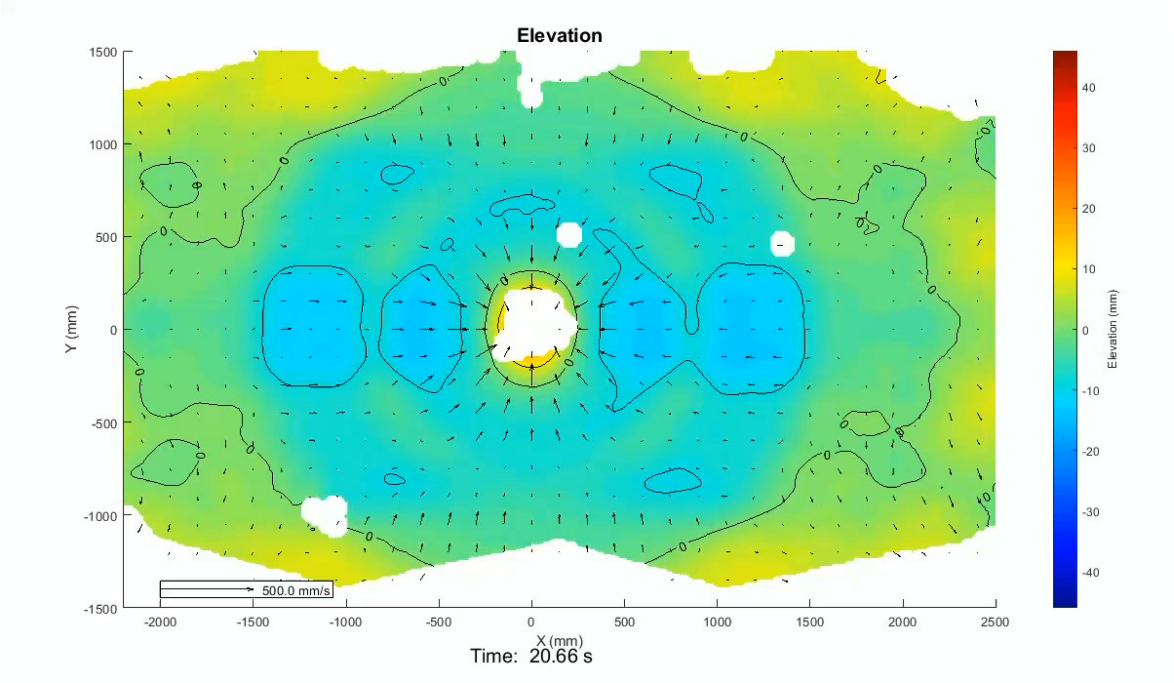

Video 5.1: Stereo-Videogrammetry time domain free surface of condition with $\nu_{WA} \approx 1.1$. The video is available at: `https://cloudstor.aarnet.edu.au/plus/s/4id1zVP7nFCTsmF`.

Video 5.2: Experimental time domain free surface of condition with $\nu_{WA} \approx 1.1$. The video is available at: `https://cloudstor.aarnet.edu.au/plus/s/dinpIOzbmzJ1SPf`.

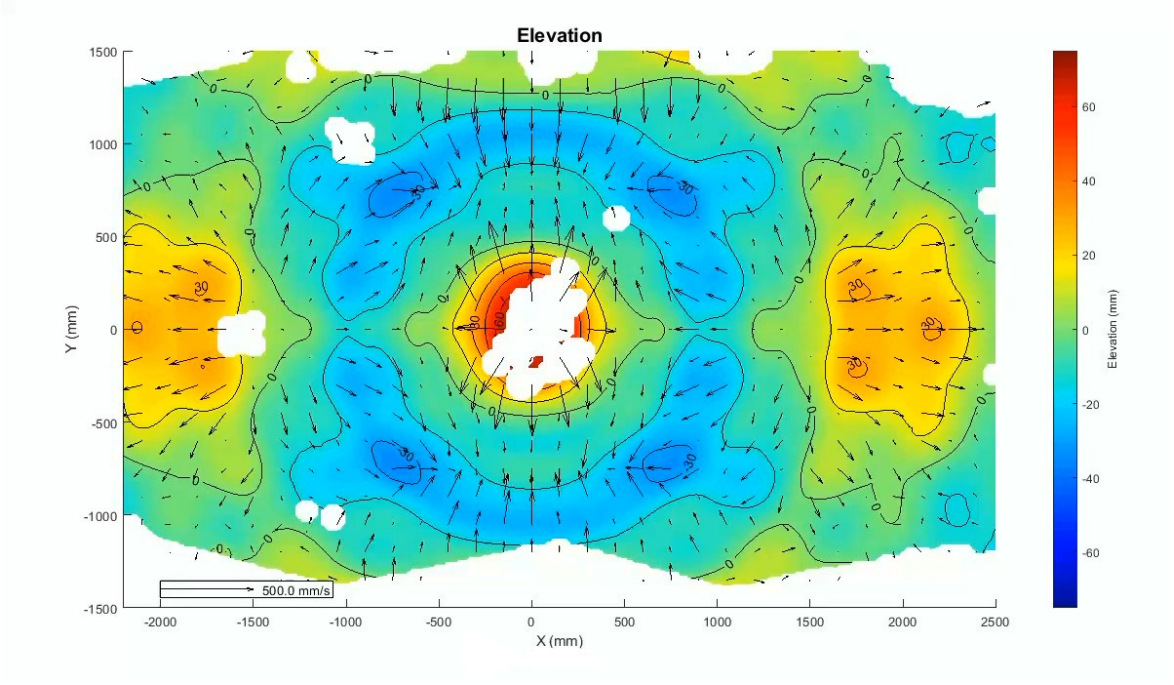

Video 5.3: Stereo-Videogrammetry time domain free surface of condition with $\nu_{WA} \approx 1.8$. The video is available at: `https://cloudstor.aarnet.edu.au/plus/s/wsyr0aSjPPxR4sJ`.

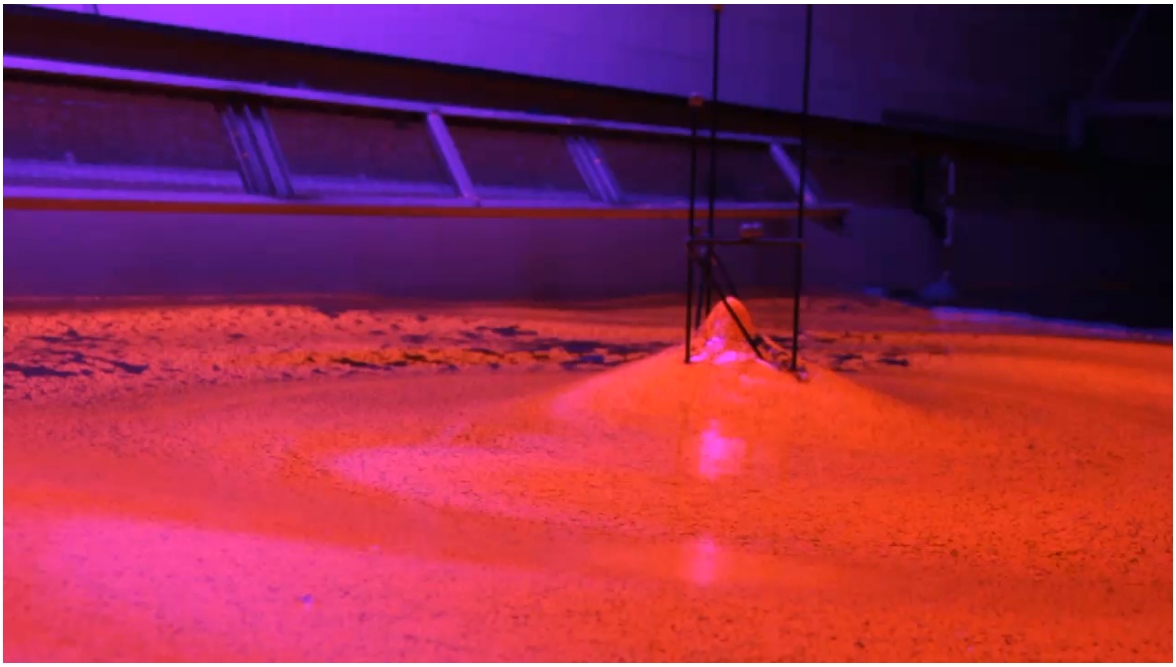

Video 5.4: Experimental time domain free surface of condition with $\nu_{WA} \approx 1.8$. The video is available at: `https://cloudstor.aarnet.edu.au/plus/s/d9ukbaEn2YzwDuz`.

5.4 Discussion

The submersion depth study exhibits many of the same characteristics of the relationship between the single and wall conditions that have been discussed in Chapter 4. There is evidence of variation in both the single device and array characteristics. Both arrangements exhibit what would colloquially be termed negative added mass. This is a label which has no real physical representation and Falnes and Kurniawan (2015) refers to this situation as negative radiation reactance. This is due to the reactive component of the radiation excitation force being in phase with the acceleration of the body. McIver and Evans (1984) observe that is not always the case, with the possibility of the reactive component being in phase with position. The driving mechanism is the difference between the kinetic and potential energy imparted due to the oscillation of the body. In instances where the displacement of the free surface is small due to the body movement, it can be shown the potential energy is insignificant; consequently for most floating devices the kinetic energy dominates. From which it can be deduced that the potential energy for the array component of work is more important under certain conditions; this is likely attributable to greater free surface oscillations due to the waves radiated from the other devices.

While convention within hydrodynamics of WECs is to consider the radiation impedance in terms of added mass and damping coefficients, here the results were presented with respect to the amplitude and phase of the radiation excitation force. As discussed by Falnes and Kurniawan (2015) the concept of negative added mass is not physical, and the prevalence of this effect is extensive throughout this investigation. Furthermore, the experimental results obtained were in form of the radiation excitation force and the balance of work presented in the thesis is in the format of amplitude and phase.

The experimental study compares very favourably with the numerical study on array effects. With the forces, Figure 5.3, it can be seen that although there is good agreement on the conditions studied it is not feasible to make a holistic statement of validity of the array effects. Instead considering the free surface measurements it is clear that array effects are notable. This offers a great potential to reduce the quantity of experimental conditions needing to be tested in order to understand broader array interaction characteristics.

The results observed in the free surface measurements in Figures 5.5, 5.6 and 5.7, especially the correlation with the numerical modelling, implicitly indicate that the reflections from the wall are near ideal to the assumptions. This suggests that the physical wall has a reflection coefficient approaching one and the wall is planar with no change in the phase of the wave as a result of the reflection. This qualitative observation is promising for studying array effects, however it does not give an explicit proof of the validity of the approach. To do this, it would be necessary to implement a reflection study which is able to quantify the variation in the

wave as a result of the wall reflection. General reflection analysis relies on assumptions of steady state plane waves and orthogonal reflections (Hughes 1993; Jung et al. 2009; McKee et al. 2018; Suh et al. 2001). For the situation considered here these assumptions are broken, with transient effects present of radially propagating waves resulting in oblique reflections. Development of such a reflection analysis approach was considered out of scope for this work; consequently an explict reflection analysis has not been completed.

The experimental results presented in the main body of work, specifically the FFT, require an assumption of steady state. This has been observed to be somewhat flawed in the study, however it is implicitly required. A brief study on the transient nature of the radiation interactions is presented in Appendix C.3. Through the analysis of the free surface interactions it was deemed necessary to trim the measurement period to exclude reflections from the wavemaker. This is in contradiction to the findings in Chapter 4 where the reflections from the wavemaker were deemed to have only minor impacts on the results. This contradiction is attributed to the relevant importance of the reflection from the wavemaker in the two studies. In the diffraction study the reflection propagates along with the intended incident wave and is small in comparison; this drives a small change in amplitude and phase of the incident wave intended for the experiment. Conversely, here in the radiation study, a new wave component is introduced to the experiment, this new wave is consequently important compared to the absence of any wave driving a large impact on the measured results.

5.5 Conclusions

This chapter has presented an investigation into the use of wall reflections to consider WEC array radiation effects. The body employed was a 1:16 scale of a CETO 5 from Carnegie Clean Energy and focuses on monopole heave radiation. Work included a numerical study with *NEMOH* and experiments in a wave channel with stereo videogrammetry.

The numerical investigation incorporated a study on the effect of the submersion depth on the array interactions considerations, which showed clear variation in both the single device and array interaction characteristics. This suggests a potential to vary control strategies to optimise power capture. Subsequently a specific submersion depth ratio, $S_{DR} = 0.39$, was considered for comparison with the experimental study. The numerical study for the specific submersion depth included geometry arrangements of one, three and wall cases. The radiation excitation force indicates a clear correlation between the experimental and numerical channel study but the multiple nodes and anti-nodes in the numerical results mean full confidence is not possible. This is as the experimental cannot explore every frequency condition, such that a true exploration of the interactions is possible. Comparison between the free surface studies give a much clearer indication of the validity of the channel method for investigation of array

effects. The compromise that needs to be balanced is between the number of runs necessary to fully populate the excitation force plot and the amount of time required to process the stereo-videogrammetry.

Chapter 6

Active Control of a Submerged WEC in a Channel

6.1 Introduction

In the previous two chapters the linear wave interaction components of diffraction and heave radiation for a submerged WEC have been independently considered using wall reflections to simulate array effects. This was completed with experimental and numerical studies from which it was shown that the use of reflections is a useful tool in simulating array effects. In this chapter the precept is extended further to consider the same device operating as a WEC and capturing energy. To achieve this an active control system was developed and implemented experimentally, with stereo-videogrammetry measurements of the resulting wave condition.

Much research has been conducted on the modelling of WEC dynamics, Babarit, Hals, et al. (2012) presents a comprehensive summary of the modelling of many styles of WECs. While Orszaghova, Wolgamot, Draper, et al. (2018) focus expressly on a submerged single point mooring WEC, very similar to the device considered in this work. A range of control strategies have been developed which have been shown to be capable of providing higher levels of energy capture (Babarit, Hals, et al. 2012; Folley, Alves, et al. 2016; Hals et al. 2011; Ringwood, Bacelli, et al. 2014).

There have been several experimental approaches developed to test WECs including the various control strategies which have been proposed. Stratigaki (2014) employed brake pads to simulate a PTO system; this was done to reduce costs where multiple units were required for array testing. An alternative which is becoming more common is to use electro-mechanical systems at model scale which are capable of modelling any of the theoretical control strategies (Mercadé Ruiz et al. 2017; Orszaghova, Wolgamot, Eatock Taylor, et al. 2017; Orszaghova, Wolgamot, Draper, et al. 2018; Ringwood, Ferri, et al. 2017), the drawback being the increased cost required for array testing.

In this chapter implementation of a WEC control system is presented and its effectiveness is considered, the control strategy applied is restricted to considering linear damping. Following this a comparison between numerical predictions from a linearized *NEMOH* study is

considered with comparisons of power capture, motions and free surface effects between the numerical and experimental studies. The broader implications of the use of wall reflections and the related array effects are also considered.

6.2 Method

6.2.1 Mechanical Arrangement

The experimental procedure considered here was completed as part of the same experimental campaign described in Chapters 4 and 5. As such the stereo-videogrammetry and inertial characteristics are the same as described in Chapter 4.

Figure 6.1 presents the revised mechanical arrangement for the model, with a schematic on the left and an image of the underwater mooring arrangement on the right. The mooring system consists of running a mooring line from the bottom of the BA through a pulley to connect with an in-line load cell and then a linear electric motor. The linear electric motor was the Linmot PS01-48x240F-SSC-FC stator and PL0127x800/720 slider. As can be seen in the schematic the revised arrangement results in the centre of the BA being 0.4 m further from the wavemaker; the revised positions of the wave gauges is presented in Table 6.1.

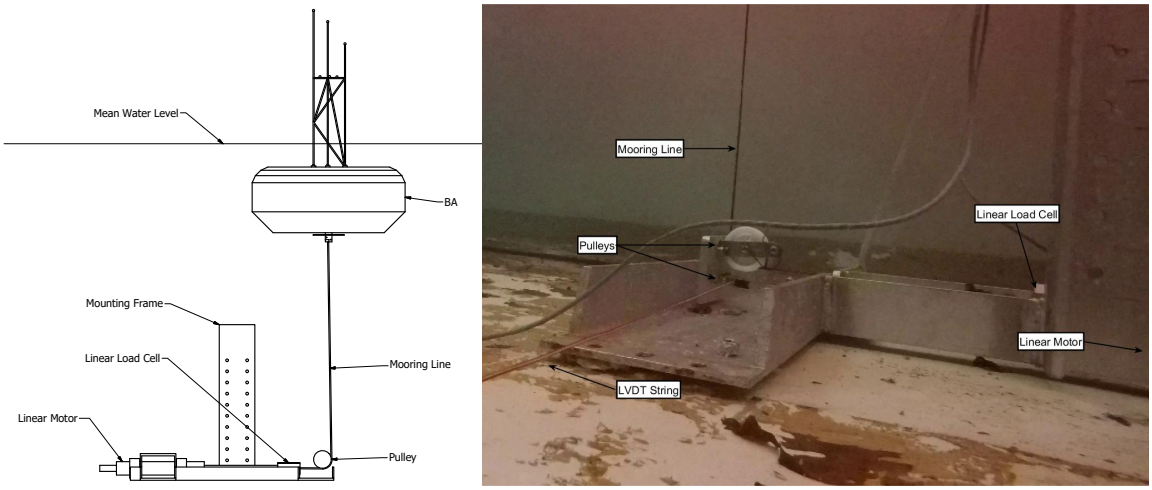

Figure 6.1: Equipment arrangement for mooring of BA (left) and image of physical set-up for control system.

Table 6.1: Resistive Wave Probe Positions. Origin of Co-ordinates is the Model with positive X being the direction of incident wave propagation.

Label	X-Coordinate (m)	Y-Coordinate (m)
WP_{IN}	-9.7	-1.425
WP_{-1}	-1.0	1.375
WP_{+0}	0	1.375
WP_{+1}	1.0	1.375
WP_{+10}	9.6	1.275
WP_{+20}	19.6	1.275

The characteristic of the mooring system is measured with a linear load cell and a linear variable displacement transformer (LVDT) for the tension and extension respectively. The key additional mechanical specifications in this system are described in Table 6.2.

Table 6.2: Key mechanical specifications

Distance below C_g of coupling point	173 mm
Height above tank floor of pulley	90 mm

6.2.2 Control System

In order to have the physical set-up operate as a WEC, a control system has been developed and implemented. The definition of the control system is,

$$F_{PTO-tar}(t) = K_{PTO}\left(\zeta(t) - \zeta_0\right) + B_{PTO}\dot{\zeta}(t) + M_{PTO}\ddot{\zeta}(t) - F_B \tag{6.1}$$

where $F_{PTO-tar}(t)$ is the PTO target force, $\zeta(t)$ is the instantaneous extension of the mooring with standard dot notation to signify a derivative and ζ_0 is the spring zero-point. K_{PTO}, B_{PTO} and M_{PTO} are the PTO spring, damping and mass coefficients respectively and F_B is a constant force accounting for the net buoyant force. This target force is then compared with the maximum ($F_{PTO-max}$) and minimum ($F_{PTO-min}$) acceptable with,

$$F_{PTO-dem}(t) = \begin{cases} F_{PTO-max}, & F_{PTO-tar}(t) > F_{PTO-max} \\ F_{PTO-tar}(t), & F_{PTO-min} < F_{PTO-tar}(t) < F_{PTO-max} \\ F_{PTO-min}, & F_{PTO-min} > F_{PTO-tar}(t) \end{cases} \tag{6.2}$$

This determines the demand force ($F_{PTO-dem}(t)$) to be requested from the linear motor. This demand force is then sent to the linear motor controller as an analogue signal. The linear motor controller was configured in a force control mode which uses a closed loop PID system (LinMot 2016a; LinMot 2016b). This force control mode requires an additional in-line external load cell. Figure 6.2 presents a block diagram of the control system employed.

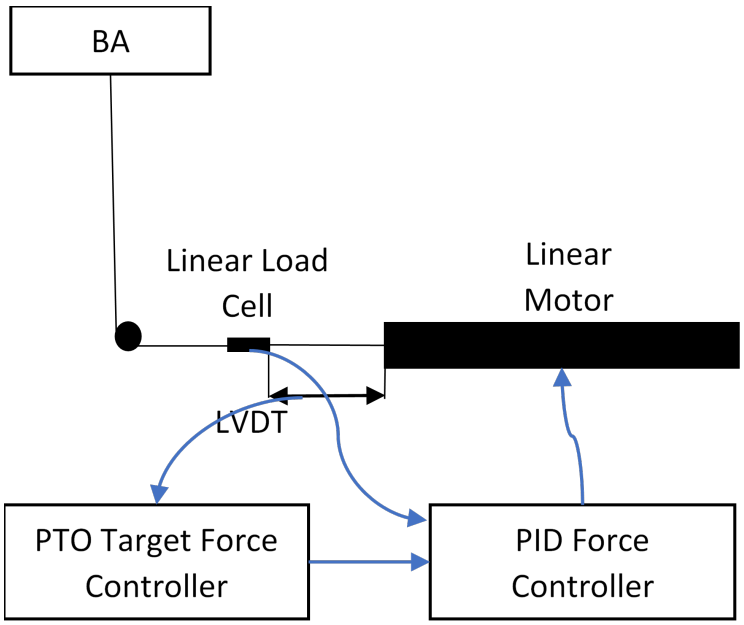

Figure 6.2: Block diagram of control system. The two bottom boxes represent two distinct control systems.

Table 6.3: PTO Control settings for conditions A and B.

	Control A	**Control B**
ζ_0 (m)	-0.10	-0.10
K_{PTO} (N/m)	1500	1500
B_{PTO} (N.s/m)	1000	1500
M_{PTO} (N.s^2/m)	0	0

The position employed in the control system is the LVDT extension and the force control uses the in-line 1-DoF load cell. A more complete explanation of the system is presented in Appendix D.1. The study has considered two settings for the PTO coefficients in testing, these are given in Table 6.3. These coefficients have been selected to be within the range of the system, however do not represent the optimum. Additionally, they are not entirely representative of the real control system employed by Carnegie Clean Energy for the actual CETO 5.

6.2.3 Data Analysis

As with Chapter 4, the time series data has been trimmed such that t_0 is the zero up-crossing preceding the first wave crest greater than 60% of the nominal wave amplitude at WP_0. The period is determined by the phase velocity of the wave and the distance the wave travels to the beach and back.

Two methods are employed to assess the mean power capture of the system, these include

use of frequency domain results and another using integration in the time domain. The time domain integral approach first applies a low pass filter, with the pass frequency at 3 times the incident wave frequency. The instantaneous power capture $P(t)$ can be determined by,

$$P(t) = F_{PTO}(t) \times \dot{\zeta}(t) \tag{6.3}$$

Where the experimental measurements of the PTO mooring force ($F_{PTO}(t)$) and velocity ($\dot{\zeta}(t)$) are employed. The integral assessment is by,

$$P_1(t) = \frac{1}{T} \int_0^T P(t)dt \tag{6.4}$$

where T is the integration period, $P_1(t)$ is the nominal average power. A sample of this process is presented in Figure 6.3, it can be seen here that this averaging process has not fully stabilised in this example. To account for this a further average is taken over the last two periods of the dominant oscillation period,

$$\overline{P_I} = \frac{1}{T_e - T_s} \int_{T_s}^{T_e} P_1(t)dt \tag{6.5}$$

where $\overline{P_I}$ is final average power and respectively T_e and T_s are the end and start of the averaging period. This is indicated by the black line in Figure 6.3.

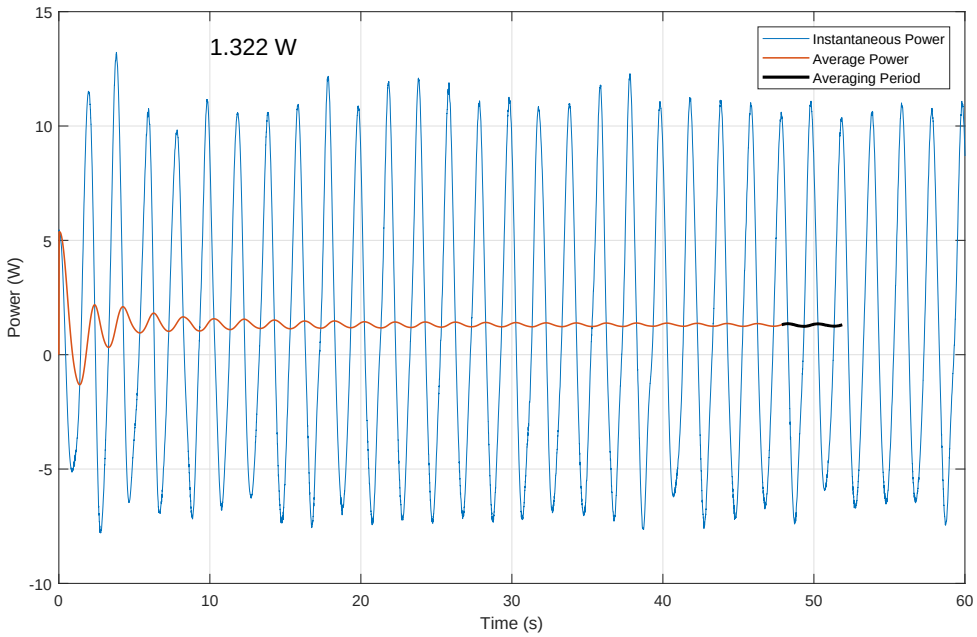

Figure 6.3: Sample of power capture time series.

The frequency domain approach to determine mean power capture ($\overline{P_F}$) is with,

$$\overline{P_F} = \frac{1}{2}\left|\dot{\tilde{\zeta}}\right| \mathrm{Im}(\tilde{F}_{PTO}) \tag{6.6}$$

where $\dot{\tilde{\zeta}}$ is the velocity of PTO and $\tilde{F}_{PTO}$ is the tension through the PTO. The tension is made to be in phase with respect to the position ($\tilde{\zeta}$). The Fourier assessment to determine the appropriate terms is the same as described in Chapter 4.

Normalisation of the absorbed power is by the Relative Capture Width (RCW) of the device.

$$P_{IN} = \frac{1}{2} L_D \rho g a^2 C_g \tag{6.7}$$

where P_{IN} is the incident wave power, L_D is the device diameter, ρ is density of water, g is gravitational acceleration, a is incident wave amplitude and C_g is the group velocity determined by,

$$C_g = \frac{\omega}{2k}\left(1 + \frac{2kh}{\sinh(2kh)}\right) \tag{6.8}$$

where ω, k and h are the angular frequency, angular wave number and water depth respectively. Phase velocity of a wave can be calculated by,

$$C_p = \sqrt{\frac{g}{k} tanh(kh)} \tag{6.9}$$

Incident wave conditions are expressed as non-dimensional linear wave number with respect to device and array critical dimensions as with Chapters 4 and 5.

From 6.1 it is possible to determine the expected frequency domain PTO force by,

$$\tilde{F}_{PTO}(\omega) = \left(K_{PTO} - \omega^2 M_{PTO} + \omega \imath B_{PTO}\right)\tilde{\zeta} \tag{6.10}$$

where ω is angular frequency, and $\imath$ is the complex component.

6.2.4 Numerical

The numerical modelling with *NEMOH* carried out for this active case draws results from Chapter 4 and with additional assessment of the radiation effects for a 100 mm submersion depth. The process for determining the radiation coefficients is presented in Chapter 5 where the submersion depth was 115 mm. The general equation of motion of the system is,

$$(m + A_\infty)\ddot{x}(t) = -\int_0^t K_r(t-\tau)d\tau + F_{ex} - F_{hs} - F_{vis} - F_{PTO} \tag{6.11}$$

where $x(t)$ is the six-dimensional position vector of the BA, m is the inertia of the BA, A_∞ is the hydrodynamic added mass, K_r is the radiation impulse response function, F_{ex} is the wave excitation force, F_{hs} is hydrostatic force and F_{vis} is viscous force. With the inclusion of the above definition of F_{PTO} it can be seen there is a mixture of spatial definition between $\zeta(t)$ and $x(t)$. To resolve this, it would be necessary to implement a transfer function between the BA position and the extension of the PTO, noting the PTO force will always act directly along the mooring line; an example of such a transfer function is given in Orszaghova, Wolgamot, Draper, et al. (2018). To ensure stability of the system when there is no external exciting force, the definition $F_B = -|F_{hs}|$ is defined; although F_B acts along the mooring line. Furthermore, viscous forces are assumed to be zero.

To linearise this equation, it was assumed that the BA will move purely in heave; this results in $\zeta(t) = x_3(t)$. This allows a switch to the frequency domain which results in,

$$m\ddot{\tilde{x}}(\omega) = \tilde{F}_{ex}(\omega) - (A(\omega) + M_{PTO})\ddot{\tilde{x}}(\omega) - (B(\omega) + B_{PTO})\dot{\tilde{x}}(\omega) - K_{PTO}\tilde{x}(\omega) \tag{6.12}$$

From which it is possible to solve for the motion of the BA with,

$$\tilde{x}(\omega) = \frac{\tilde{F}_{ex}(\omega)}{-\omega^2(m + A(\omega) + M_{PTO}) - \omega\imath((B(\omega) + B_{PTO}) + K_{PTO}} \tag{6.13}$$

With the motion determined, solving for the mean power capture is by,

$$\overline{P}(\omega) = \frac{1}{2}B_{PTO}\left|\dot{\tilde{x}}(\omega)\right|^2 \tag{6.14}$$

For comparison of the free surface it is necessary to sum the effects of the incident, scattered and radiated waves; this is done by,

$$\tilde{\eta}_C = \tilde{\eta}_I + \tilde{\eta}_S + \dot{\tilde{x}}\tilde{\eta}_R \tag{6.15}$$

where subscripts C, I, S and R represent the combined, incident, scattered and radiated wave fields respectively and $\dot{\tilde{x}}$ is the velocity of the BA. The scattered wave refers to the change in wave climate induced by placing a structure in it; by implication the diffracted wave climate is the sum of the incident and scattered wave fields.

6.3 Results

As with Chapters 4 and 5 a submersion depth study has been completed with reference to the power capture. Figure 6.4 presents the RCW curves of the controls explored experimentally,

where control A and B are indicated. The incident wave condition is expressed by device and array non-dimensional linear wavenumbers on the top and bottom axes respectively. As is to be expected, from the above work, there is variation in power capture for given incident wave conditions evident in both the single device and array characteristics. The heave response amplitude operator (RAO) results for the depth submersion study are presented in Appendix D.2, these results are presented in both amplitude and phase relative to incident wave and in polar format.

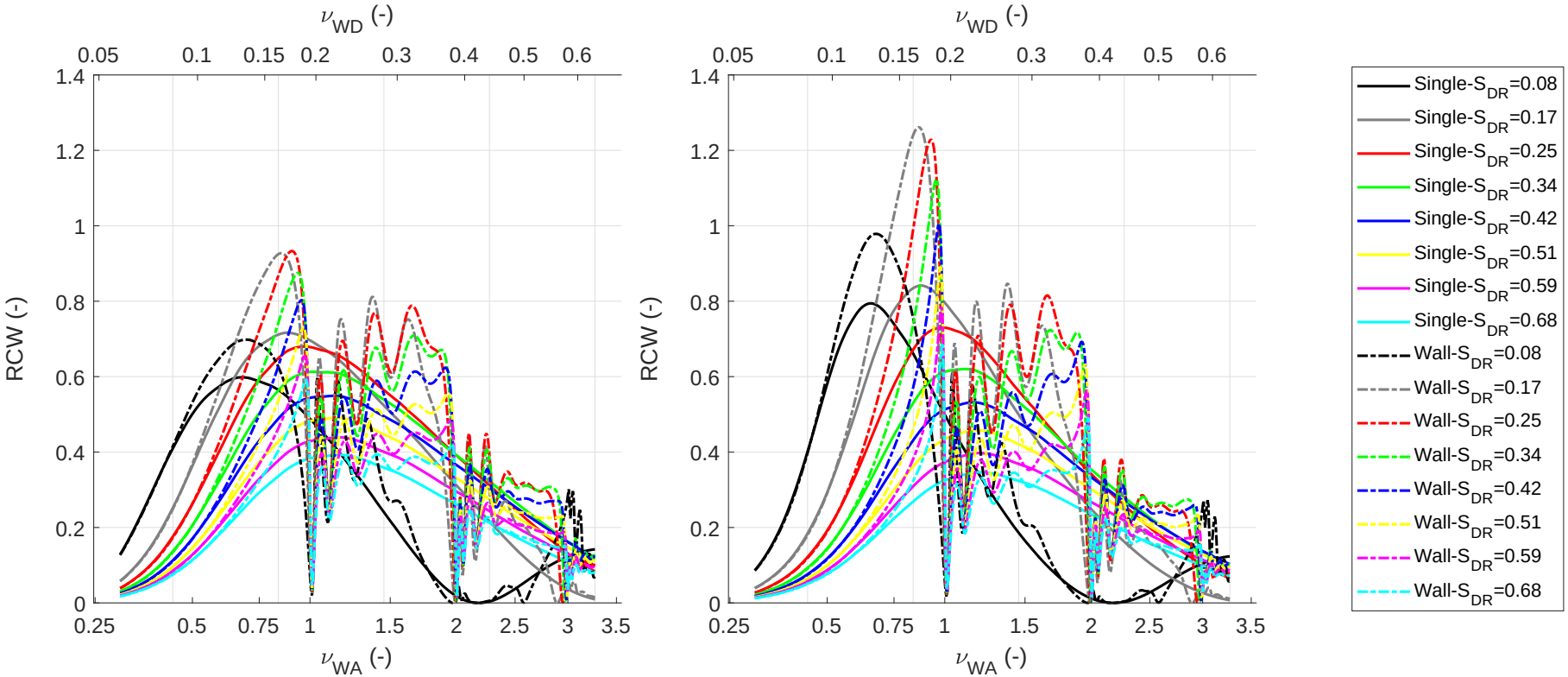

Figure 6.4: Effect of submersion depth on relative capture width for Control A (left) and Control B (right). Incident wave is expressed by the device and array non-dimensional linear wave numbers on the top and bottom x-axes respectively.

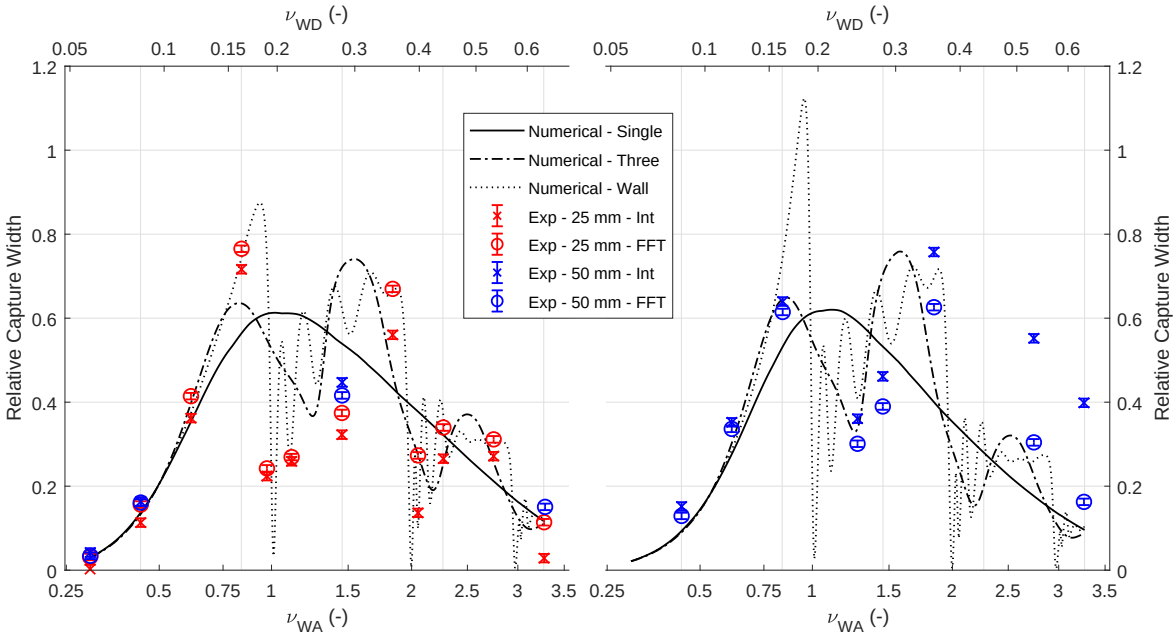

Figure 6.5: Relative Capture Width for Control A (left) and Control B (right) ($S_{DR} \approx 0.34$). Incident wave is expressed by the device and array non-dimensional linear wave numbers on the top and bottom x-axes respectively.

Figure 6.5 shows the RCW curves for the comparison between the experimental and numerical testing ($S_{DR} \approx 0.34$); it presents control coefficient sets A and B on the left and right respectively. The numerical consists of the single, three and wall conditions. The experimental results are distinguished by the two methods of calculation of the absorbed power and the two wave amplitudes considered. Incident wave frequency is expressed as non-dimensional linear wave numbers by device and array characteristic dimensions on top and bottom axes respectively. The error bars presented are the random uncertainty, which has been assessed as the highest standard uncertainty observed of all runs consisting of more than two repeats, a 95% confidence interval is considered. The randomn uncertainty for this test was very small, highlighted by the small standard error bars in Figure 6.5. The systemic uncertainty has not been assessed as the effectiveness of the force feedback control system materially effects this measurement; this is a more complex uncertainty issue which was considered out of scope for this work.

It is apparent that there is a reasonable correlation between the numerical wall condition and the experimental results assessed by the linearized FFT approach. However, it is clear that the integration approach at times has a large difference compared to both the results of the FFT and the wall condition, for example control B at $\nu_{WA} > 2.5$. This is likely due to the assumptions of linearity being less valid in certain conditions.

The control system as applied was not perfect; Figure 6.6 considers the frequency domain performance of the control system. This is done with demand PTO force, (6.10), plotted

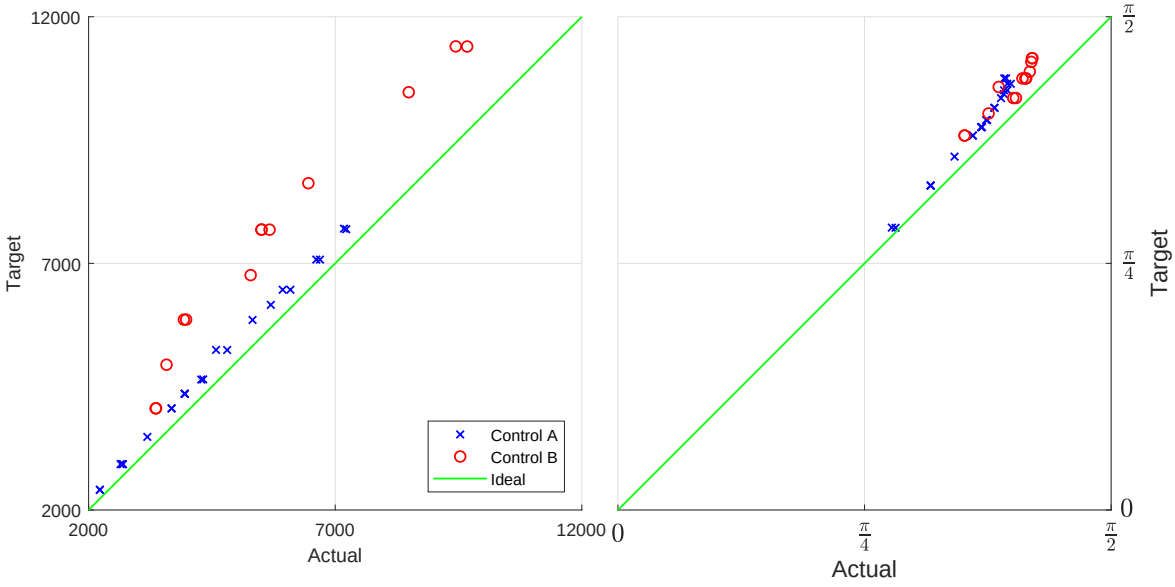

Figure 6.6: Effectiveness of Control with amplitude on left and phase on right.

against the measured PTO force for all conditions. Results are discretised by control strategy, with the amplitude plotted on the left and phase on the right. The plot indicates that the control system applied a lower force than intended and the force lagged behind in phase relative to the intended control. The two control strategies had different performance due the PID setting employed being better suited to control strategy A, noting there was no change in these PID coefficients between the runs. While this analysis of the performance of the control system is a good indication relative to the linear intent, it does not consider responses at different frequencies. These alternate frequencies were observed through the analysis, which would in part account for the variation between the frequency domain and integral approaches for the assessment of RCW as evident in Figure 6.5.

Figure 6.7 presents the heave RAO, with the numerical predictions and experimental measurements. The experimental measurements shown are the mooring extension (LVDT) and the pure heave motion measured by the Qualisys motion capture system; experimental results are separated by incident wave amplitude. Rows A and B present the results for control settings A and B respectively. The amplitude and phase are presented in the left and central columns including the numerical and experimental results, the right column shows the numerical results in a polar format. The amplitude and phase are presented with respect to non-dimensional linear wave numbers and the motion has been normalised by incident wave amplitude. It must be noted that the LVDT measurement includes the components induced by motions of the BA other than pure heave. These additional motions are primarily surge and pitch, which are presented later. In the amplitude and phase plots it is possible to perceive the wall condition as lacking in frequency resolution, with the troughs at the integer

ν_{WA} thought to reach zero. However, in the polar plot it is clear that this is not true with a clear consistent trend evident. These numerical plots are additionally presented in Appendix D.2 in a 3D cylindrical format, incorporating amplitude, phase and incident wave condition in a single rendering. Interpretation of these 3D plots in a 2D rendering is challenging, when using a computer to manipulate the plots it is evident that three device case spirals around the single case. The wall case exhibits a similar spiralling trend, except that there are more components within the spiral. The wall arrangement additionally exhibits inflection points at $\nu_{WA} \approx \{1.75, 2.75\}$.

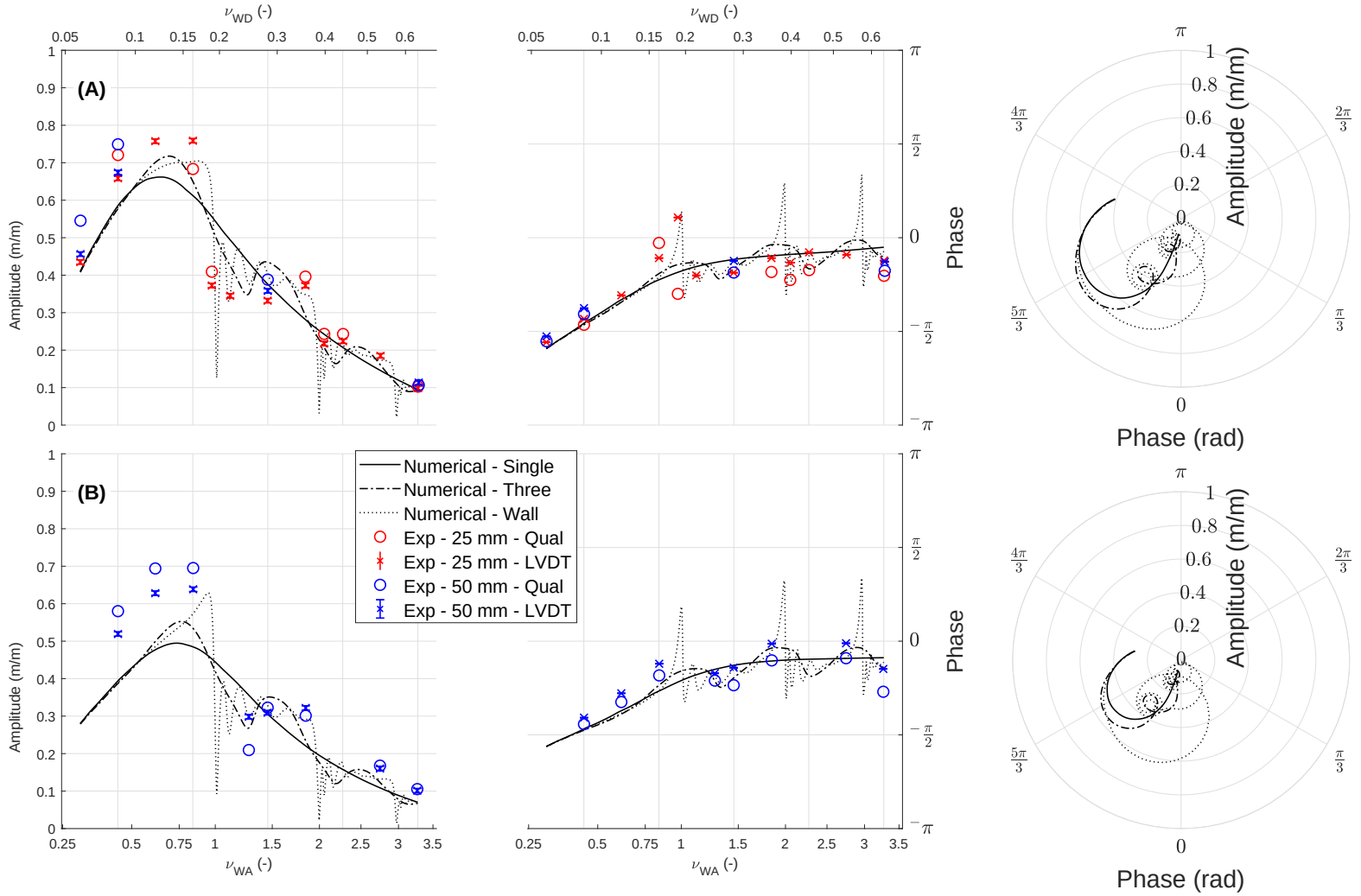

Figure 6.7: Heave Position RAO for Control A (A) and Control B (B) with amplitude on left, phase in the centre and a polar on the right. The results include both experimental and numerical results, except for the polar plot which only presents the numerical. The amplitude of motion has been non-dimensionalised by incident wave amplitude. Incident wave is expressed by the device and array non-dimensional linear wave numbers on the top and bottom x-axes respectively.

The surge and sway RAOs are presented in Figure 6.8 and the pitch and roll in Figure 6.9. The experimental results are presented with the translations non-dimensionalised by incident wave amplitude and the rotations by incident wave steepness for translations and rotations respectively. The incident wave condition is expressed as device and array non-dimensional linear wave numbers on the top and bottom axes respectively. Given the linearisations, the numerical modelling gives null results for these motions.

Comparing Figures 6.7-6.9 it can be observed that surge motions frequently exceed the heave in amplitude. Furthermore, pitch motions are also significant at times for most conditions.

Videos 6.1 and 6.2 provide the experimental condition with $\nu_{WA} \approx 1.1$; they present the stereo-videogrammetry results and the experimental observation respectively. The stereo-videogrammetry includes the free surface elevation and velocity vectors, the playback is at quarter speed with the true time step indicated at the bottom of the frame. Many of the same issues pertaining to localised discontinuities and errors in the join between the camera sets are evident as has been observed and discussed previously in Chapters 4 and 5. Additional concerns include the prevalence of erroneous velocity vectors. It is clear in the experimental video that the BA is not moving simply in heave, with pitch and roll evident. The effect of roll is clear in the stereo-videogrammetry with transverse symmetry (about the x-axis) being broken; this implies a di-polar radiation induced by either sway or roll.

Videos 6.3 and 6.4 present the experimental condition with $\nu_{WA} \approx 1.8$; they present the stereo-videogrammetry results and the experimental observation respectively in the same format as the previous videos. It can be seen in these videos that although there is pitch, there is none of the roll instability evident in the previous condition.

A selection of the free surface frequency domain first harmonic results are shown in Figures 6.10, 6.11 and 6.12 for wave conditions $\nu_{WA} \approx 0.61$, $\nu_{WA} \approx 1.1$ and $\nu_{WA} \approx 1.8$ respectively. In all figures the amplitude and phase are in the left and right columns respectively for four distinct studies. Amplitude has been normalised by the incident wave amplitude, from a separately measured incident run. From top to bottom they are a single, three and wall produced numerically and the experimental results. Additional examples are presented in Appendix D.3 with the same format for conditions $\nu_{WA} \approx \{0.97, 2.05\}$.

The frequency domain free surface results presented in Figure 6.10 indicate a reasonably good correlation on both the phase and amplitude between the experimental and numerical studies. The exception being directly over the BA, which is considered to be primarily associated to challenges in measuring the free surface in this location and not a true reduction in amplitude. This hypothesis is corroborated by the phase plots which suggest a good correlation, in line with the observations in Chapters 4 and 5.

The free surface results for the higher wave numbers, Figures 6.11 and 6.12, conversely show a

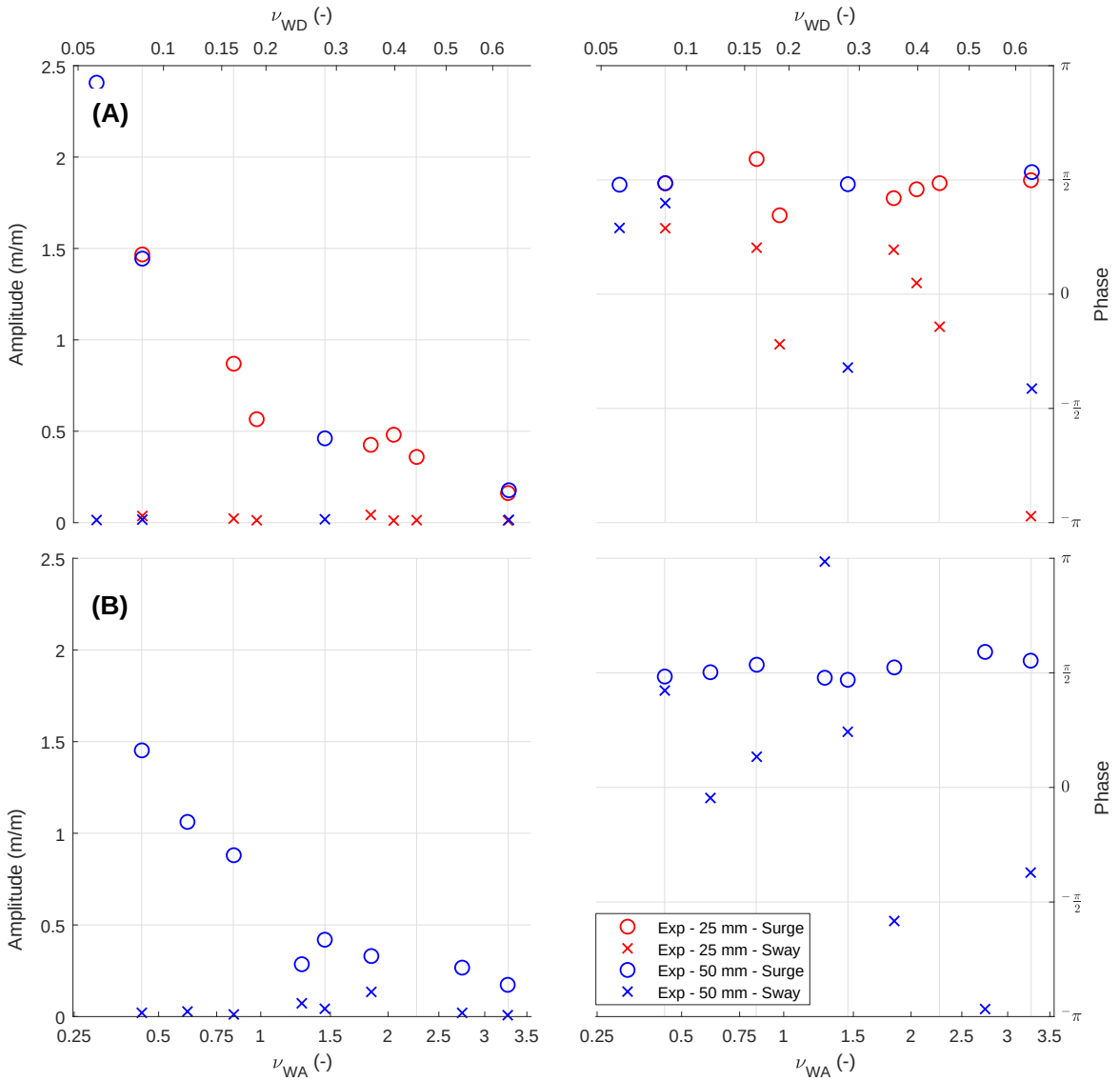

Figure 6.8: RAO for surge and sway from measured experimental motions. Controls A and B are in rows A and B respectively with amplitude on left and phase on right. Amplitude is normalised by incident wave amplitude. Incident wave is expressed by the device and array non-dimensional linear wave numbers on the top and bottom x-axes respectively.

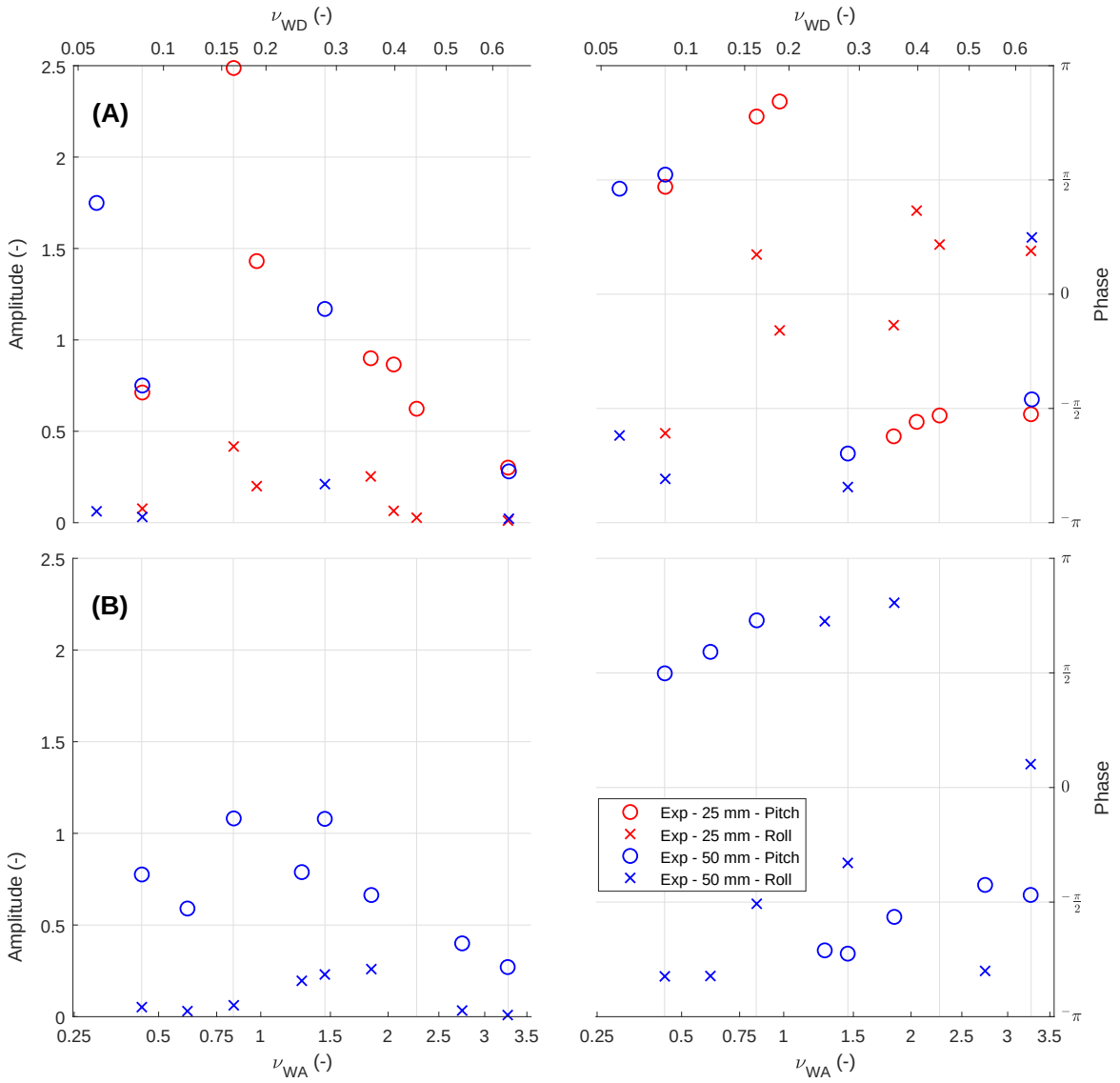

Figure 6.9: RAO for pitch and roll from measured experimental motions. Controls A and B are in rows A and B respectively with amplitude on left and phase on right. Amplitude is normalised by incident wave steepness. Incident wave is expressed by the device and array non-dimensional linear wave numbers on the top and bottom x-axes respectively.

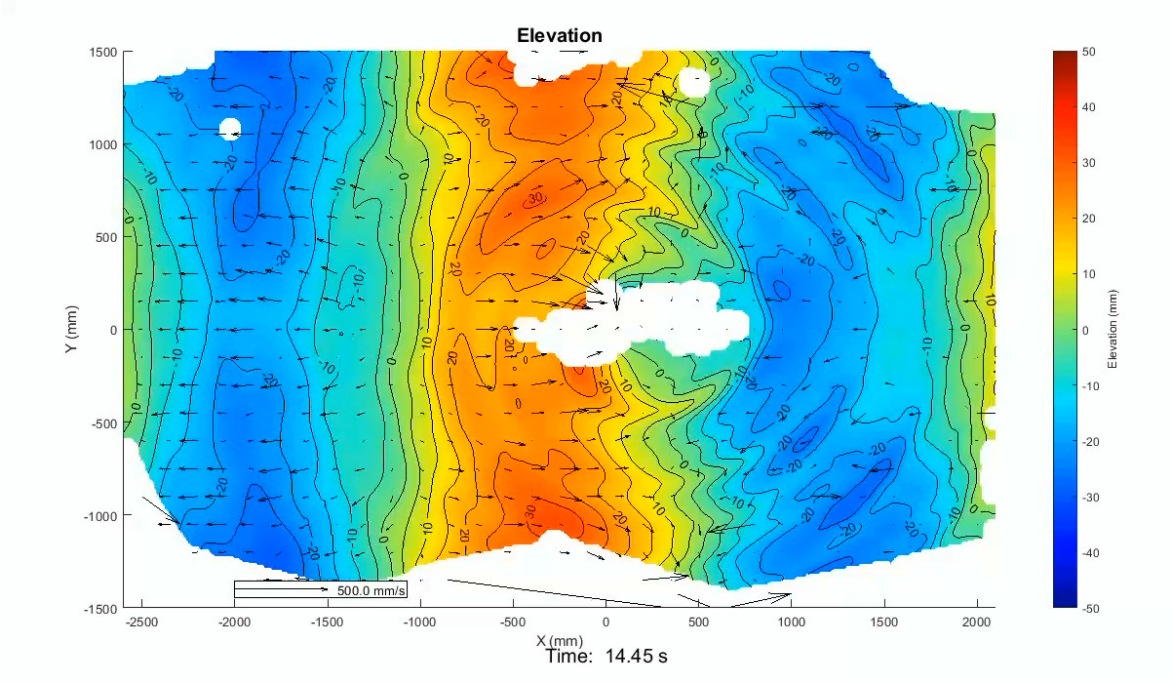

Video 6.1: Stereo-Videogrammetry time domain free surface of condition with $\nu_{WA} \approx 1.1$. The video is available at: `https://cloudstor.aarnet.edu.au/plus/s/SG9CLbWMBCNcg7L`.

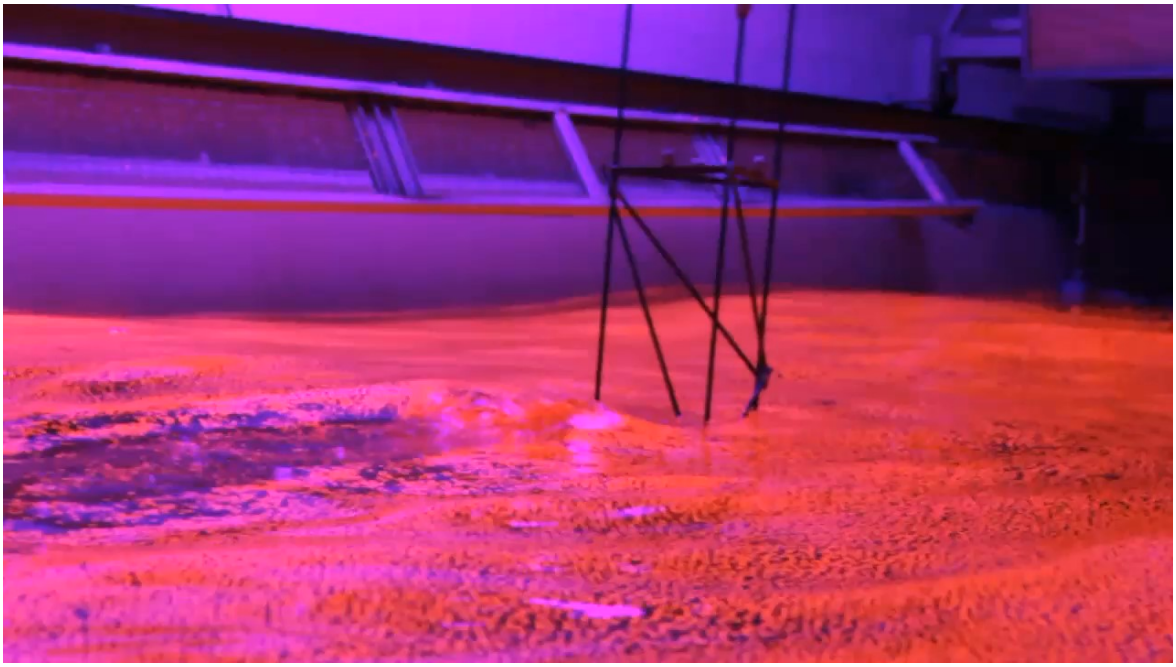

Video 6.2: Experimental time domain free surface of condition $\nu_{WA} \approx 1.1$. The video is available at: `https://cloudstor.aarnet.edu.au/plus/s/oksGNoZuBr1UYKA`.

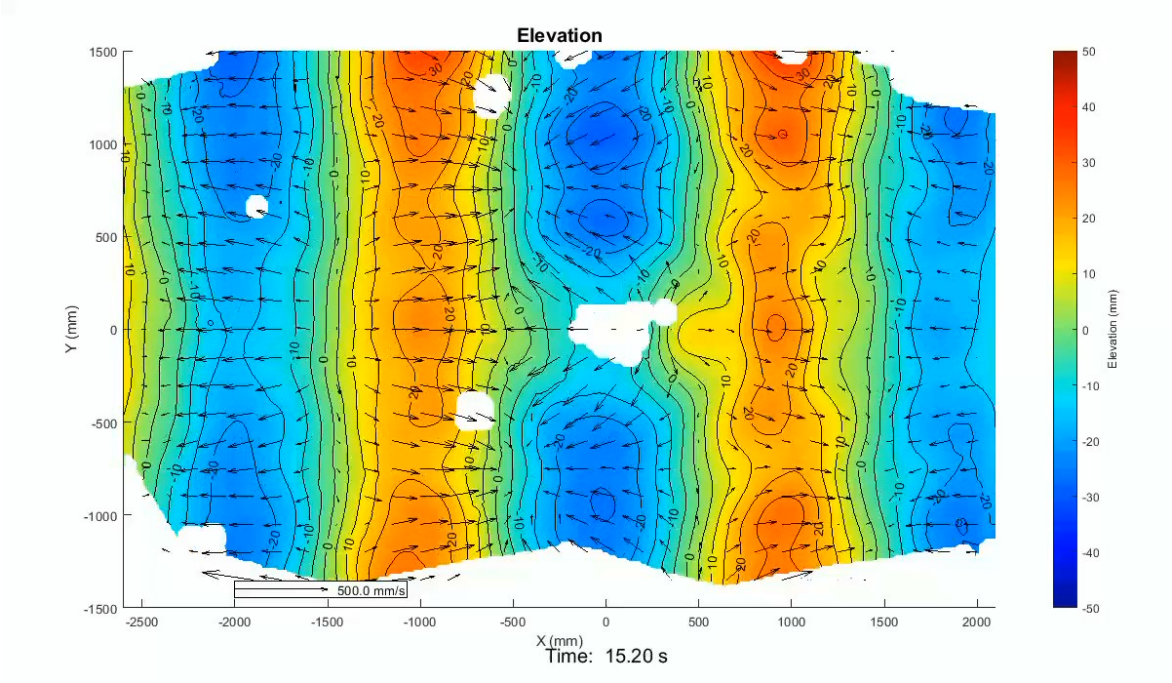

Video 6.3: Stereo-Videogrammetry time domain free surface of condition with $\nu_{WA} \approx 1.8$. The video is available at: `https://cloudstor.aarnet.edu.au/plus/s/zEwJ3JRyQHbmX7l`.

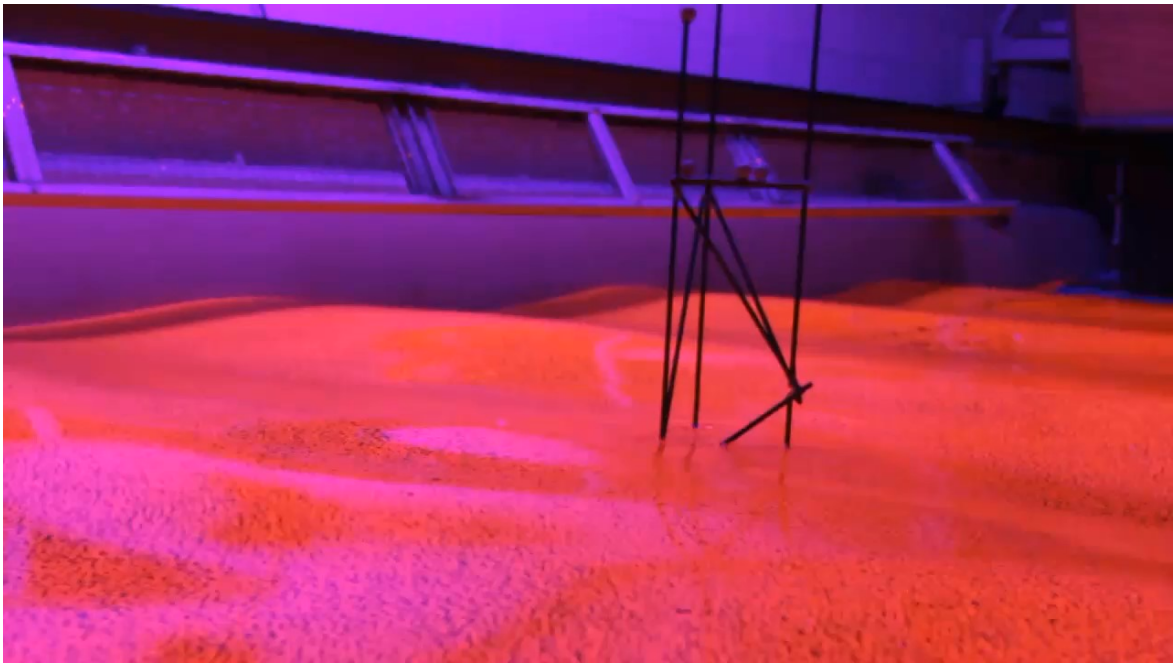

Video 6.4: Experimental time domain free surface of condition $\nu_{WA} \approx 1.8$. The video is available at: `https://cloudstor.aarnet.edu.au/plus/s/RCKQ5eHK7GunK51`.

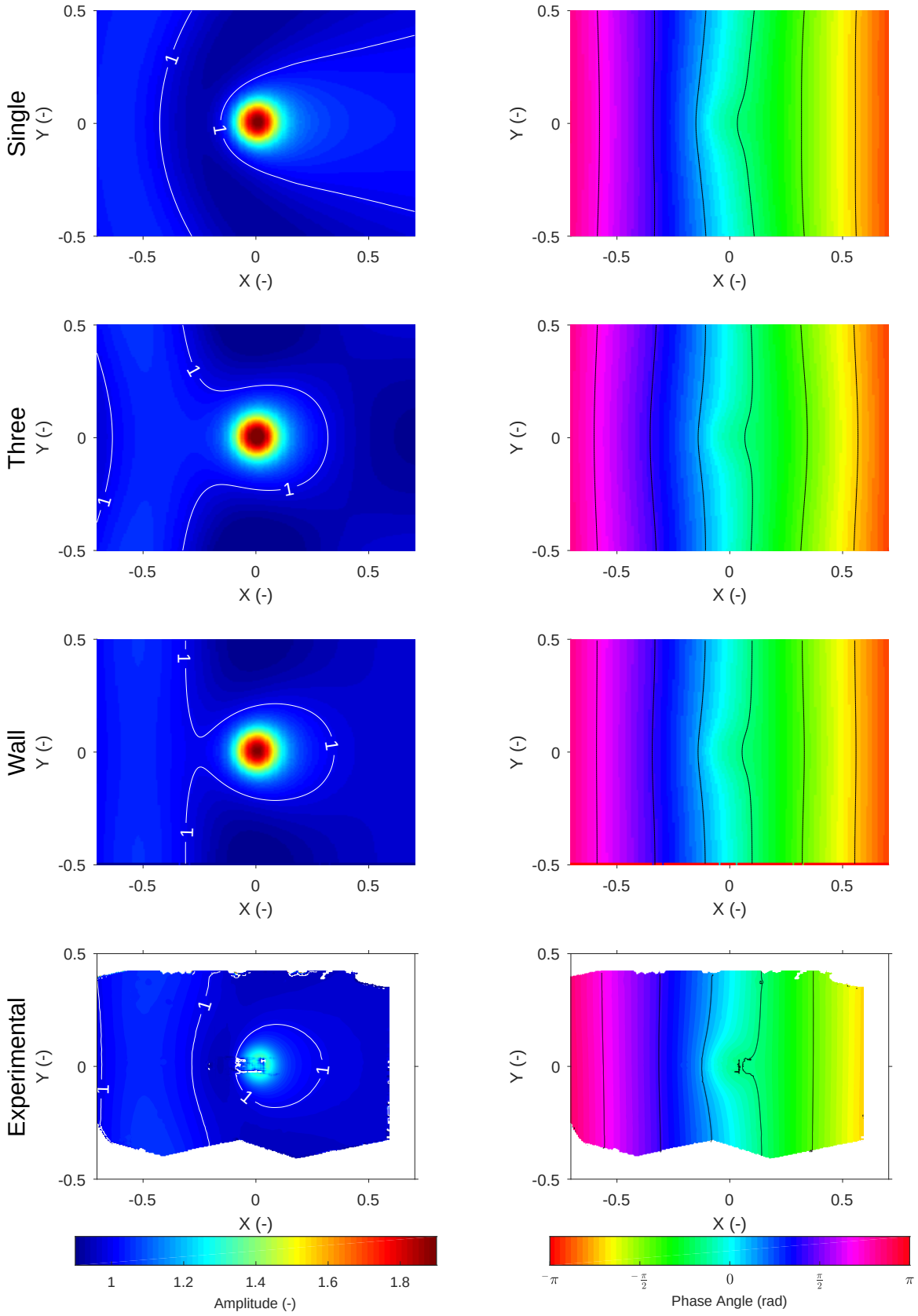

Figure 6.10: Frequency domain free surface for condition $\nu_{WA} \approx 0.61$ ($S_{DR} \approx 0.34$), this represents neutral array effects. Left column is amplitude, right column is phase. Top three rows are numerical predictions for the single, three and wall conditions; the bottom row is experimental results.

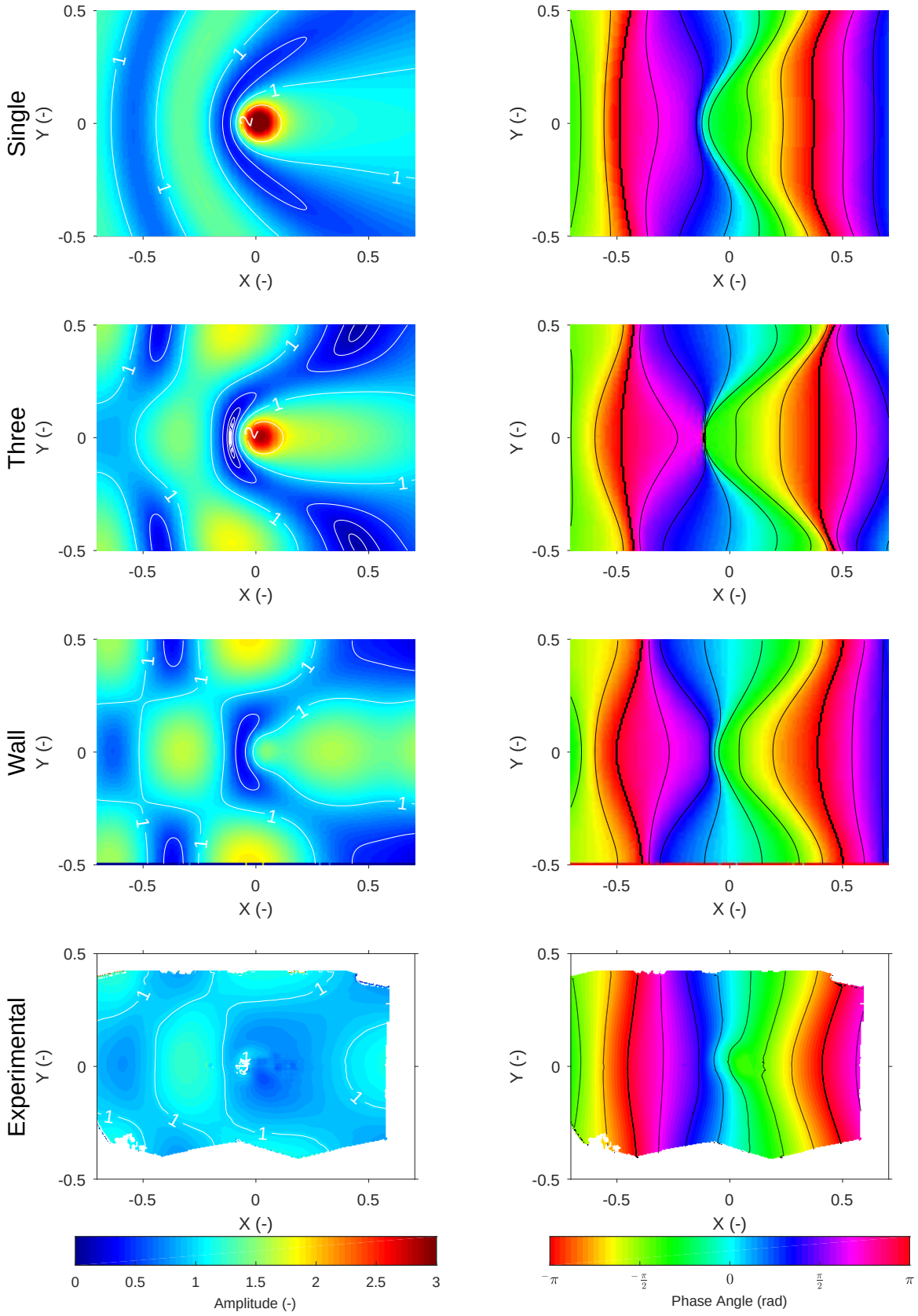

Figure 6.11: Frequency domain free surface for condition $\nu_{WA} \approx 1.1$ ($S_{DR} \approx 0.34$), this represents negative array effects. Left column is amplitude, right column is phase. Top three rows are numerical predictions for the single, three and wall conditions; the bottom row is experimental results.

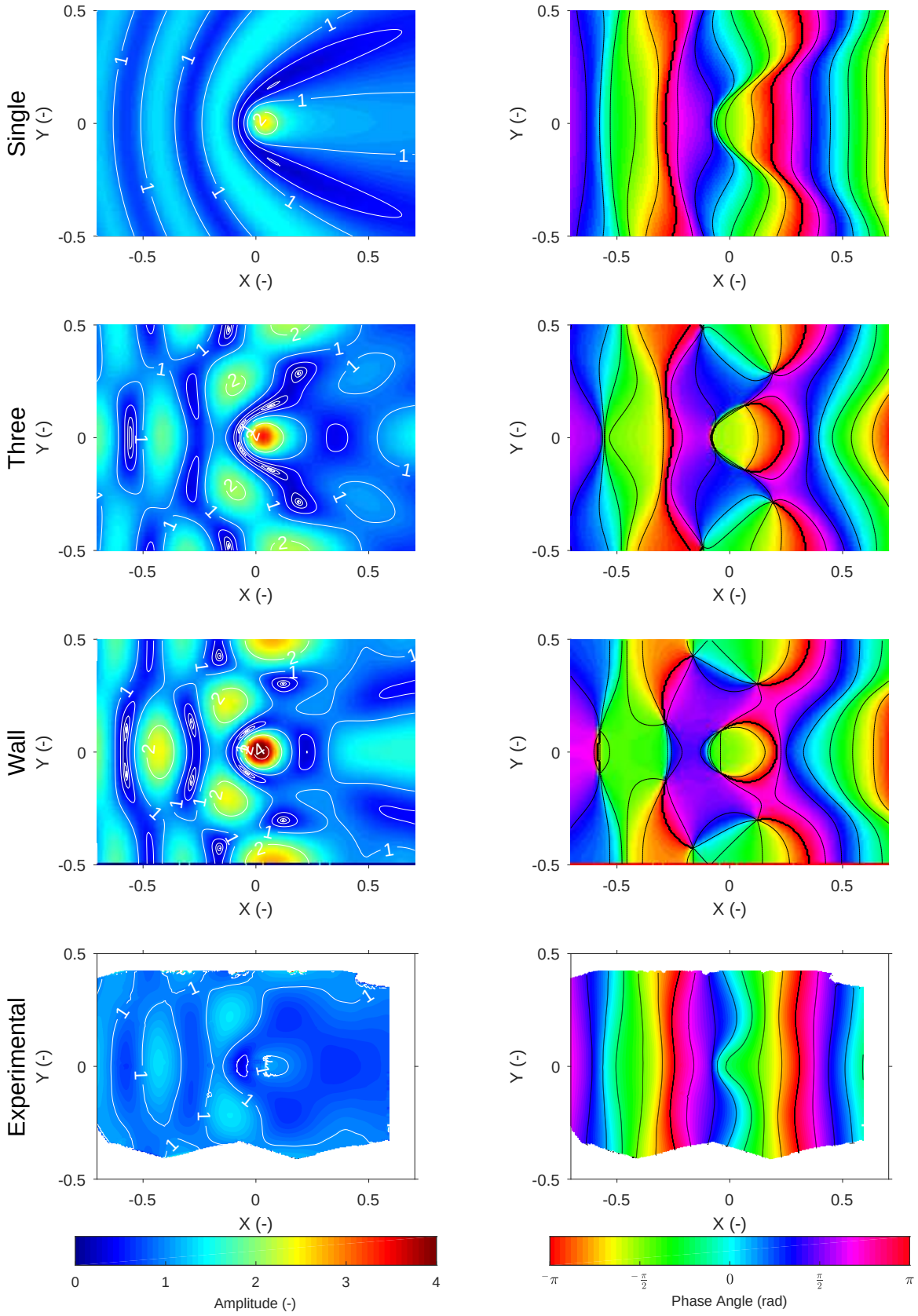

Figure 6.12: Frequency domain free surface for condition $\nu_{WA} \approx 1.8$ ($S_{DR} \approx 0.34$), this represents positive array effects. Left column is amplitude, right column is phase. Top three rows are numerical predictions for the single, three and wall conditions; the bottom row is experimental results.

considerable difference between the experimental and numerical results. This is most evident in the lee of the BA ($x > 0$) with drastically reduced wave amplitude in the experimental compared with the numerical. This is likely attributable to additional wave field components in the experimental results. The motions of surge and pitch, seen in Figures 6.8 and 6.9, suggest the sources of these additional wave field components.

6.4 Discussion

In WEC dynamics the PTO control strategy can induce large variation in the dynamics and the power capture performance of the device (Garcia-Rosa et al. 2015; Hals et al. 2011; Ringwood, Bacelli, et al. 2014; Ringwood, Ferri, et al. 2017). In this work a comparatively simple linear PTO control strategy has been implemented. As indicated by Figure 6.6 this control strategy was quite effective in its linearized implementation, although the PID tuning was better for Control A than B. This non-ideal in the performance of the control system is indicative of the challenges of assessing systematic uncertainty. While it is feasible to assess the uncertainty in the measurements to complete an uncertainty study, as in Appendix E, the fact that the control system is not perfect introduces another form of uncertainty for comparison with numerical models. The challenge is that the control system materially effects the dynamic response of the system in feedback loop, thereby changing the measurements being made. This change does not correspond to either the accuracy of the measurements systems nor the random uncertainty. Figure 6.6 furthermore does not fully account for the performance of the control system, additional frequency components were observed during post-processing which also characterise the net effectiveness of the system.

The experimental uncertainty associated with the performance of the control system is not the only type not fully accounted for in this thesis. The balance of the analysis has been completed under an assumption of steady-state, as has been observed in Chapters 4 and 5. This assumption is not strictly speaking true, with observations in Appendices B.4 and C.3. This uncertainty essentially relates to the question of what is the effective width of the array which the measurements describe. However, this is not expressly possible for reasons analogous to the Heisenberg uncertainty principle. It is theoretically possible to deduce the condition at any instance, by modelling the propagation of the wave with group and phase velocities. However, in order to make a cyclic measurement (eg. free surface elevation) a time differential is required, this is a wave period at the absolute minimum and more likely several wave periods. Figure 6.13 illustrates this concept, it presents power capture for a 0.5 Hz 25 mm amplitude incident wave condition. Period is plotted in three respects, the elapsed time and the distances the phase and energy propagates. These distances are determined with the group and phase velocity of the wave. The fluctuations evident in the amplitude

of the instantaneous power are partially accounted for through WEC array effects. In order to make a measurement these variations must be averaged to some extent. As a result it is fundamentally requisite to have uncertainty in what the measurement represents in WEC array testing. This includes approaches such as O'Boyle et al. (2017), where waves are run for a period in an attempt to reach steady state, will experience this phenomena to some extent. The array uncertainty is likely exceeding small, especially compared with uncertainty induced by non-deliberate reflections. However, it likely means it is fundamentally impossible to separate the orders of interaction from results. An alternative perspective is to consider which propagation velocity should be used, as the result will be different if phase or group velocity is employed.

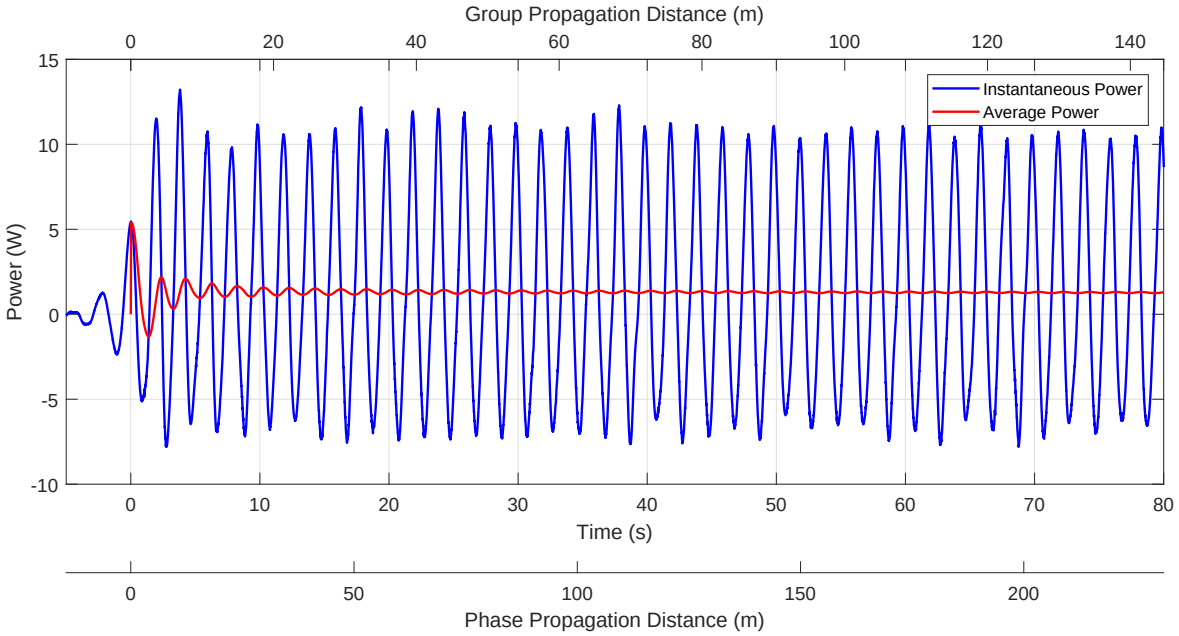

Figure 6.13: Wave propagation effects on array uncertainty.

With an understanding that various uncertainty sources have not been fully accounted for, it can still be seen that there is quite a good correlation between the numerical predictions and experimental measurements as shown in Figure 6.5. With the exception of integral approach at $\nu_{WA} > 2.5$, this variation relates to higher noise non-harmonic components in the instantaneous power capture. These non-harmonic components are not able to be attributed to a single source, the possibilities are it's a characteristic of the PTO system or they have been caused by array interactions.

The surge motions, shown in Figure 6.8, are almost identical for the two control systems employed. This is due to the PTO system having very little impact on this aspect of the dynamics of the BA. The force vector the mooring line applies is very close to vertical, except when the surge motion is large. Consequently, through the small angle, the PTO system

doesn't have a material effect on surge motions. The characteristic response of the system when motions become large is to behave like a buoyant pendulum, where surge motions induce a coupled heave motion as the mooring extension remains constant. This also explains the discrepancy at lower wave numbers ($\nu_{WA} > 1$) between the numerical and experimental results for the heave RAO, as evident in Figure 6.7.

As shown through the thesis since Chapter 4, considering both amplitude and phase can be very useful for understanding the hydrodynamics of system by plotting them on a polar plot. It is possible to extend such a concept and plot in a 3D cylindrical, in a combined amplitude, phase and incident wave condition. Figure 6.14 attempts to illustrate such a plot, though it's challenging to fully appreciate the full value in such a rendering; real and imaginary components are employed instead of amplitude and phase. Considering these illustrations it is evident that the three device case spirals around the single study, with one rotation on $\Delta\nu_{WA} = 1$. For the wall conditions there is evidence of many more spirals, with the addition of two inflection points at $\nu_{WA} \approx \{1.75, 2.75\}$.

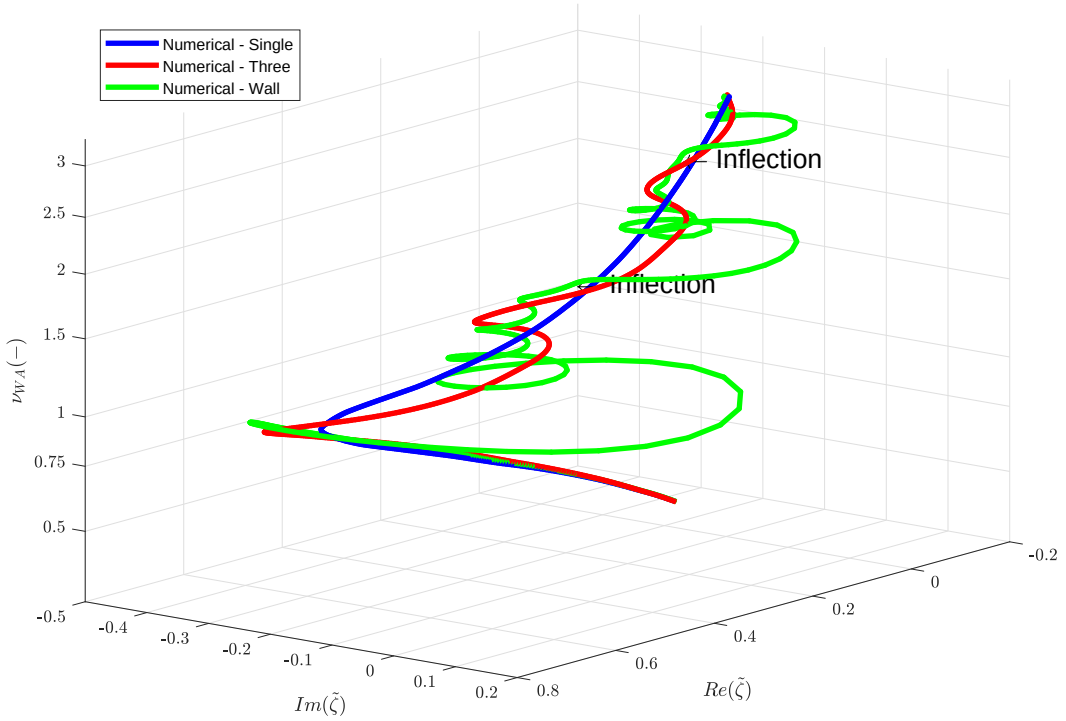

Figure 6.14: Cylindrical representation of heave RAO for Control B. Presented as real and imaginary components of RAO against incident wave condition (ν_{WA}) on the vertical axis ($S_{DR} \approx 0.34$). A dynamic rendering is available at: `https://cloudstor.aarnet.edu.au/plus/s/hB4IsU1DVIezX6B`.

It is hypothesised that were a study completed which is representative of $n = 1, 3, 5, 7, 9...$ devices there would be sequential spirals about the $n^{th} - 2$ device. At some point however, the impact of the second order of interaction of the nearest pair will become more important than the 1^{st} order of interaction harmonic of a distant pair. The inflection points evident

in the wall condition is likely representative of this transition. The explicit nature of this relationship has not been tested nor is there confirmation of this hypothesis as it is considered outside the scope for this thesis.

As observed, the numerical prediction for power capture correlates quite well with the experimentally measured observations as with the heave RAO, Figures 6.5 and 6.7. The same is not true for the free surface results, with large variation in Figures 6.11 and 6.12. This seemingly contradictory observation can be attributed to the surge and pitch motions which were observed experimentally, Figures 6.8 and 6.9. The dipolar wave radiation, which surge and pitch will induce, will both have a symmetry plane on $X = 0$. This symmetry plane will have negligible effect on the excitation force resulting in very little change to the power capture. The nature of the effects of this symmetry plane were seen in Chapter 4, where the array effects in surge and pitch were very small compared to heave. In Contardo et al. (2018) it is similarly observed that understanding of power absorption is not sufficient to fully understand wave climate variation.

While it can be deduced that the array harmonic frequency can be changed by varying the spacing, what the optimal spacing is cannot be determined from this work. Such an answer is very likely to be entirely subject on location and variation in the incident wave climate (Clément et al. 2016). It can be deduced however, that to decrease the array effects (of the nature considered in this thesis) it is necessary to place devices closer together. Placing the devices closer together would have the characteristic of shifting ν_{WA} right on all plots where it's used in this chapter. The reciprocal of increasing spacing would shift ν_{WA} left which would induce array effects over a larger proportion of the response spectra. This observation is perhaps counter intuitive, with the expectation that the closer the devices the more important array effects become. While this may be true for other physical phenomena, such as viscous forces, it is not true for the resonances observed here. A deductive perspective is that for a set of devices which are close (relative to normal wave conditions), the overlap between the incident wave spectrum and proportion of device response spectrum with array effects becomes small. Conversely the further apart the devices are, the higher the potential harmonic interactions which are possible.

The bulk of the study in this thesis has been predicated on an assumption of a unidirectional incident wave; such conditions are not typical in the real world. In the real world it some variation in wave directionality should be expected. Consequently it's not possible for all devices to be placed on a single dimension (e.g. $X = 0$) for all conditions. As such the dipolar radiation which was unimportant for the power capture in this chapter will become important. Under such a condition all DoF of a device will need to be considered, even in the instances where the DoF has negligble impact on power capture of a single unit. The alternative to this would be to employ a WEC where all DoF are important for power capture

or restrict motions such that there are no unimportant DoF.

A further consideration for realistic deployment of WECs is extreme wave conditions, as shown in Figure 4.2 the experimental conditions considered in this research have been drawn from those which are typical to the site case study. These conditions however may be considered somewhat benign when compared with the European WEC test sites such as EMEC (Babarit, Hals, et al. 2012). This raises the question on the applicability of the wave conditions used here for broader learning. Noting for more energy intensive sites have wave conditions that induce greater non-linearities in the wave dynamics and wave structure interactions. It is expected that for such studies the applicability of using wall reflections will be reduced. This deduction is through the expectation of increased energy dissipation for these more non-linear wave conditions in the interaction with the walls. As the non-linearity increases the relative velocity between the wall and the water will increase, thereby causing viscous interactions to become more important. Additionally, the importance of the harmonic components resulting from the interaction will increase also inducing energy dissipation from the primary wave component. The limit at which these unwanted response characteristics become important is unknown and likely bears further investigation. There is however the ancillary question of the importance of array effects in extreme survival sea-states.

As discussed, a study with the symmetries involved in this work, the only modes of motion which are expected to be observed are surge, heave and pitch. It is evident however in Figure 6.9 that there are instances where roll is a non-trivial mode of motion. Work in Orszaghova, Wolgamot, Eatock Taylor, et al. (2017) and Orszaghova, Wolgamot, Draper, et al. (2018) has shown that these motions are implicit to the weakly non-linear geometry of the system causing coupling between all modes of motion.

6.5 Conclusions

A study on WEC intra-array effects has been completed using wall reflections to simulate the array. Carnegie Clean Energies CETO 5 was the basis for the WEC employed at a 1:16 scale. Work included the development and implementation of linear a PTO system to simulate complete WEC effects experimentally and a numerical investigation with *NEMOH*. The experimental investigation included the use of stereo-videogrammetry.

It has been shown that the use of wall reflections is a useful tool for the exploration of WEC intra-array effects. The linearization of the WEC dynamics, with the assumptions of pure heave, indicate an acceptable ability for the prediction of power capture. However, it is shown that this does not relate to accurate assessment of the wave field effects, with a requirement to include components of radiation which are not important to power capture.

A discussion is also included on the uncertainty for WEC PTO control and arrays, where it is primarily highlighted that these uncertainties are not well understood with further work required to formalise a process.

Chapter 7

Summary, Conclusions and Future Work

7.1 Summary and Conclusions

This thesis has explored the use of reflections to simulate hydrodynamic WEC array interactions and the experimental processes to facilitate this exploration. This chapter summarises the work completed and gives the key research findings. This includes the values and limitations of the methods employed and potential future work.

At the commencement of this thesis very few WEC experimental array studies had been completed, with most (Black 2014; Haller et al. 2011; Mercadé Ruiz et al. 2017; Nader et al. 2017; O'Boyle et al. 2017; Porter 2012; Stratigaki 2014) exploring generic configurations of a few WEC units. A frequent observation is the technical complexity and associated cost of experimental array studies. By using wall reflections to simulate array interactions there is a potential to greatly reduce the cost of experimental investigation into WEC array effects.

There is additional evidence for a desire for greater levels of spatial information of the water free surface, hence ancillary investigations were developed to facilitate the investigation. These relate to the use of stereo-videogrammetry for free surface measurements and the ability of a linear potential flow boundary element method numerical solver to estimate the array effects. The stereo-videogrammetry is in response for the need to increase the spatial information of the free surface effects. The numerical study was predicated on a need to estimate the expected loads necessary for the experimental study; this however developed into a brief exploration of array effects numerically.

Given the novelty of the free surface measurement approach, the thesis commences with a consideration of the capabilities of the stereo-videogrammetry technique employed (Chapter 2). The same experimental results are then used to consider the ideal diffraction case of a cylinder in channel in comparison with numerical estimates (Chapter 3). Utilising the same experimental techniques, a realistic WEC is then tested in diffraction, heave radiation and a power absorption mode (Chapters 4, 5 and 6). The realistic work includes both experimental and numerical studies throughout.

7.2 Key Findings

- **Stereo-videogrammetry**
  - **Measurement accuracy:** The accuracy of stereo-videogrammetry is comparable to conventional wave measurement techniques (Chapter 2), with the additional capability of spatial measurement is has been shown that observation can be made beyond conventional capabilities (Chapter 4).
  - **Equipment effect:** The addition of equipment to facilitate the measurements, particles and fences, has a negligible effect of wave dynamics (Chapter 2). With the change in conditions shown to be within the variation of the wave making facility.
  - **Cost:** While the approach has value there are additional expenses compared to conventional techniques. Besides the additional physical equipment (camera, particles, etc...) and the software licenses, there is increased facility time (with respect to set-up & teardown) and post-processing (Chapters 2 and 4). The increased facility time, on the order of 5-10 days, to install and calibrate the cameras, manage the particles through the experiments and then importantly remove all particles at the end. The post-processing of the data from raw images to final FFT takes up 10 minutes per second of experimental time, this was observed in the more complex study with two distinct measurement areas (Chapters 4, 5 and 6). This means that it is not possible to assess the data quality in anything resembling real-time thus increasing experimental risk. However the likelihood of failed processing was much lower in later testing (Chapters 4, 5 and 6) as a result of the lessons learned.
  - **Value:** While stereo-videogrammetry is observed as being expensive for experimental investigations, specifically in terms of post-processing, there is no practical alternative currently available. A study such as this would not be possible to complete, at least with the same spatial region and resolution, with conventional resistive wave probes. Such a study would require numerous months in an experimental facility completing repeats to capture the domain which would simply not be feasible. Due to uncertainty management (including the number of calibrations) and the cost of such an investigation.
- ***NEMOH*:**
  - A very good correlation has been shown within the stringently controlled studies (Chapter 3, 4 and 5) between *NEMOH* and the experimental measurements. Within the constraints of the assumptions explicitly made in the *NEMOH* formulation.

  - The linearized assumptions still provide a reasonable estimate for power capture, as shown in Chapter 6. However, the assessment of free surface in this study does not correlate well; this however is more based in the assumption of dynamic linearity of the mooring system and not due to *NEMOH*.
  - The investigations of the effect of submersion depth in Chapters 4, 5 and 6 suggest that the predictions are incomplete. The results indicate that wave shoaling on top of the device must be happening given the change in array effects. This shoaling implicitly means that there must be harmonic components to both the excitation force and resulting free surface. As *NEMOH* is a linear potential flow solver these harmonic components are not resolved.

- **Capability of Wall Reflections to Simulate WEC Array Effects:** It has been clearly shown that the use of reflections is a valid tool for the study of WEC array interaction. With consistent evidence through all experimental investigations that reflections are occurring and impacting the measured wave field. The comparisons with the numerical linear potential flow estimates consistency show reasonable agreement. This suggests that for WEC experiments conducted in narrow channels

- **Uncertainty:**

  - **WEC Array Studies:** There are developed and accepted methodologies (ITTC 2017a; ITTC 2017b) to assess uncertainty with respect to measurement and random errors (loads, waves, motions, etc...) for experimental hydrodynamics studies. There are however transient effects to WEC arrays which are not yet fully understood. These transient effects must be averaged to make amplitude, phase and frequency measurements. This results in an uncertainty which relates to a lack of knowledge in the effective array condition.
  - **WEC Control:** For studies where real-time control is implemented to simulate a model scale WEC the effect of non-perfect implementation of the control system needs a technique developed for the assesment on the final experimental uncertainty. There may be techniques from other fields, such as IEEE, but they are not yet common place in WEC studies.

- **Intra-array Effects:** The use of wall reflections and stereo-videogrammetry has been demonstrated as a useful tool in the exploration of WEC array effects. While the approach does not directly allow for the assessment of a final design, it facilitates the exploration of phenomena (e.g. transient nature, harmonic components, etc...) which will be important for designers to consider.

- **Extra-array Effects:** Understanding the broader implications for WEC array deployments are an important consideration for commercial operation; for reasons relating to

environmental stewardship and governmental approval. Unfortunately, this approach of using wall reflections is not a useful tool in this type of investigation. For extra-array effects the aspect of interest is the dispersion of wave energy around the WEC array. Given the array size is effectively undefined with this reflection approach it is not feasible to extrapolate far field effects.

7.3 Implications

In this thesis, experimental and numerical work has been conducted to explore hydrodynamic intra-array effects of WECs using wall reflections to simulate multiple bodies. The approach of using walls has the benefit of much reduced complexity and cost, compared to actually modelling multiple devices. This facilitates the ability to explore the hydrodynamic interactions important in physical testing, which in turn will allow for the validation of numerical modelling tools for WEC array design.

The work completed to accomplish the research goals of the thesis have included the implementation and assessment of a range of experimental tools; specifically, stereo-videogrammetry and an electro-mechanical system for the simulation of a WEC PTO. Stereo-videogrammetry has been shown to be a valuable tool in hydrodynamic investigation where free-surface dynamics are important.

The linear potential flow, boundary element method numerical model (*NEMOH*) employed through the thesis has been demonstrated to be accurate in the prediction of first order loads, motions, power capture and free surface within the accuracy of the assumption made in the numerical model. The first order components of these facets are not however a full description, with evidence that the numerical results of dimensional studies meaning that the results are incomplete.

While extra array effects are a very important consideration for the commercial implementation of WEC arrays, it has been deduced in the course of this work that the experimental approach of employing wall reflections is not a useful tool for such effects. By using wall reflections there is no far-field, in the lateral plane, from which energy can flow to generate a normalised wave field in the lee of the WEC(s). This means that for validation of extra-array effects, experiments need to be conducted in experimental facilities where reflections are unimportant to the net wave field. Under the assumption that the re-normalisation of energy is the primary concern it is plausible to conduct validation studies with a single device. This approach could be used to correlate near-field with far-field predictions. Then combining with confidence from near field predictions, from wall-based studies, extrapolation to confidence in far-field effects from multiple devices should be achievable.

It has been shown through this thesis that the use of wall reflections can be a useful tool for the investigation of WEC intra-array effects. However, this study has focused on the specific geometry of a submerged heaving buoy with a single point mooring. In principal the approach should work for any WEC type, however such an array layout is not being proposed as optimum for any device. Instead it is being put forward that by using wall reflections it is possible to explore the interactions which are important to intra-array effects in a manner which is cheaper than alternatives. Examples of queries of interest include exploration of the transient nature of array interactions, as done in Appendices B.4 and C.3.

7.4 Further Work

The work performed in this thesis could be extended to consider the following:

- Base hydrodynamics
  - Explore the implications of how array effects cause the RAO to wind around each other (Figure D.7), and the inflection points which are evident in the wall case. This investigation could allow for an assessment of the widest array width which is hydrodynamically important.
  - Development of a reflections analysis approach which is able to assess the properties of the reflections off channel walls. Specifically, an assessment on change in amplitude and phase as a function of position.
  - The transient array effects, which are briefly observed and considered in the appendices, shows a potential for a deeper understanding of how interactions develop through time.
  - This study has essentially not employed the vector field measured by the stereo-videogrammetry. There are likely many uses to this data which has not been fully leveraged, an example is considering flow lines (Fleming and Manasseh 2017). However, the effect of the experimental equipment has not been assessed with respect to the velocity field.
  - Extend investigation from simple regular waves to irregular/polychromatic to explore broader implications.
- Numerical modelling
  - Extend to include motions not important to power capture, primarily surge and pitch. With the inclusion of the wave field components associated to these motions a better correlation between the numerical and experimental should be observed.

  - Comparison between the experimental results and other numerical methods. An investigation has been conducted comparing the experimental results with fully linearised potential flow simulation. It would be interesting to explore the correlations with more advanced numerical methods, such as CFD.
  - Use of the modelling technique employed in this thesis for comparison with Nader et al. (2017).

- WEC control poses a great potential to improve efficacy so as to allow for commercial implementation. This thesis has only considered a reasonably simple linear control strategy.
  - Improve control system to better accomplish intended control strategy.
  - Explore effects of different control strategies on array interactions.

- Conduct testing with variations on the single CETO type device centrally located in a channel to allow for broader understanding of array interactions.
  - Other device types may have different characteristics of array interactions. An exploration of different device types could facilitate a deeper understanding of what is important.
  - Place multiple devices longitudinally along the tank. This would allow for simulation of arrays with multiple rows that are very wide. This is important as the cost of arrays which are only one device deep would effectively maximise the distance needed for undersea cables/pipes for transmission of the captured energy to shore. This work could consider the effects of different spacings much easier than transverse investigations.
  - Exploration of placing multiple devices on a single transverse plane. It is possible that by placing devices at irregular points in the channel to simulate an array pattern which is not a constant spacing between devices.

- Exploration of improvement or alternatives to the stereo-videogrammetry method used here to reduce the cost of the experimental process. With a reduction in experimental cost; it is foreseeable that the approach could be very useful in many more hydrodynamic investigations into wave-structure interactions.

- Employment of the stereo-videogrammetry technique in other hydrodynamic studies, potential examples include,
  - Validation of analytical models which describe wave propagation.
  - Validation of analytical models which consider diffraction about a simple device.

- Validation of analytical models which explore radiation.
- Wake analysis to assess ship resistance.
- Exploration of ship-ship interactions for studies on replenishment at sea, or similar.

Bibliography

ATI Industrial Automation (2018). *F/T Sensor: Mini58 IP65/IP68*. 1031 Goodworth Dr. — Apex, NC 27539 USA. URL: https://www.ati-ia.com/products/ft/ft_models.aspx?id=Mini58+IP65%2fIP68.

Babarit, A. (2013). "On the park effect in arrays of oscillating wave energy converters". In: *Renewable Energy* 58, pp. 68–78. ISSN: 0960-1481. URL: http://www.sciencedirect.com/science/article/pii/S096014811300164X.

– (2018). *Ocean wave energy conversion*. Ed. by A. Dollet. Elsevier. ISBN: 978-1-78548-264-9. URL: https://www.sciencedirect.com/book/9781785482649/ocean-wave-energy-conversion#book-info.

Babarit, A. and Delhommeau, G. (2015). "Theoretical and numerical aspects of the open source BEM solver NEMOH". In: *11th European Wave and Tidal Energy Conference, Nantes, France*.

– (Mar. 2019). *NEMOH*. URL: https://lheea.ec-nantes.fr/logiciels-et-brevets/nemoh-presentation-192863.kjsp?RH=1489859622433.

Babarit, A., Hals, J., Muliawan, M. J., et al. (2012). "Numerical benchmarking study of a selection of wave energy converters". In: *Renewable Energy* 41.Supplement C. ISSN: 0960-1481. URL: http://www.sciencedirect.com/science/article/pii/S0960148111005672.

Black, C. (2014). "Analysis of waves in the near-field of wave energy converter arrays through image processing". MA thesis. Oregon State University.

Budar, K. and Falnes, J. (Aug. 1975). "A resonant point absorber of ocean-wave power". In: *Nature* 256.

Butler, B. P. and Thomas, G. P. (1993). "The diffraction of water waves by an array of circular cylinders in a channel". In: *Ocean Engineering* 20.3, pp. 295–311. ISSN: 0029-8018. URL: http://www.sciencedirect.com/science/article/pii/002980189390026E.

Campbell, A. J. (2014). "Stereo imaging techniques for three-dimensional surface wave measurement: applications and improvements". MA thesis. University of Wisconsin-madison.

Carnegie Clean Energy (2015). *3 CETO 5 Units after completion of operations*. [Online; accessed October 2018]. URL: https://www.carnegiece.com/press/media-kit/.

Chakrabarti, S. K. (1987). *Hydrodynamics of offshore structures*. WIT ress. ISBN: 0-905451-66-X.

Chatzigiannakou, M. A., Dolguntseva, I., and Leijon, M. (2017). "Offshore deployments of wave energy converters by seabased industry AB". In: *Journal of Marine Science and Engineering* 5.2, p. 15.

Clément, A. and Babarit, A. (2012). "Discrete control of resonant wave energy devices". In: *Philosophical Transactions of the Royal Society A: Mathematical, Physical and Engineering Sciences* 370.1959, pp. 288–314.

Clément, A., Winship, B., Fabregas-Flavia, F., and Meunier, P.-E. (2016). "Optimal scaling of a generic point absorber WEC in a range of production sites". In: *3rd Asian Wave and Tidal Energy Conference, Singapore, Singapore*.

Contardo, S., Hoeke, R., Hemer, M., et al. (2018). "In situ observations and simulations of coastal wave field transformation by wave energy converters." In: *Coastal Engineering* 140. ISSN: 0378-3839. URL: http://www.sciencedirect.com/science/article/pii/S0378383917304623.

Dalrymple, R. A., Seo, S. N., and Martin, P. A. (1989). "Water Wave Scattering by Rows of Circular Cylinders". In: *21st International Conference on Coastal Engineering*. DOI: 10.1061/9780872626874.165. eprint: https://ascelibrary.org/doi/pdf/10.1061/9780872626874.165. URL: https://ascelibrary.org/doi/abs/10.1061/9780872626874.165.

de Graff, K. (Dec. 2013). "The bubble dynamics and pressure field generated by a seismic airgun". PhD thesis. University of Tasmania. URL: https://eprints.utas.edu.au/18237/.

Falnes, J. and Kurniawan, A. (2015). "Fundamental formulae for wave-energy conversion". In: *Royal Society Open Science* 2.3. DOI: 10.1098/rsos.140305. eprint: http://rsos.royalsocietypublishing.org/content/2/3/140305.full.pdf. URL: http://rsos.royalsocietypublishing.org/content/2/3/140305.

Fievez, J. and Sawyer, T. (2015). "Lessons learned from building and operating a drid connected wave energy plant". In: *11th European Wave and Tidal Energy Conference, Nantes, France*.

Fleming, A. and Manasseh, R. (2017). "Experimental observation of surface currents produced by WEC radiation and diffraction". In: *12th European Wave and Tidal Energy Conference, Cork, Ireland*.

Fleming, A., Winship, B., and Macfarlane, G. (2018). "Application of photogrammetry for spatial free surface elevation and velocity measurement in wave flumes". In: *Proceedings of the Institution of Mechanical Engineers, Part M: Journal of Engineering for the Maritime Environment*. DOI: 10.1177/1475090218797785. URL: https://doi.org/10.1177/1475090218797785.

Folley, M. and Forehand, D. (2016). "Conventional Multiple Degree-of-Freedom Array Models". In: *Numerical Modelling of Wave Energy Converters*. Ed. by M. Folley. Academic Press. Chap. 8, pp. 151–164. ISBN: 978-0-12-803210-7. DOI: http://dx.doi.org/10.1016/B978-0-12-803210-7.00008-6. URL: http://www.sciencedirect.com/science/article/pii/B9780128032107000086.

Folley, M., Alves, M., Causon, D., et al. (2016). *Numerical Modelling of Wave Energy Converters: State-of-the-Art Techniques for Single Devices and Arrays*. Ed. by M. Folley. Academic Press. ISBN: 978-0-12-803210-7. URL: https://www.sciencedirect.com/science/article/pii/B9780128032107099953.

Folley, M., Babarit, A., Child, B., et al. (2012). "A review of numerical modelling of wave energy converter arrays". In: *Proceedings of the 31st International Conference on Offshore Mechanics & Arctic Engineering, Rio de Janeiro, Brazil*, pp. 10–15. ISBN: 978-0-7918-4494-6. DOI: 10.1115/OMAE2012-83807. URL: http://proceedings.asmedigitalcollection.asme.org/proceeding.aspx?articleid=1733166.

Gallego Bonet, G. (2011). "Variational image processing algorithms for the stereoscopic space-time reconstruction of water waves". PhD thesis. Georgia Institute of Technology. URL: http://hdl.handle.net/1853/39480.

Garcia-Rosa, P. B., Bacelli, G., and Ringwood, J. V. (2015). "Control-Informed optimal array layout for wave farms". In: *IEEE Transactions on Sustainable Energy*.

Gaurier, B., Ordonez-Sanchez, S., Germain, G., et al. (2018). *MaRINET2 Tidal "Round Robin" dataset: comparisons between towing and circulating tanks test results for a tidal energy converter submitted to wave and current interactions*. DOI: 10.17882/58265. URL: https://www.seanoe.org/data/00471/58265/.

Greaves, D. and Iglesias, G. (2018). *Wave and tidal energy*. Ed. by D. Greaves and G. Iglesias. Hoboken, NJ: Wiley. URL: https://onlinelibrary.wiley.com/doi/book/10.1002/9781119014492.

Haller, M. C., Porter, A., Lenee-Bluhm, P., et al. (2011). "Laboratory observation of waves in the vicinity of WEC-arrays". In: *9th European Wave and Tidal Energy Conference, Southampton, UK*.

Hals, J., Falnes, J., and Moan, T. (2011). "A comparison of selected strategies for adaptive control of wave energy converters". In: *Journal of Offshore Mechanics and Arctic Engineering* 133.3, p. 031101.

Hemer, M., Pitman, T., McInnes, K., and Rosebrock, U. (2017). *The Australian wave energy atlas project overview and final report.* Research rep. Australia: CSIRO Ocean and Atmosphere, Australia. URL: https://www.csiro.au/en/Research/OandA.

Hughes, S. A. (1993). "Laboratory wave reflection analysis using co-located gages". In: *Coastal Engineering* 20.3-4, pp. 223–247.

ITTC (Sept. 2017a). *Recommended procedures and duidlines, seakeeping experiments, 7.5-02-07-02.1, revision 06*. URL: https://www.ittc.info/media/8101/75-02-07-021.pdf.

– (Sept. 2017b). *Recommended procedures and fuidlines, uncertainty analysis for a wave energy converter, 7.5-02-07-03.12, revision 00*. URL: https://www.ittc.info/media/8135/75-02-07-0312.pdf.

Jung, T.-H., Lee, S. O., and Cho, Y.-S. (2009). "Decomposition of incident and reflected waves using a single moving wave gauge". In: *Journal of Coastal Research*, pp. 704–710.

LaVision (Nov. 2016). *DaVis - Surface Flow*. 8.4. LaVision GmbH. Anna-Vandenhoeck-Ring 19, D-37081 Göttingen.

Lazarow, N., Miller, M. L., and Blackwell, B. (2007). "Dropping in: A case study approach to understanding the socio-economic impact of recreational surfing and its value to the coastal economy". In: *Shore and Beach* 75.4, pp. 21–31. ISSN: 0037-4237.

Le Méhauteé, B. (1976). *An introduction to hydrodynamics and water waves*. Springer-Verlag. ISBN: 0-387-07232-2.

LinMot (2016a). *Technology Function Force Control*. URL: https://shop.linmot.com/.

– (2016b). *User Manual Motion Control SW*. URL: https://shop.linmot.com/.

MaRINET2 (Apr. 2019). *MaRINET2 Objectives*. URL: http://www.marinet2.eu/about/objectives/.

McInnes, K., Hemer, M., O'Grady, J., Hoeke, R., and Contardo, S. (Feb. 2018). *Wave energy deployments physical impact guidelines*. Tech. rep. CSIRO. URL: https://publications.csiro.au/rpr/download?pid=csiro:EP181064&dsid=DS3.

McIver, P. and Evans, D. V. (Mar. 1984). "The occurrence of negative added mass in free-surface problems involving submerged oscillating bodies". In: *Journal of Engineering Mathematics* 18.1, pp. 7–22. ISSN: 1573-2703. DOI: 10.1007/BF00042895. URL: https://doi.org/10.1007/BF00042895.

McKee, R., Elsäßer, B., and Schmitt, P. (2018). "Obtaining reflection coefficients from a single point velocity measurement". In: *Journal of Marine Science and Engineering* 6.2, pp. 1–11.

McNatt, J. C., Venugopal, V., Forehand, D., and Payne, G. S. (2015). "Experimental analysis of cylindrical wave fields". In: *11th European Wave and Tidal Energy Conference, Nantes, France*.

McNatt, J. C. (2016). "Cylindrical linear water waves and their application to the wave-body problem". PhD thesis. The University of Edinburgh. URL: http://hdl.handle.net/1842/20378.

Mercadé Ruiz, P., Ferri, F., and Kofoed, J. P. (2017). "Experimental validation of a wave energy converter array hydrodynamics tool". In: *Sustainability* 9.1, p. 115.

Nader, J.-R. (2013). "Interaction of ocean waves with oscillating water column wave energy convertors". Thesis. University of Wollongong. URL: http://ro.uow.edu.au/theses/4183.

Nader, J.-R., Fleming, A., Macfarlane, G., Penesis, I., and Manasseh, R. (Dec. 2017). "Novel experimental modelling of the hydrodynamic interactions of arrays of wave energy converters". In: *International Journal of Marine Energy* 20, pp. 109–124. ISSN: 2214-1669. URL: http://www.sciencedirect.com/science/article/pii/S2214166917300917.

O'Boyle, L., Elsäßer, B., and Whittaker, T. (2017). "Experimental measurement of wave field variations around wave energy vonverter arrays". In: *Sustainability* 9.1, p. 70. ISSN: 2071-1050. DOI: doi:10.3390/su9010070. URL: http://www.mdpi.com/2071-1050/9/1/70.

Ogilvie, T. F. (1963). "First- and second-order forces on a cylinder submerged under a free surface". In: *Journal of Fluid Mechanics* 16.3, pp. 451–472. DOI: 10.1017/S0022112063000896.

Orszaghova, J., Wolgamot, H., Eatock Taylor, R., et al. (2017). "Simplified dynamics of a moored submerged buoy". In: *The 32nd International Workshop on Water Waves and Floating Bodies. Dalian, China*.

Orszaghova, J., Wolgamot, H., Draper, S., et al. (2018). "Transverse motion instability of a submerged moored buoy". In: *Proceedings of The Royal Society A (Pre-print)*.

Payne, G. (2008). "Guidance for the experimental tank testing of wave energy converters". In: *SuperGen Marine, Dec.*

Payne, G., Taylor, J., and Ingram, D. (2009). "Best practice guidelines for tank testing of wave energy converters". In: *The Journal of Ocean Technology*.

Penalba Retes, M., Giorgi, G., and Ringwood, J. (2015). "A Review of Non-Linear Approaches for Wave Energy Converter Modelling". In: *11th European Wave and Tidal Energy Conference, Nantes, France*. URL: http://mural.maynoothuniversity.ie/6678/.

Porter, A. K. (2012). "Laboratory observations and numerical modeling of the effects of an array of wave energy converters". MA thesis. Oregon State University.

Qualisys AB (2017). *Qualisys Track Manager*. [Online; accessed October 2018]. URL: http://content.qualisys.com/2017/03/Getting-started.pdf.

Rafiee, A. and Fievez, J. (2015). "Numerical Prediction of Extreme Loads on the CETO Wave Energy Converter". In: *11th European Wave and Tidal Energy Conference, Nantes, France*.

Rijnsdorp, D. P., Hansen, J., and Lowe, R. (2017). "Improving predictions of the coastal impacts of wave farms using a phase-resolving wave model". In: *12th European Wave and Tidal Energy Conference, Cork, Ireland*.

Ringwood, J. V., Bacelli, G., and Fusco, F. (Oct. 2014). "Energy-Maximizing control of wave-energy converters: The development of control system technology to optimize their operation". In: *IEEE Control Systems Magazine* 34.5, pp. 30–55. ISSN: 1066-033X. DOI: 10.1109/MCS.2014.2333253.

Ringwood, J. V., Ferri, F., Ruehl, K. M., et al. (2017). "A competition for WEC control systems". In: *12th European Wave and Tidal Energy Conference, Cork, Ireland*.

Robertson, A. N., Bachynski, E. E., Gueydon, S., et al. (2018). "Assessment of Experimental Uncertainty for a Floating Wind Semisubmersible Under Hydrodynamic Loading". In: *ASME 2018 37th International Conference on Ocean, Offshore and Arctic Engineering*. American Society of Mechanical Engineers, V010T09A076–V010T09A076.

Spring, B. W. and Monkmeyer, P. L. (1975). "Interaction of plane waves with a row of cylinders". In: *Civil Engineering in the Oceans III:* ASCE, pp. 979–998.

Stratigaki, V. (2014). "Experimental study and numerical modelling of intra-array interactions and extra-array effects of wave energy converter arrays". PhD thesis. Ghent University.

Suh, K. D., Park, W. S., and Park, B. S. (2001). "Separation of incident and reflected waves in wave–current flumes". In: *Coastal Engineering* 43.3-4, pp. 149–159.

Thomas, G. P. (1991). "The diffraction of water waves by a circular cylinder in a channel". In: *Ocean Engineering* 18.1, pp. 17–44. ISSN: 0029-8018. URL: http://www.sciencedirect.com/science/article/pii/002980189190032L.

Turney, D. E., Anderer, A., and Banerjee, S. (2009). "A method for three-dimensional interfacial particle image velocimetry (3D-IPIV) of an air–water interface". In: *Measurement Science and Technology* 20.4. URL: http://stacks.iop.org/0957-0233/20/i=4/a=045403.

Wan, L., Gao, Z., Moan, T., and Lugni, C. (2016). "Comparative experimental study of the survivability of a combined wind and wave energy converter in two testing facilities". In: *Ocean Engineering* 111, pp. 82–94. ISSN: 0029-8018. URL: http://www.sciencedirect.com/science/article/pii/S0029801815005922.

Warner, J. C., Armstrong, B., He, R., and Zambon, J. B. (2010). "Development of a coupled ocean–atmosphere–wave–sediment transport (COAWST) modeling system". In: *Ocean Modelling* 35.3, pp. 230–244. ISSN: 1463-5003. URL: http://www.sciencedirect.com/science/article/pii/S1463500310001113.

Winship, B., Fleming, A., Penesis, I., Hemer, M., and Macfarlane, G. (2018). "Preliminary investigation on the use of tank wall reflections to model WEC array effects". In: *Ocean*

Engineering 164, pp. 388–401. ISSN: 0029-8018. URL: `http://www.sciencedirect.com/science/article/pii/S0029801818310576`.

Wolgamot, H. and Fitzgerald, C. (2015). "Nonlinear hydrodynamic and real fluid effects on wave energy converters". In: *Proceedings of the Institution of Mechanical Engineers, Part A: Journal of Power and Energy* 229.7, pp. 772–794.

Zurcher, K. (2015). "Waterjet testing techniques for powering performance estimation using a single catamaran demihull". PhD thesis. University of Tasmania.

Appendix A

Stereo-Videogrammetry Assessment Supplementary

Table A.1: Stereo-Videogrammetry calibration results for cylinder study.

RMS of Fit (pixels)			0.69495	
Camera Configuration		Focal length (mm)	6.31642	6.41498
		Pixel Size (mm)	0.0055	
		Pixel aspect ratio	1	
Calibration Plate Position (z=49 mm)	Translation	Tx (mm)	60.7608	34.6646
		Ty (mm)	926.428	687.849
		Tz (mm)	2579.59	2101.88
	Rotation	Rx (deg)	17.5023	-8.66808
		Ry (deg)	0.5158	0.591019
		Rz (deg)	0.506846	0.17042
Camera Scale	Origin	x_0 (px)	541.101	
		y_0 (px)	300.063	
		Scale Factor (px/mm)	0.354405	
Image Distortion	Principal Point	x_p (px)	668.086	683.143
		y_p (px)	570.712	598.61
	Radial Distortion	1^{st} order	10.1455	15.5954
		2^{nd} order	7.64925	4.92852

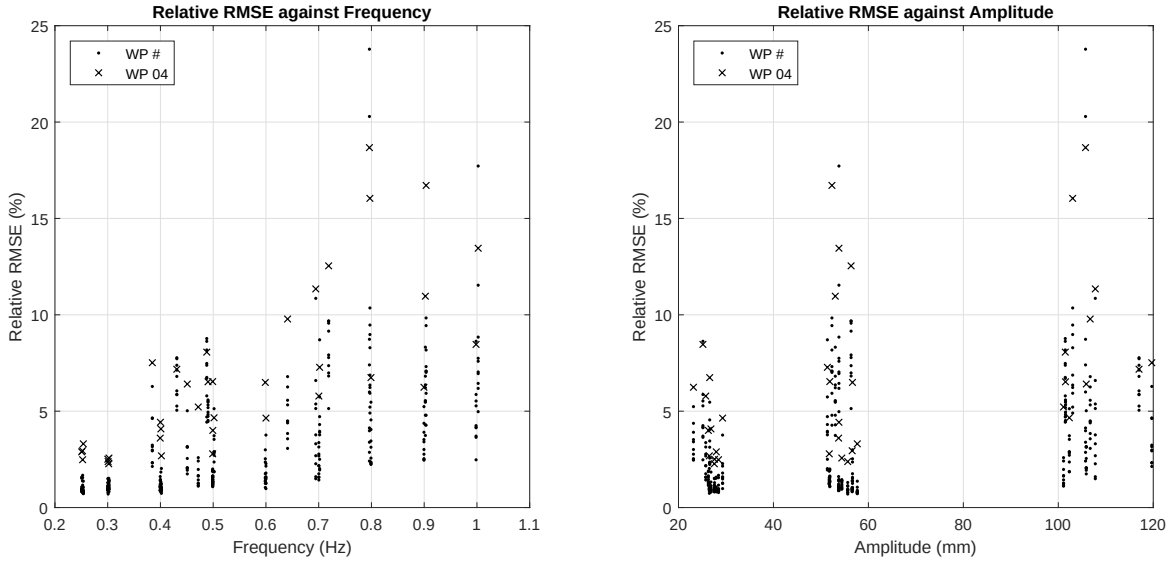

Figure A.1: Relative RMSE of stereo-videogrammetry measurements against incident wave frequency (Left) and amplitude (Right).

Appendix B

Diffraction by a Submerged WEC in a Channel Supplementary Material

B.1 Full Scale Specifications

These specifications have been removed for copyright or proprietary reasons. They consist of three pages:
PWEP GA_ single unit, Assembly PWEP GA-array plant detail,
PWEP GA-foundation locations,
BA principle dimensions

B.2 *NEMOH* Submersion Depth Dependence Study

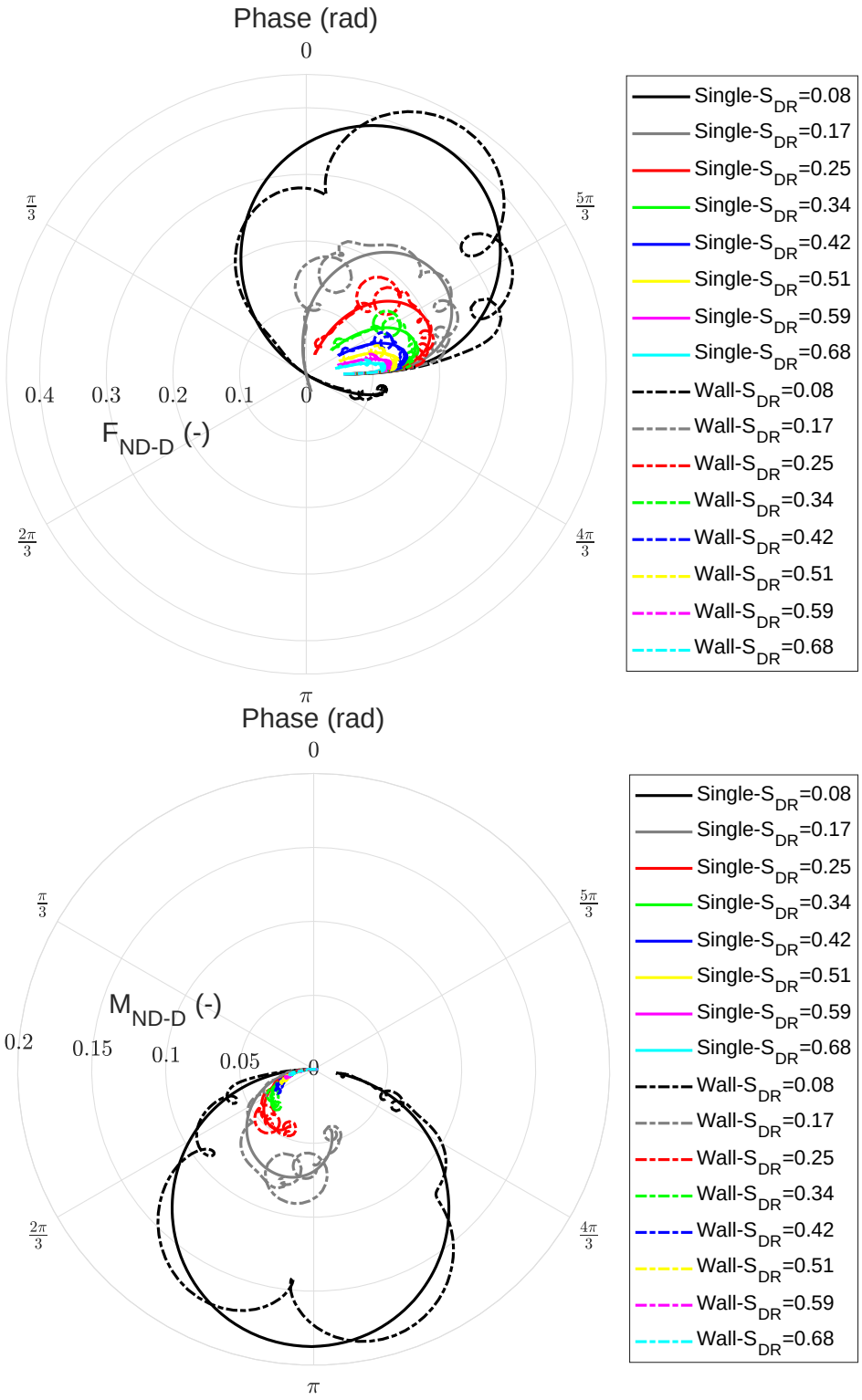

Figure B.1: Study into effect of BA submersion depth with *NEMOH*. (Top) is Surge excitation force. (Bottom) Pitch excitation moment.

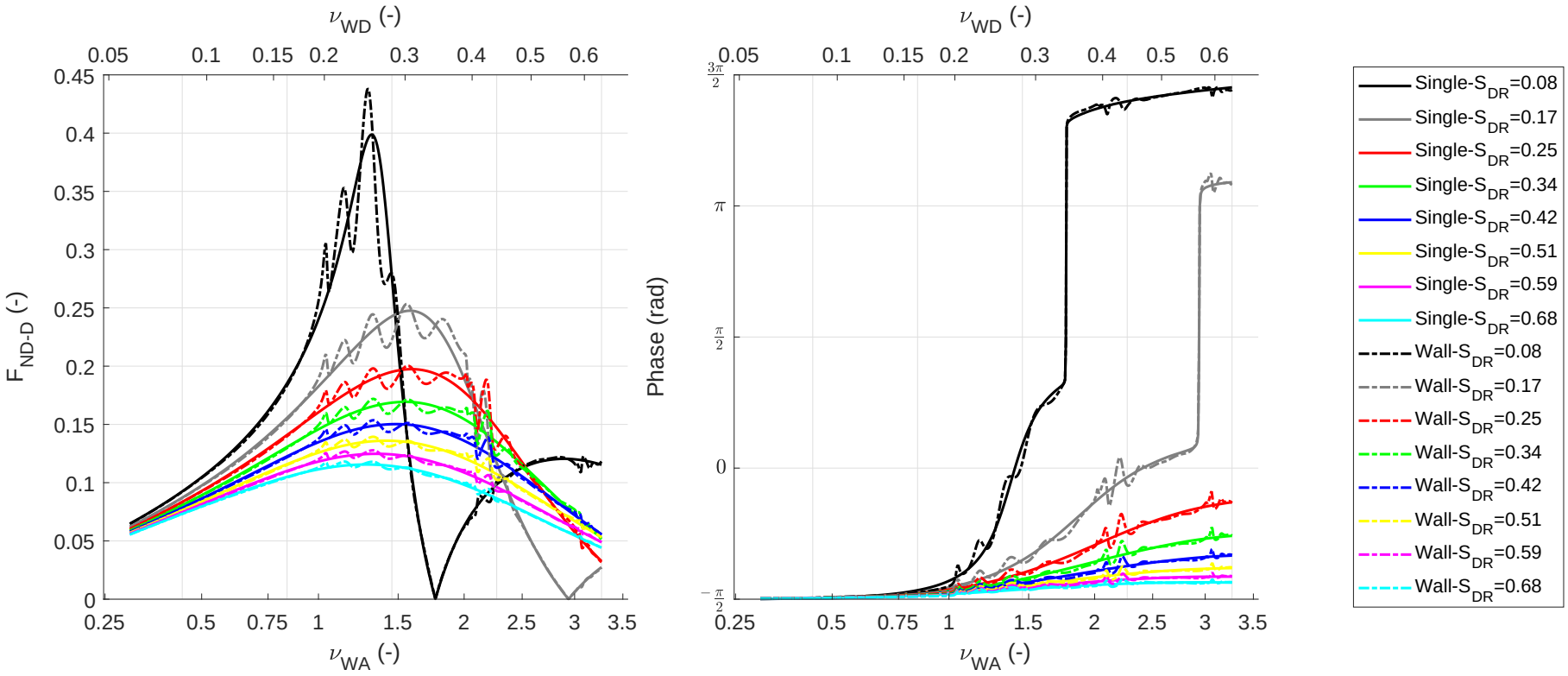

Figure B.2: Study into effect of BA submersion depth with *NEMOH* on surge excitation force. Amplitude and phase are presented. Incident wave is expressed by the device and array non-dimensional linear wave numbers on the top and bottom x-axes respectively.

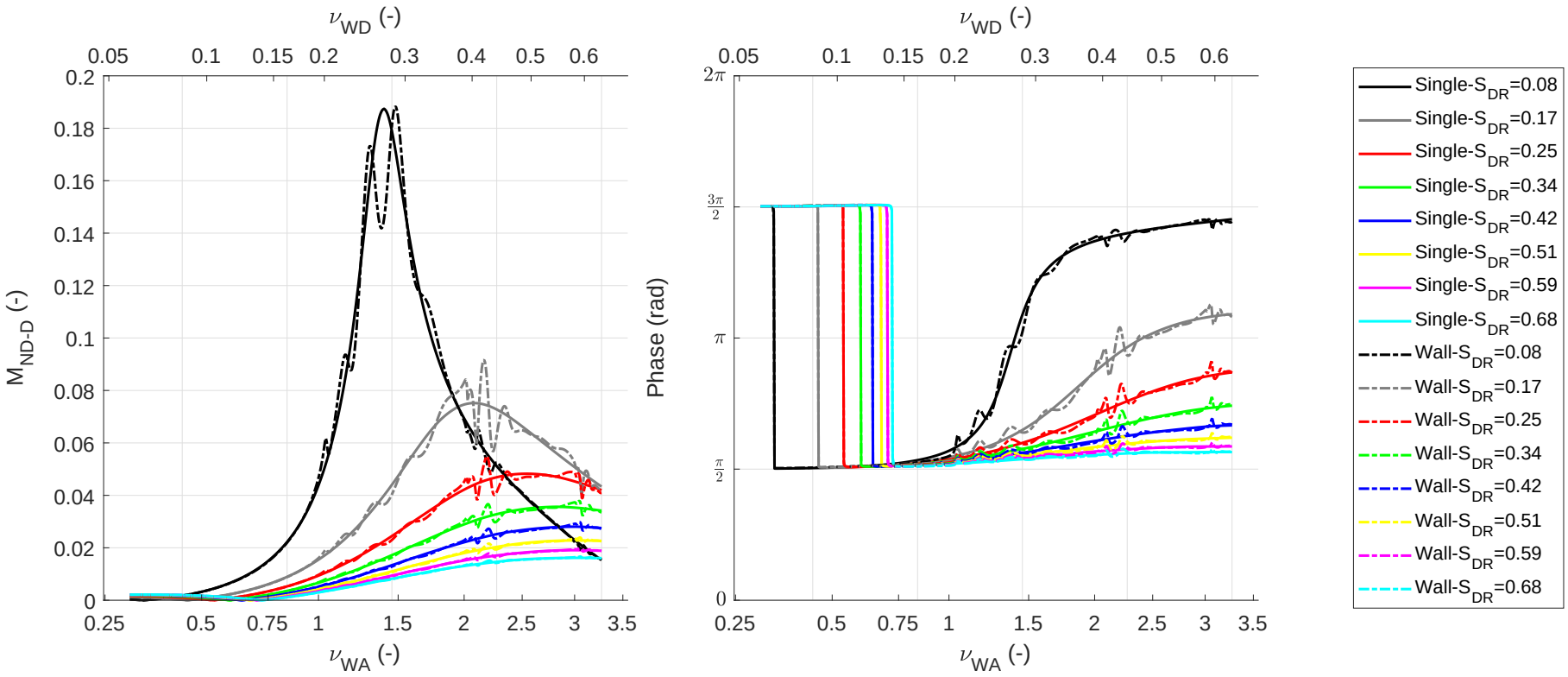

Figure B.3: Study into effect of BA submersion depth with *NEMOH* on pitch excitation moment. Amplitude and phase are presented. Incident wave is expressed by the device and array non-dimensional linear wave numbers on the top and bottom x-axes respectively.

B.3 Stereo-Videogrammetry

Table B.1: Stereo-Videogrammetry calibration coefficients for Chapters 4,5 and 6.

			Camera			
			A-1	A-2	B-1	B-2
RMS of fit (px)			0.513044		0.486519	
Camera Configuration		Focal length (mm)	9.15496	9.21909	9.13629	9.09819
		Pixel size (mm)	0.0055			
		Pixel aspect ratio	1			
Calibration Plate Position (z = 49 mm)	Translation	Tx (mm)	96.0625	-99.1526	66.6834	-64.7331
		Ty (mm)	-1079.31	1032.78	657.902	-894.021
		Tz (mm)	2893.55	2029.98	2154.69	2848.63
	Rotation	Rx (deg)	1.85452	3.03015	2.79887	248699
		Ry (deg)	22.275	-31.5447	22.7572	-240077
		Rz (deg)	91.3037	-91.02	91.8024	-89.068
Camera Scale	Origin	x_0 (px)	165.116		1675.05	
		y_0 (px)	1451.54		1713.45	
		Scale factor (px/mm)	0.62113		0.723707	
Image Distortion	Principal Point	x_p (px)	1034.23	1030.38	1045.25	1049.86
		y_p (px)	1008.53	106.23	1021.58	1049.06
	Radial Distortion	1^{st} order	10.6511	9.28881	9.93441	8.72281
		2^{nd} order	-0.694002	-0.28447	-0.428892	0.0121398

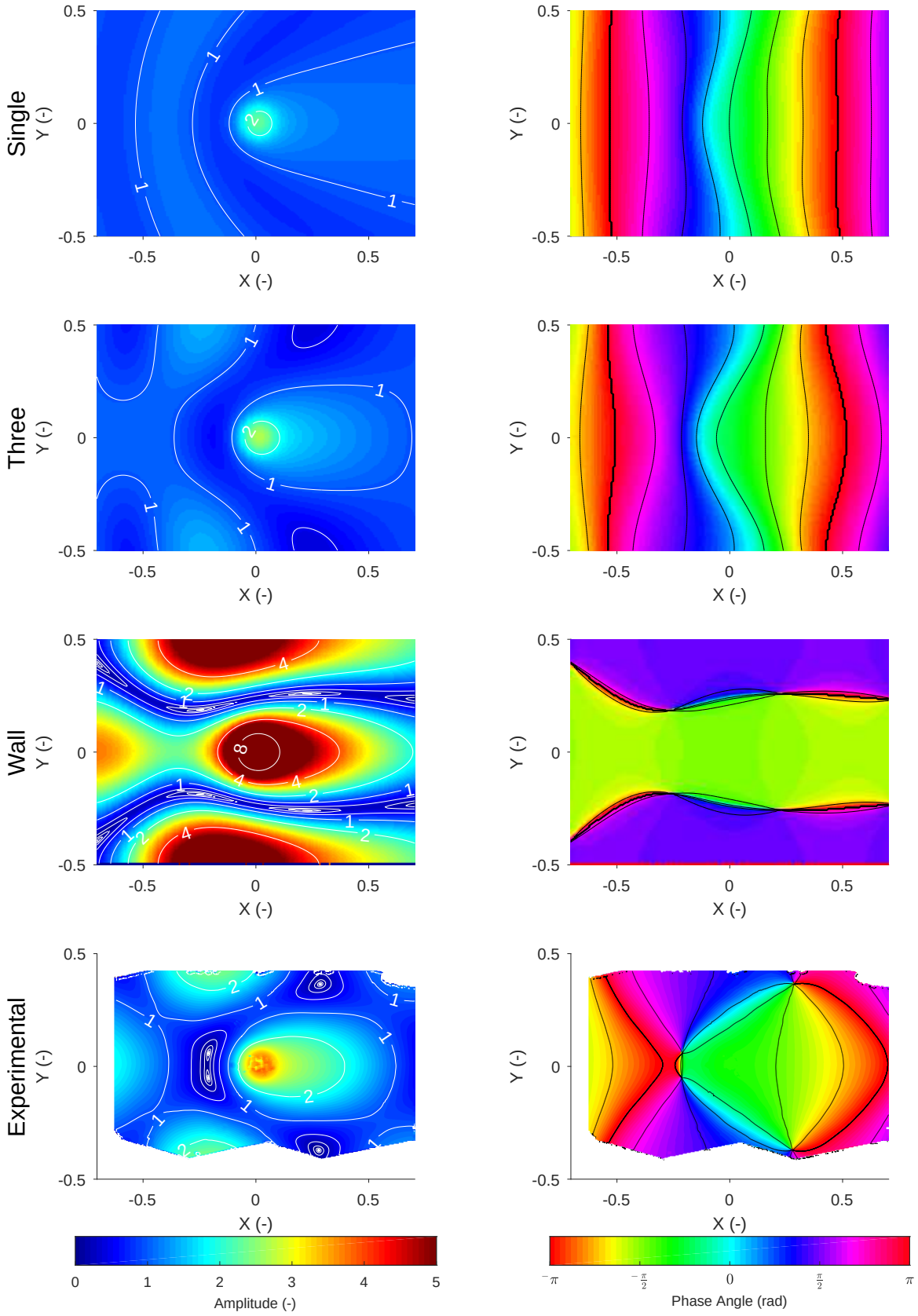

Figure B.4: Frequency domain free surface for condition $\nu_{WA} \approx 0.97$ ($S_{DR} \approx 0.34$), this represents resonant array effects. Left column is amplitude, right column is phase. Top three rows are numerical predictions for the single, three and wall conditions; the bottom row is experimental results.

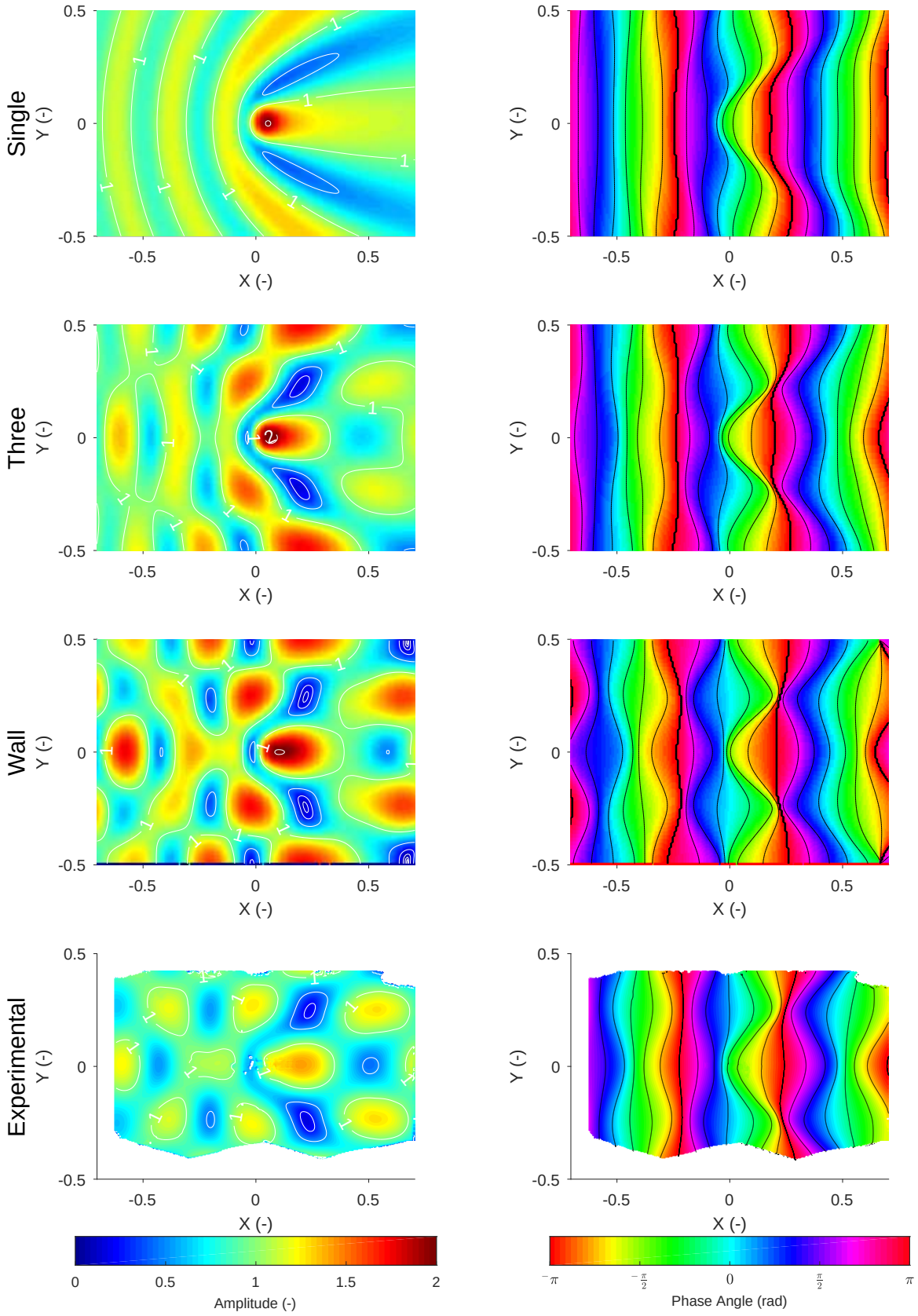

Figure B.5: Frequency domain free surface for condition $\nu_{WA} \approx 2.05$ ($S_{DR} \approx 0.34$), this represents positive array effects. Left column is amplitude, right column is phase. Top three rows are numerical predictions for the single, three and wall conditions; the bottom row is experimental results.

B.4 Transient Array Effects

Given the reflections are expected from this experimental campaign the assumption of steady-state is not entirely rational. As such a transient study with wavelet analysis has been completed; the wavelet analysis technique employed is based upon work completed in de Graff (2013). The concept of wavelet anyalsis is to explore how the change in spectrum as a function of time. Figures B.6-B.9 present the results for 0.5, 0.65, 0.7 and 0.95 Hz respectively all with a 25 mm incident wave amplitude; they share a format with five sub-plots. The top four plots present the heave excitation force, where the centre left surface is the wavelet with force shown against time and frequency. Top left is the time series of the excitation force and the primary reconstruction from the wavelet. The top right plot shows the plane of the primary frequency from the wavelet surface, so indicates the variation in the excitation force amplitude through time. The centre right plot shows the steady state measurements for this run, with an FFT and the average of the wavelet profile. The bottom most plot is a summary of the surge, heave and pitch excitation loads and four of the wave gauges, WP_{IN}, WP_{-1}, WP_0 and WP_{+1}. In this bottom plot the amplitudes are normalised by the maximum measurement in the data set; this is done as it is the variation through time that is interesting and not the absolute amplitude. The instance at which the reflected wave arrives back at the BA is indicated in dotted lines by phase velocity (blue) and group velocity (green) from the wavemaker; the dashed lines represent two wave periods preceeding where the wavelet amplitude is not effected by the reflections. The black dotted line indicates the end of the experimental period considered.

In Figure B.6 very little variation is evident in the primary frequency response for all measurements with the exception of the pitch moment (M_{YY}), which has some slight variation. This variation in pitch moment can largely be discounted however as the value is very small, as indicated by Figures 4.12 and 4.14.

Figure B.7 is the condition where $\nu_{WA} \approx 0.95$, the major array interaction indicated in the earlier numerical study. This run shows large variations in all measurements with the exception of surge force. The variation in the localised net wave, the combination of scattered and incident wave, clearly changes subjective on the location. With WP_{-1} and WP_0 indicating a steady increase as time progresses; this trend is very similar to the heave excitation force. While WP_{+1} having a local minima at $t \approx 20s$. The change in trend at $t \approx 42s$ has been attributed to reflections from the wave paddle, these are not however first order reflections, that is to say the scattered wave from when the incident wave first interacts with the BA (which would arrive at $t \approx 39s$); the time suggests it is most likely a reflection from the scattered wave after the first order of interaction with the BA. For this experimental condition there was wave breaking, it was observed that as experimental period extended the degree

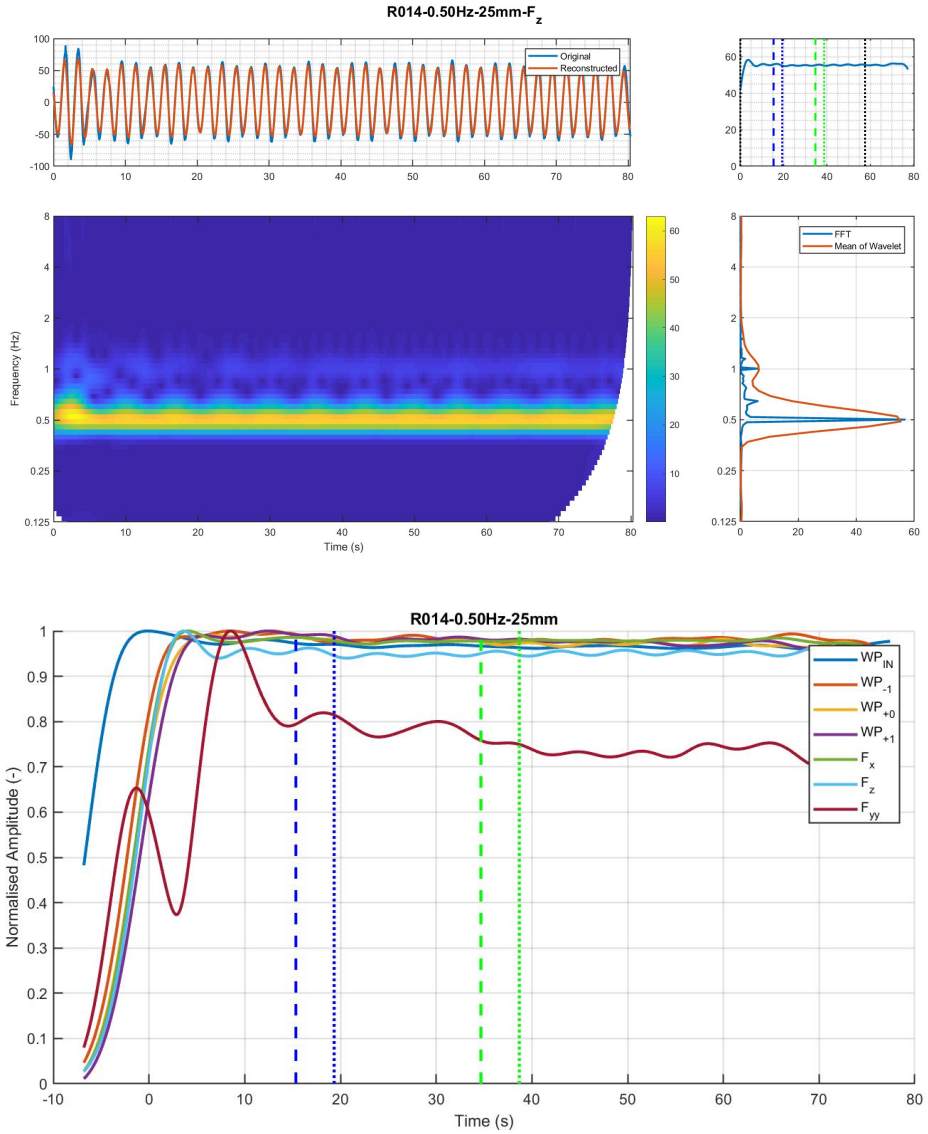

Figure B.6: Wavelet Study of Heave for incident wave of 25 mm amplitude and frequency 0.5 Hz ($\nu_{WA} \approx 0.61$). The bottom left surface is the wavelet with x-axis time, y-axis frequency and the intensity the force in newtons. The time series above that includes the original time series and a primary reconstruction. The bottom right plot as an FFT plot with frequency on y-axis and force on x-axis, it shows the FFT and the average spectrum from the wavelet. Finally the top right shows the amplitude of the 1st order as a function of time.

of breaking increased. The wave action was so extreme that the full mean submersion depth was displaced, such that the top of the BA was in contact with air. Recalling the submersion depth and wave amplitude were 100 mm and 25 mm respectively this indicates the scattered wave exceeded the incident wave amplitude by a factor of 3 (at least) in close proximity to the BA. The effects of this is represented in the wavelet surface for the heave force by the increasing amplitude of the higher frequency loads as time progresses. While one may expect that the increase of the primary frequency heave excitation force to increase linearly with time for the array resonance this is not evident for this frequency. This is likely a result of some of the energy degrading to the higher frequencies in the non-linear wave breaking and this not being the true perfect array resonance.

Figure B.8 shows a clear harmonic nature to the variation in amplitude of the different signals. Attempts have been made to predict this array harmonic frequency, which is suspected to be related to the phase progression of the diffracted wave against the incident wave. However the shoaling, which is discussed in Chapters 4-6 as part of the submergence depth studies, means prediction of the transverse wave velocity is challenging. Without an ability to predict this transverse wave velocity it is not possible to predict the cyclic nature of the array interaction.

Figure B.9 again shows effects of the transient nature. Considering the heave excitation force there are a sequence of dips and crests in the variations in the force; these variations seemingly coincide with the reflections from the wave maker. Considering the incident wave probe measurements, it can be observed that the amplitude is consistent for ≈ 20 s; then there is a large variation for the remainder of the period. This trend is related to the arrival of the initial wave, at ≈ -10 s, then a pure incident wave until the scattered wave arrives back from the BA , at ≈ 10 s. This highlights the importance of understanding all reflections which may be impacting measurements.

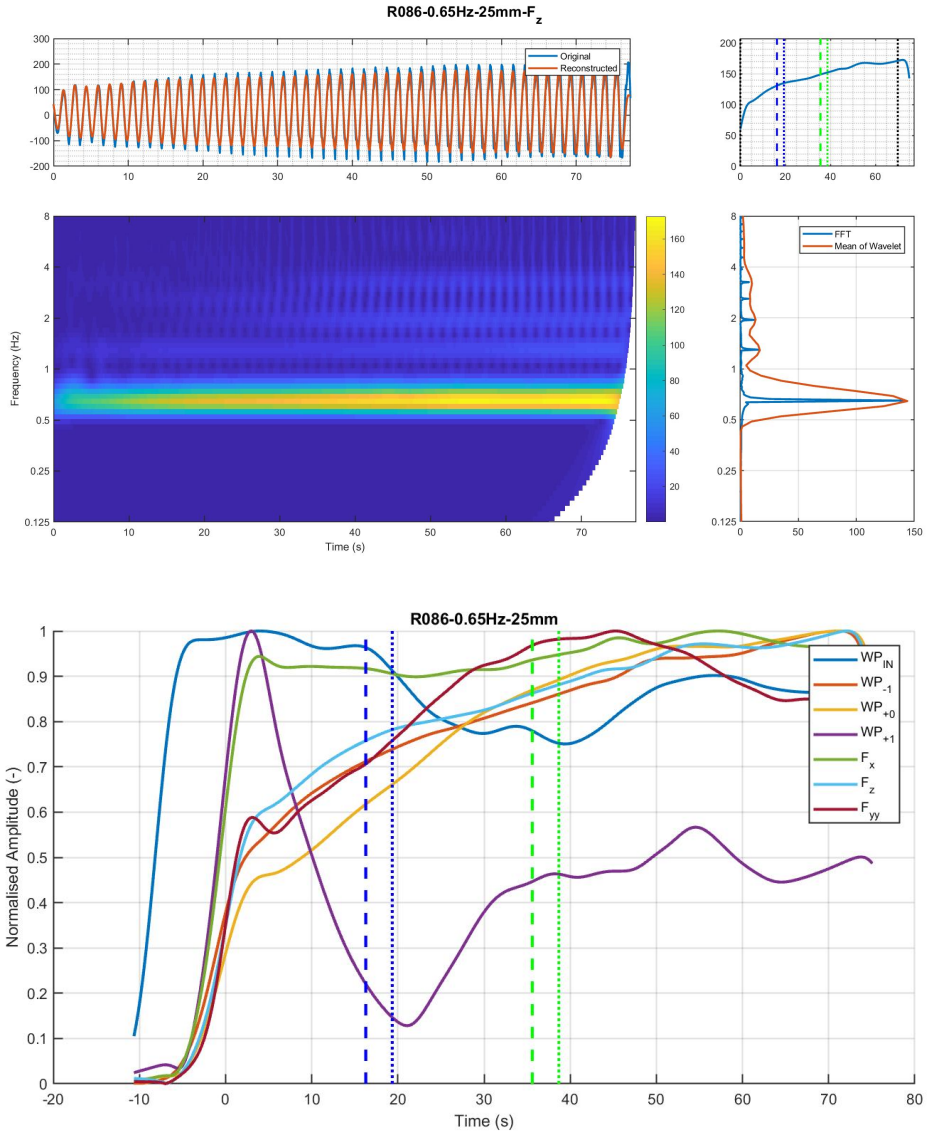

Figure B.7: Wavelet Study of Heave for incident wave of 25 mm amplitude and frequency 0.65 Hz ($\nu_{WA} \approx 1$). The bottom left surface is the wavelet with x-axis time, y-axis frequency and the intensity the force in newtons. The time series above that includes the original time series and a primary reconstruction. The bottom right plot as an FFT plot with frequency on y-axis and force on x-axis, it shows the FFT and the average spectrum from the wavelet. Finally the top right shows the amplitude of the 1st order as a function of time.

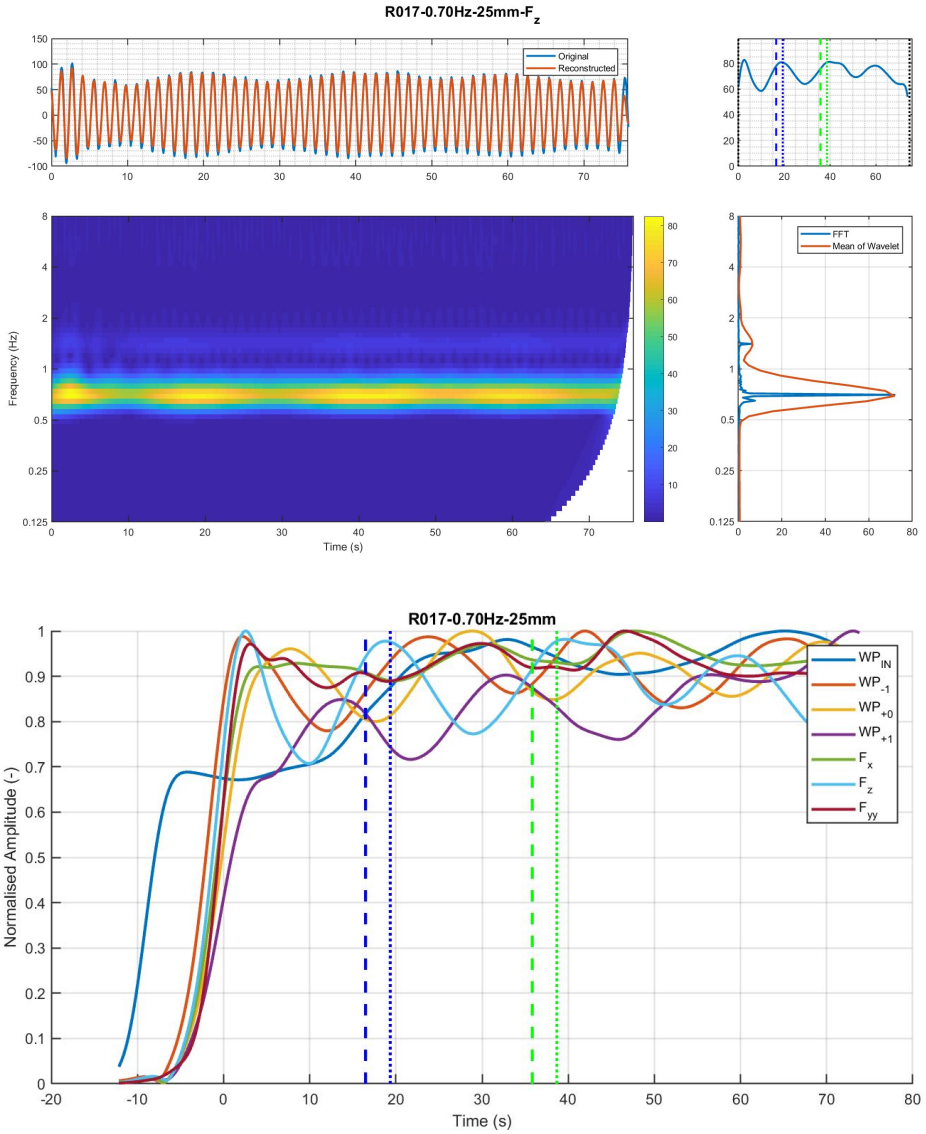

Figure B.8: Wavelet Study of Heave for incident wave of 25 mm amplitude and frequency 0.7 Hz ($\nu_{WA} \approx 1.1$). The bottom left surface is the wavelet with x-axis time, y-axis frequency and the intensity the force in newtons. The time series above that includes the original time series and a primary reconstruction. The bottom right plot as an FFT plot with frequency on y-axis and force on x-axis, it shows the FFT and the average spectrum from the wavelet. Finally the top right shows the amplitude of the 1st order as a function of time.

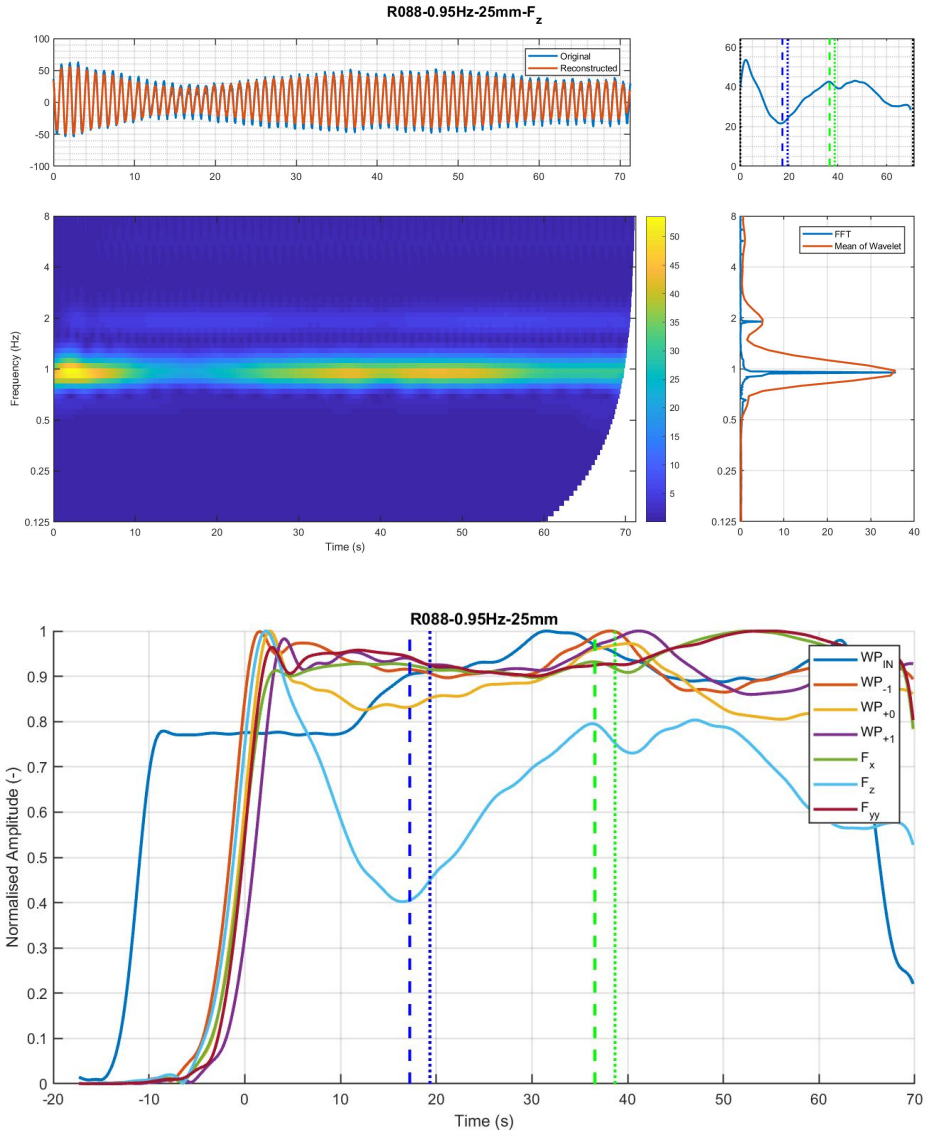

Figure B.9: Wavelet Study of Heave for incident wave of 25 mm amplitude and frequency 0.95 Hz ($\nu_{WA} \approx 2$). The bottom left surface is the wavelet with x-axis time, y-axis frequency and the intensity the force in newtons. The time series above that includes the original time series and a primary reconstruction. The bottom right plot as an FFT plot with frequency on y-axis and force on x-axis, it shows the FFT and the average spectrum from the wavelet. Finally the top right shows the amplitude of the 1st order as a function of time.

Appendix C

Heave Radiation by a Submerged WEC in a Channel Supplementary Material

C.1 Motion Control

The motion control system employed to drive the oscillation of the BA for radiation testing is a standard one included in the Motion Control software included with the linear motor system employed (LinMot 2016b). In order to determine relevant control system parameters a set of tests were performed including,

1. Constant force, spring compensation and zero position.
    - Measure force at several points through experimental range (with zero velocity).
    - Fit model which accounts for the three variables.
2. Friction force
    - Move the BA with a very low velocity (minimises hydrodynamic effects) through experimental range.
    - Fit model which includes all variables to this point.
3. Acceleration (mass) and damping
    - Essentially the coefficients that the experiments are attempting to determine.
    - Estimated with knowledge of physical mass (measured during ballasting) and numerical predictions of hydrodynamic coefficients.
4. Proportion and derivative control settings
    - Used default soft

As the system is controlling force by varying the current applied to the electromagnets, all specifications are relative to the Force Constant of the motor in units N/Amp.

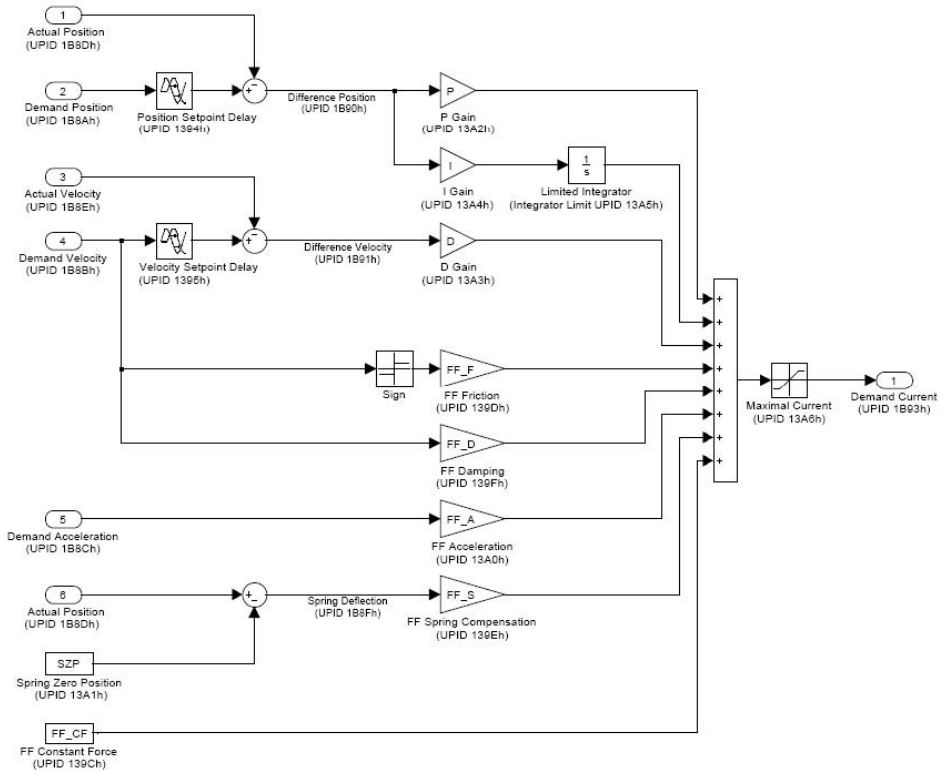

Figure C.1: Standard position control system included with linear motor (LinMot 2016b).

C.2 Additional Material

In Chapter 5 the radiation excitation force was considered, this includes the inertial forces associated with the oscillating body. Here an alternate presentation of the radiation impedance is made in terms of the added mass (A) and damping coefficient (B). To determine these coefficients the reciprocal of Eq 5.2 is applied; this results in,

$$\sum_{l} A_{i,j,k,l} = -\operatorname{Re}\left(\frac{F_{exR,i,j,k}}{a\omega^2} + I\right) \tag{C.1a}$$

$$\sum_{l} B_{i,j,k,l} = \operatorname{Re}\left(\frac{F_{exR,i,j,k}}{ia\omega}\right) \tag{C.1b}$$

Recalling $F_{exR,i,j,k}$ is the radiation excitation force (in phase with position), a is amplitude of motion and ω is angular frequency.

Figures C.2 and C.3 present the experimental comparison and depth dependence respectively. The coefficients are non-dimensionalised by,

$$\mu = \frac{A}{M} \tag{C.2a}$$

$$\lambda = \frac{B}{M\omega} \tag{C.2b}$$

$$M = \rho\pi D^3 \tag{C.2c}$$

Where μ is added mass, λ is damping, ρ is fluid density and D is critical device diameter.

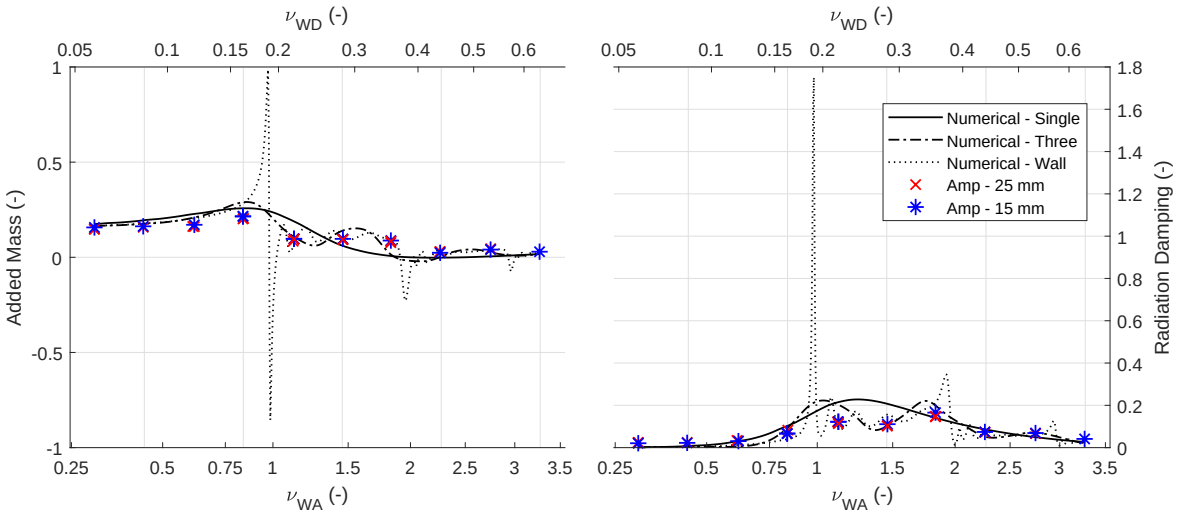

Figure C.2: First order harmonic radiation excitation force for Heave. Submersion depth of 0.115 m from experimental and numerical studies. Experimental data is differentiated by motion wave amplitude and the *NEMOH* modelling includes a single, three and infinite row studies. The coefficients are non-dimensional and have been normalised and the frequency of oscillation is expressed by the device and array non-dimensional linear wave numbers on the top and bottom x-axes respectively.

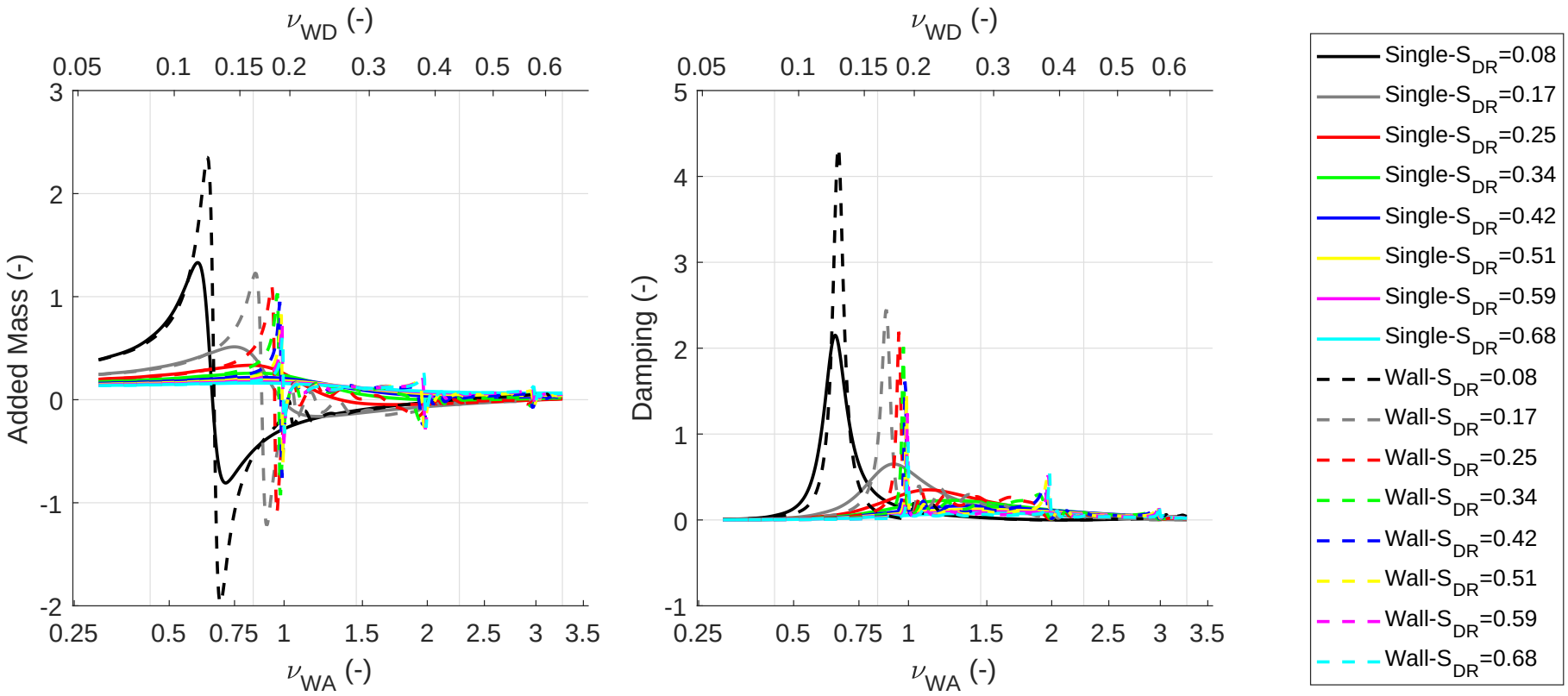

Figure C.3: Effect of submersion depth on array interactions study with *NEMOH*, non-dimensional added mass and damping coefficients are presented on the left and right respectively. The frequency of oscillation is expressed by the device and array non-dimensional linear wave numbers on the top and bottom x-axes respectively.

C.3 Transient Array Effects

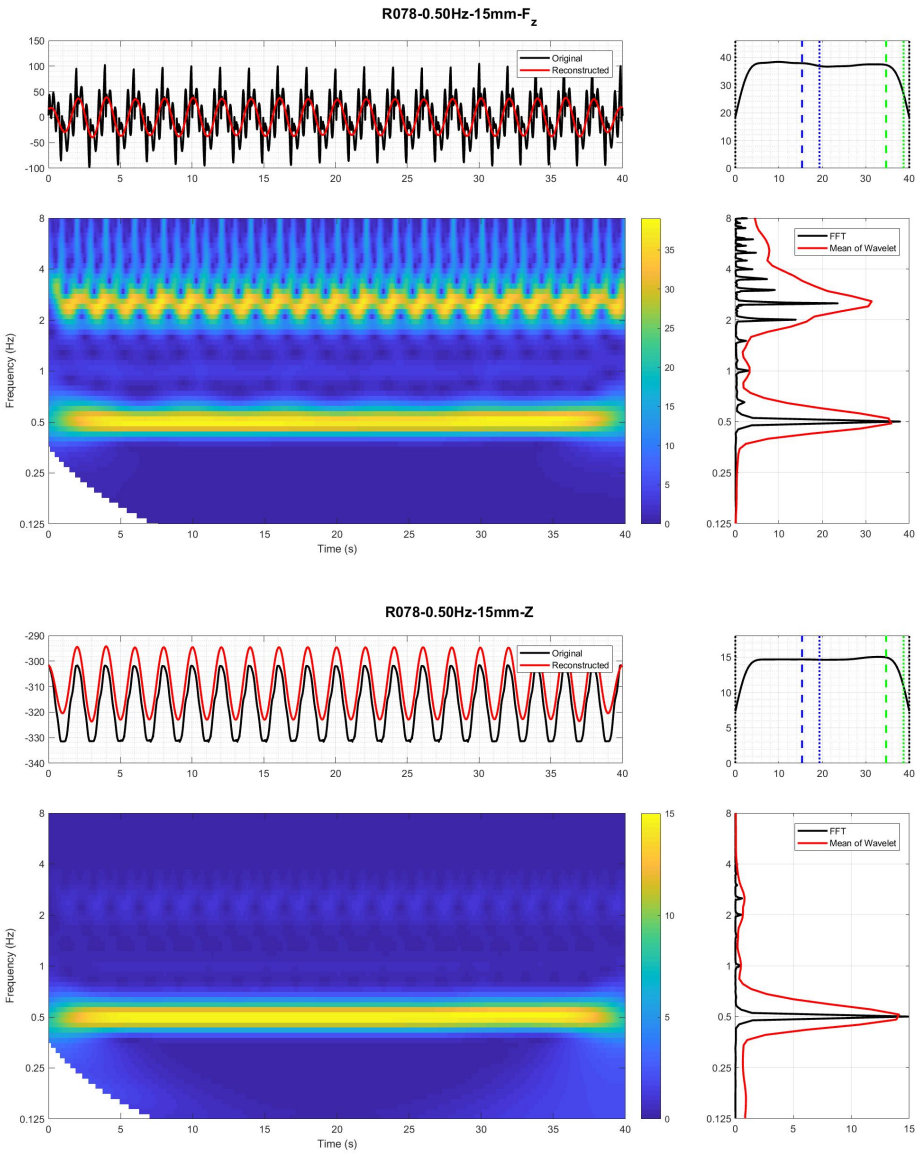

Figure C.4: Wavelet Study of Heave radiation with amplitude of motion 15 mm at 0.5 Hz ($\nu_{WA} \approx 0.61$). The two plots given are for heave excitation force (top) and heave motion (bottom); with four sub-plots in each. (Top left) Time series displaying original measurement and primary harmonic wavelet reconstruction. (Top right) Amplitude variation of the primary component, (bottom left) wavelet surface of the measuremen and (bottom right) FFT compared with average of wavelet.

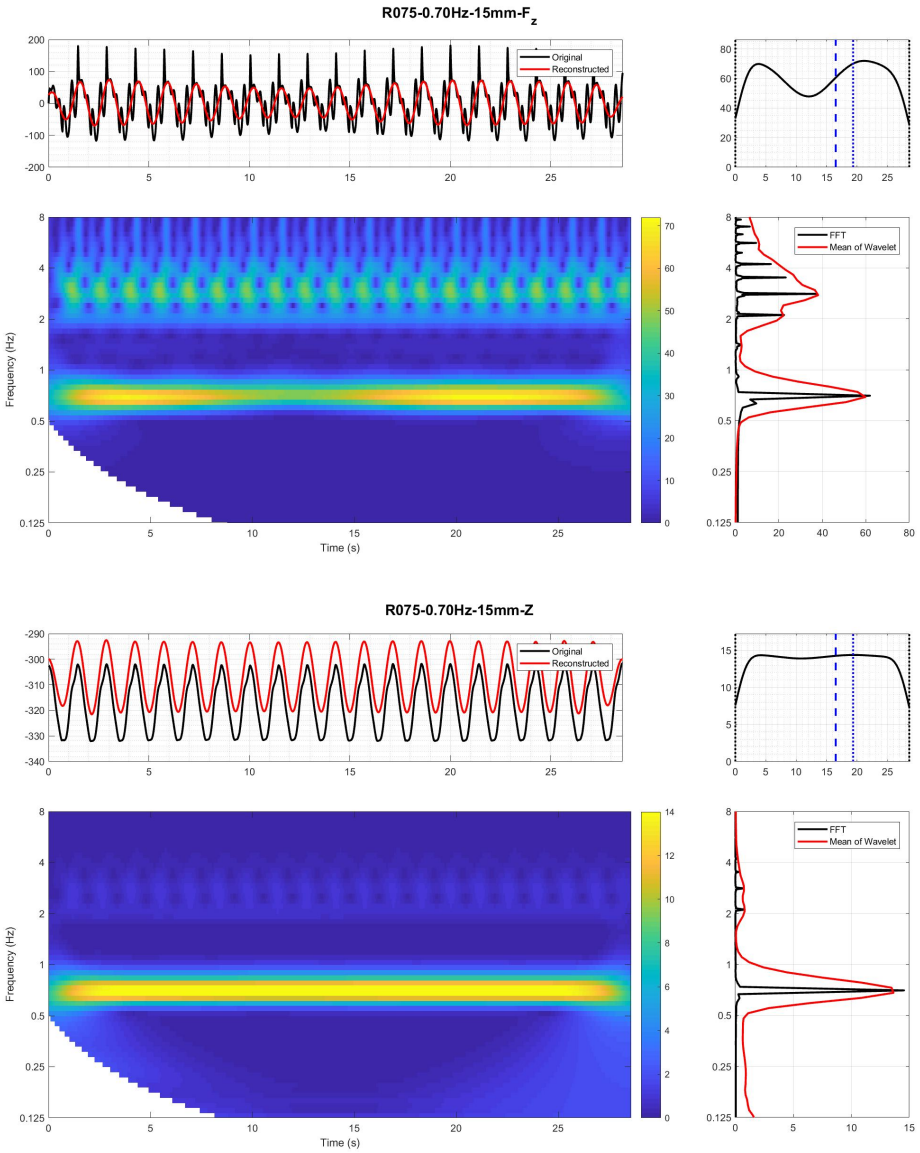

Figure C.5: Wavelet Study of Heave radiation with amplitude of motion 15 mm at 0.7 Hz ($\nu_{WA} \approx 1.1$). The two plots given are for heave excitation force (top) and heave motion (bottom); with four subplots in each. (Top left) Time series displaying original measurement and primary harmonic wavelet reconstruction. (Top right) Amplitude variation of the primary component, (bottom left) wavelet surface of the measuremen and (bottom right) FFT compared with average of wavelet.

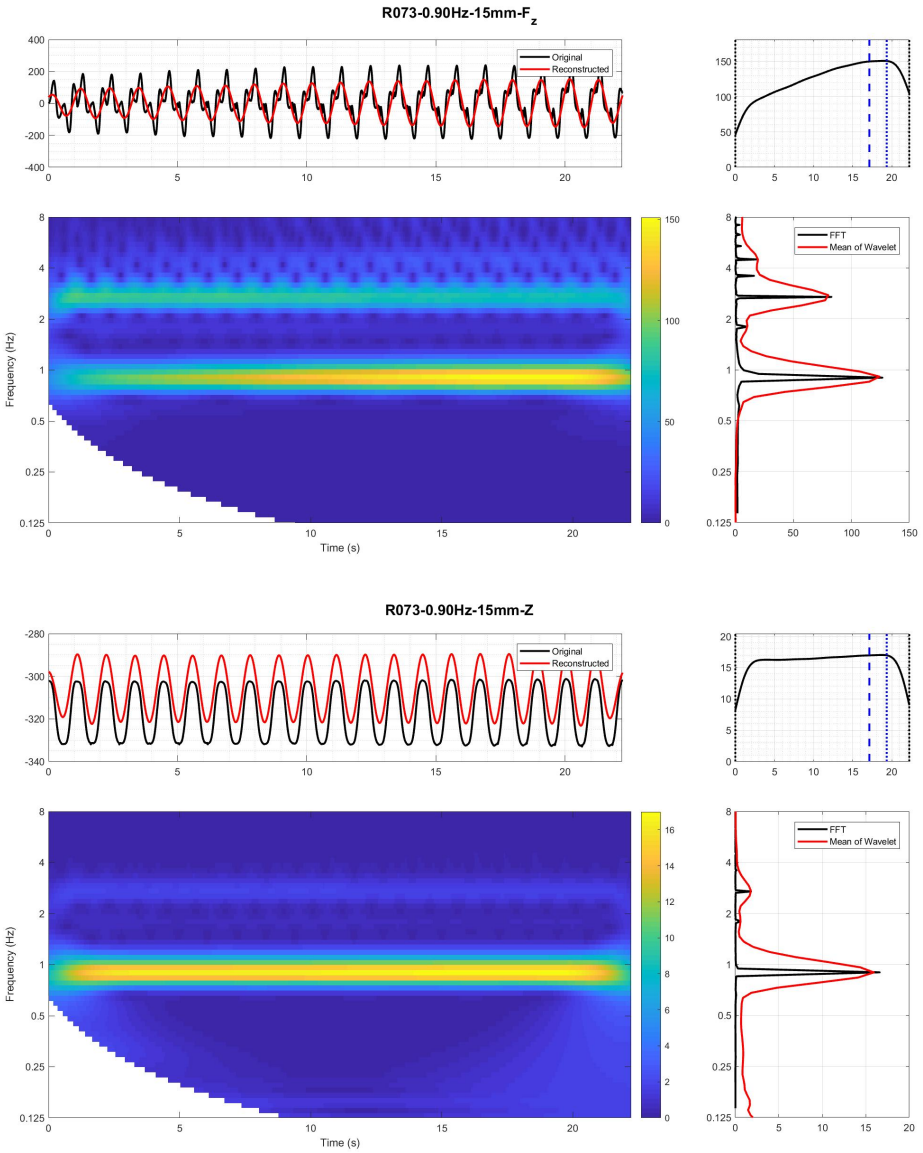

Figure C.6: Wavelet Study of Heave radiation with amplitude of motion 15 mm at 0.9 Hz ($\nu_{WA} \approx 1.8$). The two plots given are for heave excitation force (top) and heave motion (bottom); with four sub-plots in each. (Top left) Time series displaying original measurement and primary harmonic wavelet reconstruction. (Top right) Amplitude variation of the primary component, (bottom left) wavelet surface of the measuremen and (bottom right) FFT compared with average of wavelet.

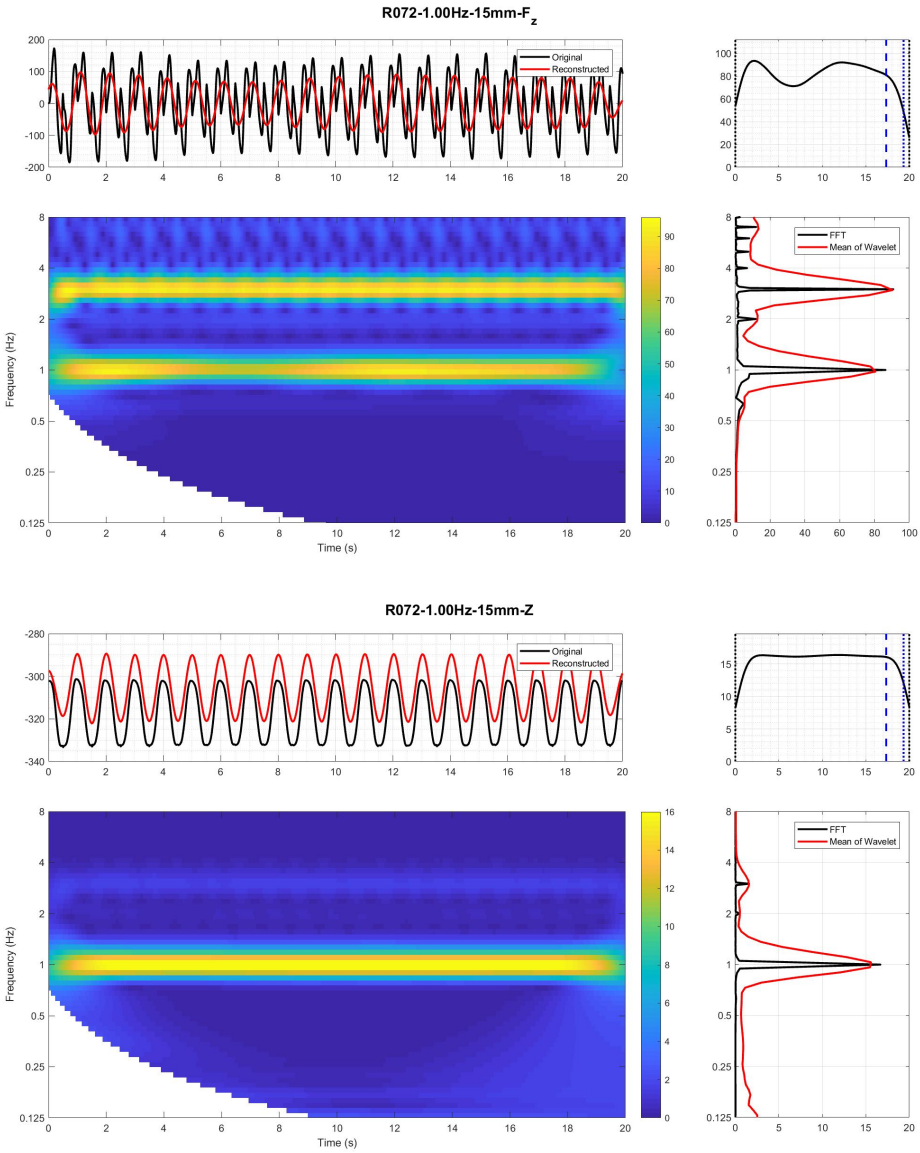

Figure C.7: Wavelet Study of Heave radiation with amplitude of motion 15 mm at 1.0 Hz ($\nu_{WA} \approx 2.3$). The two plots given are for heave excitation force (top) and heave motion (bottom); with four subplots in each. (Top left) Time series displaying original measurement and primary harmonic wavelet reconstruction. (Top right) Amplitude variation of the primary component, (bottom left) wavelet surface of the measuremen and (bottom right) FFT compared with average of wavelet.

C.4 Stereo-Videogrammetry

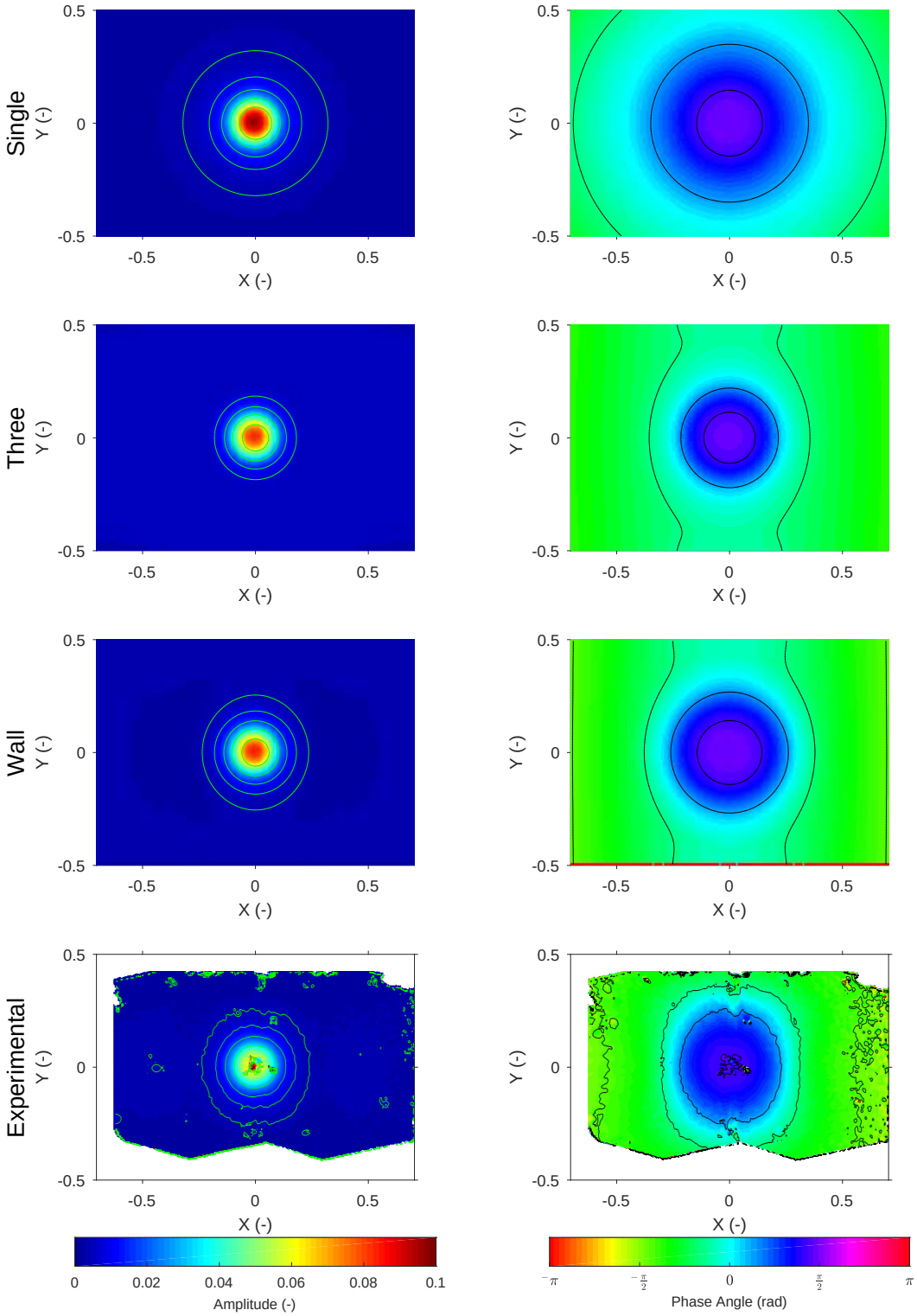

Figure C.8: Frequency domain radiation free surface for condition $\nu_{WA} \approx 0.31$ ($S_{DR} \approx 0.34$), this represents negligible array effects. Left column is amplitude, right column is phase. Top three rows are numerical predictions for the single, three and wall conditions; the bottom row is experimental results.

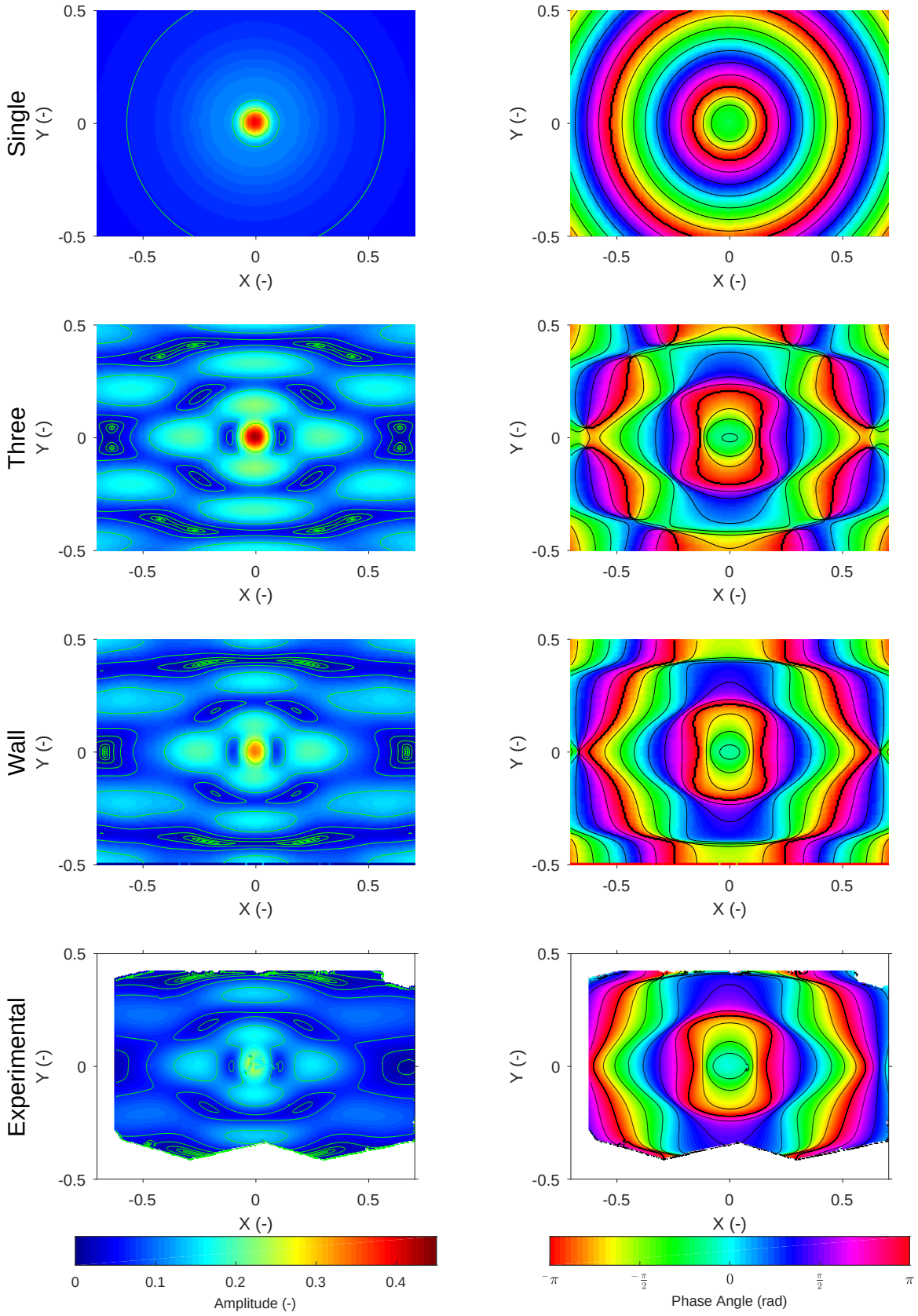

Figure C.9: Frequency domain radiation free surface for condition $\nu_{WA} \approx 2.3$ ($S_{DR} \approx 0.34$), this represents negligible array effects. Left column is amplitude, right column is phase. Top three rows are numerical predictions for the single, three and wall conditions; the bottom row is experimental results.

Appendix D

Active Control of a Submerged WEC in a Channel Supplementary Material

D.1 Control System

The force control system was implemented with LabView, the front panel and block diagram of the resulting control system are presented in Figures D.1 and D.2.

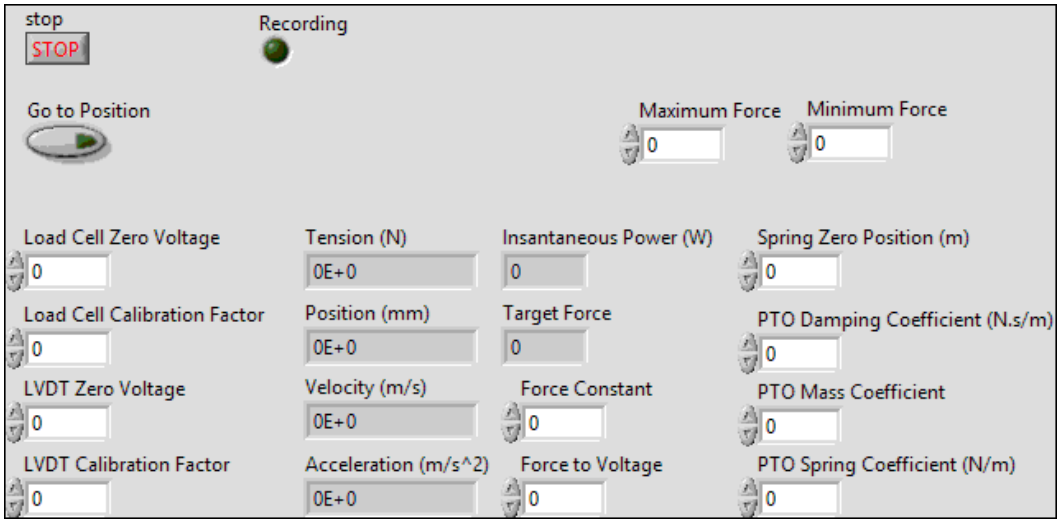

Figure D.1: Front panel of the LabView control system.

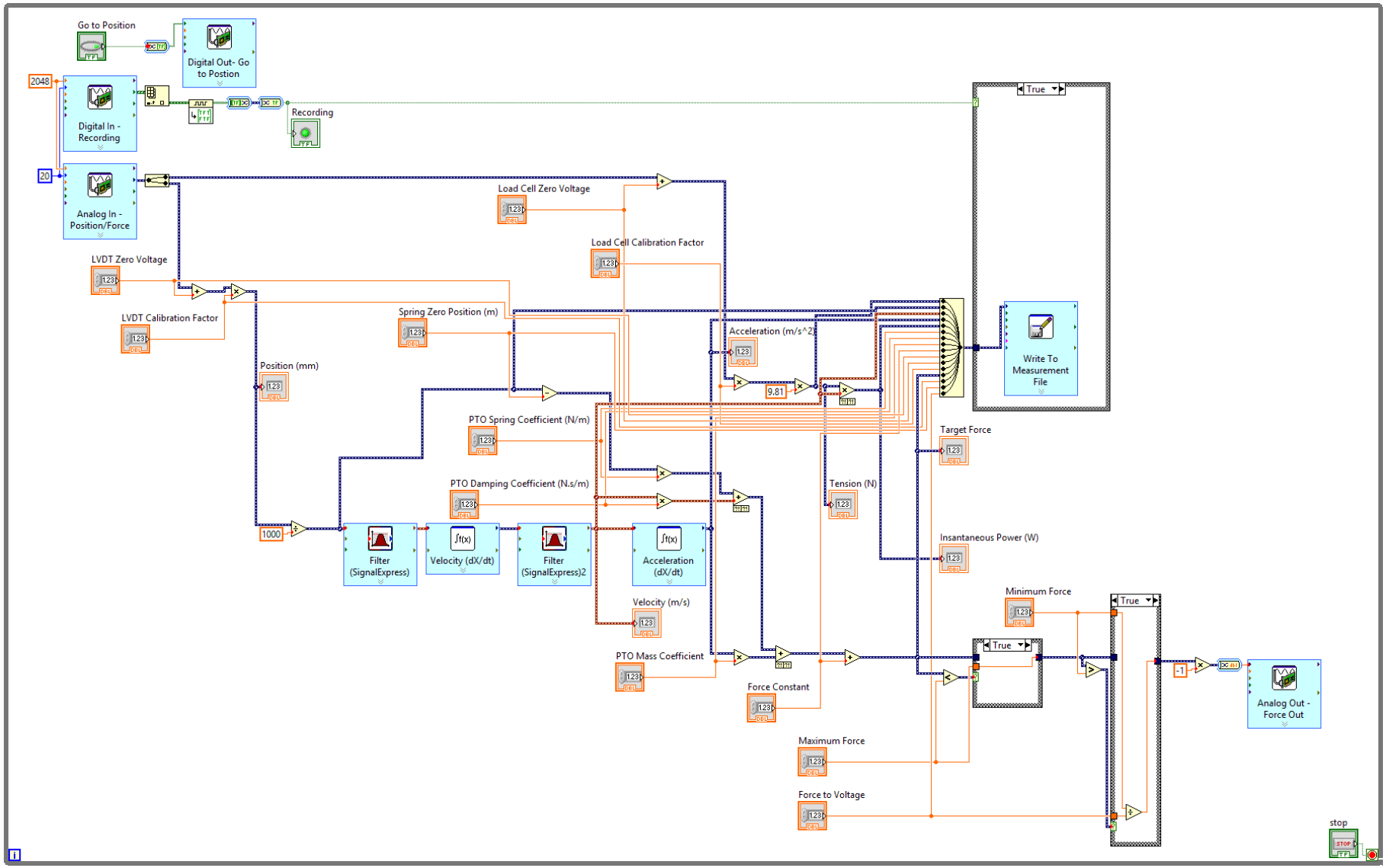

Figure D.2: Block diagram of the LabView control system.

D.2 Additional RAO

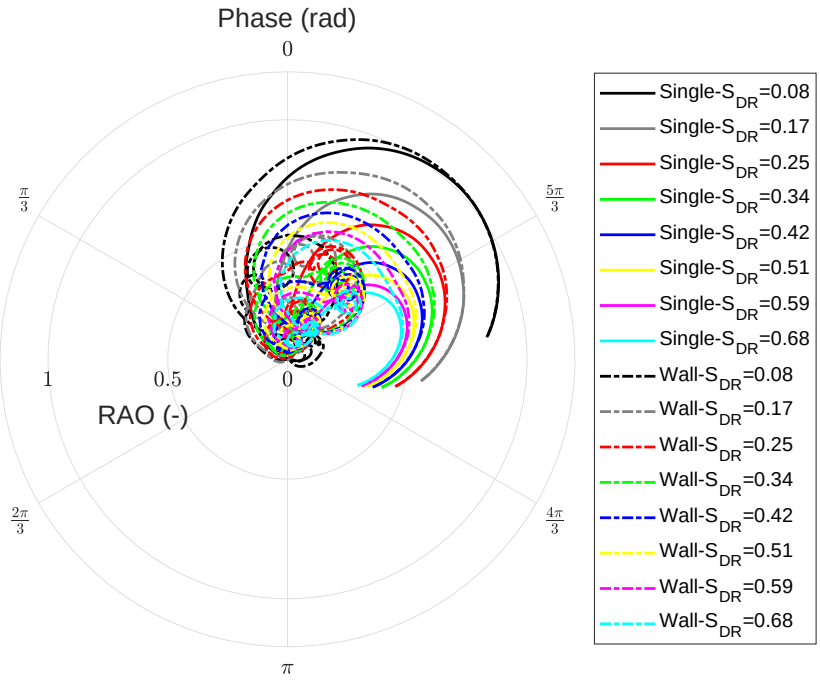

Figure D.3: Submersion depth effect on heave RAO for control A in polar format.

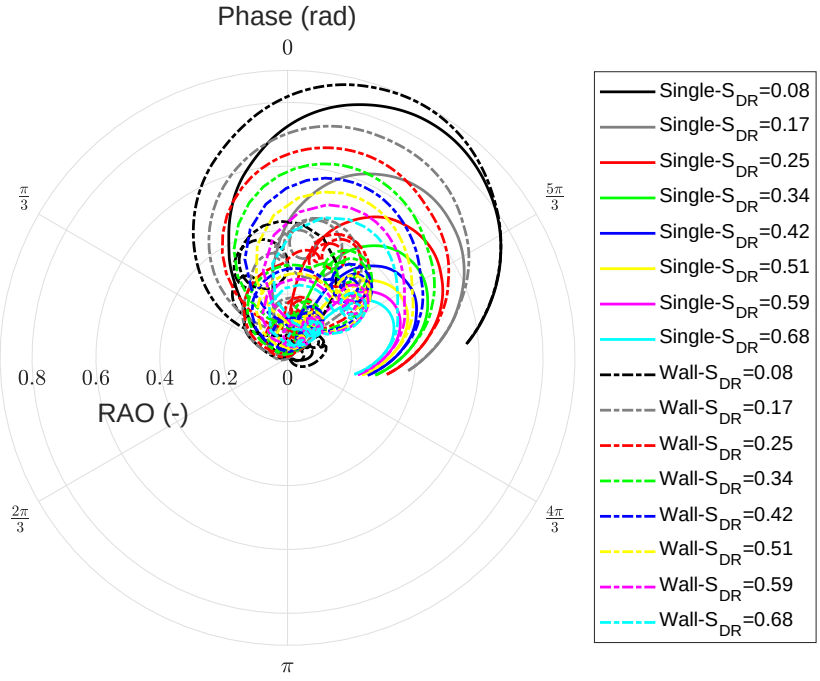

Figure D.4: Submersion depth effect on heave RAO for control B in polar format.

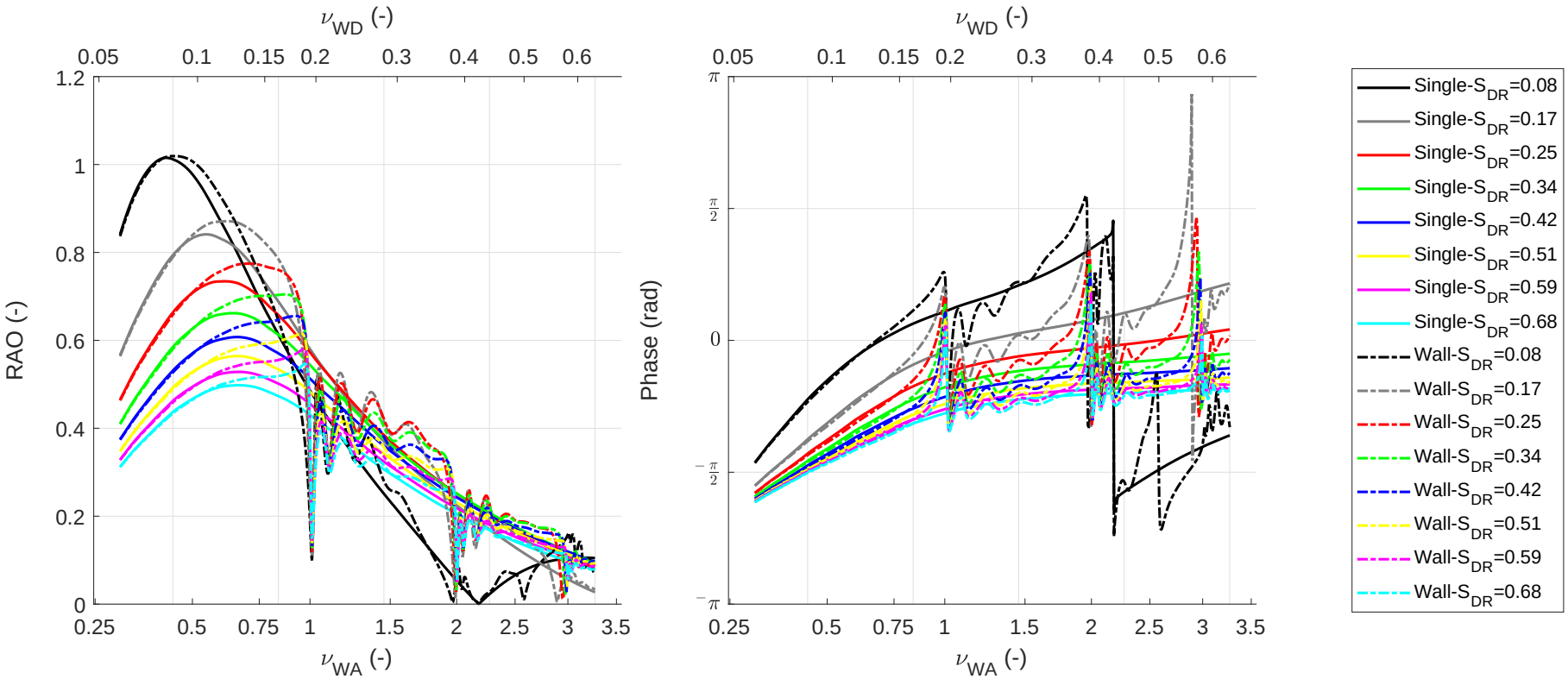

Figure D.5: Submersion depth effect on heave RAO for control A. Incident wave is expressed by the device and array non-dimensional linear wave numbers on the top and bottom x-axes respectively.

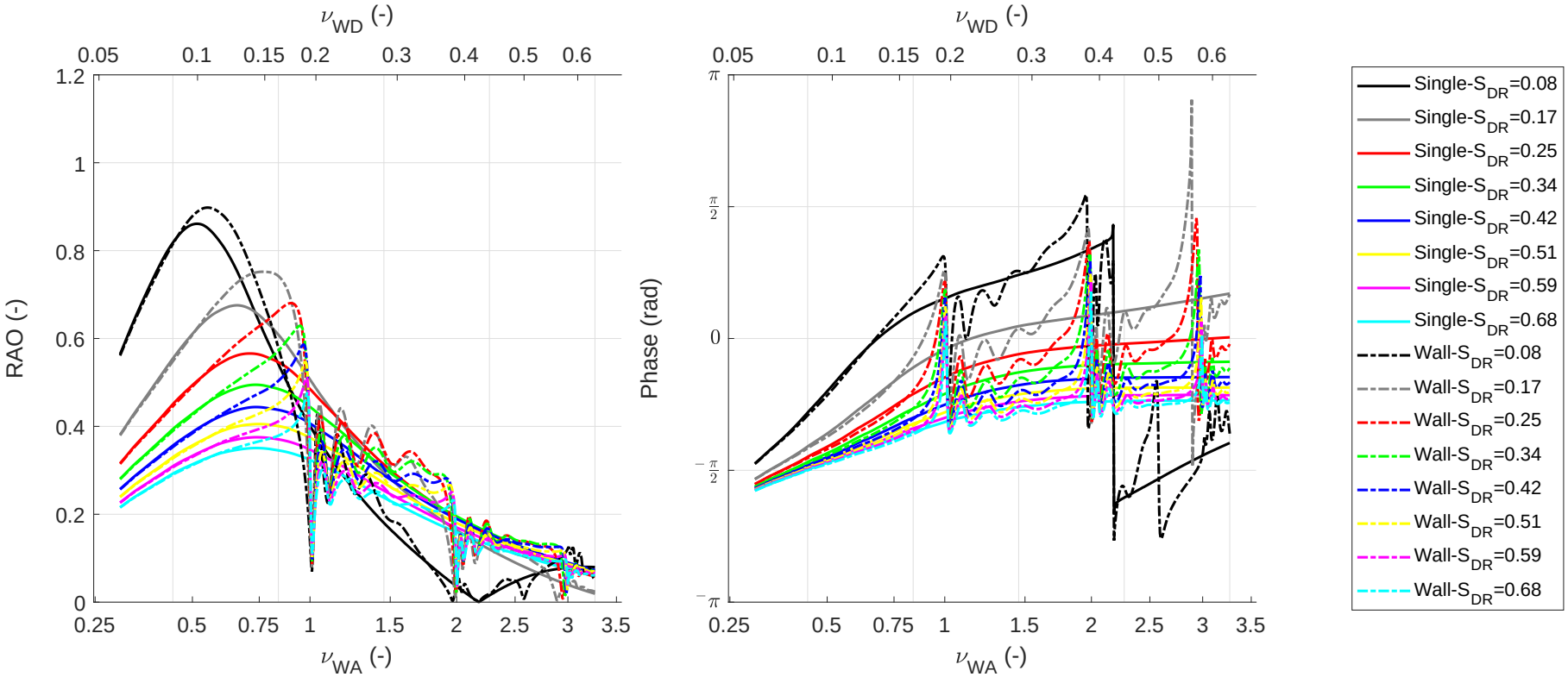

Figure D.6: Submersion depth effect on heave RAO for control B.Incident wave is expressed by the device and array non-dimensional linear wave numbers on the top and bottom x-axes respectively.

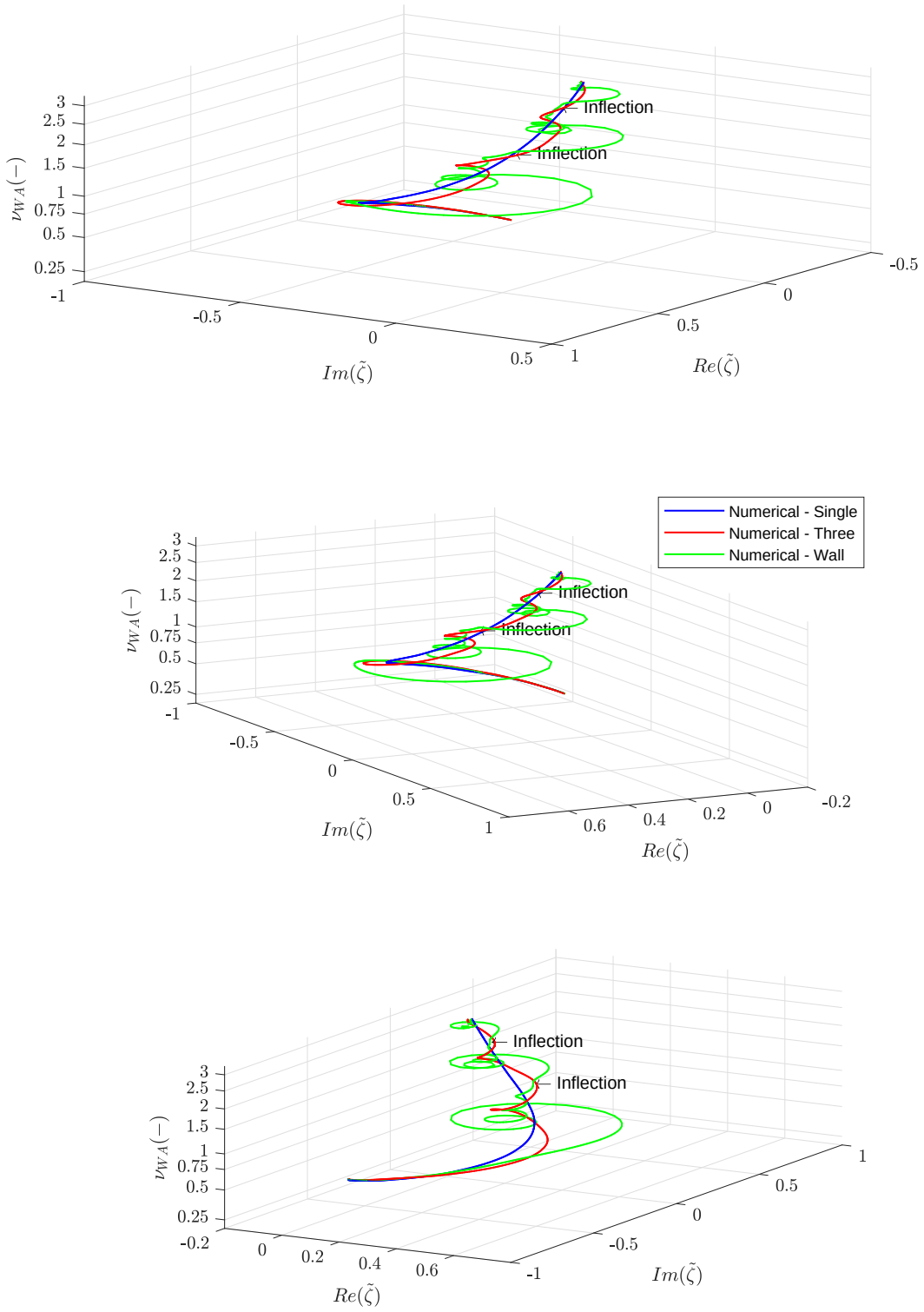

Figure D.7: Heave RAO in cylindrical coordinates for control A.

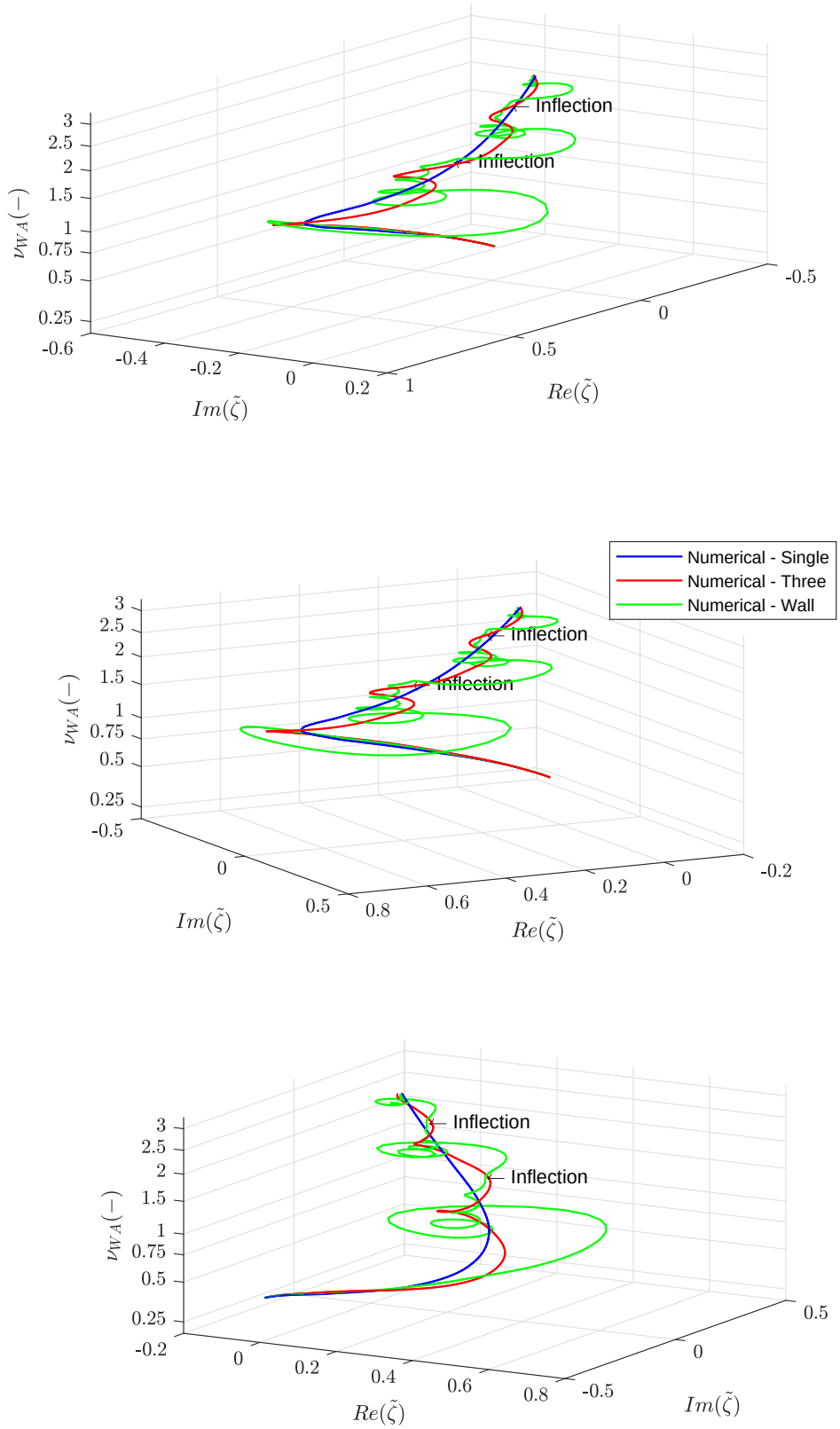

Figure D.8: Heave RAO in cylindrical coordinates for control B.

D.3 Stereo-Videogrammetry

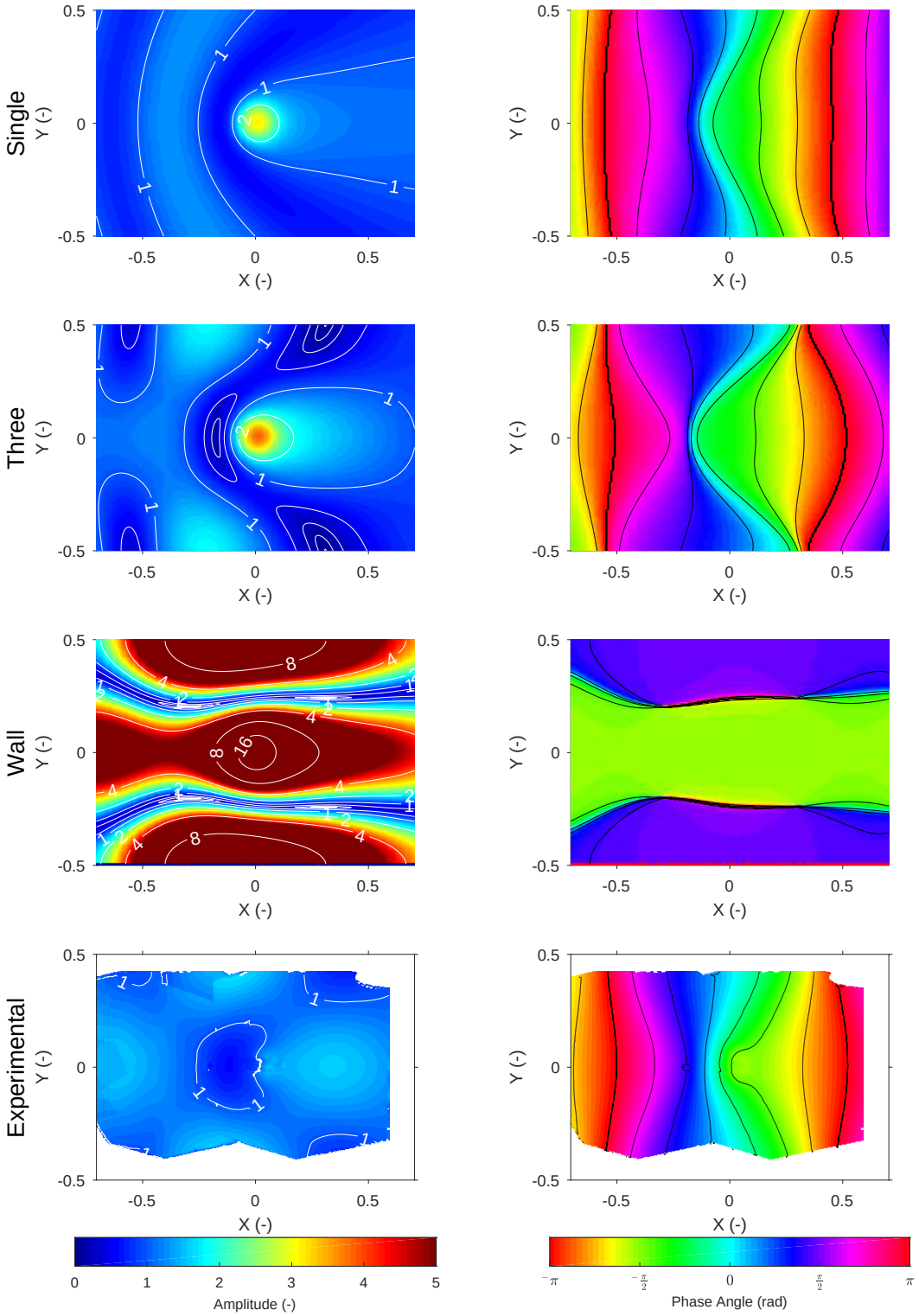

Figure D.9: Frequency domain free surface for condition $\nu_{WA} \approx 1$ ($S_{DR} \approx 0.34$). Left column is amplitude, right column is phase. Top three rows are numerical predictions for the single, three and wall conditions; the bottom row is experimental results.

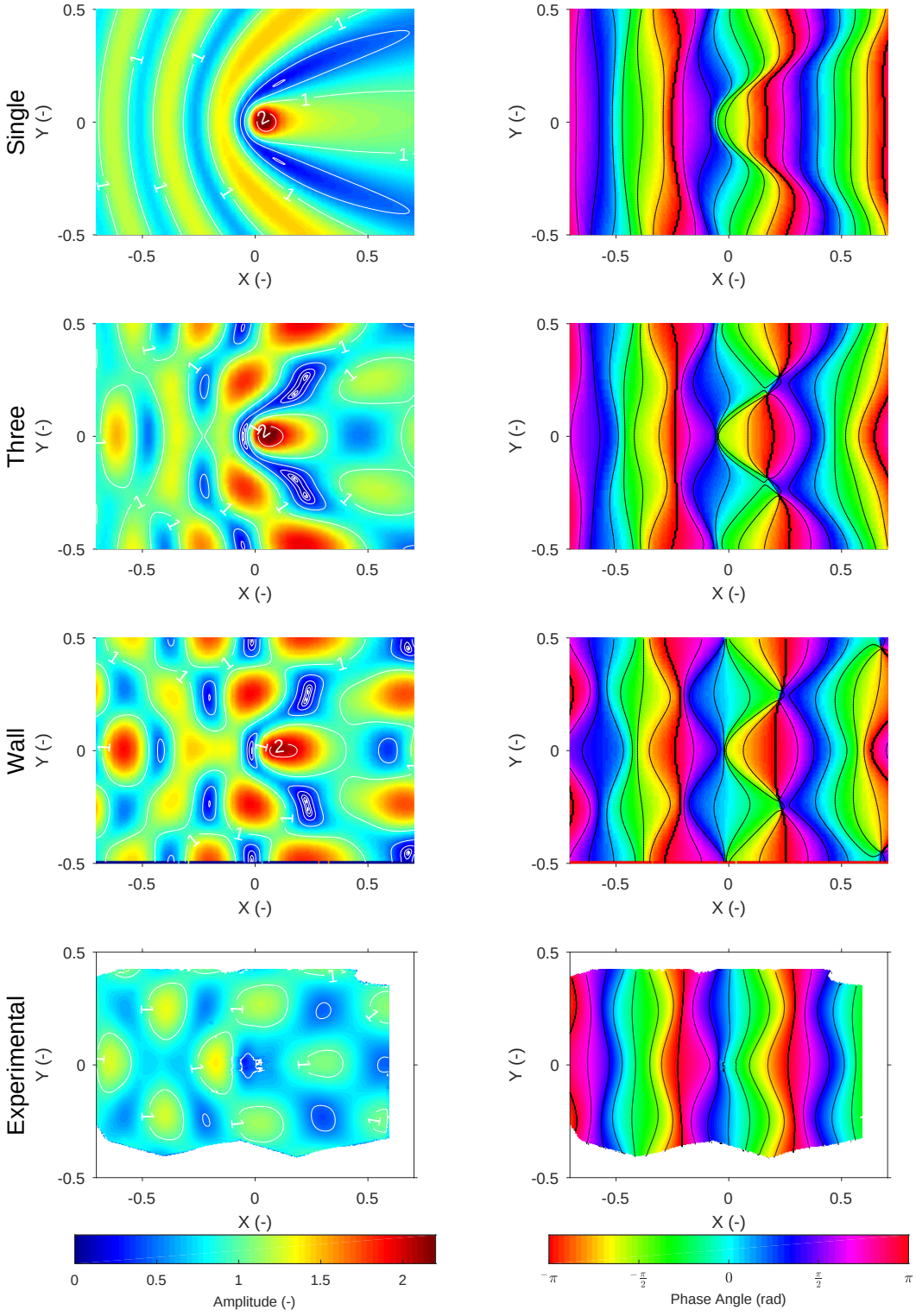

Figure D.10: Frequency domain free surface for condition $\nu_{WA} \approx 2$ ($S_{DR} \approx 0.34$). Left column is amplitude, right column is phase. Top three rows are numerical predictions for the single, three and wall conditions; the bottom row is experimental results.

Appendix E

Uncertainty Analysis

E.1 Measurement Devices

E.1.1 ATI Mini58 IP68 Axial Cable Output

The mechanical characteristics of the ATI mini 58, IP 68 variant, are described by Table E.1. While the options for the factory calibration specifications of the ATI mini 58 are specified in Table E.2.

Table E.1: Mechanical characteristics of ATI mini58 IP68 variant (ATI Industrial Automation 2018).

Single-Axis Overload	
F_x, F_y	±21000 N
F_z	±48000 N
T_{xx}, T_{yy}	±590 Nm
T_{zz}	±800 Nm
Stiffness (Calculated)	
X-axis & Y-axis forces (Kx, Ky)	2.5×10^8 N/m
Z-axis force (Kz)	3.7×10^8 N/m
X-axis & Y-axis torque (Ktx, Kty)	1.1×10^5 Nm/rad
Z-axis torque (Ktz)	2.0×10^5 Nm/rad
Resonant Frequency	
Fx, Fy, Tz	
Fz, Tx, Ty	
Physical Specifications	
Weight*	0.804 kg
Diameter*	65.4 mm
Height*	37.6 mm

* Specifications include standard interface plates.

Table E.2: Load cell factory calibration specifications (ATI Industrial Automation 2018).

Calibration	F_x, F_y	F_z	T_{xx}, T_{yy}	T_{zz}	F_x, F_y	F_z	T_{xx}, T_{yy}	T_{zz}
SI-700-30	700 N	1700 N	30 Nm	30 Nm	1/3 N	1/2 N	1/100 Nm	1/160 Nm
SI-1400-60	1400 N	3400 N	60 Nm	60 Nm	2/3 N	1 N	1/50 Nm	1/80 Nm
SI-2800-120	2800 N	6800 N	120 Nm	120 Nm	1 1/2 N	2 N	1/25 Nm	1/40 Nm
	Sensing Ranges				Resolution			

These calibration specification have not been used in the experimental process used here.

Instead an in situ calibration was performed, the results are presented in Table E.3. The standard estimation of error (SEE) has been determined with (ITTC 2017a),

$$SEE = \sqrt{\sum_{1}^{n} \frac{(y_n - y_{LS,n})^2}{n(n-1)}} \tag{E.1}$$

Where n is the number of calibration points, y_n is the calibration data point and $y_{LS,n}$ is the fitted value.

Table E.3: Load Cell in situ calibration details. With 221 calibration data points.

F_x, F_y	F_z	T_{xx}, T_{yy}	T_{zz}	F_x	F_y	F_z	T_{xx}	T_{yy}	T_{zz}
±120 N	±300 N	±12 Nm	±8 Nm	0.0446	0.0470	0.0802	0.0066	0.0068	0.0223
Calibration Ranges				Standard Estimation of Error					

E.1.2 Resistive Wave Gauges

In situ calibration were performed over a range of ±100 mm, with at least 12 data points. Any calibration with standard estimation of error exceeding 0.5 mm was discounted and repeated (after identifying the issue with the calibration).

E.1.3 Motion Capture - LVDT

In situ calibration were performed over a range of ±100 mm, with at least 12 data points. Any calibration with standard estimation of error exceeding 0.5 mm was discounted and repeated (after identifying the issue with the calibration).

E.1.4 Motion Capture - Qualisys

The Qualisys motion capture employed used four *Oqus 300+ p*, a wand calibration was employed (Qualisys AB 2017). The calibration results are presented in Table E.4.

Table E.4: Qualisys Calibration results.

Camera	X (mm)	Y (mm)	Z (mm)	Points	Average residual (mm)
01	-2189.43	-1510.61	2095.08	1221	0.46408
02	1793.69	2453.96	1744.92	1399	0.41563
03	1720.46	-1682.99	1738.90	1269	0.30698
04	-2416.61	2399.38	1656.45	1551	0.34044

Standard deviation of wand length = 0.27490 mm

E.2 Diffraction Forces and Moment

Possible sources of error in the non-dimensional and normalised diffraction loads reported include, submersion depth of the BA, motion of the BA, geometry of the BA, the motion tracking frame, water depth, incident wave amplitude, density of water, acceleration due to gravity and load measurement.

Through the testing the submersion depth was monitored closely and has been discounted as a source of error. BA motion amplitudes were deemed irrelevant through monitoring motions. The BA geometry is within measurement error to correct dimensions and so possible associated errors are ignored. The frame used to mount the motion tracking balls was deemed to have minimal effect; in certain experimental conditions it was observed that the full water volume about the frame was displaced which implies that the frame has negligible impact on the pressure wave dynamics. Density of water and acceleration due to gravity are being ignored.

The non-dimensional normalised diffraction force , $F_{ND-D}(\omega)$, and moment, $M_{ND-D}(\omega)$, are defined by,

$$F_{ND-D}(\omega) = \frac{F_{ex}(\omega)}{a\rho A_w g} \tag{E.2a}$$

$$M_{ND-D}(\omega) = \frac{M_{ex}(\omega)}{a\rho A_w g L_D} \tag{E.2b}$$

Where $F_{ex}(\omega)$ is excitation force, $M_{ex}(\omega)$ is excitation moment, a is incident wave amplitude, ρ density of water, A_w is wetted surface area, g is acceleration due to gravity and L_D is characteristic device dimension. These variables can be considered independent, with the incident wave amplitude taken from separate runs where no structure was present. The data reduction equation for these two non-dimensional quantities are given by

$$u(F_{ND-D}(\omega)) = \sqrt{\left(\frac{1}{a\rho A_w g} \cdot u(F_{ex}(\omega))\right)^2 + \left(\frac{F_{ex}(\omega)}{a^2\rho A_w g} \cdot u(a)\right)^2} \tag{E.3a}$$

$$u(F_{ND-D}(\omega)) = \sqrt{\left(\frac{1}{a\rho A_w g L_D} \cdot u(M_{ex}(\omega))\right)^2 + \left(\frac{M_{ex}(\omega)}{a^2\rho A_w g L_D} \cdot u(a)\right)^2} \tag{E.3b}$$

Where the non-important uncertainties have been discounted.

E.3 Radiation Force

Possible sources of error in the non-dimensional and normalised diffraction loads reported include, submersion depth of the BA, unwanted motion of the BA, geometry of the BA, the motion tracking frame, water depth, density of water, acceleration due to gravity, load measurement.

Through the testing the submersion depth was monitored closely and has been discounted as a source of error. BA motions from the run have been used for normalisation, any additional uncertainty is ignored. The BA geometry is within measurement error to correct dimensions and so possible associated errors are ignored. The frame used to mount the motion tracking balls was deemed to have minimal effect; in certain experimental conditions it was observed that the full water volume about the frame was displaced which implies that the frame has negligible impact on the pressure wave dynamics. Density of water and acceleration due to gravity are being ignored.

The non-dimensional normalised diffraction force , $F_{ND-D}(\omega)$, and moment, $M_{ND-D}(\omega)$, are defined by,

$$F_{ND-R} = \frac{F_{ex-R}}{aA_w g\rho\omega i} \tag{E.4}$$

Where $F_{ex-R}(\omega)$ is radiation excitation force, a is amplitude of motion, ρ density of water, A_w is wetted surface area, g is acceleration due to gravity, ω is angular oscillation frequency and i is the imaginary unit. These variables can be considered independent. The data reduction equation for these two non-dimensional quantities are given by

$$u(F_{ND-R}(\omega)) = \sqrt{\left(\frac{1}{a\rho A_w g}\cdot u(F_{ex-R}(\omega))\right)^2 + \left(\frac{F_{ex-R}(\omega)}{a^2\rho A_w g}\cdot u(a)\right)^2} \tag{E.5}$$

Where the non-important uncertainties have been discounted.

Appendix F

Publications

F.1 Preliminary investigation on the use of tank wall reflections to model WEC array effects

It is the published article: Winship, B., Fleming, A., Penesis, I., Hemer, M., Macfarlane, G., 2018. Preliminary investigation on the use of tank wall reflections to model WEC array effects, Ocean engineering, 164, 388-401

F.2 Application of photogrammetry for spatial free surface elevation and velocity measurement in wave flumes

It is the published article: Fleming, A., Winship, B., Macfarlane, G., 2018. Application of photogrammetry for spatial free surface elevation and velocity measurement in wave flumes, Proceedings of the Institution of Mechanical Engineers, Part M: Journal of engineering for the maritime environment, 233(3), 905-917